

BEADS: A canonical visualization of quantum states for applications in quantum information processing

Authors

Dennis Huber^{1,2}, Steffen J. Glaser^{1,2*}

Affiliations

¹Technical University of Munich, TUM School of Natural Sciences, Lichtenbergstrasse 4, 85747 Garching, Germany

²Munich Center for Quantum Science and Technology (MCQST), 80799 München, Germany

*glaser@tum.de

Abstract

Here, we introduce a generalized phase-space representation of qubit systems called the *BEADS* representation which makes it possible to visualize arbitrary quantum states in an intuitive and an easy to grasp way. At the same time, our representation is exact, bijective, and general. It bridges the gap between the highly abstract mathematical description of quantum mechanical phenomena and the mission to convey them to non-specialists in terms of meaningful pictures and tangible models. Several levels of simplifications can be chosen, e.g., when using the *BEADS* representation in the communication of quantum mechanics to the general public. In particular, this visualization has predictive power in contrast to simple metaphors such as Schrödinger's cat.

Teaser

An intuitive and exact approach to visualize and understand states and dynamics in quantum computing and beyond.

Introduction

The field of quantum science and technology is rapidly developing (1, 2) which creates the necessity to educate scientists beyond physics, engineers, technicians, high school students, and the general public. However, quantum physics is notoriously difficult to convey: "Studying the quantum world is not intuitive, and many researchers have difficulty communicating the weirdness of quantum physics because it's not relatable to everyday experiences.[...] Because quantum processes are extremely difficult to visualize; the processes become distant and foreign" (3). Similarly, J. Audretsch stated: "What makes the understanding of quantum theory so difficult is its lack of images. In its framework, there is no intuition evoked by memorable images and metaphors, but only the power of mathematical formulation" (translated from (4)). In fact, this problem has been around for about a century, which is vividly expressed by the following editorial introductory note to an article by Niels Bohr (5) published in 1928: "It must be confessed that the new quantum mechanics is far from satisfying the requirements of the layman who seeks to clothe his conceptions in figurative language. Indeed, its originators probably hold that such a symbolic representation is inherently impossible. It is earnestly to be hoped that this is not their last word on the subject, and that they may yet be successful in expressing the quantum postulate in picturesque form" (5).

In the following, we will present a powerful visualization technique that is able to provide meaningful pictures, animations as well as tangible models of abstract quantum phenomena. We hasten to add that we do not claim that it will be suitable for all types of quantum phenomena, yet it is well applicable to the important field of quantum information processing where typically finite-dimensional quantum systems are studied in a non-relativistic setting. In particular, the proposed visualization can be applied (but is not limited) to systems consisting of coupled quantum bits (qubits), i.e., quantum mechanical two-level system such as electron or nuclear spins- $\frac{1}{2}$, a subset of the internal states of trapped ions or atoms, or superconducting quantum bits on a chip. In this scenario, the qubits are individually addressable, and their states can be individually measured. Due to the coupling between the qubits, a system of N qubits has 2^N basis states and can be in highly entangled non-classical superpositions of these basis states. This exponential growth of the available state space is a source of the power of quantum information and at the same time makes it impossible in practice to represent the full information hidden in a general quantum state by classical means if the quantum system consists of more than a few tens of qubits. This appears to dash any hope to be able to find a useful and informationally complete visualization of quantum states. However, as we will illustrate in the following, the availability of such a visualization for few quantum bits is extremely useful both in education and in research. In fact, for simplicity and practical convenience we will limit our examples to systems of less than four qubits. It is important to note that this is not due to fundamental limitations of the approach which can be pushed to much larger systems – albeit at the cost of higher required computational power for the classical simulations and at the expense of higher complexity of the visualization which is a natural and necessary consequence of the exponential increase of the state space with the number of qubits.

At this point, it is instructive to point out another highly successful visualization of quantum systems. For the case of a single quantum bit (such as the spin of an electron), an extremely useful visualization is the Bloch vector (6, 7). This is a three-dimensional vector with real components which can be easily visualized as an arrow in 3D space. The ability to visualize and to imagine the motion of the Bloch vector is enabling scientists to understand and to design highly nontrivial experimental protocols in magnetic resonance spectroscopy and imaging (8). Unfortunately, this simple vector picture alone is not able to capture the full information encoded in the quantum state of two or more qubits. The *BEADS* representation

which we will introduce in the following can be seen as a natural (albeit perhaps not obvious) generalization of the Bloch vector representation to arbitrary multi-qubit systems. Note that the Bloch vector picture is able to represent the state of a quantum bit realized in a superconducting quantum chip and can be regarded as a physical model of the (superconducting) qubit. However, it is important to understand that physical models are in general not simply scaled versions (as, e.g., a model airplane) of another physical object. What is represented by the Bloch vector is not an upscaled version of the part of the chip hosting the qubit (or of a photon) but an equivalent mathematical representation of its abstract quantum state $|\psi\rangle$ (or its density operator) that can be visualized as a three-dimensional arrow. Similarly, the BEADS representation is able to capture the information of the quantum state $|\psi\rangle$ for multi-qubit systems but should not be misunderstood as a magnified view of the qubits which may, e.g., be arrays of cold atoms, photons or superconducting circuits. Moreover, our representation is not a mechanistic model of quantum computing and is thus not capable of performing quantum computation on its own. The scientific questions that we will address in detail in the following are

- (a) What are desirable features of graphical representations of the state of a system of a set of individually addressable and detectable qubits in quantum technology applications, such as quantum computing, quantum control, and beyond?
- (b) Can these desirable features be simultaneously realized in a canonical graphical representation?
- (c) Can such a canonical graphical representation be rigorously formulated?
- (d) What are the strengths and potential limitations of such a representation?

In this paper, we answer these questions constructively by providing the conceptual and mathematical description of the BEADS representation and by demonstrating its useful properties by illustrative examples. We have implemented an easy to use software package and created tangible models both which are being used in different educational formats (ranging from the physics quantum science and technology master program of the Technical University of Munich and the Ludwig Maximilian University of Munich, to advanced trainings for physics teachers, workshops for high-school students in the PhotonLab of the Max-Planck-Institute for Quantum Optics (MPQ), and outreach activities for the general public at science fairs and at the Deutsches Museum in Munich.

Although the detailed mathematical and physical basis of the BEADS representation is non-trivial, due to its intuitiveness, it is possible to take full advantage of this visualization approach without having to understand the intricacies of the underlying mapping.

In order to provide a gentle introduction to the BEADS representation, we have structured the Results section in two main parts.

In the first part (“A light introduction to BEADS”), we introduce the BEADS representation in a phenomenological way, similarly to how a teacher might use it to visually introduce the properties of quantum bits, the standard computational basis states, the concepts of superpositions and entanglement, and the effect of quantum gates based on simple rules and recipes how to interpret the BEADS visualization. The advantages of the BEADS representation are illustrated in comparison with alternative visualizations techniques.

In the second part, we provide the theoretical background of the mapping and detail links to standard quantum concepts, such as expectation values of projective measurements, correlations and entanglement. Also, relations to already existing visualization approaches are discussed. Technical details and additional illustrative examples are provided in the supplementary material.

For simplicity, we will focus our results on pure states. However, the BEADS representation is also suited to visualize arbitrary mixed states which we will briefly illustrate.

Results

A light introduction to BEADS

We start with a light, non-technical introduction to the *Quantum BEADS representation* (or for short, the *BEADS representation*) to fix ideas and get a feel of this unique representation of abstract quantum states (in brackets, we sparingly add auxiliary information for experts). The BEADS representation provides a cohesive and seamless approach to visualize both classical and quantum information in a way which is simple, quantitative, and complete. In general, the BEADS representation consists of one or more colored spheres, called *beads*. There are two major kinds of beads: *Q-Beads* that are associated with the state of individual physical qubits and additional correlation beads, in particular *E-Beads* (representing entanglement-based non-classical correlations). Before turning to the important correlation beads and their relation to entanglement, let us first look at Q-Beads and their connection with the well-known classical bit states.

Classical bits

A classical bit can only be in one of two possible states: either it has the value 0 or the value 1. We can represent these two states graphically, e.g., by a red and green colored square (called a *color patch*), as illustrated on the left side of Fig. 1. A concrete tangible model of a classical bit could be a card with a red (= 0) and a green (= 1) side. (We deliberately avoid representing bit states by the two sides of a coin, i.e., a *circular* disc with different colors in order to clearly distinguish them from 2D images of spherical quantum beads, which of course also look disc-shaped.)

Qubits

In the *BEADS* representation, a single qubit is represented by a *sphere* with a red and an antipodal green pole, called a *Q-Bead*, see Fig. 1 (for a pure qubit state, the vector connecting the center of the sphere and the red pole is identical to the well-known Bloch vector). With the help of the color scale at the bottom of Fig. 1, the colors of a Q-Bead can be mapped to a value in the range between 0 and 1. Physically, this value corresponds to directional measurement probabilities, as will be explained in more detail below.

Computational basis states

The computational basis states (with standard symbols $|0\rangle$ and $|1\rangle$) of a qubit correspond to Q-Bead orientations where either the red or the green pole is facing upwards (along the positive z-axis), see Fig. 1. Note that for these two special qubit states, a zoomed top view of the Q-Beads uppermost point (referred to as the Q-Bead's *north pole*) looks exactly like the red or green *color patches* that we have used to represent the classical bit values 0 and 1, cf. first two rows of Fig. 1. This provides a seamless transition between the graphical representations of qubits in computational basis states and classical bit states.

Superposition states

Whereas a classical bit is constrained to be in one of the two states 0 or 1, a qubit is not constrained to be in one of the two computational basis states $|0\rangle$ or $|1\rangle$. In fact, it can be in one of an *infinite* number of different *superposition states* of the form $c_0|0\rangle + c_1|1\rangle$ (where the coefficients c_0 and c_1 are complex numbers, normalized such that $|c_0|^2 + |c_1|^2 = 1$). Every superposition state of this form can be uniquely mapped to a three-dimensional orientation of the Q-Bead (this mapping is identical to the standard mapping from an arbitrary pure qubit state to the Bloch vector orientation (2)). For example, the Q-Bead shown in the third row of Fig. 1 is oriented such that its red pole is tilted slightly away from

the z-direction resulting in a dark-red zoomed color patch at the north pole, corresponding in this example to a numerical value of about 0.18.

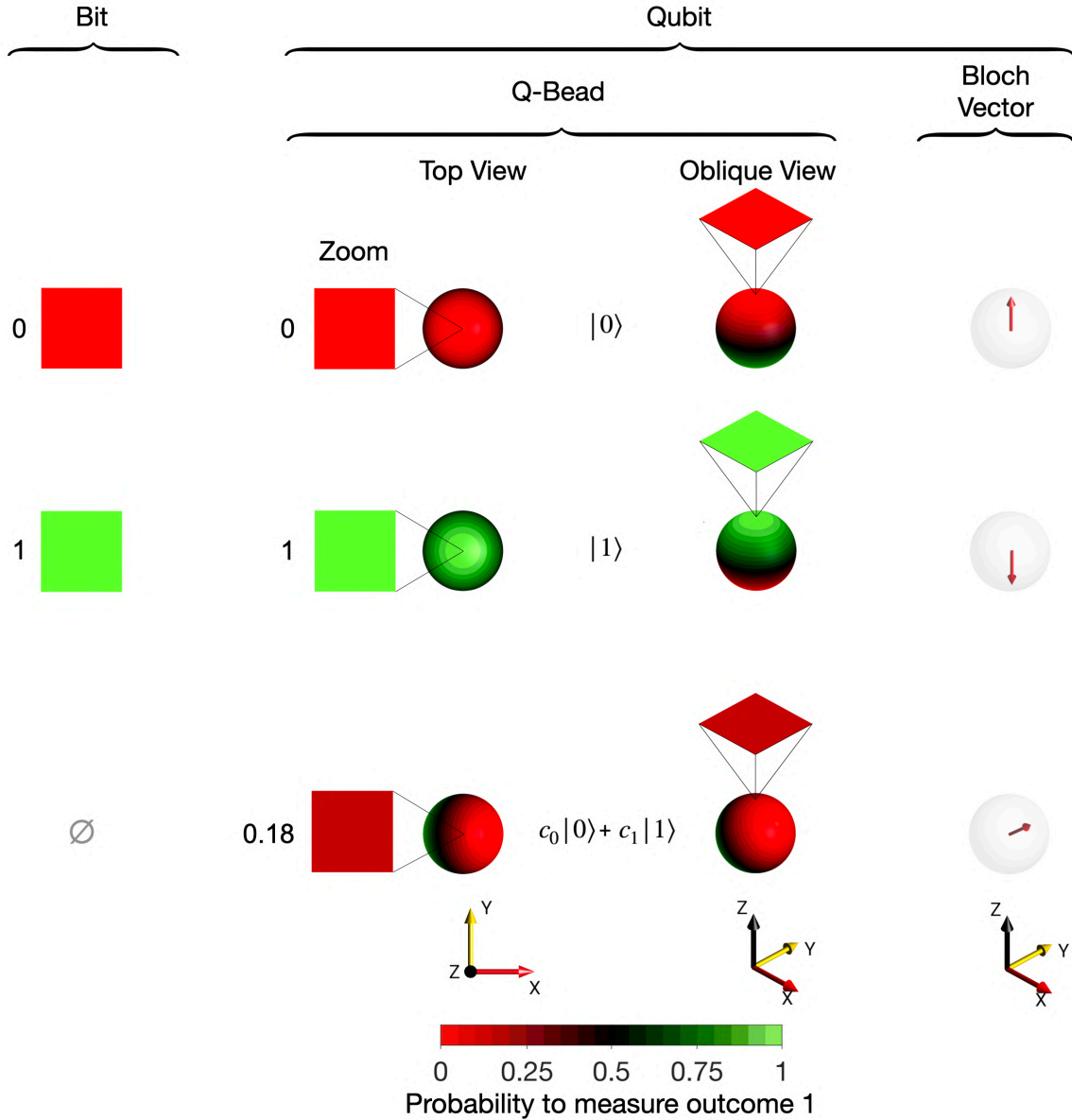


Fig. 1. Bit and corresponding qubit representations. The first two rows show visualizations of the two possible states 0 and 1 of a classical bit and of the *computational basis states* $|0\rangle$ and $|1\rangle$ of a qubit. The bit values 0 and 1 are graphically represented by a red and a green square-shaped color patch, respectively. In the BEADS representation, a qubit state is represented as a bipolar Q-Bead with a red and a green pole, shown from two different perspectives (a *top view* and an *oblique view*, see the different orientations of the coordinate system indicated below.) In addition, a zoomed view of the Q-Bead's north pole is shown as a square-shaped patch, whose color indicates the probability p_1 to obtain the outcome 1 if a measurement is performed along the z-axis (see color bar). For computational basis states, there is a one-to-one correspondence between this color patch and the color patch representation of the corresponding bit states displayed on the left. In the third row, an example of the Q-Bead representation of a *superposition state* $c_0|0\rangle + c_1|1\rangle$ is shown which has no classical equivalent. In the right column, the equivalent Bloch vector representations of the qubit states are shown for comparison.

Measurements

In order to better understand the color scheme introduced in Fig. 1, it is helpful to briefly review standard measurements (projective measurements) of a qubit and their similarities and differences to the measurement of a classical bit that is in state 0 or 1. For a classical bit, it is always possible to measure its value without altering it. When measuring a qubit along the z-axis, the same is only true if it is in one of the two computational basis states, where measuring the state $|0\rangle$ gives outcome 0 and measuring the state $|1\rangle$ gives outcome 1 without altering the respective states.

For *superposition states*, a measurement in the z-direction still provides an outcome that can only be 0 or 1. However, even if the superposition state is precisely known, it is impossible to predict the outcome of an individual measurement with certainty. Instead, we can only predict the *probabilities* p_0 and p_1 with which the outcome 0 or 1 will be obtained. (In fact, since only one of the two outcomes 0 or 1 is possible, it is sufficient to know only, e.g., p_1 , because p_0 is simply given by $p_0 = 1 - p_1$). Furthermore, the initial superposition state *is* modified by the measurement: If outcome 0 or 1 is measured, the qubit *is* found in the corresponding computational basis state $|0\rangle$ or $|1\rangle$, respectively, after the measurement.

Fig. 2 (A)-(E) schematically illustrates for five exemplary qubit states how the color scale used for Q-Beads can be related to the stochastic measurement outcomes in experiments where the measurement direction was chosen to be along the positive z-axis. For each of these states, the following (simulated) steps were repeated 100 times: After preparing a qubit in the initial state $|\psi\rangle$, a measurement of the qubit along the z-axis is performed. For each case, the 100 individual measurement outcomes were sequentially recorded and visualized in a 10-by-10 pixel matrix (shown in the first row) by coloring a pixel *red* or *green* if the outcome was 0 or 1, respectively (9). Note that (in the limit of an infinite number of repeated experiments) the percentage of *green* pixels in the top row for each case simply corresponds to the probability p_1 to obtain the measurement outcome 1 (indicated next to the zoomed color patches in the bottom of Fig. 2). We arrive at the color scheme for representing the value of p_1 on the surface of a Q-Bead in two simple steps: First, we select arbitrary pairs of pixels with complementary colors (red and green) in each matrix and color them black, indicating that for each pair the outcomes average to 0.5, see the resulting matrices in the second row of Fig. 2. Second, each of the five matrices is uniformly colored by blending the colors of all its pixels, resulting in the five color patches shown in the third row of Fig. 2. Note that these blended color patches match the color of the zoomed color patch at the upper point (north pole) for each of the five Q-Beads, see the fourth row of Fig. 2. Here, the value of p_1 given next to each color patch was directly calculated for each of the five considered states $|\psi\rangle = c_0|0\rangle + c_1|1\rangle$ using Born's rule (2) with the formula $p_1 = |c_1|^2$.

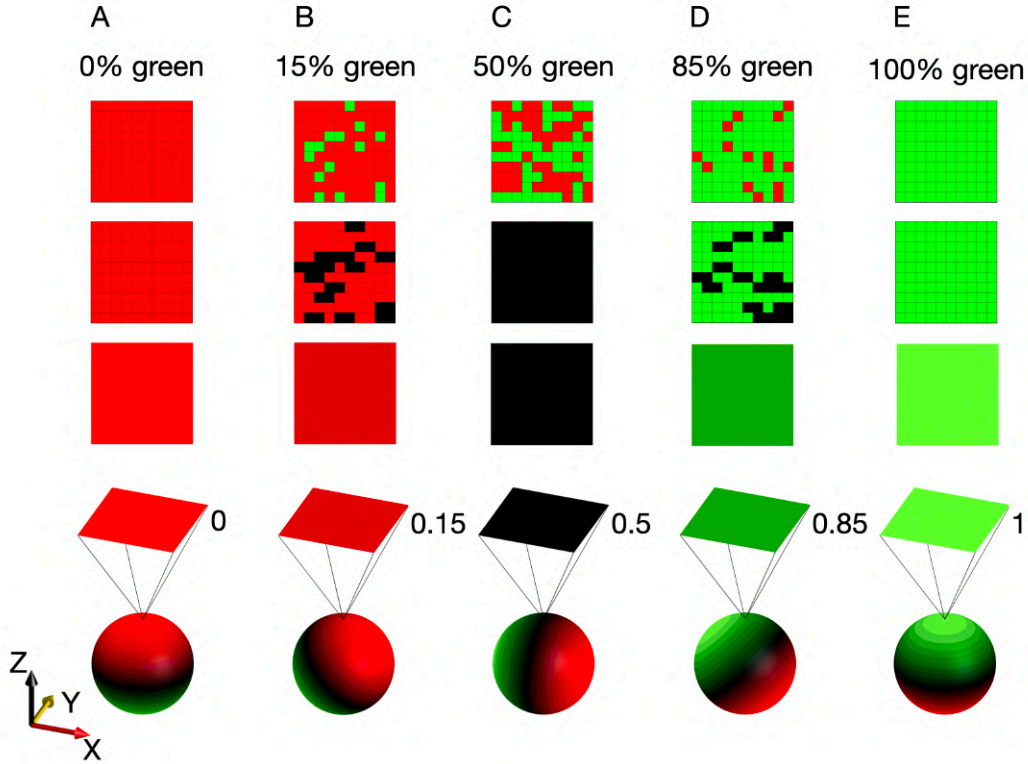


Fig. 2. Schematic relation between measurement statistics and the chosen color scheme of Q-Beads \otimes . Columns (A)-(E) correspond to five different qubit states $|\psi\rangle = c_0|0\rangle + c_1|1\rangle$ with coefficients (c_0, c_1) of $(1, 0)$ in (A), $(0.92, 0.4)$ in (B), $(0.71, 0.71)$ in (C), $(0.4, 0.85)$ in (D), and $(0, 1)$ in (E). In each column, the pixel matrix in the first row represents the statistics of 100 measurements along the z-axis, assuming that before each measurement the initial state corresponding to the respective column has been prepared (red and green pixels correspond to measurement outcomes 0 and 1). The second row shows the effect if arbitrary pairs of pixels with complementary colors are colored black. Blending the colors of the pixel matrices results in the uniformly colored color patches shown in the third row. The fourth row illustrates that these color patches correspond to the zoomed color patches at the upper point (north pole) for each of the Q-Bead representation of the five different qubit states prepared in columns A-E. The \otimes symbol at the end of the caption title indicates that this visualization is available as a dynamic simulation in the supplementary video.

The previous discussion of measurements along the z-axis can be generalized for measurements along an arbitrary measurement axis: The color of each surface point of a Q-Bead indicates the probability $p_1(r)$ to measure the outcome 1 if the measurement is performed in the direction defined by the vector r connecting the center of the Q-Bead and this surface point. Hence, the Q-Bead representation provides a convenient and compact way to display the probability $p_1(r)$ for all possible measurement directions r . (An alternative but equivalent interpretation of Q-Bead colors in terms of expectation values of Pauli operators will be discussed later.)

Multi-qubit states

In a multi-qubit system, each qubit Q_k is represented by a corresponding Q-Bead. In the absence of entanglement, the Q-Beads of a multi-qubit pure state look just like the Q-Beads

of the single-qubit states shown in Fig. 1, except for possible different orientations. However, in the presence of entanglement, the (reduced density operators of) individual qubits are in mixed (i.e., non-pure) single-qubit states, which is represented by a reduced brightness of the corresponding Q-Beads. In particular, in the case of totally mixed reduced single-qubit density operators, the corresponding Q-Beads are completely black, indicating that in any measurement direction, there is a 50:50 chance to measure the outcome 0 or 1. Even more importantly, in the BEADS representation the presence of entanglement in a qubit system is clearly visualized by the presence of additional entanglement-related correlation beads (E-Beads), as illustrated at the bottom of Fig. 3. As discussed in the following, it is rather straightforward to experimentally entangle qubits if suitable quantum gates can be applied.

Classical gates and quantum gates

In classical computing, bit states are manipulated by (logical) gate operations. In quantum computing, the role of classical gates is taken over by (unitary) quantum gates, which are always reversible. (Although not all classical gates are reversible, it is not hard to construct a reversible classical analog of any classical gate (2)). The only non-trivial reversible classical gate with a single input bit and output bit is the NOT gate which simply flips the bit state from 0 to 1 or vice versa (see the first table in the top row of Fig. 3). In contrast, there is an infinite number of possible single-qubit quantum gates. They all correspond to well-defined, simple three-dimensional rotations of the Q-Beads, which can be vividly illustrated using the BEADS representation (see section S15 of the supplementary material and the supplementary video). The effect of a quantum NOT gate (a.k.a. X-gate) is to rotate a Q-Bead by 180° about the x-axis, which also flips the input states $|0\rangle$ and $|1\rangle$ (second table). However, if the Q-Bead is initially oriented *along* the x-axis, it is clear that the 180° x-rotation of the NOT gate cannot change its orientation (see third table).

Entanglement and non-classical correlations

In the second row of Fig. 3, we see the effect of the classical and quantum versions of the *controlled*-NOT (or CNOT) gate. It plays an important role in quantum information processing, because it is able to create *entangled* multi-qubit states. This results in intriguing non-classical correlations between the outcomes of measurements performed on the individual qubits, even if they are so far apart that no communication between them is possible during the measurement process. Before looking at the creation of entanglement and its visualization in the BEADS representation, let us briefly see the effect of a CNOT gate on each of the four possible states 00, 01, 10, or 11 of two classical input bits, see the truth table at the lower left of Fig. 3. The state of the output bit B_2^{out} depends uniquely on *both* input states B_1^{in} and B_2^{in} : If $B_1^{\text{in}} = 0$ (red) then $B_2^{\text{out}} = B_2^{\text{in}}$, but if $B_1^{\text{in}} = 1$ (green) then $B_2^{\text{out}} = \text{NOT } B_2^{\text{in}}$, i.e., the state B_1^{in} of the first input bit *controls* whether or not the state B_2^{in} must be flipped by a NOT gate to obtain the state B_2^{out} . Note that in all cases $B_1^{\text{out}} = B_1^{\text{in}}$ and the only purpose of B_1^{out} is to make the gate reversible, so it is possible to construct a corresponding quantum version.

If the input state of the analogous quantum CNOT gate is one of the four two-qubit *computational basis states* $|00\rangle$, $|01\rangle$, $|10\rangle$, or $|11\rangle$, the resulting table is congruent to the classical truth table of the CNOT gate (compare the second and first tables). However, things become much more interesting if the control qubit Q_1 is initially in a *superposition state*. For example, in the third table, the first qubit is initially prepared in one of the superposition states $|+\rangle = 1/\sqrt{2}(|0\rangle + |1\rangle)$ or $|-\rangle = 1/\sqrt{2}(|0\rangle - |1\rangle)$, which correspond to the red pole of the corresponding Q-Bead pointing along the positive or negative x-direction, respectively. In this case, each of the two-qubit input states $|+0\rangle$, $|+1\rangle$, $|-0\rangle$, or $|-1\rangle$ is

transformed into one of the four fully entangled *Bell states* by the CNOT gate (2) (for more details on this transformation, see supplementary section S17). The BEADS representation of the resulting Bell state is schematically shown in the *three* output columns of the third table in the lower row of Fig. 3: The Q-Beads Q_1 and Q_2 of the output states are completely black, that is, in any possible measurement direction, the measurement outcomes 0 or 1 have equal likelihood. However, the presence of the non-zero entanglement bead $E\{1,2\}$ indicates that for most measurement directions the measurement outcomes are at least partially non-classically correlated. The yellow-blue color scheme (see color bar at the bottom right of Fig. 3) indicates the probability to measure *unequal* outcomes if measured in the same (but arbitrary) direction. For example, the E-Bead shown in the first row of the table is bright yellow along the x-axis and the z-axis, indicating that in this case, the probability to measure different outcomes is 0, i.e., although the individual measurement outcomes for the two qubits are unpredictable, they are never different, that is, they are always identical! Conversely, the E-Bead is bright blue along the y-axis indicating that the probability to measure different outcomes is 1 such that we can predict that the measurement outcomes will be different in this case with certainty. The E-Beads corresponding to the first three Bell states are identical and only differ in their *orientation*. However, the E-Bead (called the *singlet state* (2)) obtained in the fourth row of the table is clearly of a different type and cannot be obtained by simply rotating one of the other Bell states. It is entirely blue, indicating that we can predict that for any chosen common measurement direction, the outcomes for two qubits will be *different* with certainty, independent of their spatial separation. For more details on Bell states and other characteristic entangled two-qubit and three-qubit states, see sections “Three-qubit entanglement” and supplementary section S14 and S17.

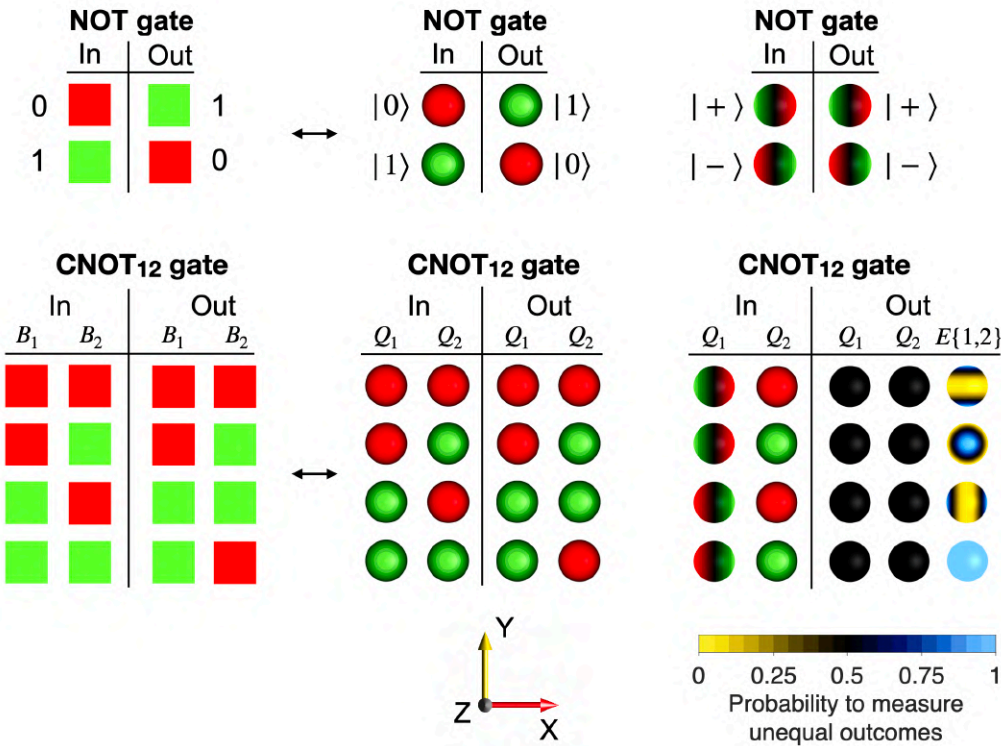


Fig. 3. Effect of the NOT and CNOT gates. Truth tables for the NOT gate (top) and the CNOT gate (bottom) for classical input states and output states are shown graphically on the left using red and green color patches as introduced in Fig. 1. The effect of the quantum versions of the NOT and controlled NOT (CNOT) gates is shown when applied to computational basis states (center) or to selected

superposition states (right) using the BEADS representation. In the center tables, the input qubit states are the computational basis states $|0\rangle$ and $|1\rangle$ for the NOT gate (top) and the two-qubit computational basis states $|00\rangle$, $|01\rangle$, $|10\rangle$, and $|11\rangle$ for the CNOT gate (bottom). In the top right table, the input qubit states for the NOT gate are the superposition states $|+\rangle = 1/\sqrt{2}(|0\rangle + |1\rangle)$ and $|-\rangle = 1/\sqrt{2}(|0\rangle - |1\rangle)$. The table at the bottom right shows the results if the CNOT gate is applied to the two-qubit states $|+0\rangle$, $|+1\rangle$, $| - 0\rangle$, or $| - 1\rangle$, where the first qubit is in one of the superposition state $|+\rangle$ or $|-\rangle$ while the second qubit is in one of the basis states $|0\rangle$ or $|1\rangle$. In this case, entangled states are created which are not fully characterized by the output Q-Beads Q_1^{out} and Q_2^{out} but also require the E-Bead (short for entanglement-related correlation bead) $E\{1,2\}$. With the help of the yellow-blue color scheme (see bottom right), each surface point of the E-Bead quantitatively indicates the probability to measure *unequal* outcomes based on non-classical correlations, if measured in this direction.

Theoretical background

From a mathematical theoretical point of view, the BEADS representation and its visualization is a generalized phase-space representation (10–17). In particular, it belongs to the class of s -parametrized representations, which includes the well-known Wigner W (18, 19), the Husimi Q (20–23) and the Glauber P (24) representations, see (25) for a unified description of s -parametrized phase-space representations of states in finite- or infinite-dimensional Hilbert spaces. More specifically, the BEADS representation is a new member of the family of *continuous* phase space representations of *finite*-dimensional quantum systems, which reflect inherent (rotational and permutational) symmetries of coupled two-level systems (also known as qubits or as spins $S = 1/2$, such as electrons or protons) or of coupled d -level systems with $d > 2$ (also known as qudits or spins $S > 1/2$ with individual Hilbert-space dimensions $d = 2S + 1$) (26–30). These types of phase-space representations are closely related to the seminal paper by Stratonovich (31). Related work in nuclear magnetic resonance (NMR) (32) can also be traced back to at least the work of Pines et al. (33) where (albeit without a formal map) selected density operator terms of a spin-1 particle and their symmetry properties were depicted using spherical harmonics.

Based on a mapping between spherical tensor basis operators and a set of corresponding spherical functions, several different multi-qubit phase-space representations have been developed which differ in the used criteria to define the spherical tensor operators and which lead to different groupings of the spherical functions. The subclass of so-called multipole representations (34–37) group the spherical tensor operator primarily according to their angular momentum properties but not with respect to the number and the identity of involved spins (qubits or qudits). Therefore, multipole representations are not ideally suited to represent states in quantum computations which require the ability to control and to detect qubits individually (38).

This problem was solved by the construction of the so-called LISA basis (37), which consists of tensor operators with defined linearity (which corresponds to the *number* of involved qubits), subsystem (the actual set or subset of involved qubits), and auxiliary criteria (permutation symmetry and fractional parentage), for more details and explicit matrix representations of the LISA basis for up to six qubits as well as for two coupled qudits, see (37, 39). Based on the LISA basis, the DROPS representation of arbitrary operators was introduced (37).

The DROPS representation is a generalized Wigner function that is based on the decomposition of the operator of interest (e.g., the density operator representing the pure or mixed state of a system of qubits) in the LISA basis $T_{j,m}^{(\ell)}$. The resulting expansion coefficients $c_{j,m}^{(\ell)}$ are directly used to calculate corresponding linear combinations of spherical harmonics $Y_{j,m}$ to create a set of spherical functions, called droplet functions (for details, see Eq. 4 in the Materials and Methods section). This mapping indeed provides a unique visualization with many favorable properties, such as natural transformations under non-selective rotations and permutations, visualization of symmetry properties, characteristic patterns depending on the coherence order of a droplet function and the immediate identification of the spins or qubits that are involved in a certain droplet function). We also implemented the DROPS representation in the *SpinDrops* app, which makes it possible to visualize and interactively control the dynamics of multi-spin states related to NMR applications (40). It is also noteworthy that it is possible to experimentally reconstruct droplet functions using a scanning-based tomography approach based on measured expectation values of rotated longitudinal LISA basis operators, as experimentally demonstrated on NMR-based quantum processors and on superconducting quantum computers (41–43).

However, the DROPS representation also has a number of shortcomings: The values of the spherical droplet functions in a given direction r are *proportional* to measurable expectation values of longitudinal tensor operators but these operators are more or less complicated combinations of simple Cartesian Pauli product operators. However, it would be highly desirable to have a representation that can easily be directly interpreted in terms of expectation values of simple Cartesian Pauli product operators or in terms of measurement probabilities of interest. Furthermore, the originally proposed DROPS representation provided only partial information about the kind of entanglement that is present in a multi-qubit state. For the special case of a two-qubit system, the concurrence C , which is an important entanglement measure, can be expressed as a function of the maximum value

$$f_{max}^{\{k\}} \text{ of the linear droplets corresponding to the two qubits: } C = \sqrt{1 - \frac{16\pi}{3} \left(f_{max}^{\{k\}}\right)^2}.$$

However, it would be highly desirable to see also in system consisting of three or more qubits not only whether entanglement exists but also what kind of entanglement-based non-classical correlations are present.

Here we present the novel BEADS representation, which is also based on the LISA operator basis. The development of the BEADS representation was inspired by the fact that the Wigner representation of a single qudit can be transformed to the corresponding Husimi representation by applying *different* scaling factors to spherical harmonics of different rank j (25). We therefore investigated the possibility to translate the DROPS representation of multi-qubit systems (which can be seen as a generalized Wigner representation) to a representation that is akin to a generalized Husimi representation. This problem was in particular interesting, because in the case of a single qudit, the value of the spherical Husimi representation is identical to experimentally important measurement probabilities (up to a simple overall scaling factor, see section S11 of the supplementary material for further details) and it would be desirable for the generalized Husimi representation to also have such a highly useful simple and intuitive interpretation. Indeed, this turns out to be the case as will be discussed in the following.

Furthermore, in the BEADS representation we also included the possibility to efficiently separate total correlations into what will be referred to as compound correlations and entanglement-based non-classical connected correlations based on the work of Schlienz and

Mahler (44–46) and related papers (47, 48). A similar approach has also been applied in (49, 50) to visualize an approximation of two-point connected spin correlations.

A canonical representation of quantum states

We designed the BEADS representation such that, while providing a unique complete visualization of quantum systems, measurement outcomes can be predicted, and entanglement and symmetry properties can be identified visually with no or little experience. This contrasts our approach from other representations which also provide faithful visualizations of multiqubit systems yet require a deep understanding to extract relevant information or do not even allow to access the discussed aspects with reasonable effort.

Before providing an in-depth physical analysis of the BEADS representation, we showcase the capability of our approach by comparing BEADS visualizations of selected non-trivial states with other representations including the Qiskit (real part) cityscape density operator plot and the Q-Sphere (51) state vector visualization in Fig. 4. Further visualizations of the same states in terms of full cityscape plots, dimensional circle notations (52), and standard state vector expressions are given in section S12 of the supplementary material.

In the BEADS representation, one can directly see whether a state is entangled or separable. The topmost example in Fig. 4 corresponds to a fully separable two-qubit state. The BEADS visualization is only composed of Q-Beads, thus indicating that there is no entanglement between the qubits in an intriguingly simple way. In contrast, using the cityscape plot and Q-Sphere for a non-expert, it is virtually impossible to make an immediate statement on the entanglement properties of the visualized state. Even experts will require some time to see if a state is entangled or not.

In the second and third state visualizations, we observe both, E-Beads and colored Q-Beads. Hence, we find the corresponding states to be (partially) entangled. Moreover, both states have a small antisymmetric component with respect to permutation represented by the $E\{1,2\}_{odd}$ E-Bead. Again, all of this does not become directly evident in the alternative representations. Even more important though, only when comparing the two BEADS visualizations, it can be readily seen that both states only differ by a global 45° -rotation around the x-axis.

The bottom three-qubits BEADS representation reveals a highly symmetric state. We will later see that this is the well-known GHZ state up to a global -60° -rotation around the xy-bisecting axis. While the symmetry properties can also be assumed from the Q-Sphere picture in this case, the discussed small difference by a simple rotation compared to the GHZ state cannot be determined without advanced knowledge. The cityscape plot again barely provides any useful insights.

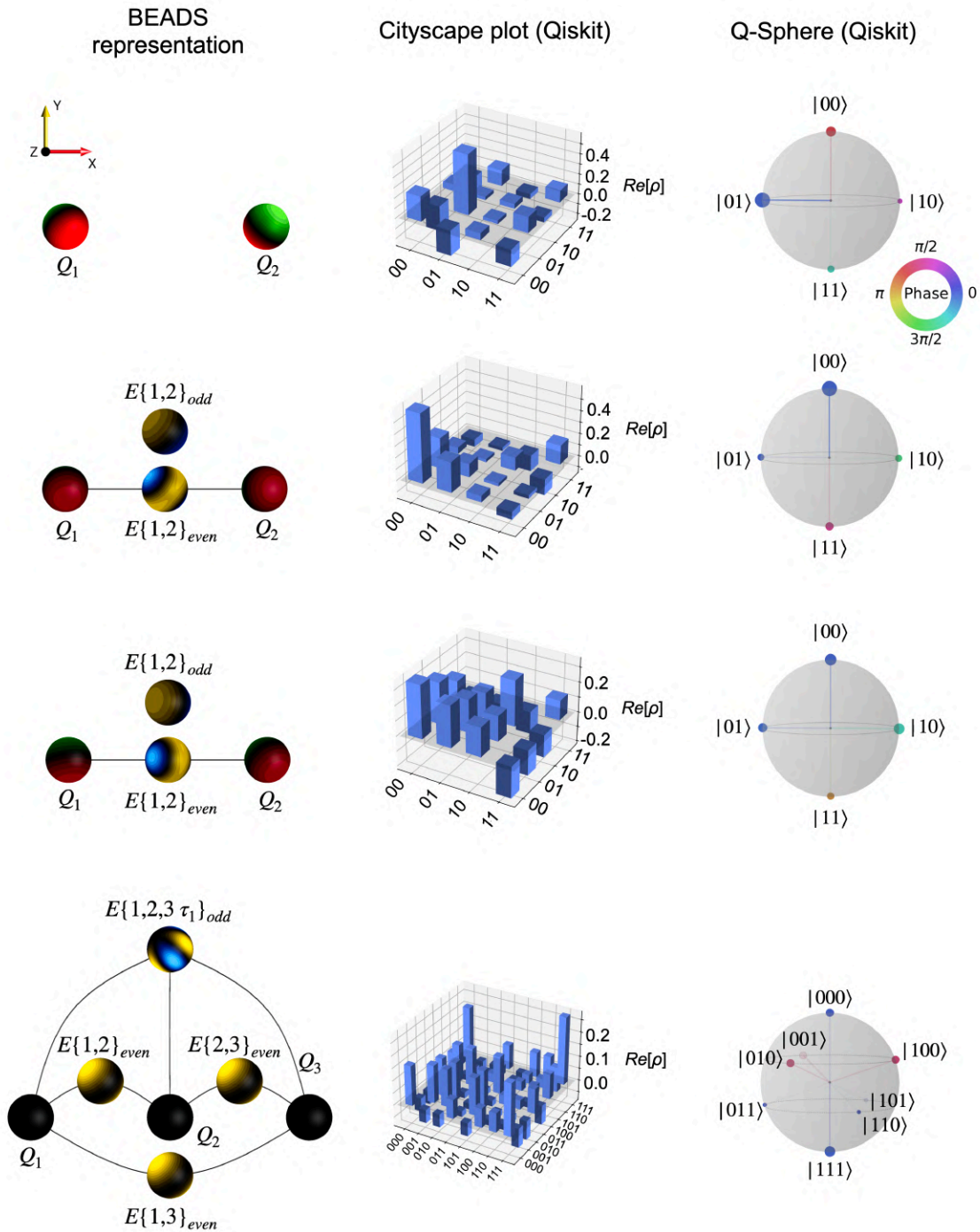


Fig. 4. BEADS, Cityscape, and Q-Sphere representation of several quantum states. The visualized states (read from top to bottom) are explicitly written out Fig. 31 of supplementary section S12. The visualized examples comprise a fully separable state (top), two partially entangled two-qubit states which only differ by a global 45° -rotation around the x-axis (center), and a maximally entangled three-qubit state which is the GHZ state rotated by a -60° -rotation around the xy-bisecting axis (bottom).

A physical interpretation of BEADS: Two-qubit systems

We will now discuss the BEADS representation on a more detailed physical conceptual level and draw connections to underlying standard concepts of quantum mechanics.

An illustrative example of two-qubit entanglement can be found in states of Schmidt form which are two-qubits states that depend on a single angular parameter, the Schmidt angle θ (53). In Fig. 5 the visualizations correspond to states of the form $|\psi_\theta\rangle = 1/\sqrt{2}(\cos(\theta/2)|00\rangle + \sin(\theta/2)|11\rangle)$ where $\theta \in \{0, \pi/8, \pi/4, 3\pi/8, \pi/2\}$. The corresponding two-qubit BEADS representations are composed of multiple beads, the two Q-Beads Q_1 and Q_2 , and the E-Bead (entanglement-related connected correlation bead) $E\{1,2\}_{even}$ which is located on an arc connecting the Q-Beads indicating that this correlation is between the corresponding qubits. As a complementary view, we provide a variant of Fig. 5 for which the absolute spherical function values are plotted as distance from the origin in Fig. 38 in section S14 of the supplementary material.

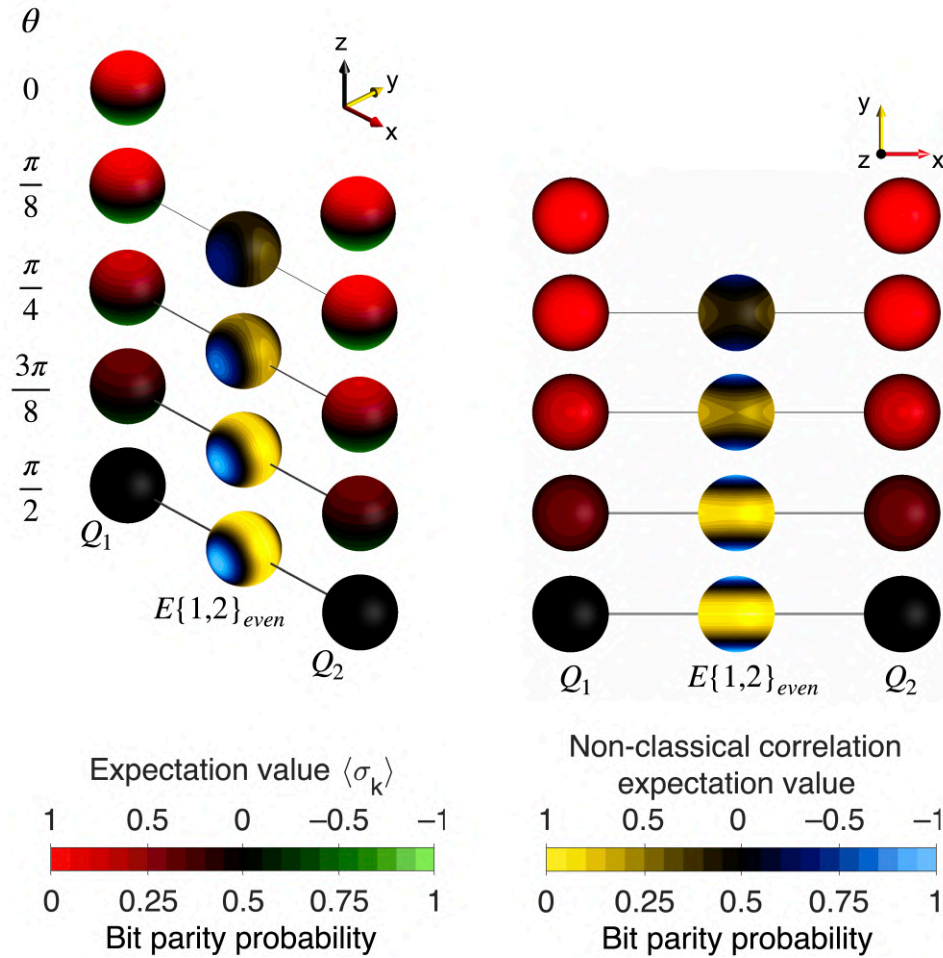


Fig. 5. BEADS representations of states of Schmidt form $|\psi_\theta\rangle = 1/\sqrt{2}(\cos(\theta/2)|00\rangle + \sin(\theta/2)|11\rangle)$. A selection of states for different Schmidt angles θ is shown in oblique and top view. The E-Bead $E\{1,2\}_{even}$ corresponds to permutation symmetric genuine two-qubit entanglement-related non-classical connected correlations. $|\psi_0\rangle$ corresponds to a fully separable state (no E-Bead) whereas $|\psi_{\pi/2}\rangle$ is maximally entangled which can be seen from black Q-Beads and maximally intense E-Bead colors. The remaining states are partially entangled. The color scales at the bottom serve as a reference for interpretation which can be made in terms of expectation values or related probabilities. The black lines connecting the Q-Beads serve as auxiliary entanglement indicators and their thickness is proportional to the

norm of the underlying density operator component visualized by $E\{1,2\}_{even}$ (see section S7 of the supplementary material)

As was discussed in the preceding sections, Q-Beads correspond to the physical qubits in the system. From a mathematical-physical perspective, Q-Beads are a visualization of the reduced density operators. Recall that the reduced density operator of a qubit is the partial trace of the density operator $\rho = |\psi\rangle\langle\psi|$ (2) with respect to all remaining qubits in the system. In addition, Q-Beads only map expectation values $\langle\sigma_k\rangle$ of single-qubit Pauli matrices σ_k and thus, they are equivalent to the individual Bloch vectors (6, 7). We will later show, that the previously introduced interpretation of Q-Beads in terms of probabilities is related to these expectation values and both can be bijectively transformed into each other. Since the reduced density operator of a qubit is pure only if the qubit is not entangled with any other qubit, we can use spherical function values of a Q-Bead (given in terms of colors) as a first indicator of entanglement. Specifically, we find that the *brightness* of the Q-Bead colors is maximum (Bloch vector of length 1) if the state is separable and minimum (Bloch vector of length 0, all-black Q-Bead) if the state is maximally entangled (37). The latter arises due to the single-qubit density matrices being maximally mixed for which $\langle\sigma_k\rangle = 0$.

Result 1: Q-Beads Q_k are a direct visualization of the reduced density operator corresponding to the k -th qubit of a system. The Q-Bead colors and brightness directly correspond to expectation values of single-qubit Pauli matrices $\langle\sigma_k\rangle$. The brightness indicates whether a pure state is fully separable (maximum brightness), partially entangled (reduced brightness) or maximally entangled (fully black Q-Beads).

Indeed, for the states shown in Fig. 5 we find that the Q-Bead colors turn darker for increasing Schmidt angles θ which corresponds to increasing entanglement. Moreover, according to the discussed relations, $|\psi_0\rangle$ represents a fully separable state whereas $|\psi_{\pi/2}\rangle$ is maximally entangled.

E-Beads, e.g., $E\{1,2\}_{even}$, are a direct visualization of entanglement-related connected correlations (see Materials and Methods). Two-qubit BEADS representations further comprise a second connected correlation component $E\{1,2\}_{odd}$, which is zero for states of the introduced Schmidt form though, and hence, is omitted in Fig. 5.

Here, $E\{1,2\}_{even}$ represents the fully permutation symmetric bilinear connected correlation component in a two-qubit system, whereas $E\{1,2\}_{odd}$ corresponds to permutation antisymmetric bilinear connected correlations (see Materials and Methods and supplementary section S2).

In Fig. 5, we observe that the correlation component $E\{1,2\}_{even}$ increases in brightness for increasing values of θ , oppositely to what we discussed for Q-Beads, which coincides with the increase of entanglement in the system. In the maximally entangled case $\theta = \pi/2$, the color brightness of $E\{1,2\}_{even}$ is maximum. In contrast, for $\theta = 0$, there is no E-Bead (and thus no entanglement) and the state must consequently be separable. Note that we omitted the E-Bead which here is black in all spatial directions. This is a subtlety in design which we chose to minimize the complexity of the representation. However, we do not omit black Q-Beads since these correspond to the state of physical objects, the qubits.

Result 2: If all E-Beads in the BEADS representation of a pure state are black in all spatial directions, the state is fully separable.

At this point, we conclude that in Fig. 5 states corresponding to Schmidt angles $0 < \theta < \pi/2$ are partially entangled. For such cases, the total correlation in the system is not merely

given in terms of connected correlations. Instead, correlations in partially entangled states comprise genuine n -qubit connected correlations and, what in the following we refer to as, *compound* correlations. The latter comprise classical correlations and lower-order connected correlations which represent redundant information and can be removed from a density operator by applying Ursell functions (44) (see Materials and Methods).

Result 3: n -linear E-Beads are a direct visualization of n -linear non-classical connected correlations which occur exclusively in entangled quantum states.

If desired, compound correlations can be additionally visualized by so-called C-Beads (see Fig. 39 in supplementary section S14 and the *Variants and simplifications* section). More importantly, it is possible to represent the *total* correlations of a system by so-called T-Beads for which we propose an extended color scheme (see supplementary section S9) which characterizes the ratio of the different correlation components in each spatial direction. BEADS representations of the discussed Schmidt form states in terms of total correlations are given in supplementary section S14. Note that C-Beads and T-Beads follow the same general principles as were introduced for E-Beads including labelling schemes.

Result 4: Compound correlations can be visualized by C-Beads (*compound* correlation beads).

Result 5: Total correlations can be visualized by T-Beads (*total* correlation beads).

Indeed, total correlations in a quantum system, and thus T-Beads, are key for predicting outcomes of projective measurements. E-Beads, while being suitable to characterize and quantify the entanglement in a system of qubits, are instead not sufficient to be used in measurement predictions except for maximally entangled states where the total correlation is solely given by non-classical connected correlations, (such as for the states in Fig. 3). Fully separable states represent a special case, where the outcomes of individual qubits are independent of each other and thus, can be predicted from the local single-qubit information encoded in Q-Beads only. For the visualizations in Fig. 5 these findings imply that a direct outcome prediction is only feasible for $\theta = 0$ and $\pi/2$.

Result 6: In the BEADS representation, measurement outcomes can be predicted from Q-Beads and total correlations (T-Beads). For maximally entangled states, total correlations are equivalent to non-classical connected correlations and thus, E-Beads can be used. Correlations in fully separable states are trivial and the prediction can be made using Q-Beads only.

Recall that the color of Q-Beads and E-Beads (for maximally entangled states) along arbitrary directions was shown to correspond to measurement probabilities which can be deduced from color scales. We have previously introduced these color scales in Fig. 1 and Fig. 3, yet we provided simple descriptions which were specifically simplified and tailored to the discussed examples. Indeed, the interpretation of colors can be unified to so-called *bit parity probabilities* p which specify the likelihood of measuring an odd number of qubits in the “down” states, that is, the eigenstate corresponding to eigenvalue -1 (2) of the measurement operator $\sigma_{kr} = r_x \sigma_{kx} + r_y \sigma_{ky} + r_z \sigma_{kz}$ for the k -th qubit in the corresponding measurement direction r . In the case of a single qubit, this simply corresponds to the probability of measuring the qubit in the down state (see Fig. 1).

As was briefly indicated for Q-Beads, an alternative and generally applicable interpretation of the utilized color scales is given in terms of expectation values. Indeed, the color of Q-Beads and fully symmetric T-Beads (e.g., $T\{1,2\}_{even}$) along direction r then directly corresponds to expectation values $\langle M \rangle = \langle \prod_{k \in G} \sigma_{kr} \rangle$ where G is the set of all qubits involved in the bead, respectively. $\langle M \rangle$ adopts values in the range between -1 and 1 and is called *correlation expectation value* for T-Beads. It is related to the bit parity probability p by

$$p = \frac{1 - \langle M \rangle}{2} \quad (1)$$

Full correlation corresponds to an expectation value $\langle M \rangle = 1$ and a bit parity probability of $p = 0$ and is equivalent to measuring an even number of qubits in the down state of the associated measurement basis whereas $\langle M \rangle = -1$ (or $p = 1$) represents full anticorrelation, i.e., measuring an odd number of down states (cf. Fig. 5 and Fig. 22 of the supplementary material).

Note that for T-Beads corresponding to other symmetries (e.g., $T\{1,2\}_{odd}$), $\langle M \rangle$ is generally defined by linear combinations of Pauli product operators which do not correspond to a single projective measurement. While bit parity probabilities can still be calculated according to Eq. 1 for these beads, they have no direct physical interpretation. Further, one should not mistakenly conclude that outcomes of asymmetric measurements, i.e., measurements where qubits are measured in different directions, can be merely predicted from beads which do not represent fully permutation symmetric components. In fact, predictions of asymmetric measurements require more elaborate methods that involve symmetric and antisymmetric T-Beads alike which are explained in supplementary sections S8 and S22.

Result 7: In the BEADS representation, colors can be consistently interpreted as expectation values of visualized single-qubit and correlation components. T-Beads with full permutation symmetry can equivalently be interpreted in terms of bit parity probabilities.

Result 8: The correlation expectation value and the related bit parity probability associated with a symmetric measurement of n qubits in a set G , that is, all qubits in G are measured along the same direction r , is represented by the color along direction r of the fully permutation symmetric n -linear T-Bead corresponding to G .

Applying these findings to the maximally entangled state ($\theta = \pi/2$) shown in Fig. 5, by analyzing the colors of $E\{1,2\}_{even}$ we find full positive correlation and hence, a bit parity probability of $p = 0$ for symmetric measurements along the z- or x-axes (or any other direction in the xz-plane) whereas the state is fully anti-correlated along the y-axis. Black regions indicate uncorrelated measurement outcomes in the corresponding directions, i.e., all possible outcomes are obtained statistically with equal probabilities. Indeed, the state $|\psi_{\pi/2}\rangle$ is the Bell state $|\Phi^+\rangle = 1/\sqrt{2}(|00\rangle + |11\rangle)$ for which correlations along Cartesian coordinate axes are well-known but not directly evident for any other direction and must usually be calculated individually for specific direction. In contrast, the BEADS representation provides a holistic view of the correlations along all possible measurement directions.

Moreover, the BEADS representation is symmetry-adapted. Besides permutational symmetries, it also captures spatial symmetries, e.g., rotational, point reflection, and reflection symmetries through a plane. These are directly evident from the types and surface

patterns of beads, respectively. For the Bell state $|\psi_{\pi/2}\rangle = |\Phi^+\rangle$, Fig. 5 makes it immediately clear that the state is fully axially symmetric with respect to rotations around the y-axis and has a two-fold rotational symmetry around any axis in the zx-plane (for an overview of symmetries in the BEADS representation, refer to section S2 of the supplementary material).

Result 9: Spatial symmetries of expectation values, i.e., rotational, point reflection, and reflection symmetries through a plane of a quantum states are directly evident in the BEADS representation.

Three-qubit entanglement

Based on the concepts introduced in the preceding chapter we now visit the most prominent examples of three-qubit entanglement which are the GHZ state $|GHZ\rangle = 1/\sqrt{2}(|000\rangle + |111\rangle)$ (54, 55) and the W state $|W\rangle = 1/\sqrt{3}(|001\rangle + |010\rangle + |100\rangle)$ (56) and examine the standard protocols to generate the states both of which are shown in Fig. 6. Here, we introduce *BEADS-augmented circuits* which use standard circuit notation to outline the quantum circuit and display the Q-Bead Q_k corresponding to the k -th qubit on the corresponding wire after every operation step. Additionally, we also show E-Beads (or alternatively T- or C-Beads) on additional grey lines (the lighter color indicating the virtual nature of the associated correlations). All beads are visualized in top view. This allows us to monitor the entire system evolution during the circuit on a compact visual level. Note that we use *most significant bit first* qubit numbering to define our quantum circuits which is standard in most quantum information textbooks (but different to what is used, e.g., in Qiskit (51)). For simplicity, we only show fully permutation symmetric E-Beads (see supplementary section S2 for further information on beads permutation symmetries) in this chapter which is sufficient to provide a complete visualization of the GHZ and W states. Simple examples of Bell-state-generating BEADS-augmented circuits are provided in supplementary section S17.

The GHZ state (54, 55) is generated by first creating a Bell pair $|\Phi^+\rangle$ between the first and second qubit. This is achieved by applying a Hadamard gate on the first qubit represented by Q_1 in Fig. 6 followed by a $CNOT_{12}$ operation which acts according to what was introduced in Fig. 3. Indeed, we can directly see that the Hadamard gate transforms the initial computational basis ($|0\rangle$) state of the first qubit to the equal superposition state $|+\rangle = 1/\sqrt{2}(|0\rangle + |1\rangle)$. The equal superposition can be recognized by the black color of Q_1 along the z-axis which corresponds to a 50% probability of measuring $|1\rangle$. Importantly, while the circuit visualization is sufficient to understand the overall effect of the Hadamard gate, it does not reveal the dynamics which occur when the gate is acting on the system and which is vital to obtain a deeper understanding of quantum operations. Indeed, the BEADS representation is particularly useful to visualize such dynamics. Among various single- and multi-qubit examples, we visualize the dynamics of the Hadamard gate in supplementary section S15 and the animations in the supplementary video which reveal a 180° -rotation around the xz-bisecting axis.

Result 10: The BEADS representation can be used to show the state of a quantum system after a gate but is also applicable to visualize system dynamics, e.g., during the action of a quantum gate.

After the following CNOT_{12} operation, we observe only subsystem $\{1,2\}$ to be maximally entangled (forming a Bell pair $|\Phi^+\rangle$ which we encountered in the preceding chapter) while the third qubit remains separable. These first two quantum operations further reveal the principal transformations of Q-Beads: *rotations* and *scaling*, the latter of which is observed as a change of brightness. Local transformations, that is, single-qubit gates act on a Q-Bead simply by rotating it whereas multiqubit gates can induce both rotations and scaling.

Result 11: Quantum gates transform Q-Beads in terms of rotations and scaling of brightness.

When a CNOT_{23} (or a CNOT_{13}) is applied subsequently, the maximally entangled three-qubit state, the GHZ state is generated. The GHZ state is fully characterized by four E-Beads: three E-Beads corresponding to symmetric two-qubit correlation $E\{k,l\}_{\text{even}}$, where $\{k,l\} \in \{\{1,2\}, \{1,3\}, \{2,3\}\}$ denotes the possible bilinear subsystems, and the trilinear E-Bead $E\{1,2,3\}_{\tau_1\text{odd}}$. Following result 3, the latter corresponds to fully symmetric connected correlations which here arise due to genuine three-qubit entanglement.

Observing the action of the last gate in the circuit on $E\{1,2\}_{\text{even}}$, it becomes clear that E-Beads (and any other type of correlation bead, i.e., T-Beads and C-Beads) are not only rotated or scaled but can undergo a third type of transformation which we term *morphing* and which corresponds to a change in surface pattern independent of changes in brightness. Morphing arises due to beads involving spherical harmonics of higher ranks ($j > 1$) which do not exclusively transform in terms of simple rotations. In general, local selective rotations, that is, local gates applied to a subset of the qubits involved in a correlation component can cause morphing, whereas global rotations (i.e., the same local operation being applied to all qubits involved in the correlation) induce simple rotations of the bead. Multiqubit gates can induce any of the possible transformations. Various examples of transformations of E-Beads are shown in supplementary section S15.

Result 12: Quantum gates act on correlation beads (i.e., E-Beads, T-Beads, and C-Beads) in terms of rotation, scaling, and/or morphing.

Since the resulting BEADS visualization only comprises fully permutation symmetric E-Beads, one can directly tell that the GHZ state is totally symmetric with respect to permutations of qubits, and it is immediately clear from the BEADS representation in Fig. 6 that any bilinear correlation component is invariant under rotations around the z-axis. In contrast, the $E\{1,2,3\}_{\tau_1\text{odd}}$ bead displays a threefold rotational symmetry with respect to global rotations around the z-axis, i.e., any 120° z-rotation of all three qubits in the system, leaves the entire state invariant. Moreover, we immediately see that the state is fully correlated for each two-qubit pair, yet there is no genuine tripartite z-correlation (see color scales in Fig. 5 for reference). Given the observed bipartite correlations, this implies that if any qubit is measured along the z-axis, all qubits, which are bilinearly correlated with the former, adopt the same state. For instance, if the first qubit is measured in state $|0\rangle$, the correlations represented by $E\{1,2\}_{\text{even}}$ and $E\{1,3\}_{\text{even}}$ imply that the second and third qubit will also be in state $|0\rangle$, and thus, the GHZ collapses to $|000\rangle$ overall.

In the BEADS representation, we can see that the GHZ state is in fact fully trilinearly correlated for symmetric measurements along the x-axis, and in directions $(90^\circ, 120^\circ)$ and $(90^\circ, -120^\circ)$ given in terms of spherical coordinates. In contrast, the state is fully trilinearly anti-correlated along the $-x$ -axis and directions $(90^\circ, 60^\circ)$ and $(90^\circ, -60^\circ)$.

Using the BEADS representation, the W state (56), which is well-known to be fundamentally different from the GHZ state, can be identified to *not* be maximally entangled due to non-zero Q-Beads (σ_z -expectation value along z-axis $\langle\sigma_z\rangle = 1/3$). Based on the

resulting BEADS representation we can directly tell the obtained W state to be fully axially symmetric with respect to arbitrary rotations about the z-axis. As the W state is not maximally entangled, it is necessary to look at the corresponding total correlation BEADS representation to understand its behavior under measurements. This visualization is provided and analyzed in supplementary section S14.

Another important class of entangled states are graph states (57). These states can be transformed into each other following well-known rules and represent a natural choice in measurement-based quantum computing. Using the BEADS representation, it is easily possible to illustrate graph state transformation rules and to get insights into the topologies and symmetries of the underlying non-classical connected correlations. Examples of such graph states and associated transformations are provided in supplementary section S18.

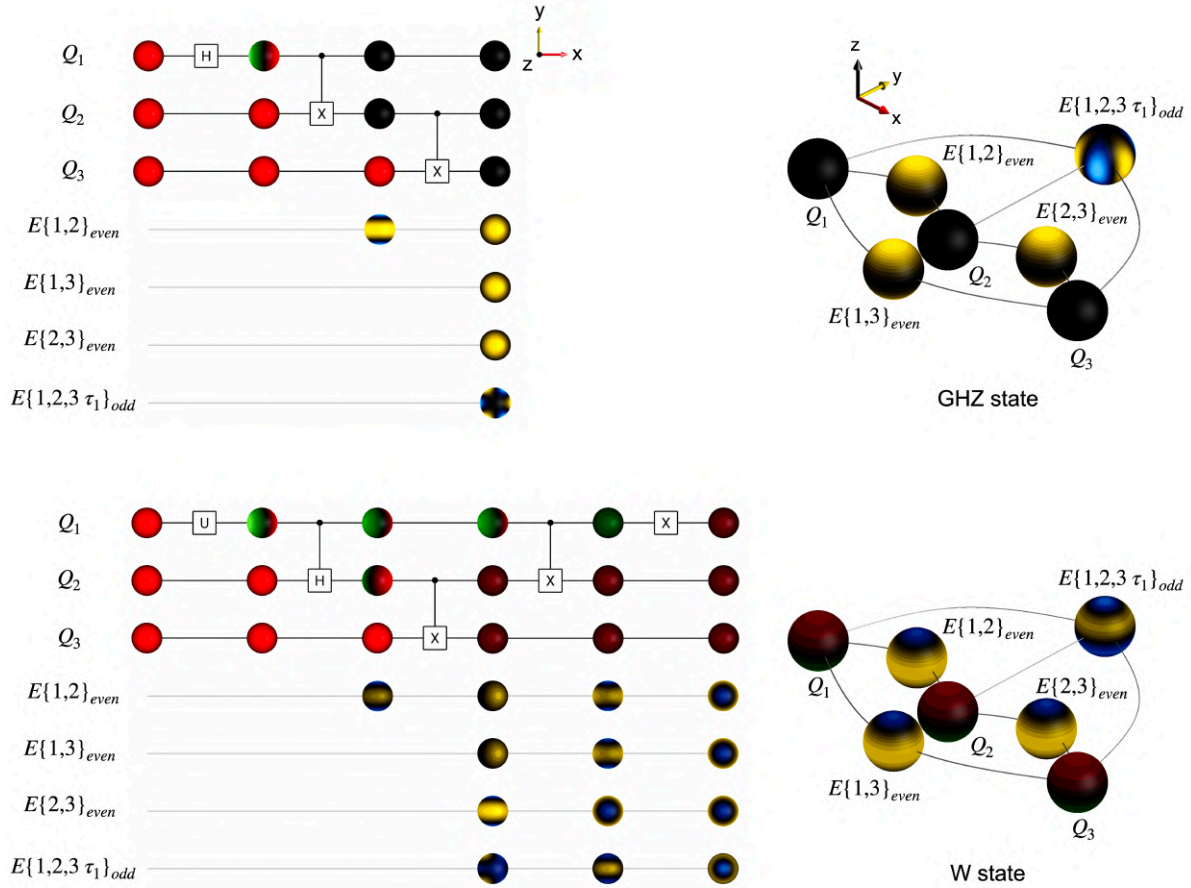


Fig. 6. BEADS-augmented circuit representations of the three-qubit GHZ and W state generation \otimes . Top views of beads representing the system state before and after gates in circuits to generate the GHZ state (top) and the W state (bottom) starting with an initial state $|000\rangle$ are shown on the left. Oblique view visualizations of the resulting final states are displayed on the right. Using the BEADS representation, it is obvious that the GHZ state is maximally entangled whereas the W state is not. Moreover, the W state is totally axially symmetric with respect to rotations around the z-axis while the GHZ has a threefold rotational symmetry around the same axis which can be deduced from the surface pattern of the trilinear E-Bead $E\{1,2,3 \tau_1\}_{odd}$. Lines connecting individual beads serve as auxiliary entanglement indicators.

In the following, we show how key features of quantum algorithms can be analyzed using the BEADS-augmented circuit representation, which provides a compact visualization of

the quantum states obtained by each quantum gate, in particular, the generation and manipulation of entanglement. This is illustrated for Grover’s algorithm and the teleportation protocol.

Grover’s algorithm

Grover’s algorithm (58) is also known as quantum search algorithm. It is one of the most prominent examples of quantum algorithms and it is specifically designed for efficiently searching solutions to a black box function, i.e., computational input strings for which the function yields a specific output (e.g., 1). In Fig. 7, we provide BEADS visualizations of two- and three-qubit Grover searches with a single solution, respectively, and show how our representation provides an overview of the algorithm.

The two-qubit circuit (2) highlights the individual steps of the algorithm. During the Grover iteration U_G , maximum genuine two-qubit entanglement is created. It is immediately clear that the generated entangled states which have antisymmetric components $E\{1,2\}_{odd}$ are different to the maximally entangled Bell states (see Fig. 2).

The resulting output state of U_G corresponds to a computational basis state $|01\rangle$, the sought solution in this example, which we can directly deduce from the Q-Beads orientations, i.e., the visible color in the center of the upper hemisphere that is visible in top view. Based on the perfect alignment parallel to the measurement direction and vanishing E-Beads, it is clear that a single application of U_G is sufficient to obtain the solution with certainty in a two-qubit single-solution Grover algorithm. Here, entanglement is created during the Grover iteration U_G by the phase oracle U_ω and subsequently eliminated in the diffusion gate U_S by the U_0 operation.

The bottom circuit in Fig. 7 corresponds to a three-qubit Grover quantum search, again for a case with only one solution (here, 011). Here, Grover iterations U_G are summarized in single blocks and for simplicity we only show fully symmetric E-Beads. It is well-known, how the number of required iterations depends on the number of qubits and solutions (see supplementary section S19), and the BEADS-augmented circuit makes it clear that unlike in the two-qubit case a single iteration does not yield the solution with certainty (59). By examining the Q-Beads after each iteration, the likelihood to measure the correct solution is visible. Using the BEADS representation, one can then directly see that the correct solution is almost, yet not precisely ($p = 78.13\%$) achieved after two iterations. The subsequent iterations worsen the performance. After six iterations the correct solution is almost found with certainty ($p = 99.98\%$) when the qubits are measured. We provide an extended analysis of Grover’s algorithm in supplementary section S19.

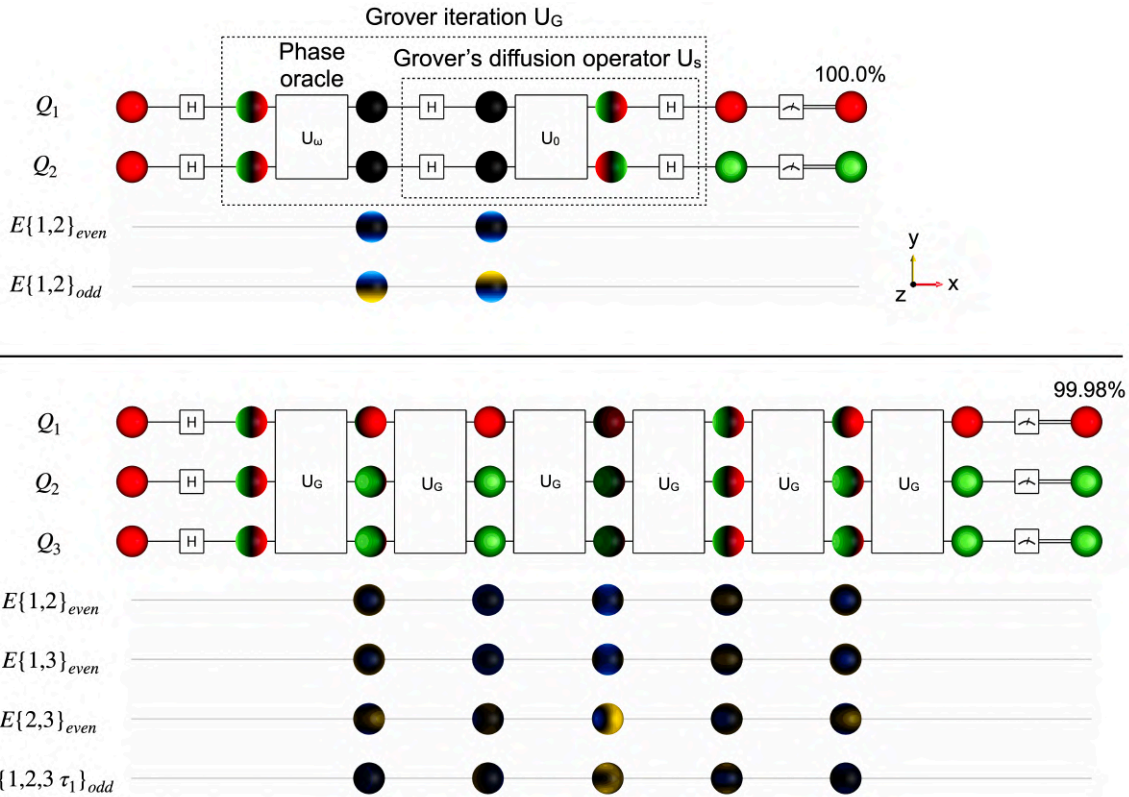


Fig. 7. BEADS-augmented circuit representation of Grover's algorithm \otimes . Grover's quantum search algorithm (58) is visualized for two qubits (top) and three qubits (bottom). Using the BEADS representation, steps where entanglement is maximum or minimum, can be readily identified and one can directly read off the state of interest based on the Q-Bead colors: 01 (red, green) for the two-qubit case on top and 011 (red, green, green) for the three-qubit case shown at the bottom. For three qubits, visualizing the outcomes of each Grover iteration U_G reveals where a solution can be measured with high probability. The measurement probabilities for the shown measurement outcomes are displayed above the final states.

Based on the properties and capabilities of different hardware platforms, a compilation of quantum gates results in different control sequences, the effects of which can be visually compared to the action of the ideal target gates. An experimental implementation of a CNOT gate is visualized and explained in supplementary section S16 using the BEADS representation. Furthermore, in realistic simulations the effects of gate imperfections can be visualized in the BEADS-augmented circuit representation.

Result 13: The BEADS representation can be used to analyze and compare idealized gates or entire quantum algorithms with differently compiled experimental implementations and to visualize the effect of experimental imperfections. It provides an overview over the evolution of entanglement-related connected correlations, the effects of gates, and measurements.

Quantum teleportation

In quantum information, quantum teleportation is a fundamental protocol which is specifically applied to transfer the state of a qubit onto another qubit by using entanglement and classical communication (60). For instance, we visualize the teleportation of the state

$|R\rangle = 1/\sqrt{2}(|0\rangle + i|1\rangle)$ in Fig. 8 using the BEADS representation. As the intermediate two-qubit measurement is symmetric (both qubits are measured along the z-axis), we simplify the representation by just showing fully permutation symmetric E-Beads. A non-simplified BEADS visualization of the provided circuit is given among further teleportation examples in supplementary section S20.

We consider a system of three qubits where Q_1 and Q_2 are located in Alice's lab and Q_3 is located in Bob's remote lab. Q_1 is prepared in the state $|R\rangle$ and the remaining qubits form a Bell pair $|\Phi^+\rangle$ which has been previously generated as was shown in Fig. 3 and supplementary section S17. The goal is to transfer the unknown state of Q_1 to Q_3 . First, a Bell measurement is performed by Alice on the first two qubits. This is implemented by a CNOT_{12} gate and a Hadamard gate H_1 followed by a measurement in the computational basis. Indeed, it is clearly visible that the initial CNOT_{12} operation maximally entangles the first qubit with the already entangled EPR pair creating genuine three-qubit entanglement and additional non-classical connected two-qubit correlations between Q_1 and Q_2 , and Q_1 and Q_3 . As was discussed before, the following Hadamard gate morphs the E-Beads which are associated with the first qubit, that is, $E\{1,2\}_{\text{even}}$, $E\{1,3\}_{\text{even}}$, and $E\{1,2,3\}_{\text{odd}}$. For the subsequent measurement, we can predict the outcomes based on the colors of the Q-Beads Q_1 , Q_2 , and the E-Bead $E\{1,2\}_{\text{even}}$ along the measurement direction (z-axis). Since all these beads are black, i.e., the probability to measure $|1\rangle$ for the individual qubits is 50% and the zz -correlation is zero (i.e., the bit parity probability is 50% as well), we expect any of the four possible outcomes with a probability of 25% (fully uncorrelated outcomes). Indeed, we observe this constellation of outcomes in Fig. 8 where each possible outcome is visualized as a beads column after the measurement.

Note that here the measurement outcomes are fully zzy -correlated. As was briefly mentioned before, such asymmetric correlations can also be predicted based on the BEADS representation. We provide several approaches that use the complete BEADS picture to deduce asymmetric correlations as applied examples in the context of Bell's theorem in supplementary section S22.

Result 14: Comparing possible measurement outcomes in the BEADS representation allows to identify hidden correlations on a visual level.

If Alice sends the actually obtained measurement results to Bob through classical communication, the teleportation protocol requires Bob to apply an X-gate to Q_3 if the measurement outcome of Q_2 is 1 (corresponding to a classically controlled X-gate) followed by a Z-gate on Q_3 if the measurement outcome of Q_1 is 1 (corresponding to a classically controlled Z-gate).

These corrections finally ensure that the correct state is encoded on Q_3 , and one can visually monitor but also directly predict the required corrections on Q_3 for every possible outcome in the BEADS picture.

An alternative way to view the system state after a measurement in the BEADS representation, is given in terms of a corresponding mixed state. This is achieved by forming the weighted sum of the density operators of all possible outcome states, the outcome probabilities serving as weights, respectively. Despite the BEADS representation being especially useful to visualize pure states, it can also be used for representing mixed states. In Fig. 8, we thus show an operation Σ which does not correspond to a gate but which symbolizes the discussed mixed state formation and we visualize the resulting mixed state as the last step in the circuit. Indeed, we find that Q_1 and Q_2 are now fully black which corresponds to maximally mixed reduced states of both qubits, yet Q_3 retains the desired

state. We provide an analogous visualization which directly uses a mixed state visualization after the measurement in supplementary section S20.

Result 15: The BEADS representation is suitable to visualize pure and mixed states.

At this point, it shall be emphasized that the BEADS representation is generally well-suited to visualize and understand quantum information protocols such as quantum teleportation. For instance, the ability to visualize entanglement-related connected correlations in the BEADS representation makes it an optimal choice to investigate entanglement swapping (61, 62) where entanglement between two distant qubits is created by generating four-qubit entanglement using two Bell pairs. We provide an exemplary BEADS visualization of entanglement swapping in supplementary section S21.

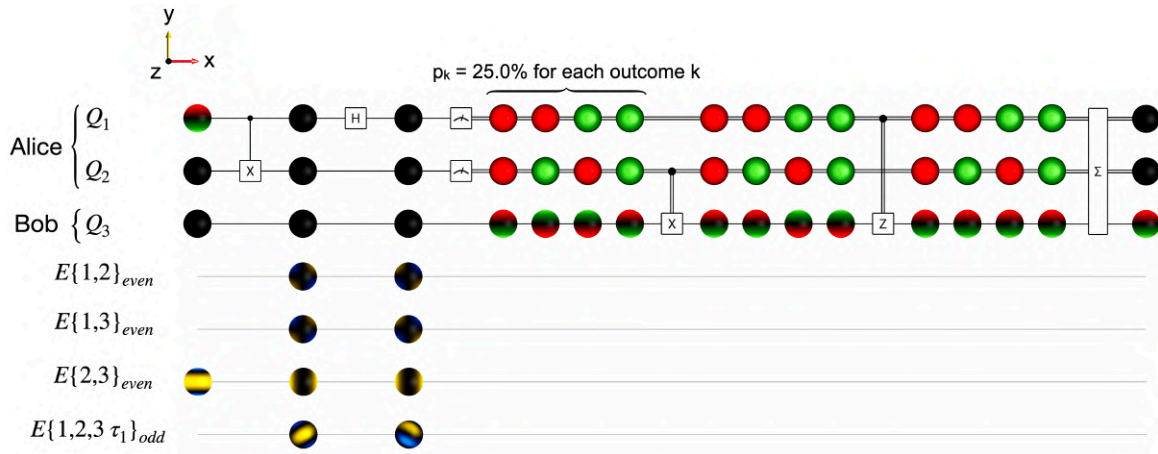


Fig. 8. BEADS representation of the quantum teleportation protocol \otimes . The state $|R\rangle = 1/\sqrt{2}(|0\rangle + i|1\rangle)$ is teleported from Q_1 onto Q_3 . The protocol first involves entangling Q_1 with the Bell pair formed by Q_2 and Q_3 . The three-qubit entanglement is then manipulated by a local Hadamard gate, which causes morphing of the affected E-Beads. Subsequently, the first and second qubits are measured in the computational basis. Together with the preceding gates, this implements a Bell measurement. The effect of the classically controlled correction gates indicated by double wires can be directly seen. In the last step, we provide the equivalent mixed state representation that comprises all possible outcomes.

Variants and simplifications

As we indicated throughout the preceding sections, the BEADS representation can be tailored such that specific aspects of interest can be faithfully visualized in a simplified fashion. In the following, we summarize and discuss different simplifications of BEADS visualizations, point out potential use-cases and address implications for the completeness of the representation.

In Fig. 9 we provide different BEADS visualizations of an arbitrary two-qubit quantum state which is highly asymmetric and partially entangled. The most general complete BEADS variant is given in terms of (A) Q- and T-Beads including all symmetry components. As was discussed before, this visualization is suitable to predict measurement outcomes of quantum states, yet connected correlations are merely indicated by the specialized coloring (see supplementary section S9 for a detailed explanation).

A natural extension (**B**) thus involves the previously outlined separation of correlation types into non-classical connected and compound correlations. While this variant provides direct insights into the intrinsic structures, that is, the topologies and symmetries of the different correlation types, it is less intuitive to be used to predict measurement outcomes unless the visualized states are either fully separable or maximally entangled in which case the total correlation is entirely represented by one correlation type.

If one is instead only interested in characterizing the entanglement in the system, it is also possible (**C**) to omit all compound correlations. As was discussed earlier, this still yields a complete representation because compound correlations represent redundant information.

One may further (**D**) omit beads that do not correspond to fully symmetric correlations if one is only interested in predicting measurement outcomes of symmetric measurements, which are encountered frequently in quantum information processing where measurements are commonly conducted along the z-axis, that is, in the computational basis. Indeed, we chose this simplification in the sections *Grover's algorithm* and *Quantum teleportation* as the examined circuits only involve multiqubit z-measurements. Visualizations of this type are not complete, yet very clear and sufficient to cover many examples of quantum algorithms and protocols.

Last, one may even choose to omit all correlation beads. This may serve as an entry point when first introducing quantum mechanics which then allows to, e.g., focus on the effects of local gates in multiqubit separable states or the implications of entangling operations on the reduced states corresponding to individual qubits.

Further simplifications and alternative plotting variants are shown in section S10 of the supplementary material and involve combinations of beads of different spherical function point symmetry to reduce the overall number of beads. However, such approaches do not ensure a uniform interpretation of the introduced color schemes and may complicate the prediction of measurement outcomes.

A minor simplification which we apply throughout this paper is given in terms of omitting the identity bead $\{\emptyset\}$. In quantum states, the expectation value of the identity operator \mathbb{I} is always 1. The corresponding bead is given by a spherical harmonic of rank $j = 0$, that is, a spherical function with value 1 in all spatial directions which does not provide any further implications other than the direct representation of the state norm for which it can be omitted in the visualization.

Most importantly, combinations of the suggested simplifications are possible. For instance, it is always possible to visualize only fully permutation symmetric beads while viewing total correlations or separate correlation types.

Result 16: The BEADS representation is adaptable with respect to visualized correlation types and permutation symmetry components to highlight different aspects of interest. Simplifications can be made which however correspond to incomplete representations but allow to capture relevant information and to provide a clear and intuitive picture.

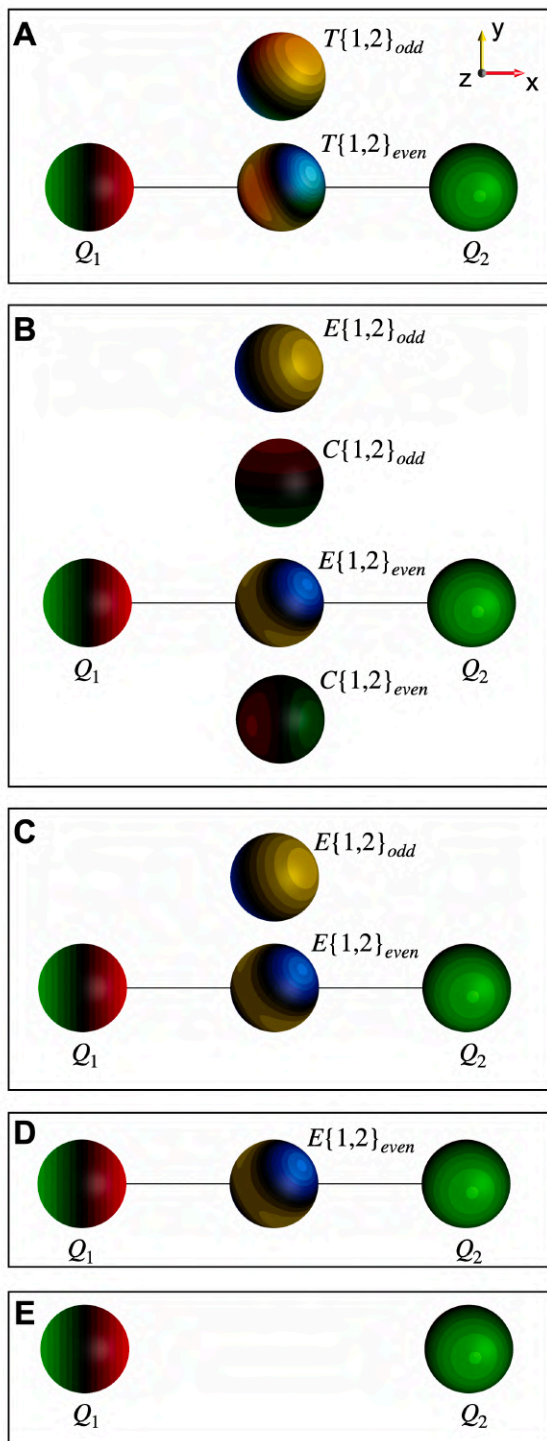


Fig. 9. BEADS variants. Possible variants of BEADS representations of quantum states include total correlations (see supplementary section S9 for details on the applied color scheme) with full symmetry display (**A**, complete information), separate correlations with full symmetry display (**B**, complete information), connected correlations only with full symmetry display (**C**, complete information), fully symmetric entanglement (**D**, incomplete information), or no correlation (**E**, incomplete information).

Discussion

The BEADS representation introduced in this article provides a general, accurate, complete, and easy to interpret visualization of quantum states which is highly adaptive. It can be tailored to only show relevant information of interest, thus enabling the user to choose a suitable balance between completeness of the representation and simplicity of the visualized information depending on the application or intended recipients. The representation is based on the decomposition of an arbitrary operator into LISA tensor operators (37, 39) that can be directly mapped onto spherical harmonics (see Materials and Methods), which was previously introduced for the DROPS representation (37). For increasing dimensions of a Hilbert space, i.e., for systems consisting of an increasing number of qubits, the number of required LISA operators grows exponentially. However, due to the various possibilities to simplify the BEADS representation, this growth can be counteracted to some extent. We extend the DROPS mapping by introducing non-trivial scaling factors (see Materials and Methods) providing a novel phase-space representation that directly visualizes expectation values of interest for systems of individually addressable particles and which we deem particularly useful for the visualization of pure or mixed quantum states represented by the density operator. With this, we achieve a representation which has significantly enhanced applicability. Differences between BEADS and DROPS are further graphically illustrated in Fig. 33 in supplementary section S12.

Using selected examples, we demonstrated applications of the universal BEADS representation in the case of single-qubit, two-qubit, or systems consisting of three or more qubits. Indeed, the visualization is not even restricted to the visualization of qubit system states and can be extended to the visualization of states of arbitrary qudit systems as well.

In the BEADS representation, Q-Beads are a representation of the reduced single-qubit density operators and provide a direct visualization of the spatial orientation of qubits, rotations of qubits, direction-dependent expectation values and measurement probabilities. Although Q-Beads are essentially equivalent to the Bloch vector, the alternative visualization approach by spherical functions notably facilitates an interpretation of expectation values and probabilities in arbitrary directions (see supplementary section S12). The BEADS representation further gives a direct and intuitive visualization of correlations. Different types of beads allow to visualize non-classical connected (E-Beads), total (T-Beads), and compound correlations (C-Beads) between all qubits or subsets of qubits in a system and provide corresponding direction-dependent expectation values and measurement probabilities in quantum states. E-Beads, which are obtained by removing compound correlations from the density operator (see supplementary section S7) (44), offer the possibility to directly view the spatial orientation of entanglement-based correlations and provide non-classical connected correlation expectation values in arbitrary directions. Notably, this represents an important innovation, as previous Ursell-function-based visualization approaches such as correlation matrix visuals (CMVs) (49) achieve visualizations that merely provide approximations to genuine n -qubit connected correlations along selected spatial directions and are less intuitive for correlations between more than two qubits. For the interested reader, we also provide a detailed comparison and analysis of BEADS representations and CMVs of two-qubit connected correlations in supplementary section S12. The applied separation of correlation types is currently restricted to visualizations of pure states and direct representations of mixed state entanglement-related correlations by Ursell-function-based approaches is an open problem which is currently under investigation.

The BEADS representation is symmetry adapted and thus reproduces spatial, e.g., rotational symmetries and permutation symmetries of correlations of a given state in a visual way. Since the BEADS representation is based on the decomposition of a density operator, it does

not visualize the global phase. If the global phase is of interest, the BEADS representation can be supplemented by the state vector or state-vector-based alternative representations such as the dimensional circle notation (DCN) (52).

We showed that a clear link between classical bits and qubits exists in the BEADS representation. In addition, due to the ability to visualize and observe rotations by single-qubit gates, the more intricate transformations induced by multiqubit gates, and the effects of projective measurements, together with the possibility to simultaneously represent all possible measurement outcomes, the BEADS representation is useful for didactic and scientific purposes with target audiences ranging from the general public to researchers in quantum information processing. Indeed, the visualization is particularly useful for understanding and designing quantum gates, predicting measurement outcomes and understanding and analyzing quantum algorithms. However, since BEADS are expectation-value-based, they do not provide a direct visualization of probability amplitudes which are central in the design of quantum algorithms. Hence, alternative representations such as DCN (52) may be more suitable for such applications.

Besides offering a dynamical simulation software (QuBeads, see supplementary section S23), which allows to use the BEADS representation in a highly interactive manner, we find it beneficial to provide tangible three-dimensional BEADS models as a hands-on approach for educational purposes, thus allowing to literally grasp the otherwise abstract mathematical concepts of quantum mechanics and especially quantum computing. Note that here, we do use the term model to denote a physical tactile object (alternatively referred to as a token). As was briefly mentioned in the introduction, the BEADS representation is not a mechanistic model of quantum computing and is not capable of performing computations on its own. Instead, it is a representation of the abstract quantum states of a system of qubits which is independent of the experimental platform which qubits are implemented on. We provide a detailed hierarchical overview on models and representations in context of the BEADS representation in supplementary section S13.

In addition, we summarize the aspects mentioned in this discussion in tabular form in supplementary section S12 where we also provide a comparative assessment of existing alternative representations which were briefly addressed throughout this article.

The BEADS representation provides a new way to see quantum information. In particular, the effect of extending the standard circuit representation to the BEADS-augmented circuit representation is akin to switching on the light to reveal what is happening during a quantum algorithm.

Materials and Methods

The LISA tensor operator basis

In order to map an operator A , e.g., the density operator describing a quantum state, to a corresponding BEADS representation, A is decomposed in a suitable spherical tensor basis. In (37), we introduced the so-called LISA spherical tensor basis, which is especially suited for applications in which the qubits are distinguishable. In particular, this is the case for quantum computing, for which the DiVincenzo criteria (38) include single-qubit gates (as part of a universal set of quantum gates) and the capability to perform qubit-specific measurements.

The LISA tensor operators $T_{j,m}^{(\ell)}$ with the rank j and order $m \in \{-j, \dots, j\}$ form a complete basis and can be organized in sets ℓ that are hierarchically defined based on their **l**inearity (i.e., the number of qubits on which the basis operator acts), **s**ubsystem (the involved qubits on which the basis operator acts), and **a**uxiliary criteria, such as permutation symmetry, parentage and (for systems consisting of more than five qubits) additional sublabels (37,

39). Explicit expressions of the standard LISA operators for systems consisting of up to six qubits can be found in (37) and (39).

General visualization approach

As shown in (37, 39), any operator A can be uniquely decomposed in the form

$$A = \sum_{\ell \in L} A^{(\ell)} \quad (2)$$

where each of the components $A^{(\ell)}$ correspond to a specific set ℓ , such that $A^{(\ell)}$ can be expressed as a linear combination of LISA basis operators $T_{j,m}^{(\ell)}$

$$A^{(\ell)} = \sum_{j \in J(\ell)} \sum_{m=-j}^j c_{jm}^{(\ell)} T_{j,m}^{(\ell)} \quad (3)$$

where the set of ranks $J(\ell)$ contains each value j not more than once (37).

For example, in the case of a system consisting of two qubits, $A^{(\ell)}$ can be one of the *linear* operators $A^{\{1\}}$ or $A^{\{2\}}$ acting only on the first or second qubit, respectively. Furthermore, $A^{(\ell)}$ can be the *bilinear* operator $A^{\{1,2\}}$ acting on both qubits, and the operator $A^{\{\emptyset\}}$, which is proportional to the identity operator.

Similarly, in the case of a system consisting of three qubits, there can be *linear* operator components ($A^{\{1\}}$, $A^{\{2\}}$, $A^{\{3\}}$), *bilinear* operator components ($A^{\{1,2\}}$, $A^{\{1,3\}}$, $A^{\{2,3\}}$), and the identity term $A^{\{\emptyset\}}$. In addition, there can be *trilinear* operator components acting on all three qubits. However, unlike for the *bilinear* components $A^{\{k,l\}}$, it is not possible to combine all trilinear components in a single set ℓ because in this case the condition would be violated that the set of ranks $J(\ell)$ must not contain any value j more than once, as otherwise a bijective mapping between spherical tensor operators and simple spherical functions would not be possible (for details, see Table 1 of (37)). In the LISA basis, this problem is solved by adding an additional label τ_k based on the symmetry of operator components with respect to permutation of qubits. This results in the four trilinear operator components ($A^{\{k,l,m \tau_1\}}$, $A^{\{k,l,m \tau_2\}}$, $A^{\{k,l,m \tau_3\}}$, $A^{\{k,l,m \tau_4\}}$), where τ_1 corresponds to completely symmetric and τ_4 to completely antisymmetric permutation symmetry, (whereas τ_2 and τ_3 correspond to symmetric and antisymmetric permutation symmetry with respect to a permutation of only the first and second qubit) (37).

In the DROPS representation (37), each of the operator components $A^{(\ell)}$ is directly mapped to a unique spherical function $f_A^{(\ell)}$ (called a ‘‘droplet function’’) by simply replacing the spherical tensor operator in Eq. 3 by spherical harmonics:

$$A^{(\ell)} = \sum_{j \in J(\ell)} \sum_{m=-j}^j c_{j,m}^{(\ell)} T_{j,m}^{(\ell)} \Leftrightarrow f_A^{(\ell)} = \sum_{j \in J(\ell)} \sum_{m=-j}^j c_{j,m}^{(\ell)} Y_{j,m} \quad (4)$$

Hence, any operator A can be bijectively mapped on a discrete *set* of droplet functions $f_A^{(\ell)}$ (37):

$$A = \sum_{\ell \in L} A^{(\ell)} \Leftrightarrow \bigcup_{\ell \in L} f_A^{(\ell)} \quad (5)$$

The obtained set of spherical functions satisfies generalized Stratonovich conditions (26, 27, 31) for which the achieved mapping can be viewed as a generalized Wigner-type representation (37).

BEADS mapping

Based on the mapping of Eq. 4, the following extensions are introduced in the BEADS representation:

(A) Spherical function symmetry-adapted sets ℓ'

We introduce new sets ℓ' with respect to the spherical function symmetries. In particular, we subdivide the original sets ℓ (36) according to *spherical function point symmetry*, that is, the behavior under space inversion where odd point symmetry of spherical functions corresponds to a sign flip whereas even point symmetry implies invariance under space inversion. This is equivalent to subdividing spherical functions in ℓ according to even or odd ranks of the underlying LISA tensor operators such that modified mapping is

$$\sum_{\ell' \in \mathcal{L}} A^{(\ell')} \Leftrightarrow \bigcup_{\ell' \in \mathcal{L}} b_A^{(\ell')} \quad (6)$$

As the point symmetries of spherical functions $b_A^{(\ell')}$ are well-defined, seeing the spherical functions from a single perspective provides complete information as the spherical function values on the hidden hemisphere can be directly inferred. Thus, we use this as a standard approach for our representation.

In the BEADS representation, spherical functions $b_A^{(\ell')}$ are called “beads”. We use a general labelling scheme where involved qubits and additional labels are written in curly brackets and the spherical function point symmetry is provided as a subscript, e.g., $\{1,2,3 \tau_1\}_{odd}$. An overview of all bead spherical function point symmetries and permutation symmetries is given in supplementary section S2.

(B) Introduction of novel bead scaling factors $s_j^{(\ell')}(N, g)$

Compared to the Wigner-type DROPS representation, we introduce bead ℓ' and rank j specific scaling factors $s_j^{(\ell')}(N, g)$ which depend on the total number N of qubits in the system and the linearity g .

By this, we scale spherical harmonics of different ranks j which belong to the same bead ℓ' independently such that the resulting bead function values directly correspond to expectation values of interest.

The original mapping introduced in Eq. 4 thus generalizes to:

$$\begin{aligned} A^{(\ell')} &= \sum_{j \in J(\ell')} \sum_{m=-j}^j c_{j,m}^{(\ell')} T_{j,m}^{(\ell')} \Leftrightarrow f_A^{(\ell')} = \sum_{j \in J(\ell')} \sum_{m=-j}^j c_{j,m}^{(\ell')} Y_{j,m} \\ &= \sum_{j \in J(\ell')} \sum_{m=-j}^j s_j^{(\ell')}(N, g) c_{j,m}^{(\ell')} Y_{j,m} \quad (7) \end{aligned}$$

The scaling factors $s_j^{(\ell')}(N, g)$ are formed by a product of the three individual scaling factors

$$s_j^{(\ell')}(N, g) = \zeta(N) \cdot \xi_j^{(\ell')}(g) \cdot \eta_j \quad (8)$$

Here, $\zeta(N)$ depends on the total number N of qubits in a system, η_j is a rank-dependent scaling factor, and $\xi_j^{(\ell')}(g)$ denotes additional rank- and linearity-dependent factors which are specific for each bead. The latter are determined by one of two approaches: Scaling factors of fully permutationally symmetric beads are calculated such that the resulting spherical function values directly correspond to experimentally measurable expectation values of Pauli product operators. We give a detailed derivation in supplementary section S3. Scaling factors $\xi_j^{(\ell')}(g)$ of spherical functions corresponding to beads which do not represent fully permutation symmetric components are instead determined based on the global unitary bound of the underlying spherical tensor operator which is explained in supplementary section S4. In both cases, scaling factors are determined with respect to axial LISA tensor operators, i.e., LISA operators of order $m = 0$. Operator components of order $m \neq 0$ are scaled with the scaling factors determined for the corresponding axial operators. We summarize the scaling factors for systems of up to three qubits in supplementary section S5. Note that unlike in (37, 39) where non-Hermitian LISA tensor operators are mapped onto complex spherical harmonics, here, we use corresponding Hermitian LISA operators (see supplementary section S1) in derivations and descriptions throughout this article. These operators are mapped onto real spherical harmonics. This is motivated by the fact that we focus on visualizing density operators which are Hermitian by definition (yet, both approaches are entirely equivalent and yield the exact same results). The introduced scaling factors give a set of spherical functions which do not satisfy all Stratonovich conditions. In particular, the scaling approach prevents satisfying the norm condition $\sum_{\ell' \in L'} \int_{S^2} f_A^{(\ell')}(\theta, \phi) f_{\text{Id}}^{(\ell')}(\theta, \phi) d\mu = \text{Tr}(A)$ and hence the BEADS representation cannot be interpreted as a generalized Wigner function. Instead, it can be viewed as generalization of the Husimi function (see supplementary section S11).

Analogous to what was shown by Leiner et al. (41), it is then possible to derive corresponding scaled axial tensor operators which can be used to experimentally reconstruct the BEADS representation in tomography experiments. We give an overview of the reconstruction method and outline the required operators in supplementary section S6.

Importantly, the generalized mapping (Eq. 7) is still bijective since the beads expansion coefficients $c'_{j,m}^{(\ell')}$ can always be mapped to the tensor operator coefficients

$$c_{j,m}^{(\ell')} = \frac{c'_{j,m}^{(\ell')}}{s_j^{(\ell')}(N, g)} \quad (9)$$

Separation of correlation types

As was shown by Schlienz et al. (44, 45), in a quantum system, different types of correlations can be distinguished that are denoted *non-classical connected* correlations, which arise exclusively in entangled states (47), *lower-order* quantum correlations, and *classical* correlations.

We summarize the latter two correlation types as *compound* correlations as they are generally formed by products of multiple components. *Classical* correlations are products of single-qubit expectation values and thus represent trivial redundant information. Similarly, g -linear lower-order quantum correlations mathematically emerge from products of genuine n -qubit connected correlations and $(g - n)$ local variables.

As was shown in (44–48), it is possible to calculate connected correlation coefficients, and thus, to eliminate compound correlations, by applying *Ursell* correlation functions (63). For example, bipartite and tripartite connected correlation coefficients are obtained by the following relations (44):

$$C_{\alpha,\beta}^{12} = \langle \sigma_{1\alpha} \sigma_{2\beta} \rangle - \langle \sigma_{1\alpha} \rangle \langle \sigma_{2\beta} \rangle \quad (10a)$$

$$\begin{aligned} C_{\alpha,\beta,\gamma}^{123} &= \langle \sigma_{1\alpha} \sigma_{2\beta} \sigma_{3\gamma} \rangle - \langle \sigma_{1\alpha} \rangle C_{\beta,\gamma}^{23} - \langle \sigma_{2\beta} \rangle C_{\alpha,\gamma}^{13} - \langle \sigma_{3\gamma} \rangle C_{\alpha,\beta}^{12} - \langle \sigma_{1\alpha} \rangle \langle \sigma_{2\beta} \rangle \langle \sigma_{3\gamma} \rangle \\ &= \langle \sigma_{1\alpha} \sigma_{2\beta} \sigma_{3\gamma} \rangle - \langle \sigma_{1\alpha} \rangle \langle \sigma_{2\beta} \sigma_{3\gamma} \rangle - \langle \sigma_{2\beta} \rangle \langle \sigma_{1\alpha} \sigma_{3\gamma} \rangle - \langle \sigma_{3\gamma} \rangle \langle \sigma_{1\alpha} \sigma_{2\beta} \rangle + \\ &\quad 2 \langle \sigma_{1\alpha} \rangle \langle \sigma_{2\beta} \rangle \langle \sigma_{3\gamma} \rangle \end{aligned} \quad (10b)$$

where $\alpha, \beta, \gamma \in \{x, y, z\}$ and σ_k are the Pauli matrices corresponding to the k -th qubit. Indeed, we adapt this approach to calculate non-classically correlated terms of the density operators which we can map to give BEADS representations of entanglement-related correlations. We provide detailed mathematical derivations and instructions in supplementary section S7.

We further utilize the separation of connected and compound correlations to characterize total correlations by means of a specialized color scheme which allows to indicate the ratio of n -qubit connected and compound correlations in arbitrary directions for each bead. This is explained in detail in supplementary section S9.

Representation of spherical functions

In the BEADS representation, we use three-dimensional polar plots to visualize spherical functions, that is, we plot the function on a spherical surface of constant size and represent the value at any vertex by a color defined by a color scheme. This is indeed different to other finite-dimensional phase-space representations such as DROPS (37) which are commonly plotted such that the magnitude of a spherical function value is represented by the distance from the origin to the spherical function surface in the corresponding direction. The choice of plotting methods is in general arbitrary. However, we deem our approach to be more suitable to provide a predictive visualization from all viewing perspectives.

Moreover, the standard BEADS color scheme is specifically designed to visualize quantum states described by density operators (or of Hamiltonians) which are Hermitian by definition. For such state visualizations, the phase component is restricted to real values ± 1 and can be represented by two colors. This allows to optionally use a different non-classical connected correlation color scheme to provide a clear distinction from compound correlations or single-qubit components.

We apply a red-green color scheme to represent any component which does not correspond to entanglement in pure states. Entanglement-based correlations are instead visualized by applying a yellow-blue color scale. The choice of color schemes is also arbitrary, and we present and discuss a selection of alternative schemes in supplementary section S9. For the visualization of non-Hermitian operators such as propagators (gates), adapted color schemes can be used (37).

Software

We created a software package, QuBeads, with which it is possible to simulate quantum circuits, i.e., the evolution of systems consisting of up to three qubits dynamically and which offers an easy-to-use interactive user interface. All figures in this paper were created from simulations in QuBeads. We provide a short overview of the software and installation binary files for all common operating systems in supplementary section S23.

Acknowledgments

The authors acknowledge helpful discussions with B. Kraus and T. Schulte-Herbrüggen.

Funding

The authors acknowledge funding from the Digital Europe Programme for the project DigiQ: Digitally Enhanced Quantum Technology Master (DigiQ) under grant agreement ID 101084035

Kekulé stipend of the Verband der chemischen Industrie e.V. (VCI)

TUM EDU grant 3170573

Munich Center of Quantum Science and Technology (MCQST)

Munich Quantum Valley

Bavarian NMR Center (BNMRZ)

Author contributions:

Examples: DH, SG

Conceptualization: DH, SG

Methodology: DH, SG

Investigation: DH, SG

Visualization: DH, SG

Supervision: SG

Writing—original draft: DH, SG

Writing—review & editing: DH, SG

Competing interests

Authors declare that they have no competing interests.

Data and materials availability

All data are available in the main text, the supplementary materials, or via the link to the software repository provided in supplementary section S23.

References

1. A. Acín, I. Bloch, H. Buhrman, T. Calarco, C. Eichler, J. Eisert, D. Esteve, N. Gisin, S. J. Glaser, F. Jelezko, S. Kuhr, M. Lewenstein, M. F. Riedel, P. O. Schmidt, R. Thew, A. Wallraff, I. Walmsley, F. K. Wilhelm, The quantum technologies roadmap: a European community view. *New J. Phys.* **20**, 80201 (2018).
2. M. A. Nielsen, I. L. Chuang, *Quantum computation and quantum information* (Cambridge Univ. Press, Cambridge [u.a.], ed. 10, 2010).
3. K. Castleberry, *The Gap in Quantum Understanding: How to Accurately Communicate Quantum Ideas* (2021) (available at <https://jila.colorado.edu/news->

- events/articles/gap-quantum-understanding-how-accurately-communicate-quantum-ideas).
4. J. Audretsch, *Die sonderbare Welt der Quanten, Eine Einführung* (Beck, München, ed. 2, 2012).
 5. N. Bohr, The Quantum Postulate and the Recent Development of Atomic Theory1. *Nature* **121**, 580–590 (1928).
 6. F. Bloch, Nuclear Induction. *Phys. Rev.* **70**, 460–474 (1946).
 7. R. P. Feynman, F. L. Vernon, R. W. Hellwarth, Geometrical Representation of the Schrödinger Equation for Solving Maser Problems. *Journal of Applied Physics* **28**, 49–52 (1957).
 8. R. R. Ernst, G. Bodenhausen, A. Wokaun, *Principles of Nuclear Magnetic Resonance in One and Two Dimensions* (Oxford University PressOxford, 1990).
 9. S. Heusler, W. Dür, Was man von zwei Qubits über Quantenphysik lernen kann: Verschränkung und Quantenkorrelationen. *PhyDid A - Physik und Didaktik in Schule und Hochschule* **13** (2014).
 10. T. L. Curtright, D. B. Fairlie, C. K. Zachos, *A Concise Treatise on Quantum Mechanics in Phase Space* (WORLD SCIENTIFIC, 2014).
 11. C. Ferrie, Quasi-probability representations of quantum theory with applications to quantum information science. *Rep. Prog. Phys.* **74**, 116001 (2011).
 12. M. de Gosson, *The Wigner transform* (World Scientific Publishing Europe Ltd, London, 2017).
 13. B. Koczor, F. vom Ende, M. de Gosson, S. J. Glaser, R. Zeier, Phase Spaces, Parity Operators, and the Born–Jordan Distribution. *Ann. Henri Poincaré* **24**, 4169–4236 (2023).
 14. W. P. Schleich, *Quantum Optics in Phase Space* (Wiley, 2001).
 15. F. E. Schroeck, *Quantum Mechanics on Phase Space* (Springer, Dordrecht, 1996).
 16. J. Weinbub, D. K. Ferry, Recent advances in Wigner function approaches. *Applied Physics Reviews* **5** (2018).
 17. C. K. Zachos, D. B. Fairlie, T. L. Curtright, *Quantum Mechanics in Phase Space* (WORLD SCIENTIFIC, 2005).
 18. E. Wigner, On the Quantum Correction For Thermodynamic Equilibrium. *Phys. Rev.* **40**, 749–759 (1932).
 19. J. P. Dowling, G. S. Agarwal, W. P. Schleich, Wigner distribution of a general angular-momentum state: Applications to a collection of two-level atoms. *Physical review. A, Atomic, molecular, and optical physics* **49**, 4101–4109 (1994).
 20. Kôdi HUSIMI, Some Formal Properties of the Density Matrix. *Proceedings of the Physico-Mathematical Society of Japan. 3rd Series* **22**, 264–314 (1940).
 21. G. S. Agarwal, Relation between atomic coherent-state representation, state multipoles, and generalized phase-space distributions. *Phys. Rev. A* **24**, 2889–2896 (1981).
 22. M. Auzinsh, R. Ferber, *Optical Polarization of Molecules* (Cambridge University Press, 2009).
 23. S. M. Rochester, D. Budker, Atomic polarization visualized. *American Journal of Physics* **69**, 450–454 (2001).

24. K. E. Cahill, R. J. Glauber, Density Operators and Quasiprobability Distributions. *Phys. Rev.* **177**, 1882–1902 (1969).
25. B. Koczor, R. Zeier, S. J. Glaser, Continuous phase-space representations for finite-dimensional quantum states and their tomography. *Phys. Rev. A* **101** (2020).
26. C. Brif, A. Mann, A general theory of phase-space quasiprobability distributions. *J. Phys. A: Math. Gen.* **31**, L9-L17 (1998).
27. C. Brif, A. Mann, Phase-space formulation of quantum mechanics and quantum-state reconstruction for physical systems with Lie-group symmetries. *Phys. Rev. A* **59**, 971–987 (1999).
28. R. P. Rundle, M. J. Everitt, Overview of the Phase Space Formulation of Quantum Mechanics with Application to Quantum Technologies. *Adv Quantum Tech* **4** (2021).
29. R. P. Rundle, T. Tilma, J. H. Samson, V. M. Dwyer, R. F. Bishop, M. J. Everitt, General approach to quantum mechanics as a statistical theory. *Phys. Rev. A* **99** (2019).
30. T. Tilma, M. J. Everitt, J. H. Samson, W. J. Munro, K. Nemoto, Wigner Functions for Arbitrary Quantum Systems. *Physical review letters* **117**, 180401 (2016).
31. R. L. Stratonovich, On Distributions in Representation Space. *J. Exp. Theor. Phys.*, 1012–1020 (1956).
32. D. J. Philp, P. W. Kuchel, A way of visualizing NMR experiments on quadrupolar nuclei. *Concepts Magn. Reson.* **25A**, 40–52 (2005).
33. A. Pines, S. Vega, D. J. Ruben, T. W. Shattuck, D. E. Wemmer, Eds., *Magnetic resonance in condensed matter - recent developments : proceedings of the IVth Ampere International Summer School, Pula, Yugoslavia, September 13-23, 1976* (Ljubljana, Yugoslavia, 1976).
34. P. S. Jessen, D. L. Haycock, G. Klose, G. A. Smith, I. H. Deutsch, G. K. Brennen, Quantum control and information processing in optical lattices. *Quantum Information and Computation* **1**, 20–32 (2001).
35. B. C. Sanctuary, F. P. Temme, Multipole N.M.R. *Molecular Physics* **55**, 1049–1062 (1985).
36. J. Xu, D. Budker, D. A. Barskiy, Visualization of dynamics in coupled multi-spin systems. *Magnetic resonance (Gottingen, Germany)* **3**, 145–160 (2022).
37. A. Garon, R. Zeier, S. J. Glaser, Visualizing operators of coupled spin systems. *Phys. Rev. A* **91** (2015).
38. D. P. DiVincenzo, The Physical Implementation of Quantum Computation. *Fortschritte der Physik* **48**, 771–783 (2000).
39. D. Leiner, R. Zeier, S. J. Glaser, Symmetry-adapted decomposition of tensor operators and the visualization of coupled spin systems. *J. Phys. A: Math. Theor.* **53**, 495301 (2020).
40. M. Tesch, N. J. Glaser, B. Koczor, S. J. Glaser, *SpinDrops* (Garching, Germany, 2018).
41. D. Leiner, R. Zeier, S. J. Glaser, Wigner tomography of multispin quantum states. *Phys. Rev. A* **96** (2017).
42. D. Leiner, S. J. Glaser, Wigner process tomography: Visualization of spin propagators and their spinor properties. *Phys. Rev. A* **98** (2018).

43. A. Devra, N. J. Glaser, D. Huber, S. J. Glaser, "Wigner State and Process Tomography on Near-Term Quantum Devices". (2023).
44. J. Schlienz, G. Mahler, Description of entanglement. *Physical review. A, Atomic, molecular, and optical physics* **52**, 4396–4404 (1995).
45. J. Schlienz, G. Mahler, The maximal entangled three-particle state is unique. *Physics Letters A* **224**, 39–44 (1996).
46. G. Mahler, M. Keller, R. Wawer, Quantum-networks: master equation and local measurements. *Zeitschrift für Physik B Condensed Matter* **104**, 153–164 (1997).
47. M. C. Tran, J. R. Garrison, Z.-X. Gong, A. V. Gorshkov, Lieb-Robinson bounds on n-partite connected correlation functions. *Physical review. A* **96** (2017).
48. A. Kumar, M. S. Krishnan, Quantum entanglement and teleportation using statistical correlations. *J Chem Sci* **121**, 767–775 (2009).
49. R. Mukherjee, A. E. Mirasola, J. Hollingsworth, I. G. White, K. R. A. Hazzard, Geometric representation of spin correlations and applications to ultracold systems. *Phys. Rev. A* **97** (2018).
50. B. Sundar, K. C. Wang, K. R. A. Hazzard, Analysis of continuous and discrete Wigner approximations for spin dynamics. *Phys. Rev. A* **99** (2019).
51. A. Javadi-Abhari, M. Treinish, K. Krsulich, C. J. Wood, J. Lishman, J. Gacon, S. Martiel, P. D. Nation, L. S. Bishop, A. W. Cross, B. R. Johnson, J. M. Gambetta, *Quantum computing with Qiskit* (2024).
52. J. Bley, E. Rexigel, A. Arias, N. Longen, L. Krupp, M. Kiefer-Emmanouilidis, P. Lukowicz, A. Donhauser, S. Küchemann, J. Kuhn, A. Widera, Visualizing entanglement in multiqubit systems. *Phys. Rev. Research* **6** (2024).
53. K. B. Wharton, "Natural Parameterization of Two-Qubit States". (1/15/2016; <http://arxiv.org/pdf/1601.04067v1>).
54. D. M. Greenberger, M. A. Horne, A. Zeilinger, in *Bell's theorem, quantum theory and conceptions of the universe* (Springer, 1989), pp. 69–72.
55. N. D. Mermin, Quantum mysteries revisited. *American Journal of Physics* **58**, 731–734 (1990).
56. W. Dür, G. Vidal, J. I. Cirac, Three qubits can be entangled in two inequivalent ways. *Phys. Rev. A* **62** (2000).
57. M. Hein, J. Eisert, H. J. Briegel, Multiparty entanglement in graph states. *Phys. Rev. A* **69** (2004).
58. L. K. Grover, in *Proceedings of the twenty-eighth annual ACM symposium on Theory of computing* (1996), pp. 212–219.
59. M. Boyer, G. Brassard, P. Høyer, A. Tapp, Tight bounds on quantum searching. *Fortschritte der Physik: Progress of Physics* **46**, 493–505 (1998).
60. C. H. Bennett, G. Brassard, C. Crépeau, R. Jozsa, A. Peres, W. K. Wootters, Teleporting an unknown quantum state via dual classical and Einstein-Podolsky-Rosen channels. *Physical review letters* **70**, 1895–1899 (1993).
61. H.-J. Briegel, W. Dür, J. I. Cirac, P. Zoller, Quantum Repeaters: The Role of Imperfect Local Operations in Quantum Communication. *Phys. Rev. Lett.* **81**, 5932–5935 (1998).

62. W. Dür, H.-J. Briegel, J. I. Cirac, P. Zoller, Quantum repeaters based on entanglement purification. *Phys. Rev. A* **59**, 169–181 (1999).
63. H. D. Ursell, The evaluation of Gibbs' phase-integral for imperfect gases. *Math. Proc. Camb. Phil. Soc.* **23**, 685–697 (1927).
64. O. W. Sørensen, A universal bound on spin dynamics. *Journal of Magnetic Resonance* (1969) **86**, 435–440 (1990).
65. J. Stoustrup, O. Schedletzky, S. J. Glaser, C. Griesinger, N. C. Nielsen, O. W. Sorensen, Generalized bound on quantum dynamics: Efficiency of unitary transformations between non-Hermitian states. *Physical review letters* **74**, 2921–2924 (1995).
66. S. J. Glaser, T. Schulte-Herbruggen, M. Sieveking, O. Schedletzky, N. C. Nielsen, O. W. Sorensen, C. Griesinger, Unitary control in quantum ensembles: maximizing signal intensity in coherent spectroscopy. *Science* (New York, N.Y.) **280**, 421–424 (1998).
67. S. Brandt, *Data Analysis* (Springer International Publishing, Cham, 2014).
68. R. F. Werner, Quantum states with Einstein-Podolsky-Rosen correlations admitting a hidden-variable model. *Phys. Rev. A General physics* **40**, 4277–4281 (1989).
69. F. Mintert, K. Życzkowski, Wehrl entropy, Lieb conjecture, and entanglement monotones. *Phys. Rev. A* **69** (2004).
70. A. Sugita, Moments of generalized Husimi distributions and complexity of many-body quantum states. *J. Phys. A: Math. Gen.* **36**, 9081–9103 (2003).
71. B. Koczor, R. Zeier, S. J. Glaser, Time evolution of coupled spin systems in a generalized Wigner representation. *Annals of Physics* **408**, 1–50 (2019).
72. R. Frigg, S. Hartmann, in *The Stanford Encyclopedia of Philosophy*, Edward N. Zalta, Uri Nodelman, Eds. (Metaphysics Research Lab, Stanford University, ed. 2024, 2024).
73. R. Frigg, J. Nguyen, in *The Stanford Encyclopedia of Philosophy*, Edward N. Zalta, Ed. (Metaphysics Research Lab, Stanford University, ed. 2021, 2021).
74. H. W. de Regt, *Understanding Scientific Understanding* (Oxford University Press, 2017).
75. G. E. Crooks, "Quantum Gates". (2/03/2024; https://threeplusone.com/pubs/on_gates.pdf).
76. Daniel Gottesman, "Stabilizer Codes and Quantum Error Correction". (5/28/1997; <https://arxiv.org/pdf/quant-ph/9705052>).
77. E. Kubischta, I. Teixeira, Family of Quantum Codes with Exotic Transversal Gates. *Phys. Rev. Lett.* **131**, 240601 (2023).
78. Patrick Rall, "Signed quantum weight enumerators characterize qubit magic state distillation". (2/22/2017; <https://arxiv.org/pdf/1702.06990v1>).
79. R. Marx, A. F. Fahmy, J. M. Myers, W. Bermel, S. J. Glaser, Approaching five-bit NMR quantum computing. *Phys. Rev. A* **62** (2000).
80. S. J. Glaser, NMR Quantum Computing. *Angew. Chem., Int. Ed.* **40**, 147–149 (2001).
81. J. S. Bell, On the Einstein Podolsky Rosen paradox. *Physics Physique Fizika* **1**, 195–200 (1964).
82. M. Hein, W. Dür, J. Eisert, R. Raussendorf, M. van den Nest, H.-J. Briegel, *Entanglement in Graph States and its Applications*. (2006).
83. J. F. Clauser, M. A. Horne, A. Shimony, R. A. Holt, Proposed Experiment to Test Local Hidden-Variable Theories. *Phys. Rev. Lett.* **23**, 880–884 (1969).
84. D. M. Greenberger, M. A. Horne, A. Shimony, A. Zeilinger, Bell's theorem without inequalities. *Am. J. Phys.* **58**, 1131–1143 (1990).
85. T. Maudlin, *Quantum Non-Locality and Relativity* (Wiley, 2011).

Supplementary Materials for
**BEADS: A canonical visualization of quantum states for applications in
quantum information processing**

Dennis Huber, Steffen J. Glaser*

*glaser@tum.de

Supplementary Text

1 Theory	40
S1 Hermitian LISA tensor operators	40
S2 Spherical function point symmetries, permutation symmetries, and bit parities	43
S3 Canonical BEADS scaling factors of permutation symmetric density operator components	49
S4 Global unitary bound scaling factors of density operator components which are not fully permutation symmetric	54
S5 Overview of BEADS scaling factors	69
S6 Canonical axial tensor operators and tomography	70
S7 Correlation isolation using Ursell functions	72
S8 Asymmetric correlations	84
2 Technical details, concepts, and design	91
S9 BEADS color schemes	91
S10 Further simplifications and plotting variants	99
3 Comparison and classification	103
S11 Interpretation of the BEADS representation as a generalization of the Husimi function	103
S12 Comparison with other representations	105
S13 Hierarchy of models, representations, and material tokens	112
4 Application examples	114
S14 Partially entangled states	114
S15 Quantum gates and system dynamics	119
S16 NMR implementations of quantum gates	127
S17 Bell states	129
S18 Graph states	130
S19 Extended analysis of Grover's algorithm	135
S20 Quantum teleportation examples	137
S21 Entanglement swapping	142
S22 Bell's theorem	144
S23 QuBeads – a dynamical simulation software using the BEADS representation	153

1 Theory

S1 Hermitian LISA tensor operators

Hermitian LISA operators for (sub)systems of up to $N = 3$ qubits are defined as follows:

$$T_{0,0}^{\emptyset} = \frac{1}{\sqrt{2^N}} \mathbb{I} \quad (11)$$

$$T_{1,-1}^{\{k\}} = \frac{1}{\sqrt{2^N}} \sigma_{ky} \quad (12a)$$

$$T_{1,0}^{\{k\}} = \frac{1}{\sqrt{2^N}} \sigma_{kz} \quad (12b)$$

$$T_{1,1}^{\{k\}} = \frac{1}{\sqrt{2^N}} \sigma_{kx} \quad (12c)$$

$$T_{0,0}^{\{k,l\}even} = \frac{1}{\sqrt{2^N}} \frac{1}{\sqrt{3}} (\sigma_{kx}\sigma_{lx} + \sigma_{ky}\sigma_{ly} + \sigma_{kz}\sigma_{lz}) \quad (13)$$

$$T_{2,-2}^{\{k,l\}even} = \frac{1}{\sqrt{2^N}} \frac{1}{\sqrt{2}} (\sigma_{kx}\sigma_{ly} + \sigma_{ky}\sigma_{lx}) \quad (14b)$$

$$T_{2,-1}^{\{k,l\}even} = \frac{1}{\sqrt{2^N}} \frac{1}{\sqrt{2}} (\sigma_{ky}\sigma_{lz} + \sigma_{kz}\sigma_{ly}) \quad (14c)$$

$$T_{2,0}^{\{k,l\}even} = \frac{1}{\sqrt{2^N}} \frac{1}{\sqrt{6}} (2\sigma_{kz}\sigma_{lz} - \sigma_{kx}\sigma_{lx} - \sigma_{ky}\sigma_{ly}) \quad (14d)$$

$$T_{2,1}^{\{k,l\}even} = \frac{1}{\sqrt{2^N}} \frac{1}{\sqrt{2}} (\sigma_{kz}\sigma_{lx} + \sigma_{kx}\sigma_{lz}) \quad (14e)$$

$$T_{2,2}^{\{k,l\}even} = \frac{1}{\sqrt{2^N}} \frac{1}{\sqrt{2}} (\sigma_{kx}\sigma_{lx} - \sigma_{ky}\sigma_{ly}) \quad (14f)$$

$$T_{1,-1}^{\{k,l\}odd} = \frac{1}{\sqrt{2^N}} \frac{1}{\sqrt{2}} (\sigma_{kz}\sigma_{lx} - \sigma_{kx}\sigma_{lz}) \quad (15a)$$

$$T_{1,0}^{\{k,l\}odd} = \frac{1}{\sqrt{2^N}} \frac{1}{\sqrt{2}} (\sigma_{kx}\sigma_{ly} - \sigma_{ky}\sigma_{lx}) \quad (15b)$$

$$T_{1,1}^{\{k,l\}odd} = \frac{1}{\sqrt{2^N}} \frac{1}{\sqrt{2}} (\sigma_{ky}\sigma_{lz} - \sigma_{kz}\sigma_{ly}) \quad (15c)$$

$$T_{1,-1}^{\{k,l,m \tau_1\}odd} = \frac{1}{\sqrt{2^N}} \frac{1}{\sqrt{15}} \left[3\sigma_{ky}\sigma_{ly}\sigma_{my} + (\sigma_{ky}\sigma_{lx}\sigma_{mx} + \sigma_{kx}\sigma_{ly}\sigma_{mx} + \sigma_{kx}\sigma_{lx}\sigma_{my}) + \right. \\ \left. (\sigma_{ky}\sigma_{lz}\sigma_{mz} + \sigma_{kz}\sigma_{ly}\sigma_{mz} + \sigma_{kz}\sigma_{lz}\sigma_{my}) \right] \quad (16a)$$

$$T_{1,0}^{\{k,l,m \tau_1\}odd} = \frac{1}{\sqrt{2^N}} \frac{1}{\sqrt{15}} \left[3\sigma_{kz}\sigma_{lz}\sigma_{mz} + (\sigma_{kz}\sigma_{lx}\sigma_{mx} + \sigma_{kx}\sigma_{lz}\sigma_{mx} + \sigma_{kx}\sigma_{lx}\sigma_{mz}) + \right. \\ \left. (\sigma_{kz}\sigma_{ly}\sigma_{my} + \sigma_{ky}\sigma_{lz}\sigma_{my} + \sigma_{ky}\sigma_{ly}\sigma_{mz}) \right] \quad (16b)$$

$$T_{1,1}^{\{k,l,m \tau_1\}odd} = \frac{1}{\sqrt{2^N}} \frac{1}{\sqrt{15}} \left[3\sigma_{kx}\sigma_{lx}\sigma_{mx} + (\sigma_{kx}\sigma_{ly}\sigma_{my} + \sigma_{ky}\sigma_{lx}\sigma_{my} + \sigma_{ky}\sigma_{ly}\sigma_{mx}) + \right. \\ \left. (\sigma_{kx}\sigma_{lz}\sigma_{mz} + \sigma_{kz}\sigma_{lx}\sigma_{mz} + \sigma_{kz}\sigma_{lz}\sigma_{mx}) \right] \quad (16c)$$

$$T_{3,-3}^{\{k,l,m \tau_1\}odd} = \frac{1}{\sqrt{2^N}} \frac{1}{2} \left[-\sigma_{ky}\sigma_{ly}\sigma_{my} + (\sigma_{ky}\sigma_{lx}\sigma_{mx} + \sigma_{kx}\sigma_{ly}\sigma_{mx} + \sigma_{kx}\sigma_{lx}\sigma_{my}) \right] \quad (17a)$$

$$T_{3,-2}^{\{k,l,m \tau_1\}odd} = \frac{1}{\sqrt{2^N}} \frac{1}{\sqrt{6}} \left[(\sigma_{kx}\sigma_{ly}\sigma_{mz} + \sigma_{ky}\sigma_{lz}\sigma_{mx} + \sigma_{kz}\sigma_{lx}\sigma_{my}) + \right. \\ \left. (\sigma_{kx}\sigma_{lz}\sigma_{my} + \sigma_{kz}\sigma_{ly}\sigma_{mx} + \sigma_{ky}\sigma_{lx}\sigma_{mz}) \right] \quad (17b)$$

$$T_{3,-1}^{\{k,l,m \tau_1\}odd} = \frac{1}{\sqrt{2^N}} \frac{1}{2\sqrt{15}} \left[-3\sigma_{ky}\sigma_{ly}\sigma_{my} - (\sigma_{ky}\sigma_{lx}\sigma_{mx} + \sigma_{kx}\sigma_{ly}\sigma_{mx} + \sigma_{kx}\sigma_{lx}\sigma_{my}) + \right. \\ \left. 4(\sigma_{ky}\sigma_{lz}\sigma_{mz} + \sigma_{kz}\sigma_{ly}\sigma_{mz} + \sigma_{kz}\sigma_{lz}\sigma_{my}) \right] \quad (17c)$$

$$T_{3,0}^{\{k,l,m \tau_1\}odd} = \frac{1}{\sqrt{2^N}} \frac{1}{\sqrt{10}} \left[2\sigma_{kz}\sigma_{lz}\sigma_{mz} - (\sigma_{kz}\sigma_{lx}\sigma_{mx} + \sigma_{kx}\sigma_{lz}\sigma_{mx} + \sigma_{kx}\sigma_{lx}\sigma_{mz}) + \right. \\ \left. (\sigma_{kz}\sigma_{ly}\sigma_{my} + \sigma_{ky}\sigma_{lz}\sigma_{my} + \sigma_{ky}\sigma_{ly}\sigma_{mz}) \right] \quad (17d)$$

$$T_{3,1}^{\{k,l,m \tau_1\}odd} = \frac{1}{\sqrt{2^N}} \frac{1}{2\sqrt{15}} \left[-3\sigma_{kx}\sigma_{lx}\sigma_{mx} - (\sigma_{kx}\sigma_{ly}\sigma_{my} + \sigma_{ky}\sigma_{lx}\sigma_{my} + \sigma_{ky}\sigma_{ly}\sigma_{mx}) + \right. \\ \left. 4(\sigma_{kx}\sigma_{lz}\sigma_{mz} + \sigma_{kz}\sigma_{lx}\sigma_{mz} + \sigma_{kz}\sigma_{lz}\sigma_{mx}) \right] \quad (17e)$$

$$T_{3,2}^{\{k,l,m \tau_1\}odd} = \frac{1}{\sqrt{2^N}} \frac{1}{\sqrt{6}} \left[(\sigma_{kz}\sigma_{lx}\sigma_{mx} + \sigma_{kx}\sigma_{lz}\sigma_{mx} + \sigma_{kx}\sigma_{lx}\sigma_{mz}) - \right. \\ \left. (\sigma_{kz}\sigma_{ly}\sigma_{my} + \sigma_{ky}\sigma_{lz}\sigma_{my} + \sigma_{ky}\sigma_{ly}\sigma_{mz}) \right] \quad (17f)$$

$$T_{3,3}^{\{k,l,m \tau_1\}odd} = \frac{1}{\sqrt{2^N}} \frac{1}{2} \left[\sigma_{kx}\sigma_{lx}\sigma_{mx} - (\sigma_{kx}\sigma_{ly}\sigma_{my} + \sigma_{ky}\sigma_{lx}\sigma_{my} + \sigma_{ky}\sigma_{ly}\sigma_{mx}) \right] \quad (17g)$$

$$T_{1,-1}^{\{k,l,m \tau_2\}odd} = \frac{1}{\sqrt{2^N}} \frac{1}{\sqrt{12}} \left[(-2\sigma_{kx}\sigma_{lx}\sigma_{my} + \sigma_{ky}\sigma_{lx}\sigma_{mx} + \sigma_{kx}\sigma_{ly}\sigma_{mx}) + \right. \\ \left. (-2\sigma_{kz}\sigma_{lz}\sigma_{my} + \sigma_{ky}\sigma_{lz}\sigma_{mz} + \sigma_{kz}\sigma_{ly}\sigma_{mz}) \right] \quad (18a)$$

$$T_{1,0}^{\{k,l,m \tau_2\}odd} = \frac{1}{\sqrt{2^N}} \frac{1}{\sqrt{12}} \left[(-2\sigma_{kx}\sigma_{lx}\sigma_{mz} + \sigma_{kz}\sigma_{lx}\sigma_{mx} + \sigma_{kx}\sigma_{lz}\sigma_{mx}) + \right. \\ \left. (-2\sigma_{ky}\sigma_{ly}\sigma_{mz} + \sigma_{kz}\sigma_{ly}\sigma_{my} + \sigma_{ky}\sigma_{lz}\sigma_{my}) \right] \quad (18b)$$

$$T_{1,1}^{\{k,l,m \tau_2\}odd} = \frac{1}{\sqrt{2^N}} \frac{1}{\sqrt{12}} \left[(-2\sigma_{ky}\sigma_{ly}\sigma_{mx} + \sigma_{kx}\sigma_{ly}\sigma_{my} + \sigma_{ky}\sigma_{lx}\sigma_{my}) + \right. \\ \left. (-2\sigma_{kz}\sigma_{lz}\sigma_{mx} + \sigma_{kx}\sigma_{lz}\sigma_{mz} + \sigma_{kz}\sigma_{lx}\sigma_{mz}) \right] \quad (18c)$$

$$T_{2,-2}^{\{k,l,m \tau_2\}even} = \frac{1}{\sqrt{2^N}} \frac{1}{\sqrt{12}} [(2\sigma_{kx}\sigma_{lx}\sigma_{mz} - \sigma_{kz}\sigma_{lx}\sigma_{mx} - \sigma_{kx}\sigma_{lz}\sigma_{mx}) + (-2\sigma_{ky}\sigma_{ly}\sigma_{mz} + \sigma_{kz}\sigma_{ly}\sigma_{my} + \sigma_{ky}\sigma_{lz}\sigma_{my})] \quad (19a)$$

$$T_{2,-1}^{\{k,l,m \tau_2\}even} = \frac{1}{\sqrt{2^N}} \frac{1}{\sqrt{12}} [(2\sigma_{ky}\sigma_{ly}\sigma_{mx} - \sigma_{kx}\sigma_{ly}\sigma_{my} - \sigma_{ky}\sigma_{lx}\sigma_{my}) + (-2\sigma_{kz}\sigma_{lz}\sigma_{mx} + \sigma_{kx}\sigma_{lz}\sigma_{mz} + \sigma_{kz}\sigma_{lx}\sigma_{mz})] \quad (19b)$$

$$T_{2,0}^{\{k,l,m \tau_2\}even} = \frac{1}{\sqrt{2^N}} \frac{1}{2} [-\sigma_{kx}\sigma_{lz}\sigma_{my} - \sigma_{kz}\sigma_{lx}\sigma_{my} + \sigma_{ky}\sigma_{lz}\sigma_{mx} + \sigma_{kz}\sigma_{ly}\sigma_{mx}] \quad (19c)$$

$$T_{2,1}^{\{k,l,m \tau_2\}even} = \frac{1}{\sqrt{2^N}} \frac{1}{\sqrt{12}} [(-2\sigma_{kx}\sigma_{lx}\sigma_{my} + \sigma_{ky}\sigma_{lx}\sigma_{mx} + \sigma_{kx}\sigma_{ly}\sigma_{mx}) + (2\sigma_{kz}\sigma_{lz}\sigma_{my} - \sigma_{ky}\sigma_{lz}\sigma_{mz} - \sigma_{kz}\sigma_{ly}\sigma_{mz})] \quad (19d)$$

$$T_{2,2}^{\{k,l,m \tau_2\}even} = \frac{1}{\sqrt{2^N}} \frac{1}{\sqrt{12}} [(-2\sigma_{kx}\sigma_{ly}\sigma_{mz} + \sigma_{ky}\sigma_{lz}\sigma_{mx} + \sigma_{kz}\sigma_{lx}\sigma_{my}) + (-2\sigma_{ky}\sigma_{lx}\sigma_{mz} + \sigma_{kx}\sigma_{lz}\sigma_{my} + \sigma_{kz}\sigma_{ly}\sigma_{mx})] \quad (19e)$$

$$T_{1,-1}^{\{k,l,m \tau_3\}odd} = \frac{1}{\sqrt{2^N}} \frac{1}{2} [(\sigma_{ky}\sigma_{lx}\sigma_{mx} - \sigma_{kx}\sigma_{ly}\sigma_{mx}) + (\sigma_{ky}\sigma_{lz}\sigma_{mz} - \sigma_{kz}\sigma_{ly}\sigma_{mz})] \quad (20a)$$

$$T_{1,0}^{\{k,l,m \tau_3\}odd} = \frac{1}{\sqrt{2^N}} \frac{1}{2} [(\sigma_{kz}\sigma_{lx}\sigma_{mx} - \sigma_{kx}\sigma_{lz}\sigma_{mx}) + (\sigma_{kz}\sigma_{ly}\sigma_{my} - \sigma_{ky}\sigma_{lz}\sigma_{my})] \quad (20b)$$

$$T_{1,1}^{\{k,l,m \tau_3\}odd} = \frac{1}{\sqrt{2^N}} \frac{1}{2} [(\sigma_{kx}\sigma_{ly}\sigma_{my} - \sigma_{ky}\sigma_{lx}\sigma_{my}) + (\sigma_{kx}\sigma_{lz}\sigma_{mz} - \sigma_{kz}\sigma_{lx}\sigma_{mz})] \quad (20c)$$

$$T_{2,-2}^{\{k,l,m \tau_3\}even} = \frac{1}{\sqrt{2^N}} \frac{1}{2} [(-\sigma_{kz}\sigma_{lx}\sigma_{mx} + \sigma_{kx}\sigma_{lz}\sigma_{mx}) + (\sigma_{kz}\sigma_{ly}\sigma_{my} - \sigma_{ky}\sigma_{lz}\sigma_{my})] \quad (21a)$$

$$T_{2,-1}^{\{k,l,m \tau_3\}even} = \frac{1}{\sqrt{2^N}} \frac{1}{2} [(-\sigma_{kx}\sigma_{ly}\sigma_{my} + \sigma_{ky}\sigma_{lx}\sigma_{my}) + (\sigma_{kx}\sigma_{lz}\sigma_{mz} - \sigma_{kz}\sigma_{lx}\sigma_{mz})] \quad (21b)$$

$$T_{2,0}^{\{k,l,m \tau_3\}even} = \frac{1}{\sqrt{2^N}} \frac{1}{\sqrt{12}} [(-2\sigma_{kx}\sigma_{ly}\sigma_{mz} + \sigma_{ky}\sigma_{lz}\sigma_{mx} + \sigma_{kz}\sigma_{lx}\sigma_{my}) + (2\sigma_{ky}\sigma_{lx}\sigma_{mz} - \sigma_{kx}\sigma_{lz}\sigma_{my} - \sigma_{kz}\sigma_{ly}\sigma_{mx})] \quad (21c)$$

$$T_{2,1}^{\{k,l,m \tau_3\}even} = \frac{1}{\sqrt{2^N}} \frac{1}{2} [(-\sigma_{ky}\sigma_{lz}\sigma_{mz} + \sigma_{kz}\sigma_{ly}\sigma_{mz}) + (\sigma_{ky}\sigma_{lx}\sigma_{mx} - \sigma_{kx}\sigma_{ly}\sigma_{mx})] \quad (21d)$$

$$T_{2,2}^{\{k,l,m \tau_3\}even} = \frac{1}{\sqrt{2^N}} \frac{1}{2} [(-\sigma_{kx}\sigma_{lz}\sigma_{my} + \sigma_{kz}\sigma_{lx}\sigma_{my}) + (\sigma_{kz}\sigma_{ly}\sigma_{mx} - \sigma_{ky}\sigma_{lz}\sigma_{mx})] \quad (21e)$$

$$T_{0,0}^{\{k,l,m \tau_4\}even} = \frac{1}{\sqrt{2^N}} \frac{1}{\sqrt{6}} [(\sigma_{kx}\sigma_{ly}\sigma_{mz} + \sigma_{ky}\sigma_{lz}\sigma_{mx} + \sigma_{kz}\sigma_{lx}\sigma_{my}) - (\sigma_{kx}\sigma_{lz}\sigma_{my} + \sigma_{ky}\sigma_{lx}\sigma_{mz} + \sigma_{kz}\sigma_{ly}\sigma_{mx})] \quad (22)$$

S2 Spherical function point symmetries, permutation symmetries, and bit parities

The BEADS representation is highly symmetry-adapted. Thus, several different types of symmetries are visualized. In addition, as was discussed in the Results section, an interpretation in terms of bit parity probabilities is possible for some beads. In Fig. 10, we provide an overview of properties captured by the BEADS representation which must not be confused with each other.

In the BEADS representation, bit parity, which was originally introduced to define the oddness of an integer, is used in a generalized sense to describe whether after a measurement the number of qubits in the down state of the respective measurement bases is even (parity 0) or odd (parity 1). Bit parity must not be confused with the parity of a spherical function. The latter is equivalent to the point reflection symmetry of a spherical function, that is, the symmetry under space inversion. As pointed out in the Materials and Methods section we use labels *even* (no sign inversion) and *odd* (sign inversion) to indicate the point symmetry of beads. Illustrative examples of different spherical function point symmetries are provided in Fig. 11. The permutation symmetry associated with a bead corresponds to the permutation symmetry of a visualized operator component. As outlined in the Materials and Methods section, we use the LISA tensor operator basis to decompose such operators, specifically the density operator describing quantum states. The symmetry of the *density operator* under permutation of particles (that is, particle exchange) is not identical to the symmetry of a given *state* under exchange of qubit labels because a change of sign of the state corresponds simply to a different global phase and hence corresponds to the identical density operator. For example, for a system of two qubits, the singlet state function $|\Psi^-\rangle = 1/\sqrt{2}(|01\rangle - |10\rangle)$ is *antisymmetric* under exchange of qubit labels, but the corresponding density operator $\rho = 1/2(|01\rangle - |10\rangle)(\langle 01| - \langle 10|) = (\mathbb{I} - X_1X_2 - Y_1Y_2 - Z_1Z_2)/4$, using the short forms X , Y , and Z to denote corresponding Pauli matrices, is fully permutation *symmetric*. Permutation symmetries of two- and three-qubit states are visualized by examples in Fig. 12 and Fig. 13, respectively. Contributing spherical tensor operators of beads corresponding to full permutation symmetry have ranks j that are of the same parity as the linearity g of the bead. For instance, the fully permutationally symmetric bilinear ($g = 2$) bead $E\{1,2\}_{even}$ corresponds to spherical tensor operators with ranks $j \in \{0,2\}$, i.e., both, the linearity and all possible ranks are even.

Spherical function point symmetries and permutation symmetries of beads for systems consisting of up to three qubits are summarized in Table 1. Note that the identity operator \mathbb{I} has expectation value 1 and the associated bead $\{\emptyset\}$ has the same value of 1 at every point on its surface for any pure or mixed quantum state. Therefore, this bead does not provide any state-specific information and hence is omitted in visualizations of the main text for simplicity.

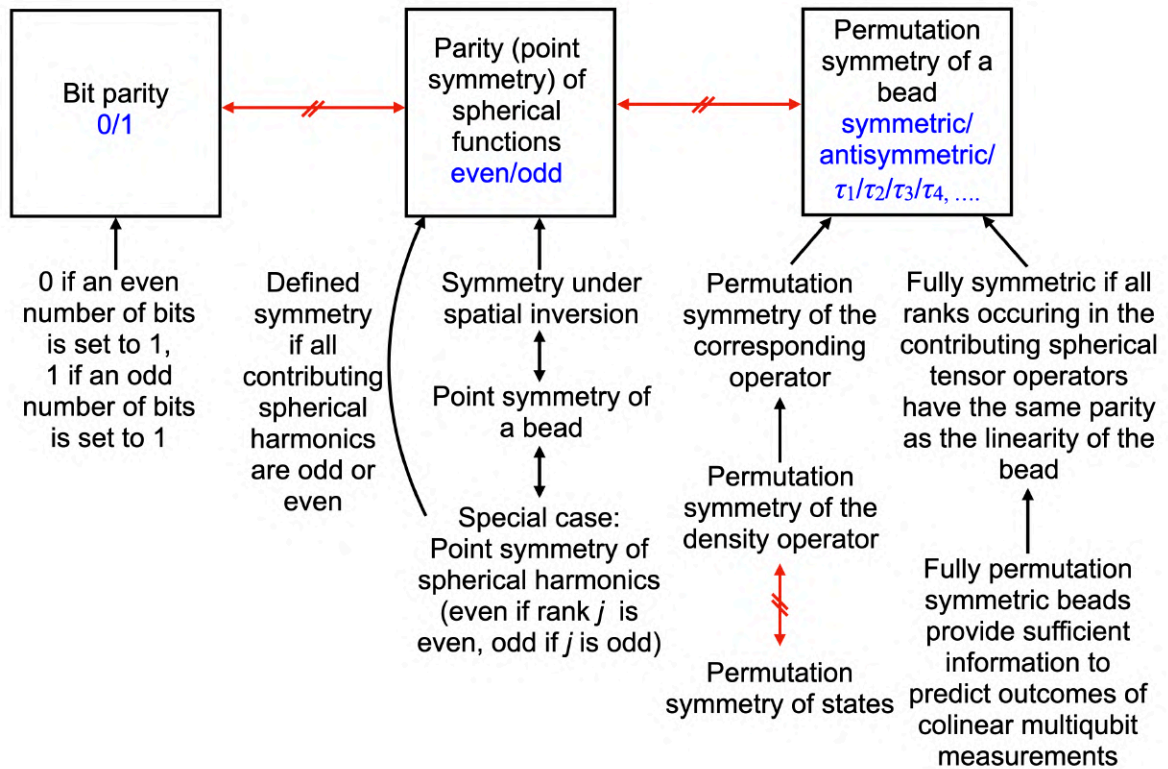


Fig. 10. Overview of parities and symmetries in the BEADS representation. Red crossed out double-headed arrows indicate that two items are inequivalent. Labels which are used in the BEADS representation to describe specific properties are written in blue color.

Linearity g	Bead ℓ'	Ranks j	Spherical function point symmetry	Permutation symmetry	Full permutation symmetry
0	$\{\emptyset\}$	0	even	–	–
1	$\{k\}$	1	odd	–	–
2	$\{k,l\}_{even}$	0 2	even	symmetric (k,l)	✓
	$\{k,l\}_{odd}$	1	odd	antisymmetric (k,l)	✗
3	$\{k,l,m \tau_1\}_{odd}$	1 3	odd	symmetric (k,l,m)	✓
	$\{k,l,m \tau_2\}_{even}$	2	even	symmetric (k,l)	✗
	$\{k,l,m \tau_2\}_{odd}$	1	odd		
	$\{k,l,m \tau_3\}_{even}$	2	even	antisymmetric (k,l)	✗
	$\{k,l,m \tau_3\}_{odd}$	1	odd		
	$\{k,l,m \tau_4\}_{even}$	0	even	antisymmetric (k,l,m)	✗

Table 1: Overview of spherical function and permutation symmetries for beads in systems consisting of up to three qubits. All symmetry properties of beads of linearity $g \geq 2$ apply to T-, E-, and C-Beads. Fully permutation symmetric components are given by beads $\{k,l\}_{even}$ and $\{k,l,m \tau_1\}_{odd}$.

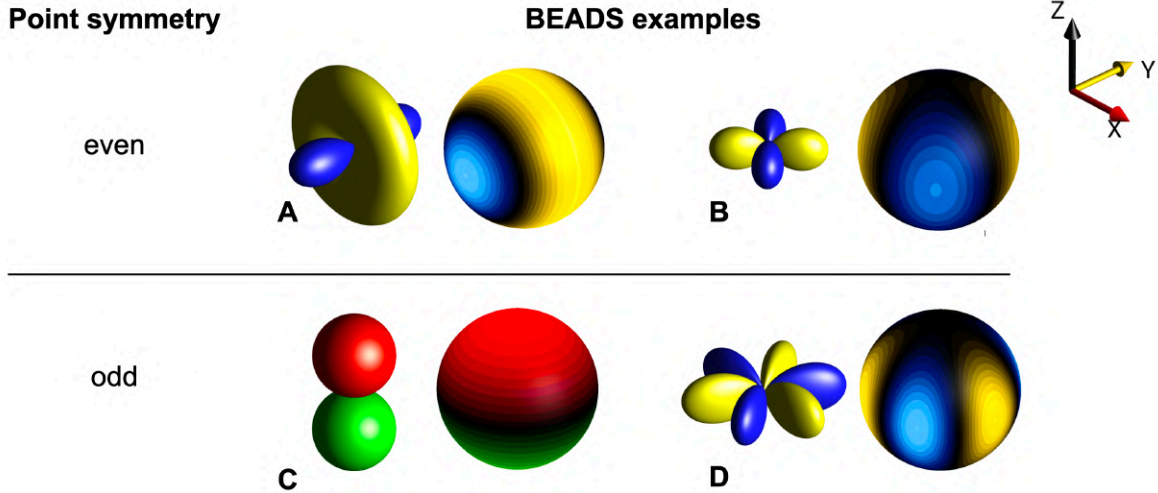


Fig. 11. Spherical function point symmetry in the BEADS representation. We plot exemplary beads of various states by using the magnitude of the spherical function values as distance from the origin and standard spherical color plots to allow for an easy understanding. Beads have even (even ranks j) or odd (odd ranks) spherical function point symmetry. Beads of even point symmetry such as the $E\{1,2\}_{even}$ E-Bead visualized exemplarily (A) for the Bell state $|\Phi^+\rangle = 1/\sqrt{2}(|00\rangle + |11\rangle)$, or (B) $E\{1,2,3 \tau_2\}_{even}$ which is here shown for the state $|\psi\rangle = 1/2(|000\rangle - |011\rangle - |101\rangle + |110\rangle)$ are invariant under spatial inversion, i.e., for any spherical direction, have the same value in the opposite direction. Odd point symmetry such as is given by (C) Q-Beads, e.g., Q_1 exemplarily visualized in the state $|0\rangle$, or (D) $E\{1,2,3 \tau_1\}_{odd}$ shown for the GHZ state $|GHZ\rangle = 1/\sqrt{2}(|000\rangle + |111\rangle)$ undergo sign inversion under spatial inversion, that is, for any arbitrary spherical direction these beads have oppositely signed values in opposite directions.

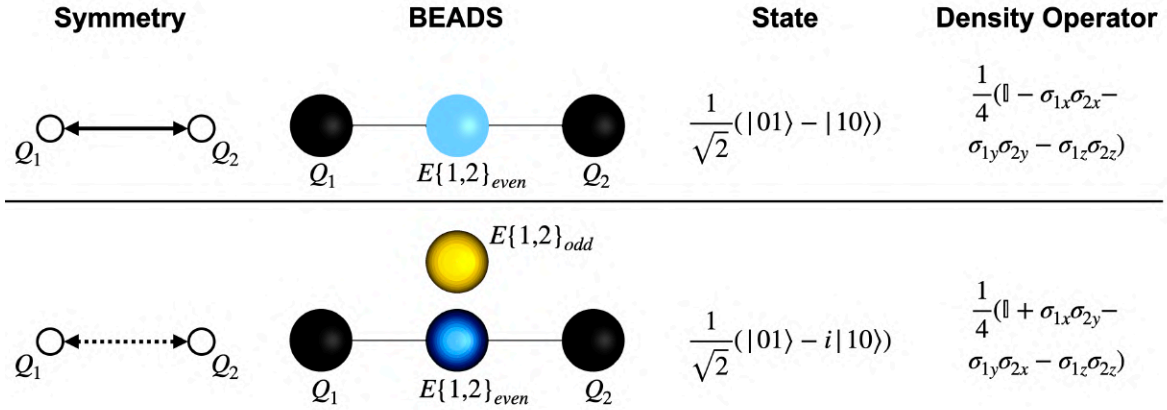


Fig. 12. Two-qubit permutation (particle exchange) symmetries in the BEADS representation. Two-qubit correlation components such as given in the displayed maximally entangled states can be symmetric (solid double-headed arrow) or antisymmetric (dashed double-headed arrow). In the BEADS representation of quantum states, these symmetries refer to the density operator and not to the state. For example, we find that the Bell state $|\Psi^-\rangle = 1/\sqrt{2}(|01\rangle - |10\rangle)$ only has fully permutation symmetric density operator components, i.e., is only represented by the permutation and point symmetric component $E\{1,2\}_{even}$ whereas the state $|\psi\rangle = 1/\sqrt{2}(|01\rangle - i|10\rangle)$ has a maximum antisymmetric component $E\{1,2\}_{odd}$ (corresponding to $\sigma_{1x}\sigma_{1y} - \sigma_{1y}\sigma_{2x}$). Note that the bottom state still has an additional symmetric component $E\{1,2\}_{even}$ (corresponding to $-\sigma_{1z}\sigma_{2z}$).

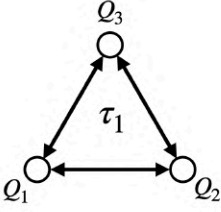
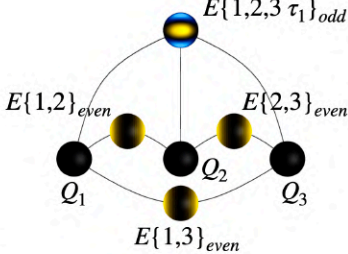
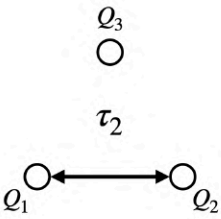
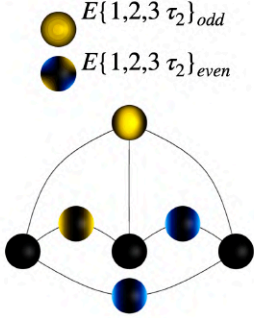
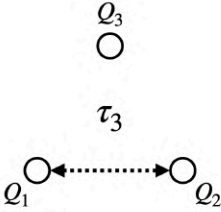
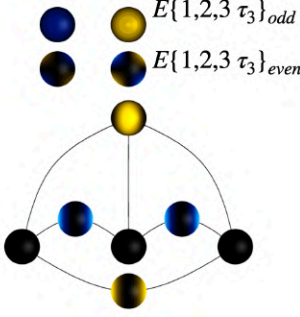
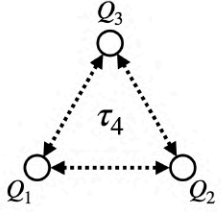
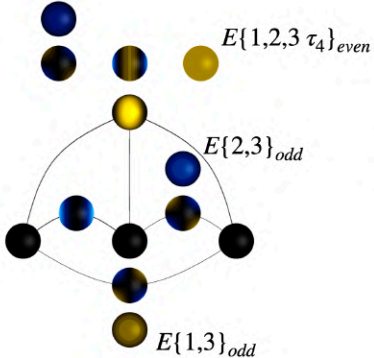
Symmetry type	BEADS	State	Density Operator
		$\frac{1}{2}(000\rangle + 011\rangle + 101\rangle + 110\rangle)$	$\frac{1}{8}(\mathbb{1} + \sigma_{1x}\sigma_{2x} + \sigma_{1x}\sigma_{3x} + \sigma_{2x}\sigma_{3x} - \sigma_{1z}\sigma_{2y}\sigma_{3y} - \sigma_{1y}\sigma_{2z}\sigma_{3y} - \sigma_{1y}\sigma_{2y}\sigma_{3z} + \sigma_{1z}\sigma_{2z}\sigma_{3z})$
		$\frac{1}{2}(000\rangle - 011\rangle - 101\rangle + 110\rangle)$	$\frac{1}{8}(\mathbb{1} + \sigma_{1x}\sigma_{2x} - \sigma_{1x}\sigma_{3x} - \sigma_{2x}\sigma_{3x} + \sigma_{1z}\sigma_{2y}\sigma_{3y} + \sigma_{1y}\sigma_{2z}\sigma_{3y} - \sigma_{1y}\sigma_{2y}\sigma_{3z} + \sigma_{1z}\sigma_{2z}\sigma_{3z})$
		$\frac{1}{2}(000\rangle - 011\rangle + 101\rangle - 110\rangle)$	$\frac{1}{8}(\mathbb{1} - \sigma_{1x}\sigma_{2x} + \sigma_{1x}\sigma_{3x} - \sigma_{2x}\sigma_{3x} - \sigma_{1z}\sigma_{2y}\sigma_{3y} - \sigma_{1y}\sigma_{2z}\sigma_{3y} + \sigma_{1y}\sigma_{2y}\sigma_{3z} + \sigma_{1z}\sigma_{2z}\sigma_{3z})$
		$\frac{1}{2}(000\rangle - i 011\rangle + i 101\rangle - 110\rangle)$	$\frac{1}{8}(\mathbb{1} - \sigma_{1x}\sigma_{2x} + \sigma_{1x}\sigma_{3y} - \sigma_{2x}\sigma_{3y} + \sigma_{1y}\sigma_{2y}\sigma_{3z} + \sigma_{1y}\sigma_{2z}\sigma_{3x} - \sigma_{1z}\sigma_{2y}\sigma_{3x} + \sigma_{1z}\sigma_{2z}\sigma_{3z})$

Fig. 13. Three-qubit permutation symmetries in the BEADS representation. By construction (37) (see Materials and Methods section), three-qubit correlation components of the density operator such as given in the displayed maximally entangled states can be totally symmetric (τ_1), symmetric with respect to permutations of qubits 1 and 2 (τ_2), antisymmetric with respect to permutations of qubits 1 and 2 (τ_3) or totally antisymmetric (τ_4) but do not correspond to the symmetries of a state under particle exchange.

S3 Canonical BEADS scaling factors of permutation symmetric density operator components

Compared to the Wigner-type DROPS representation of operators (37), we introduce additional scaling factors $s_j^{(\ell')}(N, g)$ for the spherical functions in the BEADS representation (see Eq. 7 and 8 in Materials and Methods). In a first approach, we choose these scaling factors such that the spherical function values directly correspond to experimentally measurable expectation values of Pauli product operators. Although the approach is valid for arbitrary Pauli product operators, for concreteness and simplicity, we focus the following discussion on expectation values of (products of) Pauli-Z operators, using the compact notation $Z_k = \sigma_{kz}$, such as the expectation values $\langle Z_k \rangle$, $\langle Z_k Z_l \rangle$, or $\langle Z_k Z_l Z_m \rangle$, etc., of linear operators Z_k , bilinear operators $Z_k Z_l$, trilinear operators $Z_k Z_l Z_m$, etc., respectively. These are the standard expectation values which are directly measurable in most experimental implementations of quantum information processing tasks and quantum computing algorithms.

In the LISA basis, Pauli-Z (product) operators only contribute to Tensor operators $T_{j,0}^{(\ell')}$ (i.e., operators $T_{j,m}^{(\ell')}$ with $m = 0$). For example, the linear LISA operator $T_{1,0}^{\{k\}}$ (which acts exclusively on the set $\ell' = \{k\}$ consisting only of the k -th qubit) is proportional to Z_k (37):

$$T_{1,0}^{\{k\}} = \frac{1}{\sqrt{2^N}} \cdot Z_k \quad (23a)$$

$$Z_k = \sqrt{2^N} \cdot T_{1,0}^{\{k\}} \quad (23b)$$

The scaling factor $\frac{1}{\sqrt{2^N}}$ normalizes the LISA basis operator $T_{1,0}^{\{k\}}$ for a quantum system consisting of n qubits. Conversely, $Z_k = \sqrt{2^N} \cdot T_{1,0}^{\{k\}}$ and hence

$$\langle Z_k \rangle = \zeta(N) \cdot \langle T_{1,0}^{\{k\}} \rangle \quad (24)$$

with the N -dependent scaling factor

$$\zeta(N) = \sqrt{2^N} \quad (25)$$

As shown in (41), the expectation value $\langle T_{j,0}^{\{k\}} \rangle$ of an axial LISA basis operator is proportional to the value of the corresponding droplet function $f_j^{\{k\}}(\theta, \phi)$ in the z -direction (i.e., at the north pole, where $\theta = 0$ and ϕ is arbitrary, e.g., $\phi = 0$):

$$\langle T_{j,0}^{(\ell')} \rangle = \eta_j \cdot f_j^{\{k\}}(0,0) \quad (26)$$

with

$$\eta_j = \sqrt{4\pi/(2j+1)} \quad (27)$$

Hence, with the help of the two scaling factors $\zeta(N)$ (Eq. 25) and η_1 (Eq. 27), we can express an expectation value $\langle Z_k \rangle$ in terms of the value of the droplet function $f_1^{\{k\}}(0,0)$ in the z direction:

$$\langle Z_k \rangle = \zeta(N) \cdot \eta_1 \cdot f_1^{\{k\}}(0,0) \quad (28)$$

Similarly, the expectation value $\langle Z_k Z_l \rangle$ of a bilinear Pauli-Z product operator can be expressed in terms of spherical functions $f_j^{\{k,l\}even}(0,0)$ in the z-direction. However, this case is more complicated because the operator $Z_k Z_l$ contributes not only to one but to several bilinear LISA basis operators $T_{j,0}^{\{k,l\}even}$. Although bilinear LISA basis operators $T_{j,0}^{\{k,l\}even/odd}$ can have ranks $j \in \{0,1,2\}$, the operator $Z_k Z_l$ only contributes to the two LISA basis operators $T_{0,0}^{\{k,l\}even}$ and $T_{2,0}^{\{k,l\}even}$ (37) which in the BEADS representation are comprised in the fully symmetric subset $\ell' = \{k, l\}_{even}$:

$$T_{0,0}^{\{k,l\}even} = \frac{1}{\sqrt{2^N}} \frac{Z_k Z_l + (X_k X_l + Y_k Y_l)}{\sqrt{3}} \quad (29)$$

$$T_{2,0}^{\{k,l\}even} = \frac{1}{\sqrt{2^N}} \frac{2 Z_k Z_l - (X_k X_l + Y_k Y_l)}{\sqrt{6}} \quad (30)$$

By multiplying the second equation by $\sqrt{2}$ and adding this to the first equation, the term $(X_k X_l + Y_k Y_l)$ is eliminated and we obtain

$$\begin{aligned} T_{0,0}^{\{k,l\}even} + \sqrt{2} T_{2,0}^{\{k,l\}even} &= \frac{1}{\sqrt{2^N}} \left(\frac{Z_k Z_l}{\sqrt{3}} + \frac{2 Z_k Z_l}{\sqrt{3}} \right) \\ &= \frac{1}{\sqrt{2^N}} \frac{3 Z_k Z_l}{\sqrt{3}} = \frac{1}{\sqrt{2^N}} \sqrt{3} Z_k Z_l \end{aligned} \quad (31)$$

Hence, we can express the bilinear Pauli product operator $Z_k Z_l$ as the following linear combination of $T_{0,0}^{\{k,l\}even}$ and $T_{2,0}^{\{k,l\}even}$:

$$\begin{aligned} Z_k Z_l &= \sqrt{2^N} \left(\frac{1}{\sqrt{3}} \cdot T_{0,0}^{\{k,l\}even} + \frac{\sqrt{2}}{\sqrt{3}} \cdot T_{2,0}^{\{k,l\}even} \right) \\ &= \zeta(N) \left(\xi_0^{\{k,l\}even}(2) \cdot T_{0,0}^{\{k,l\}even} + \xi_2^{\{k,l\}even}(2) \cdot T_{2,0}^{\{k,l\}even} \right) \end{aligned} \quad (32)$$

where we used the scaling factor $\zeta(N) = \sqrt{2^N}$ (cf. Eq. 25) and the scaling factors $\xi_j(g)$ for $j \in \{0,2\}$ and linearity $g = 2$ (corresponding to the bilinearity of the LISA basis operators $T_{0,0}^{\{k,l\}even}$ and $T_{2,0}^{\{k,l\}even}$) with $\xi_0^{\{k,l\}even}(2) = \sqrt{1/3}$ and $\xi_2^{\{k,l\}even}(2) = \sqrt{2/3}$.

Based on Eq. 32, the expectation value $\langle Z_k Z_l \rangle$ can finally be expressed in the form

$$\begin{aligned} \langle Z_k Z_l \rangle &= \zeta(N) \cdot \left(\xi_0^{\{k,l\}even}(2) \cdot \langle T_{0,0}^{\{k,l\}even} \rangle + \xi_2^{\{k,l\}even}(2) \cdot \langle T_{2,0}^{\{k,l\}even} \rangle \right) \\ &= \zeta(N) \cdot \left(\xi_0^{\{k,l\}even}(2) \cdot \eta_0 \cdot f_0^{\{k,l\}even} + \xi_2^{\{k,l\}even}(2) \cdot \eta_2 \cdot f_2^{\{k,l\}even} \right) \\ &= \zeta(N) \cdot \xi_0^{\{k,l\}even}(2) \cdot \eta_0 \cdot f_0^{\{k,l\}even} + \zeta(N) \cdot \xi_2^{\{k,l\}even}(2) \cdot \eta_2 \cdot f_2^{\{k,l\}even} \\ &= s_0^{\{k,l\}even}(N, 2) \cdot f_0^{\{k,l\}even} + s_2^{\{k,l\}even}(N, 2) \cdot f_2^{\{k,l\}even} \end{aligned} \quad (33)$$

with the overall scaling factors

$$\begin{aligned} s_j^{(\ell')} (N, g) &= \zeta(N) \cdot \xi_j^{(\ell')} (g) \cdot \eta_j \\ &= \sqrt{2^N} \cdot \xi_j^{(\ell')} (g) \cdot \sqrt{4\pi/(2j+1)} \end{aligned} \quad (34)$$

For example, for a system consisting of three qubits ($N = 3$) we find

$$\begin{aligned} s_0^{\{k,l\}even} (3,2) &= \sqrt{2^3} \cdot \xi_0^{\{k,l\}even} (2) \cdot \sqrt{4\pi} \\ &= 2\sqrt{2} \cdot \sqrt{1/3} \cdot 2\sqrt{\pi} \\ &= 4\sqrt{2\pi/3} \\ &\approx 5.78881 \end{aligned} \quad (35)$$

and

$$\begin{aligned} s_2^{\{k,l\}even} (3,2) &= \sqrt{2^3} \cdot \xi_2^{\{k,l\}even} (2) \cdot \sqrt{4\pi/(4+1)} \\ &= 2\sqrt{2} \cdot \sqrt{2/3} \cdot 2\sqrt{\pi/5} \\ &= 8\sqrt{\pi/15} \\ &\approx 3.66116 \end{aligned} \quad (36)$$

Similarly, the trilinear ($g = 3$) Pauli product operator $Z_k Z_l Z_m$ can be expressed as the following linear combination of LISA basis operators:

$$Z_k Z_l Z_m = \zeta(N) \left(\xi_1^{\{k,l,m \tau_1\}odd} (3) \cdot T_{1,0}^{\{k,l,m \tau_1\}odd} + \xi_3^{\{k,l,m \tau_1\}odd} (3) \cdot T_{3,0}^{\{k,l,m \tau_1\}odd} \right) \quad (37)$$

with $\xi_1(3) = \sqrt{3/5}$ and $\xi_3(3) = \sqrt{2/5}$ and

$$\langle Z_k Z_l Z_m \rangle = s_1^{\{k,l,m \tau_1\}odd} (N, 2) \cdot f_1^{\{k,l,m \tau_1\}odd} + s_3^{\{k,l,m \tau_1\}odd} (N, 2) \cdot f_3^{\{k,l,m \tau_1\}odd} \quad (38)$$

In general, a g -linear Pauli Z product operator can be expressed as a linear combination

$$\zeta(N) \cdot \sum_j \xi_j^{(\ell')} (g) T_{j,0}^{(\ell')} \quad (39)$$

where $j \in \{0, 2, 4, \dots, g\}$ if g is even and $j \in \{1, 3, 5, \dots, g\}$ if g is odd and the set ℓ' includes the g qubits on which the g -linear Pauli product operator acts. For $g \leq 6$ the scaling factors $\xi_j^{(\ell')} (g)$ are summarized in Table 2. Note that the linear combination $\sum_j \xi_j^{(\ell')} (g) T_{j,0}^{(\ell')}$ represents a normalized operator as the unscaled LISA operators are normalized and the scaling factors $\xi_j^{(\ell')} (g)$ satisfy the relation $\sum_j \left(\xi_j^{(\ell')} (g) \right)^2 = 1$.

It is important to point out that axial LISA tensor operators that contribute to Pauli-Z operators (cf. Eq. 23b, 32, and 37) naturally correspond to fully symmetric density operator components with

respect to permutations of qubits. We scale all non-axial operators $T_{j,m \neq 0}^{(\ell')}$ of the same rank j and set ℓ' with the same scaling factors as the corresponding axial operators $T_{j,0}^{(\ell')}$.

Axial tensor operators $T_{j,0}^{(\ell')}$ and non-axial tensor operators $T_{j,m \neq 0}^{(\ell')}$ corresponding to components which are not fully symmetric with respect to permutations of qubits can in principle be scaled in an analogue fashion. However, the resulting bead spherical function values may be larger than 1 which prevents a uniform interpretation of the color schemes introduced in the Results section. Thus, to ensure a uniform interpretation of color scales, we scale such components by using alternative scaling factors which are based on the global unitary bounds of the underlying tensor operators (see section S4).

An overview of the scaling factors $\xi_j^{(\ell')}(g)$ for all axial operators up to linearity $g = 3$ is given in Table 4 in section S5.

$\xi_j^{(\ell')}(g)$	$j = 0$	$j = 1$	$j = 2$	$j = 3$	$j = 4$	$j = 5$	$j = 6$
$g = 0$	1	-	-	-	-	-	-
$g = 1$	-	1	-	-	-	-	-
$g = 2$	$\sqrt{1/3}$	-	$\sqrt{2/3}$	-	-	-	-
$g = 3, \ell' = \tau_1^{[3]}$	-	$\sqrt{3/5}$	-	$\sqrt{2/5}$	-	-	-
$g = 4, \ell' = \tau_1^{[4]}$	$\sqrt{7/35}$	-	$\sqrt{20/35}$	-	$\sqrt{8/35}$	-	-
$g = 5, \ell' = \tau_1^{[5]}$	-	$\sqrt{27/63}$	-	$\sqrt{28/63}$	-	$\sqrt{8/63}$	-
$g = 6, \ell' = \tau_1^{[6]}$	$\sqrt{33/231}$	-	$\sqrt{110/231}$	-	$\sqrt{72/231}$	-	$\sqrt{16/231}$

Table 2: Scaling factors $\xi_j^{(\ell')}(g)$ of axial tensor operators $T_{j,0}^{(\ell')}$ of rank j and linearity g that contribute to Pauli-Z operators.

S4 Global unitary bound scaling factors of density operator components which are not fully permutation symmetric

As we discussed in the Materials and Methods section, in the BEADS representation, we can scale the spherical functions of fully permutation symmetric density operator components by factors $s_j^{(\ell')}(N, g)$ such that the resulting spherical function values match expectation values of Pauli-Z operators. While the introduced approach (see section S3) would in principle be applicable to any bead, the resulting scaling factors may cause the absolute bead function values to become larger than 1. This is because non-fully permutation symmetric tensor operator components correspond to linear combinations of correlation expectation values of multiple measurements for which physical scenarios exist where the individual expectation values constructively add up.

For instance, $T_{1,0}^{\{1,2\}odd} = (\sigma_{1x}\sigma_{1y} - \sigma_{1y}\sigma_{1x})/(2\sqrt{2})$. For the state $|\psi\rangle = (|01\rangle - i|10\rangle)$, $\langle\sigma_{1x}\sigma_{1y}\rangle = 1$ and $\langle\sigma_{1y}\sigma_{1x}\rangle = -1$ such that by using scaling factors as introduced above, we would find the bead spherical function value along the z-axis to be $b^{\{1,2\}odd}(0,0) = 2$. In fact, this would prevent a uniform interpretation of the color schemes introduced in the Results section. Specifically, this is the case for beads that represent bilinear antisymmetric components or those corresponding to permutational symmetries τ_k , with $k > 1$.

Here, we suggest a different scaling approach for density operator components that are not fully permutation symmetric by defining additional scaling factors $\xi_j^{(\ell')}(g)$ which ensure the absolute spherical function values to be upper-bounded by 1. These scaling factors can be found by considering the *global unitary bounds* between arbitrary pure state density operators and LISA tensor operator components $T_{j,m}^{(\ell')}$. Note that it is sufficient to consider pure states as the maximum beads spherical function values $\max|b^{(\ell')}(\theta, \phi)|$ over all pure states is equal or larger than the values obtained for mixed states.

The global unitary bound $u = \langle UAU^\dagger | B \rangle$ corresponds to the maximum overlap between a unitarily transformed initial operator A and a target operator B , where A and B are normalized. If both operators are Hermitian, the global unitary bound can be readily calculated using eigen decompositions of A and B (64).

To determine the scaling factors, we are interested in the global unitary bound $u_{j,0}^{(\ell')}$ between an arbitrary pure state and a bead of interest. Without loss of generality, we choose A as the state $\rho_0 = |0\rangle^{\otimes N} \langle 0|^{\otimes N}$ and B as the axial LISA operator $T_{j,0}^{(\ell')}$ associated to the bead of interest. The global unitary bound is then given by (64–66)

$$u_{j,0}^{(\ell')} = \max_U \langle T_{j,0}^{(\ell')} \rangle = \max_U \langle U \rho_0 U^\dagger | T_{j,0}^{(\ell')} \rangle = \max_U \langle U | 0 \rangle^{\otimes N} \langle 0 |^{\otimes N} U^\dagger | T_{j,0}^{(\ell')} \rangle \quad (40)$$

and the maximally overlapping state is the normalized eigenvector $|V\rangle$ (where $|V\rangle = U|0\rangle^{\otimes N}$) corresponding to the largest absolute eigenvalue of $T_{j,0}^{(\ell')}$.

The scaling factors $\xi_j^{(\ell')}(g)$ can then be determined by considering the global unitary bound $u_{j,0}^{(\ell')}$ and the scaling factor $\zeta(N)$ (see section S3).

$$\xi_j^{(\ell')}(g) = \left(\zeta(N) \cdot u_{j,0}^{(\ell')} \right)^{-1} \quad (41)$$

A list of global unitary bounds of two- and three-qubit LISA tensor operators and corresponding scaling factors $\xi_j^{(\ell')}(g)$ that are applied in the BEADS representation is given in Table 3.

Note that the global unitary bound approach causes beads to be scaled such that resulting numerical ranges of beads values are bound by ± 1 which adds quantitative information on how closely the individual symmetry components of a visualized density operator approach the corresponding global unitary bounds, that is, how large the symmetry components in a quantum state are compared to the maximally reachable components.

However, applying scaling factors as described in Eq. 41 can lead to beads appearing very bright even if the underlying unscaled expectation values are relatively small. This is specifically the case for permutational symmetries τ_k , with $k > 1$. Thus, an alternative scaling which we call *natural expectation value scaling* is given by omitting $u_{j,0}^{(\ell')}$ in Eq. 41 such that the beads spherical function values directly correspond to the expectation values of the underlying LISA tensor operators.

The three-qubit pure states corresponding to the global unitary bounds of the tensor operators listed in Table 3, respectively, are given in Eqs. 42–49 and include states $|\psi_+^{(\ell')}\rangle$ which achieve maximally positive expectation values and states $|\psi_-^{(\ell')}\rangle$ with maximally negative expectation values with respect to the symmetry component represented by the bead ℓ' . Note that in case of degenerate eigenvalues, any normalized vector that is represented by a combination of orthogonal eigenvectors, which we express by an additional angular parameter θ , is also an eigenvector and a state representing the global unitary bound of the corresponding tensor operator.

Fig. 14 – Fig. 21 exemplarily show the BEADS representations of these three-qubit global unitary bound states which incorporate the calculated scaling factors. Here, we visualize total correlations (T-Beads $T(\ell')$) as the states are in general not maximally entangled. For cases of degenerate eigenvalues we show the fully axially symmetric states ($\theta = 0$) to simplify the visualization.

$\ell' = \{1,2\}_{odd}$:

$$|\psi_+^{\{1,2\}_{odd}}\rangle = \cos \theta \left[\frac{1}{\sqrt{2}}(|010\rangle - i|100\rangle) \right] + \sin \theta \left[\frac{1}{\sqrt{2}}(|011\rangle - i|101\rangle) \right] \quad (42a)$$

$$|\psi_-^{\{1,2\}_{odd}}\rangle = \cos \theta \left[\frac{1}{\sqrt{2}}(|010\rangle + i|100\rangle) \right] + \sin \theta \left[\frac{1}{\sqrt{2}}(|011\rangle + i|101\rangle) \right] \quad (42b)$$

$\ell' = \{1,3\}_{odd}$:

$$|\psi_+^{\{1,3\}_{odd}}\rangle = \cos \theta \left[\frac{1}{\sqrt{2}}(|001\rangle - i|100\rangle) \right] + \sin \theta \left[\frac{1}{\sqrt{2}}(|011\rangle - i|110\rangle) \right] \quad (43a)$$

$$|\psi_-^{\{1,3\}_{odd}}\rangle = \cos \theta \left[\frac{1}{\sqrt{2}}(|001\rangle + i|100\rangle) \right] + \sin \theta \left[\frac{1}{\sqrt{2}}(|011\rangle + i|110\rangle) \right] \quad (43b)$$

$\ell' = \{2,3\}_{odd}$:

$$|\psi_+^{\{2,3\}_{odd}}\rangle = \cos \theta \left[\frac{1}{\sqrt{2}}(|001\rangle - i|010\rangle) \right] + \sin \theta \left[\frac{1}{\sqrt{2}}(|101\rangle - i|110\rangle) \right] \quad (44a)$$

$$|\psi_-^{\{2,3\}_{odd}}\rangle = \cos \theta \left[\frac{1}{\sqrt{2}}(|001\rangle + i|010\rangle) \right] + \sin \theta \left[\frac{1}{\sqrt{2}}(|101\rangle + i|110\rangle) \right] \quad (44b)$$

$\ell' = \{1,2,3 \tau_2\}_{odd}$:

$$|\psi_+^{\{1,2,3 \tau_2\}_{odd}}\rangle = \frac{1}{2} \sqrt{1 + \frac{1}{\sqrt{3}}} (|011\rangle + |101\rangle) - \frac{1}{\sqrt{2}} \sqrt{1 - \frac{1}{\sqrt{3}}} |110\rangle \quad (45a)$$

$$|\psi_-^{\{1,2,3 \tau_2\}_{odd}}\rangle = \frac{1}{2} \sqrt{1 + \frac{1}{\sqrt{3}}} (|010\rangle + |100\rangle) - \frac{1}{\sqrt{2}} \sqrt{1 - \frac{1}{\sqrt{3}}} |001\rangle \quad (45b)$$

$\ell' = \{1,2,3 \tau_2\}_{even}$:

$$|\psi_+^{\{1,2,3 \tau_2\}_{even}}\rangle = \cos \theta \left[\frac{1}{2} (|100\rangle + |010\rangle) - \frac{i}{\sqrt{2}} |001\rangle \right] + \sin \theta \left[\frac{1}{2} (|011\rangle + |101\rangle) - \frac{i}{\sqrt{2}} |110\rangle \right] \quad (46a)$$

$$|\psi_-^{\{1,2,3 \tau_2\}_{even}}\rangle = \cos \theta \left[\frac{1}{2} (|100\rangle + |010\rangle) + \frac{i}{\sqrt{2}} |001\rangle \right] + \sin \theta \left[\frac{1}{2} (|011\rangle + |101\rangle) + \frac{i}{\sqrt{2}} |110\rangle \right] \quad (46b)$$

$\ell' = \{1,2,3 \tau_3\}_{odd}$:

$$|\psi_+^{\{1,2,3 \tau_3\}_{odd}}\rangle = \cos \theta \left[\frac{1}{2} (|010\rangle - |100\rangle) + \frac{1}{\sqrt{2}} |001\rangle \right] + \sin \theta \left[\frac{1}{2} (|011\rangle - |101\rangle) + \frac{1}{\sqrt{2}} |110\rangle \right] \quad (47a)$$

$$|\psi_-^{\{1,2,3 \tau_3\}_{odd}}\rangle = \cos \theta \left[\frac{1}{2} (|100\rangle - |010\rangle) + \frac{1}{\sqrt{2}} |001\rangle \right] + \sin \theta \left[\frac{1}{2} (|101\rangle - |011\rangle) + \frac{1}{\sqrt{2}} |110\rangle \right] \quad (47b)$$

$\ell' = \{1,2,3 \tau_3\}_{even}$:

$$\begin{aligned} |\psi_+^{\{1,2,3 \tau_3\}_{even}}\rangle &= \cos \theta \left[\frac{1}{\sqrt{6}} |001\rangle + i \frac{1 - \sqrt{6}}{2} |010\rangle + i \frac{1 + \sqrt{6}}{2} |100\rangle \right] \\ &+ \sin \theta \left[\frac{1}{\sqrt{6}} |110\rangle + i \frac{1 - \sqrt{6}}{2} |101\rangle + i \frac{1 + \sqrt{6}}{2} |011\rangle \right] \end{aligned} \quad (48a)$$

$$\begin{aligned} |\psi_-^{\{1,2,3 \tau_3\}_{even}}\rangle &= \cos \theta \left[\frac{1}{\sqrt{6}} |001\rangle + i \frac{1 + \sqrt{6}}{2} |010\rangle + i \frac{1 - \sqrt{6}}{2} |100\rangle \right] \\ &+ \sin \theta \left[\frac{1}{\sqrt{6}} |110\rangle + i \frac{1 + \sqrt{6}}{2} |101\rangle + i \frac{1 - \sqrt{6}}{2} |011\rangle \right] \end{aligned} \quad (48b)$$

$\ell' = \{1,2,3 \tau_4\}_{even}$:

$$\begin{aligned} \left| \psi_+^{\{1,2,3 \tau_4\}_{even}} \right\rangle &= \cos \theta \left[\frac{1}{\sqrt{3}} \left(|001\rangle - \frac{1 + \sqrt{3}i}{2} |010\rangle - \frac{1 - \sqrt{3}i}{2} |100\rangle \right) \right] \\ &+ \sin \theta \left[\frac{1}{\sqrt{3}} \left(|110\rangle - \frac{1 + \sqrt{3}i}{2} |101\rangle - \frac{1 - \sqrt{3}i}{2} |011\rangle \right) \right] \end{aligned} \quad (49a)$$

$$\begin{aligned} |\psi_-^{\{1,2,3 \tau_4\}_{even}}\rangle &= \cos \theta \left[\frac{1}{\sqrt{3}} \left(|001\rangle - \frac{1 - \sqrt{3}i}{2} |010\rangle - \frac{1 + \sqrt{3}i}{2} |100\rangle \right) \right] \\ &+ \sin \theta \left[\frac{1}{\sqrt{3}} \left(|110\rangle - \frac{1 - \sqrt{3}i}{2} |101\rangle - \frac{1 + \sqrt{3}i}{2} |011\rangle \right) \right] \end{aligned} \quad (49b)$$

For the simple case where $\theta = 0$, the density operators $\rho_{\pm}^{(\ell')}$ corresponding to the states $|\psi_{\pm}^{(\ell')}\rangle$ defined in Eq. 42 to 49 read as follows. Here, the components which contribute to the bead of interest $b^{(\ell')}$ are written in **blue color**. The corresponding BEADS representations are shown in Fig. 14 to Fig. 21.

$\ell' = \{1,2\}_{odd}$:

$$\rho_{\pm, \theta=0}^{\{1,2\}_{odd}} = \frac{1}{8} (\mathbb{I} - \sigma_{3z} \pm \sigma_{1x}\sigma_{2y} \mp \sigma_{1y}\sigma_{2x} - \sigma_{1z}\sigma_{2z} \mp \sigma_{1x}\sigma_{2y}\sigma_{3z} \pm \sigma_{1y}\sigma_{2x}\sigma_{3z} + \sigma_{1z}\sigma_{2z}\sigma_{3z}) \quad (50)$$

$\ell' = \{1,3\}_{odd}$:

$$\rho_{\pm, \theta=0}^{\{1,3\}_{odd}} = \frac{1}{8} (\mathbb{I} - \sigma_{2z} \pm \sigma_{1x}\sigma_{3y} \mp \sigma_{1y}\sigma_{3x} - \sigma_{1z}\sigma_{3z} \mp \sigma_{1x}\sigma_{2z}\sigma_{3y} \pm \sigma_{1y}\sigma_{2z}\sigma_{3x} + \sigma_{1z}\sigma_{2z}\sigma_{3z}) \quad (51)$$

$\ell' = \{2,3\}_{odd}$:

$$\rho_{\pm, \theta=0}^{\{2,3\}_{odd}} = \frac{1}{8} (\mathbb{I} - \sigma_{1z} \pm \sigma_{2x}\sigma_{3y} \mp \sigma_{2y}\sigma_{3x} - \sigma_{2z}\sigma_{3z} \mp \sigma_{1z}\sigma_{2x}\sigma_{3y} \pm \sigma_{1z}\sigma_{2y}\sigma_{3x} + \sigma_{1z}\sigma_{2z}\sigma_{3z}) \quad (52)$$

$\ell' = \{1,2,3 \tau_2\}_{odd}$:

$$\begin{aligned} \rho_{\pm, \theta=0}^{\{1,2,3 \tau_2\}_{odd}} = \frac{1}{8} & \left[(\mathbb{I} \pm \sigma_{1z}\sigma_{2z}\sigma_{3z}) + \frac{1}{3 + \sqrt{3}} (\mp \sigma_{1z} \mp \sigma_{2z} - \sigma_{1z}\sigma_{3z} - \sigma_{2z}\sigma_{3z}) \right. \\ & + \frac{1}{\sqrt{3}} (\mp \sigma_{3z} - \sigma_{1z}\sigma_{2z} - \sigma_{1x}\sigma_{3x} - \sigma_{1y}\sigma_{2y} - \sigma_{2x}\sigma_{3x} - \sigma_{2y}\sigma_{3y} \\ & \quad \left. \pm \sigma_{1x}\sigma_{2z}\sigma_{3x} \pm \sigma_{1y}\sigma_{2z}\sigma_{3y} \pm \sigma_{1z}\sigma_{2x}\sigma_{3x} \pm \sigma_{1z}\sigma_{2y}\sigma_{3y}) \right. \\ & \left. + \frac{3 + \sqrt{3}}{6} (\sigma_{1x}\sigma_{2x} + \sigma_{1y}\sigma_{2y} \mp \sigma_{1x}\sigma_{2x}\sigma_{3z} \pm \sigma_{1y}\sigma_{2y}\sigma_{3z}) \right] \quad (53) \end{aligned}$$

$\ell' = \{1,2,3 \tau_2\}_{even}$:

$$\begin{aligned} \rho_{\pm, \theta=0}^{\{1,2,3 \tau_2\}_{even}} = \frac{1}{8} & \left[(\mathbb{I} - \sigma_{1z}\sigma_{2z}\sigma_{3z}) \right. \\ & + \frac{1}{2} (\sigma_{1z} + \sigma_{2z} + \sigma_{1x}\sigma_{2x} + \sigma_{1y}\sigma_{2y} - \sigma_{1z}\sigma_{3z} - \sigma_{2z}\sigma_{3z} \\ & \quad \left. + \sigma_{1x}\sigma_{2x}\sigma_{3z} + \sigma_{1y}\sigma_{2y}\sigma_{3z}) \right. \\ & + \frac{1}{\sqrt{2}} (\mp \sigma_{1x}\sigma_{3y} \pm \sigma_{1y}\sigma_{3x} \mp \sigma_{2x}\sigma_{3y} \pm \sigma_{2y}\sigma_{3x} \\ & \quad \left. \mp \sigma_{1x}\sigma_{2z}\sigma_{3y} \pm \sigma_{1y}\sigma_{2z}\sigma_{3x} \mp \sigma_{1z}\sigma_{2x}\sigma_{3y} \pm \sigma_{1z}\sigma_{2y}\sigma_{3x}) \right] \quad (54) \end{aligned}$$

$\ell' = \{1,2,3 \tau_3\}_{odd}$:

$$\begin{aligned} \rho_{\pm, \theta=0}^{\{1,2,3 \tau_3\}_{odd}} = \frac{1}{8} & \left[(\mathbb{I} - \sigma_{1z}\sigma_{2z}\sigma_{3z}) \right. \\ & + \frac{1}{2} (\sigma_{1z} + \sigma_{2z} - \sigma_{1x}\sigma_{2x} - \sigma_{1y}\sigma_{2y} - \sigma_{1z}\sigma_{3z} - \sigma_{2z}\sigma_{3z} \\ & \quad \left. - \sigma_{1x}\sigma_{2x}\sigma_{3z} - \sigma_{1y}\sigma_{2y}\sigma_{3z}) \right. \\ & + \frac{1}{\sqrt{2}} (\mp \sigma_{1x}\sigma_{3x} \mp \sigma_{1y}\sigma_{3y} \pm \sigma_{2x}\sigma_{3x} \pm \sigma_{2y}\sigma_{3y} \\ & \quad \left. \mp \sigma_{1x}\sigma_{2z}\sigma_{3x} \mp \sigma_{1y}\sigma_{2z}\sigma_{3y} \pm \sigma_{1z}\sigma_{2x}\sigma_{3x} \pm \sigma_{1z}\sigma_{2y}\sigma_{3y}) \right] \quad (55) \end{aligned}$$

$\ell' = \{1,2,3 \tau_3\}_{even}$:

$$\begin{aligned}
\rho_{\pm, \theta=0}^{\{1,2,3 \tau_3\}_{even}} &= \frac{1}{8} \left[(\mathbb{I} - \sigma_{1z} \sigma_{2z} \sigma_{3z}) \right. \\
&+ \frac{1}{6} (\sigma_{1z} + \sigma_{2z} - \sigma_{1x} \sigma_{2x} - \sigma_{1y} \sigma_{2y} - \sigma_{1z} \sigma_{3z} - \sigma_{2z} \sigma_{3z} \\
&\quad - \sigma_{1x} \sigma_{2x} \sigma_{3z} - \sigma_{1y} \sigma_{2y} \sigma_{3z}) \\
&+ \frac{1}{3} (\sigma_{1x} \sigma_{3x} + \sigma_{1y} \sigma_{3y} + \sigma_{2x} \sigma_{3x} + \sigma_{2y} \sigma_{3y} \\
&\quad + \sigma_{1x} \sigma_{2z} \sigma_{3x} + \sigma_{1y} \sigma_{2z} \sigma_{3y} + \sigma_{1z} \sigma_{2x} \sigma_{3x} + \sigma_{1z} \sigma_{2y} \sigma_{3y}) \\
&+ \frac{2}{3} (\sigma_{3z} - \sigma_{1z} \sigma_{2z}) \\
&+ \frac{1}{\sqrt{6}} (\sigma_{1x} \sigma_{3y} - \sigma_{1y} \sigma_{3x} - \sigma_{2x} \sigma_{3y} + \sigma_{1y} \sigma_{3x} \\
&\quad + \sigma_{1x} \sigma_{2z} \sigma_{3y} - \sigma_{1y} \sigma_{2z} \sigma_{3x} - \sigma_{1z} \sigma_{2x} \sigma_{3y} + \sigma_{1z} \sigma_{2y} \sigma_{3x}) \\
&\left. + \frac{2}{\sqrt{6}} (\sigma_{1x} \sigma_{2y} - \sigma_{1y} \sigma_{2x} + \sigma_{1x} \sigma_{2y} \sigma_{3z} - \sigma_{1y} \sigma_{2x} \sigma_{3z}) \right] \tag{56}
\end{aligned}$$

$\ell' = \{1,2,3 \tau_4\}_{even}$:

$$\begin{aligned}
\rho_{\pm, \theta=0}^{\{1,2,3 \tau_4\}_{even}} &= \frac{1}{8} \left[(\mathbb{I} - \sigma_{1z} \sigma_{2z} \sigma_{3z}) \right. \\
&+ \frac{1}{3} (\sigma_{1z} + \sigma_{2z} + \sigma_{3z} - \sigma_{1x} \sigma_{2x} - \sigma_{1y} \sigma_{2y} - \sigma_{1z} \sigma_{2z} \\
&\quad - \sigma_{1x} \sigma_{3x} - \sigma_{1y} \sigma_{3y} - \sigma_{1z} \sigma_{3z} - \sigma_{2x} \sigma_{3x} - \sigma_{2y} \sigma_{3y} - \sigma_{2z} \sigma_{3z} \\
&\quad - \sigma_{1x} \sigma_{2x} \sigma_{3z} - \sigma_{1x} \sigma_{2z} \sigma_{3x} - \sigma_{1y} \sigma_{2y} \sigma_{3z} \\
&\quad - \sigma_{1y} \sigma_{2z} \sigma_{3y} - \sigma_{1z} \sigma_{2x} \sigma_{3x} - \sigma_{1z} \sigma_{2y} \sigma_{3y}) \\
&+ \frac{1}{\sqrt{3}} (\pm \sigma_{1x} \sigma_{2y} \mp \sigma_{1y} \sigma_{2x} \mp \sigma_{1x} \sigma_{3y} \pm \sigma_{1y} \sigma_{3x} \pm \sigma_{2x} \sigma_{3y} \mp \sigma_{2y} \sigma_{3x}) \\
&\quad \pm \sigma_{1x} \sigma_{2y} \sigma_{3z} \mp \sigma_{1x} \sigma_{2z} \sigma_{3y} \mp \sigma_{1y} \sigma_{2x} \sigma_{3z} \\
&\quad \left. \pm \sigma_{1y} \sigma_{2z} \sigma_{3x} \pm \sigma_{1z} \sigma_{2x} \sigma_{3y} \mp \sigma_{1z} \sigma_{2y} \sigma_{3x}) \right] \tag{57}
\end{aligned}$$

LISA tensor operator	Global unitary bound		Scaling factor $\xi_j^{(\ell')}(g)$
	$N = 2$	$N = 3$	
$T_{1,0}^{\{k,l\}_{odd}}$	$\frac{1}{\sqrt{2}}$	$\frac{1}{2}$	$\frac{1}{\sqrt{2}}$
$T_{1,0}^{\{k,l,m \tau_2\}_{odd}}$	–	$\sqrt{\frac{\sqrt{3} + 2}{12}}$	$\frac{3}{3 + \sqrt{3}}$
$T_{2,0}^{\{k,l,m \tau_2\}_{even}}$	–	$\frac{1}{2}$	$\frac{1}{\sqrt{2}}$
$T_{1,0}^{\{k,l,m \tau_3\}_{odd}}$	–	$\frac{1}{2}$	$\frac{1}{\sqrt{2}}$
$T_{2,0}^{\{k,l,m \tau_3\}_{even}}$	–	$\frac{1}{2}$	$\frac{1}{\sqrt{2}}$
$T_{0,0}^{\{k,l,m \tau_4\}_{even}}$	–	$\frac{1}{2}$	$\frac{1}{\sqrt{2}}$

Table 3: Additional scaling factors $\xi_j^{(\ell')}(g)$ for bilinear and trilinear beads which do not correspond to fully permutation symmetric components of the density operator calculated based on the global unitary bounds of the corresponding LISA tensor operator.

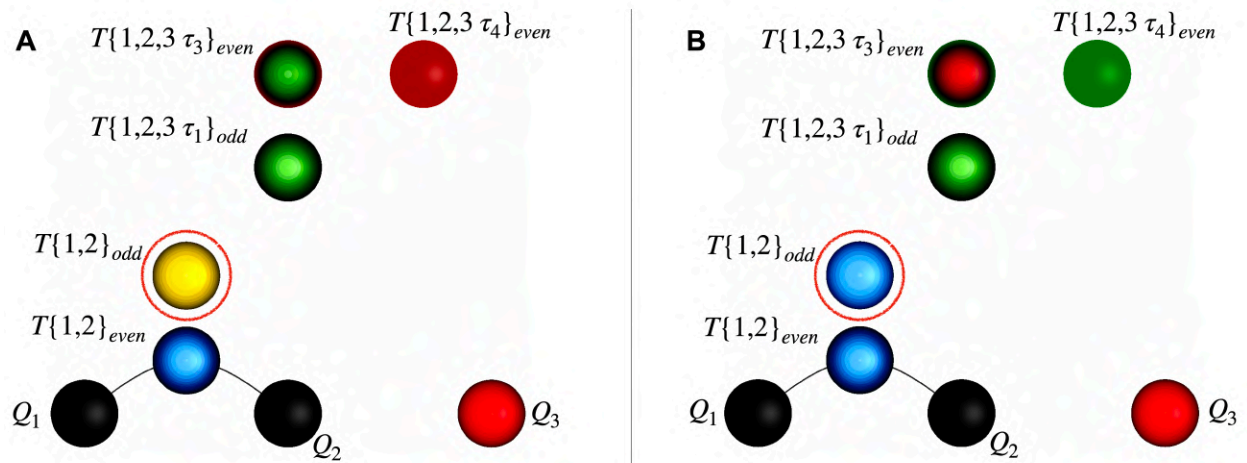


Fig. 14. BEADS representation of $|\psi_+^{\{1,2\}odd}\rangle$ (A) and $|\psi_-^{\{1,2\}odd}\rangle$ (B) for $\theta = 0$. The visualized states reach maximum values ± 1 for the bead $T\{1,2\}_{odd}$ marked by red circles.

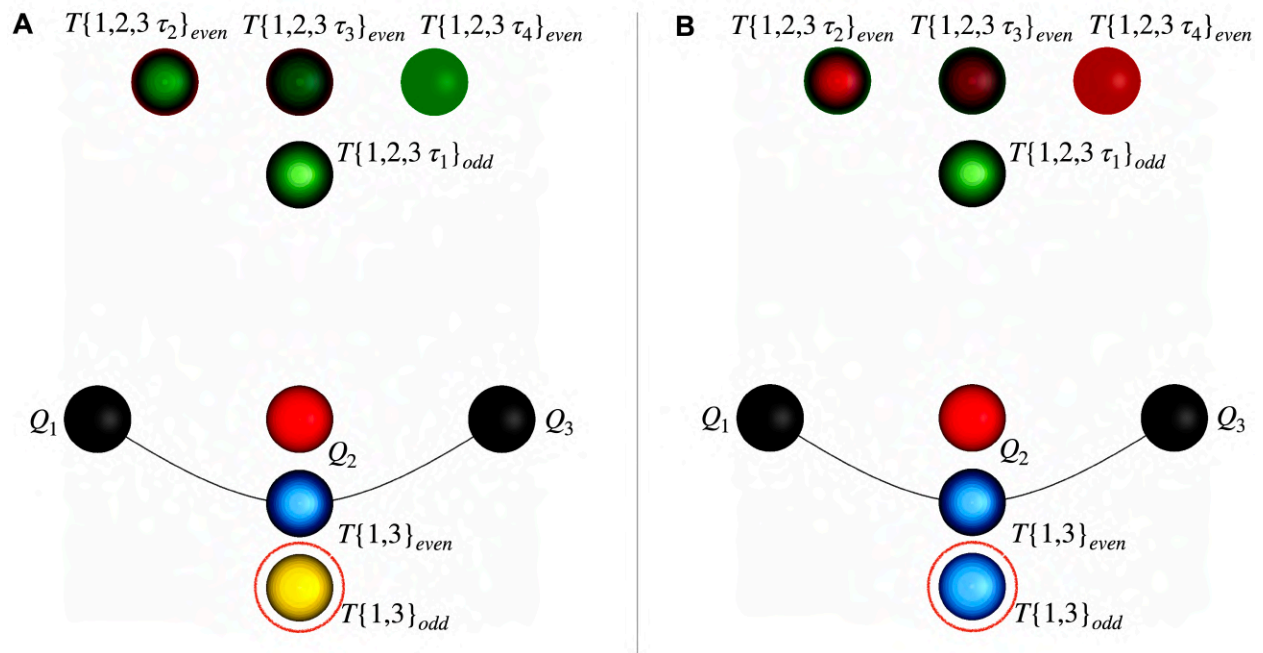


Fig. 15. BEADS representation of $|\psi_+^{\{1,3\}odd}\rangle$ (A) and $|\psi_-^{\{1,3\}odd}\rangle$ (B) for $\theta = 0$. The visualized states reach maximum values ± 1 for the bead $T\{1,3\}_{odd}$ marked by red circles.

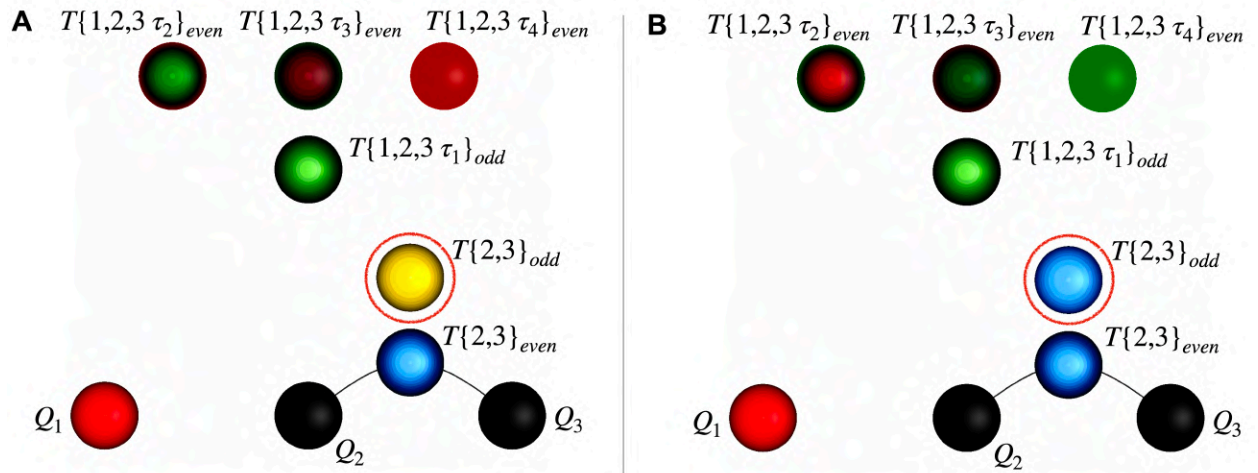


Fig. 16. BEADS representation of $|\psi_{+}^{\{2,3\}odd}\rangle$ (A) and $|\psi_{-}^{\{2,3\}odd}\rangle$ (B) for $\theta = 0$. The visualized states reach maximum values ± 1 for the bead $T\{2,3\}_{odd}$ marked by red circles.

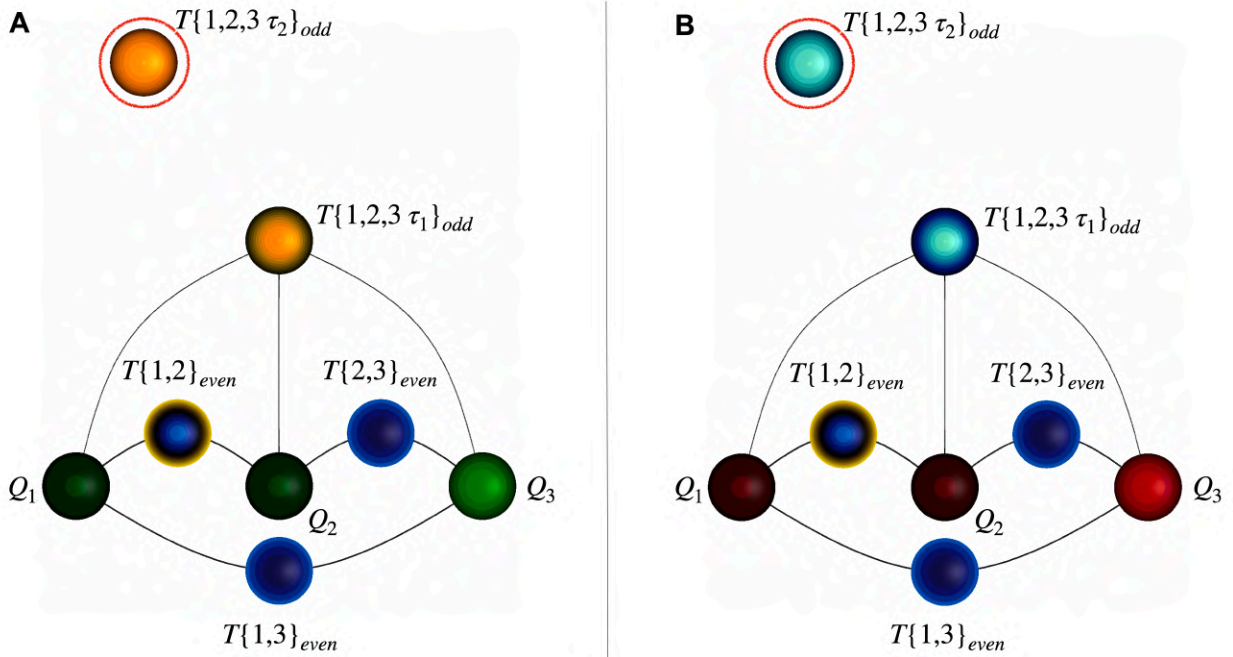


Fig. 17. BEADS representation of $|\psi_+^{\{1,2,3 \tau_2\} odd}\rangle$ (A) and $|\psi_-^{\{1,2,3 \tau_2\} odd}\rangle$ (B). The visualized states reach maximum values ± 1 for the bead $T\{1,2,3 \tau_2\} odd$ marked by red circles.

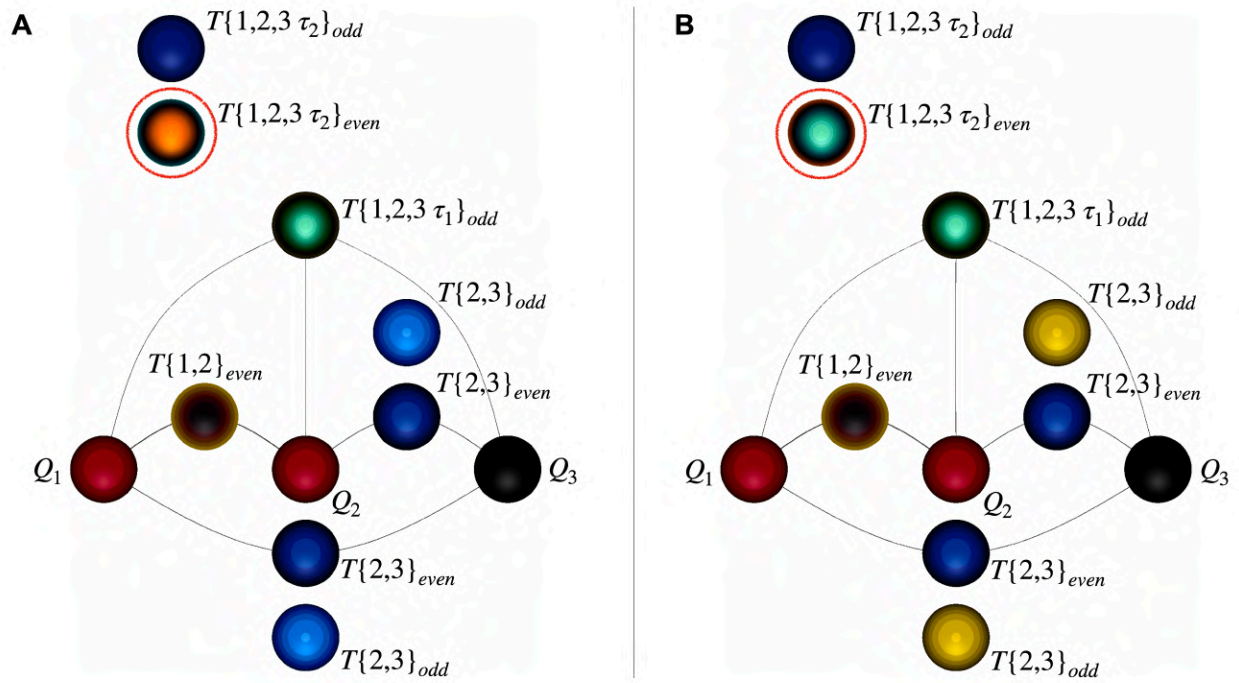


Fig. 18. BEADS representation of $|\psi_+^{\{1,2,3 \tau_2\}_{even}}\rangle$ (A) and $|\psi_-^{\{1,2,3 \tau_2\}_{even}}\rangle$ (B) for $\theta = 0$. The visualized states reach maximum values ± 1 for the bead $T\{1,2,3 \tau_2\}_{even}$ marked by red circles.

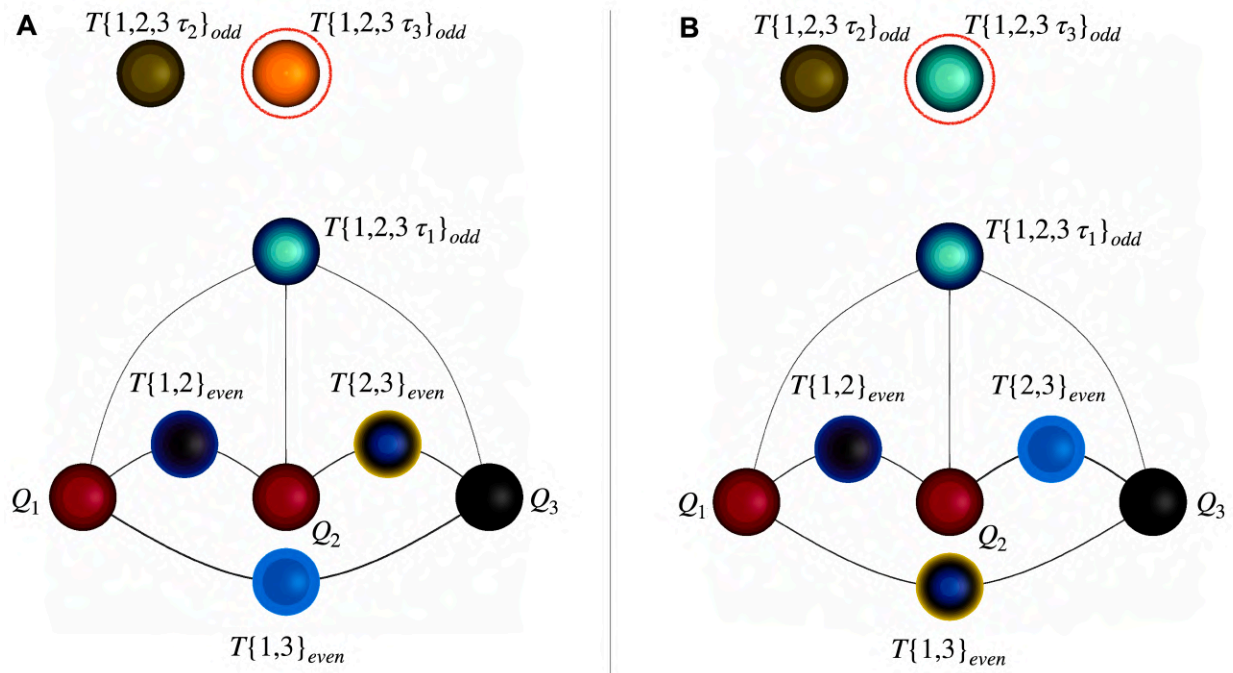


Fig. 19. BEADS representation of $|\psi_+^{\{1,2,3 \tau_3\} odd}\rangle$ (A) and $|\psi_-^{\{1,2,3 \tau_3\} odd}\rangle$ (B) for $\theta = 0$. The visualized states reach maximum values ± 1 for the bead $T\{1,2,3 \tau_3\} odd$ marked by red circles.

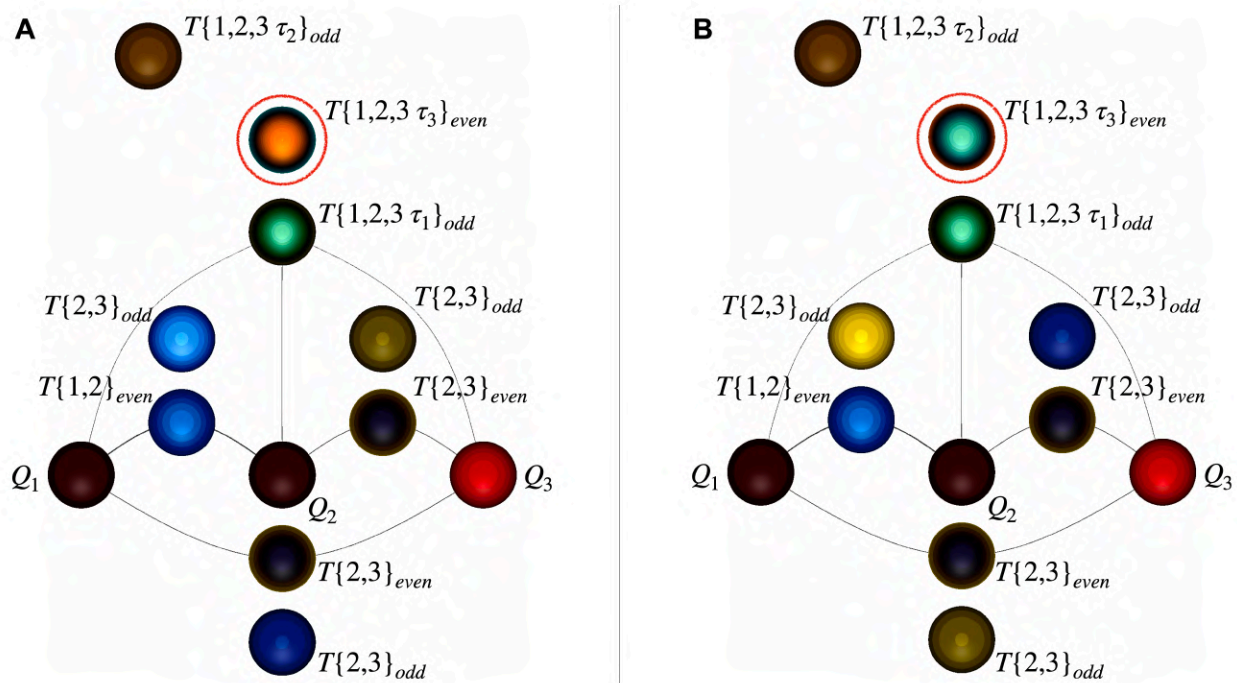


Fig. 20. BEADS representation of $|\psi_+^{\{1,2,3 \tau_3\} \text{even}}\rangle$ (A) and $|\psi_-^{\{1,2,3 \tau_3\} \text{even}}\rangle$ (B) for $\theta = 0$. The visualized states reach maximum values ± 1 for the bead $T\{1,2,3 \tau_3\} \text{even}$ marked by red circles.

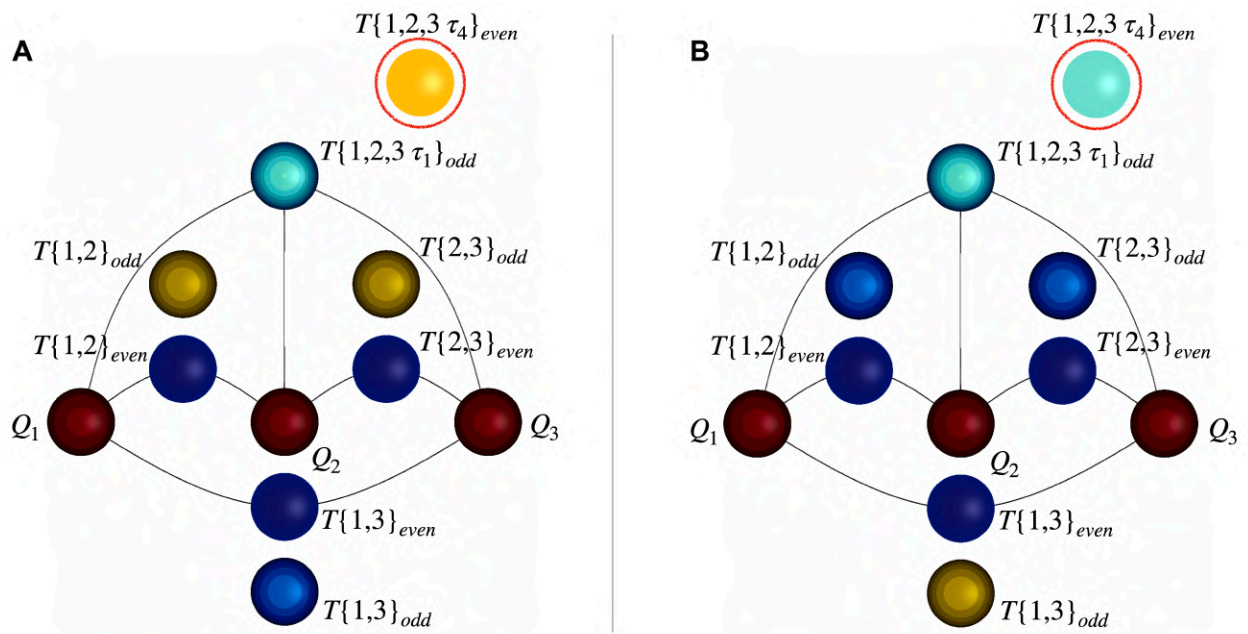


Fig. 21. BEADS representation of $|\psi_+^{\{1,2,3\tau_4\}_{even}}\rangle$ (A) and $|\psi_-^{\{1,2,3\tau_4\}_{even}}\rangle$ (B) for $\theta = 0$. The visualized states reach maximum values ± 1 for the bead $T\{1,2,3\tau_4\}_{even}$ marked by red circles.

S5 Overview of BEADS scaling factors

Table 4 displays the scaling factors $\xi_j^{(\ell')}(g)$ which are applied to compose the overall bead scaling factor $s_j^{(\ell')}(N, g)$. Recall, that in the BEADS representation all non-axial operators of the same rank j and set ℓ' are scaled by using the same scaling factors as for the axial component.

Bead ℓ'	Rank j	Scaling factor $\xi_j^{(\ell')}(g)$	Scaling method
$\{\emptyset\}$	0	–	–
$\{\mathbf{k}\}$	1	–	–
$\{k, l\}_{\text{even}}$	0	$\sqrt{\frac{1}{3}}$	canonical
	2	$\sqrt{\frac{2}{3}}$	canonical
$\{k, l\}_{\text{odd}}$	1	$\frac{1}{\sqrt{2}}$	GUB
$\{k, l, m \tau_1\}_{\text{odd}}$	1	$\sqrt{\frac{3}{5}}$	canonical
	3	$\sqrt{\frac{2}{5}}$	canonical
$\{k, l, m \tau_2\}_{\text{even}}$	2	$\frac{1}{\sqrt{2}}$	GUB
$\{k, l, m \tau_2\}_{\text{odd}}$	1	$\frac{3}{3+\sqrt{3}}$	GUB
$\{k, l, m \tau_3\}_{\text{even}}$	2	$\frac{1}{\sqrt{2}}$	GUB
$\{k, l, m \tau_3\}_{\text{odd}}$	1	$\frac{1}{\sqrt{2}}$	GUB
$\{k, l, m \tau_4\}_{\text{even}}$	0	$\frac{1}{\sqrt{2}}$	GUB

Table 4: Overview of scaling factors $\xi_j^{(\ell')}(g)$ for up to trilinear LISA tensor operators. The scaling method specifies whether the displayed scaling factor was calculated by using the canonical scaling approach (section S3) or based on the global unitary bound (GUB, explained in section S4).

S6 Canonical axial tensor operators and tomography

As was previously shown by Leiner et al. (41, 42), the DROPS representation can be reconstructed experimentally by using tomography techniques. Indeed, this can be achieved as the droplet function $f_j^{(\ell)}(\beta, \alpha)$ corresponding to a specific set ℓ is proportional to the expectation value of the associated rotated axial LISA basis operator $R_{\alpha\beta} T_{j,0}^{(\ell)}$ for which it can be directly mapped to the corresponding axial spherical harmonics function $Y_{j,0}$ which has a value of

$$f_j^{(\ell)}(\beta, \alpha) = \sqrt{\frac{2j+1}{4\pi}} \cdot \langle R_{\alpha\beta} T_{j,0}^{(\ell)} \rangle \quad (58)$$

along angular direction (β, α) and where $R_{\alpha\beta}$ denotes a rotation matrix (41). In particular, for an (unrotated) axial LISA basis operator $T_{j,0}^{(\ell)}$, the value of the droplet function along the z-axis is given by

$$f_j^{(\ell)}(0,0) = \sqrt{\frac{2j+1}{4\pi}} \cdot \langle T_{j,0}^{(\ell)} \rangle \quad (59)$$

Since the BEADS representation remains bijective, despite introducing additional scaling factors $s_j^{(\ell')}(N, g)$, it can also be reconstructed experimentally by directly applying the scaled non-normalized rotated axial tensor operators $\tilde{T}_{j,0}^{(\ell')} = \zeta(N) \xi_j^{(\ell')}(g) T_{j,0}^{(\ell')}$ in Eq. 58. The spherical function bead value along angular direction (β, α) is then given by

$$b_j^{(\ell')}(\beta, \alpha) = \langle R_{\alpha\beta} \tilde{T}_{j,0}^{(\ell')} \rangle = \langle R_{\alpha\beta} \sqrt{2^N} \xi_j^{(\ell')}(g) T_{j,0}^{(\ell')} \rangle \quad (60)$$

where $\zeta(N) = \sqrt{2^N}$ and $\xi_j^{(\ell')}(g)$ are the scaling factors introduced in sections S3 and S4 and N is the number of qubits in the system. Using Pauli matrices σ and the identity operator \mathbb{I} , the scaled axial LISA tensor operators $\tilde{T}_{j,0}^{(\ell')}$ (up to linearity $g = 3$) then result in:

$$\begin{aligned} \ell' = \{\emptyset\}: \\ \tilde{T}_{0,0}^{\{\emptyset\}} = \mathbb{I} \end{aligned} \quad (61)$$

$$\begin{aligned} \ell' = \{k\}: \\ \tilde{T}_{1,0}^{\{k\}} = \sigma_{kz} \end{aligned} \quad (62)$$

$$\begin{aligned} \ell' = \{k, l\}_{\text{even}}: \\ \tilde{T}_{0,0}^{\{k,l\}_{\text{even}}} = \frac{1}{3} (\sigma_{kx} \sigma_{lx} + \sigma_{ky} \sigma_{ly} + \sigma_{kz} \sigma_{lz}) \end{aligned} \quad (63a)$$

$$\tilde{T}_{2,0}^{\{k,l\}_{\text{even}}} = \frac{1}{3} (-\sigma_{kx} \sigma_{lx} - \sigma_{ky} \sigma_{ly} + 2\sigma_{kz} \sigma_{lz}) \quad (63b)$$

$$\ell' = \{k, l\}_{odd}:$$

$$\tilde{T}_{1,0}^{\{k,l\}_{odd}} = \frac{1}{2}(\sigma_{kx}\sigma_{ly} - \sigma_{ky}\sigma_{lx}) \quad (64)$$

$$\ell' = \{k, l, m \tau_1\}_{odd}:$$

$$\tilde{T}_{1,0}^{\{k,l,m \tau_1\}_{odd}} = \frac{2}{5} [(\sigma_{kx}\sigma_{lx}\sigma_{mz} + \sigma_{kx}\sigma_{lz}\sigma_{mx} + \sigma_{kz}\sigma_{lx}\sigma_{mx}) + (\sigma_{ky}\sigma_{ly}\sigma_{mz} + \sigma_{ky}\sigma_{lz}\sigma_{my} + \sigma_{kz}\sigma_{ly}\sigma_{my}) + 3\sigma_{kz}\sigma_{lz}\sigma_{mz}] \quad (65a)$$

$$\tilde{T}_{3,0}^{\{k,l,m \tau_1\}_{odd}} = \frac{2}{5} [-(\sigma_{kx}\sigma_{lx}\sigma_{mz} + \sigma_{kx}\sigma_{lz}\sigma_{mx} + \sigma_{kz}\sigma_{lx}\sigma_{mx}) - (\sigma_{ky}\sigma_{ly}\sigma_{mz} + \sigma_{ky}\sigma_{lz}\sigma_{my} + \sigma_{kz}\sigma_{ly}\sigma_{my}) + 2\sigma_{kz}\sigma_{lz}\sigma_{mz}] \quad (65b)$$

$$\ell' = \{k, l, m \tau_2\}_{odd}:$$

$$\tilde{T}_{1,0}^{\{k,l,m \tau_2\}_{odd}} = \frac{\sqrt{3}}{3 + \sqrt{3}} [(\sigma_{kx}\sigma_{lz}\sigma_{mx} + \sigma_{kz}\sigma_{lx}\sigma_{mx}) + (\sigma_{ky}\sigma_{lz}\sigma_{my} + \sigma_{kz}\sigma_{ly}\sigma_{my}) - 2(\sigma_{kx}\sigma_{lx}\sigma_{mz} + \sigma_{ky}\sigma_{ly}\sigma_{mz})] \quad (66)$$

$$\ell' = \{k, l, m \tau_2\}_{even}:$$

$$\tilde{T}_{2,0}^{\{k,l,m \tau_2\}_{even}} = \frac{1}{\sqrt{2}} [(\sigma_{ky}\sigma_{lz}\sigma_{mx} + \sigma_{kz}\sigma_{ly}\sigma_{mx}) - (\sigma_{kx}\sigma_{lz}\sigma_{my} + \sigma_{kz}\sigma_{lx}\sigma_{my})] \quad (67)$$

$$\ell' = \{k, l, m \tau_3\}_{odd}:$$

$$\tilde{T}_{1,0}^{\{k,l,m \tau_3\}_{odd}} = \frac{1}{\sqrt{2}} [(\sigma_{kz}\sigma_{lx}\sigma_{mx} - \sigma_{kx}\sigma_{lz}\sigma_{mx}) + (\sigma_{kz}\sigma_{ly}\sigma_{my} - \sigma_{ky}\sigma_{lz}\sigma_{my})] \quad (68)$$

$$\ell' = \{k, l, m \tau_3\}_{even}:$$

$$\tilde{T}_{2,0}^{\{k,l,m \tau_3\}_{even}} = \frac{1}{\sqrt{6}} [-(2\sigma_{kx}\sigma_{ly}\sigma_{mz} + \sigma_{kx}\sigma_{lz}\sigma_{my} - \sigma_{kz}\sigma_{lx}\sigma_{my}) + (2\sigma_{ky}\sigma_{lx}\sigma_{mz} + \sigma_{ky}\sigma_{lz}\sigma_{mx} - \sigma_{kz}\sigma_{ly}\sigma_{mx})] \quad (69)$$

$$\ell' = \{k, l, m \tau_4\}_{even}:$$

$$\tilde{T}_{0,0}^{\{k,l,m \tau_4\}_{even}} = \frac{1}{\sqrt{3}} [\sigma_{kx}\sigma_{ly}\sigma_{mz} + \sigma_{ky}\sigma_{lz}\sigma_{mx} + \sigma_{kz}\sigma_{lx}\sigma_{my} - \sigma_{kx}\sigma_{lz}\sigma_{my} - \sigma_{ky}\sigma_{lx}\sigma_{mz} - \sigma_{kz}\sigma_{ly}\sigma_{mx}] \quad (70)$$

S7 Correlation isolation using Ursell functions

In qubit systems described by a *pure* state $|\psi\rangle$ and the corresponding density operator $\rho = |\psi\rangle\langle\psi|$, it is possible to distinguish between compound, i.e., classical correlations and lower-order quantum correlations, and so-called non-classical *connected correlations* which only occur in entangled states (44-47). By applying Ursell correlation functions (44–48, 63) all compound correlation components are eliminated, and we obtain non-classical correlation coefficients C corresponding to connected correlations only. In general, correlation coefficients are defined to adopt values between -1 and 1 (67). Total correlations are sometimes referred to as disconnected correlations (47).

Compound correlations are commonly of lesser interest as they comprise redundant information which is already encoded in local single-qubit components (classical correlation) or quantum correlations of lower order, i.e., connected correlations between less qubits than involved in the observed correlation component, and thus, do not provide a gain in information. Note that here, we denote correlations classical only if the underlying correlation expectation values factorize into expectation values of local single-qubit components which is in line with the definition of classical correlations in (68). Connected correlation coefficients $C_{\alpha,\beta,\dots,\omega}^{12\dots n}$ can be utilized to form a modified density operator $\tilde{\rho}$ that only comprises genuine n -qubit non-classical connected correlations visualized by E-Beads and separable single-qubit components (e.g., corresponding to spin polarization) which can be visualized by Q-Beads. When further removing all single-qubit components and the identity from $\tilde{\rho}$, the norm of the resulting operator is referred to as the entanglement norm of a state and serves as a measure to quantify the entanglement in a system (44). In our approach, it is further possible to determine the entanglement norms corresponding to individual symmetry components. Compound correlation components can be further applied for additional visualizations or to characterize total correlations such as is shown in section S9.

n -qubit connected correlation functions $C_{\alpha,\beta,\dots,\omega}^{12\dots n} = \langle\sigma_{1\alpha}\sigma_{2\beta}\dots\sigma_{n\omega}\rangle_{ent}$ are defined recursively based on n -linear total correlations which gives the following expressions for two-qubit (Eq. 71) and three-qubit correlations (Eq. 72)

$$\langle\sigma_{1\alpha}\sigma_{2\beta}\rangle = \langle\sigma_{1\alpha}\rangle\langle\sigma_{2\beta}\rangle + \langle\sigma_{1\alpha}\sigma_{2\beta}\rangle_{ent} = \langle\sigma_{1\alpha}\rangle\langle\sigma_{2\beta}\rangle + C_{\alpha,\beta}^{12} \quad (71)$$

$$\begin{aligned} \langle\sigma_{1\alpha}\sigma_{2\beta}\sigma_{3\gamma}\rangle &= \langle\sigma_{1\alpha}\rangle\langle\sigma_{2\beta}\rangle\langle\sigma_{3\gamma}\rangle \\ &+ \langle\sigma_{3\gamma}\rangle\langle\sigma_{1\alpha}\sigma_{2\beta}\rangle_{ent} + \langle\sigma_{2\beta}\rangle\langle\sigma_{1\alpha}\sigma_{3\gamma}\rangle_{ent} + \langle\sigma_{1\alpha}\rangle\langle\sigma_{2\beta}\sigma_{3\gamma}\rangle_{ent} \\ &+ \langle\sigma_{1\alpha}\sigma_{2\beta}\sigma_{3\gamma}\rangle_{ent} \\ &= \langle\sigma_{1\alpha}\rangle\langle\sigma_{2\beta}\rangle\langle\sigma_{3\gamma}\rangle \\ &+ \langle\sigma_{1\alpha}\rangle C_{\beta,\gamma}^{23} + \langle\sigma_{2\beta}\rangle C_{\alpha,\gamma}^{13} + \langle\sigma_{3\gamma}\rangle C_{\alpha,\beta}^{12} \\ &+ C_{\alpha,\beta,\gamma}^{123} \end{aligned} \quad (72)$$

where σ are the Pauli operators with $\alpha, \beta, \gamma \in \{x, y, z\}$ and number indices indicate the qubit. Thus, two-qubit non-classical connected correlation coefficients are given by (44, 47, 48)

$$C_{\alpha,\beta}^{12} = \langle\sigma_{1\alpha}\sigma_{2\beta}\rangle - \langle\sigma_{1\alpha}\rangle\langle\sigma_{2\beta}\rangle \quad (73)$$

and we obtain the two-qubit non-classically correlated density operator as

$$\tilde{\rho} = \rho - \frac{1}{4} \sum_{\alpha, \beta=x,y,z} \langle \sigma_{1\alpha} \rangle \langle \sigma_{2\beta} \rangle \sigma_{1\alpha} \sigma_{2\beta} \quad (74)$$

Thus, in two-qubit systems, compound correlations only comprise products of local linear components $\langle \sigma_{1\alpha} \rangle \langle \sigma_{2\beta} \rangle$, i.e., classical correlations.

Trilinear non-classical connected correlation coefficients are defined as (44, 48)

$$C_{\alpha, \beta, \gamma}^{123} = \langle \sigma_{1\alpha} \sigma_{2\beta} \sigma_{3\gamma} \rangle - \langle \sigma_{1\alpha} \rangle C_{\beta, \gamma}^{23} - \langle \sigma_{2\beta} \rangle C_{\alpha, \gamma}^{13} - \langle \sigma_{3\gamma} \rangle C_{\alpha, \beta}^{12} - \langle \sigma_{1\alpha} \rangle \langle \sigma_{2\beta} \rangle \langle \sigma_{3\gamma} \rangle \quad (75)$$

Note that unlike in the two-qubit case, multiple correlation components need to be subtracted which, apart from the classical components $\langle \sigma_{1\alpha} \rangle \langle \sigma_{2\beta} \rangle \langle \sigma_{3\gamma} \rangle$, also involve lower-order bipartite non-classical correlations denoted by two-qubit connected correlation coefficients. Indeed, it is possible to express these trilinear correlation coefficients as a linear combination of products of single-qubit components and n -qubit total correlations by applying the relations from Eq. 72 which gives

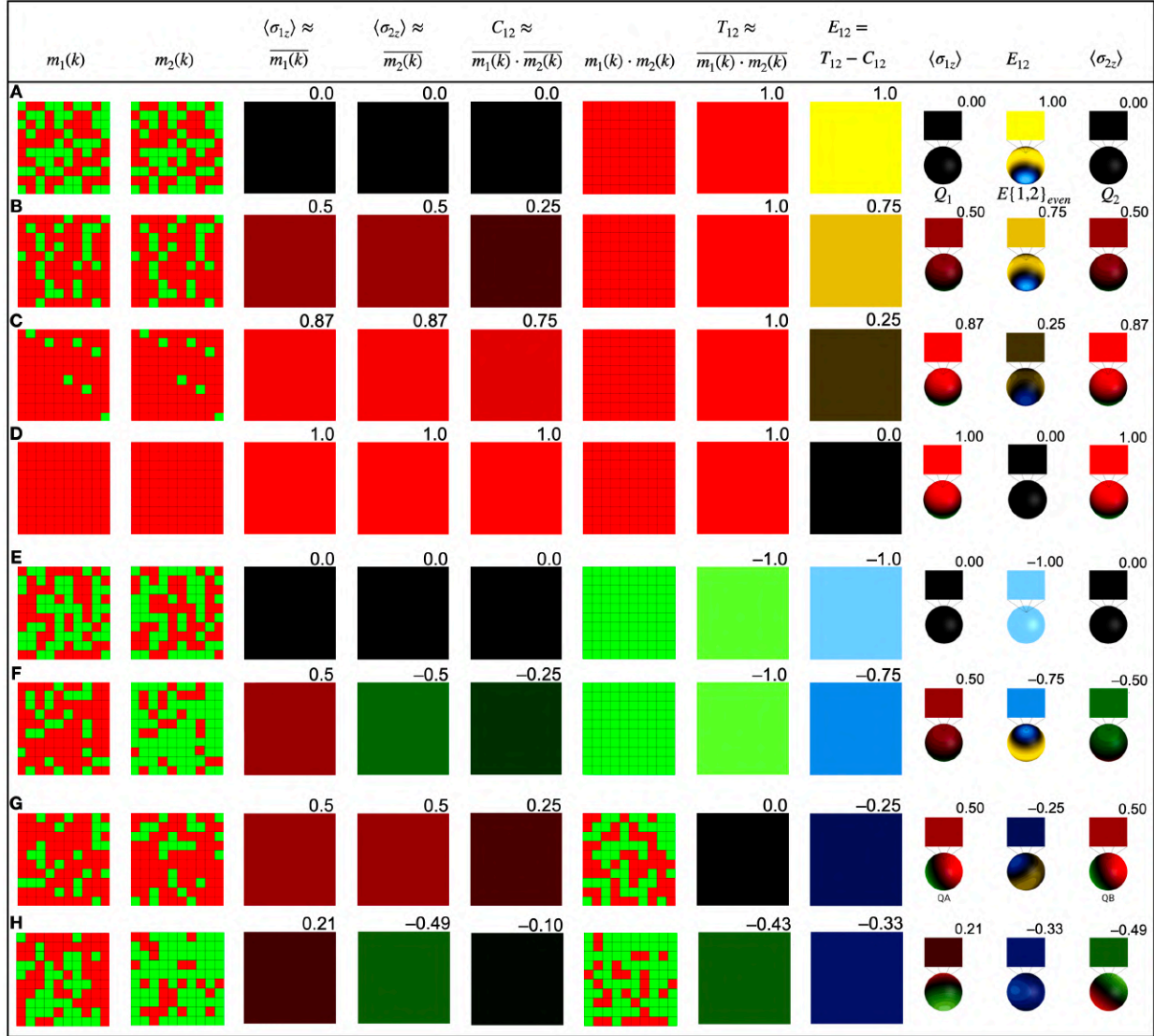
$$\begin{aligned} C_{\alpha, \beta, \gamma}^{123} &= \langle \sigma_{1\alpha} \sigma_{2\beta} \sigma_{3\gamma} \rangle - \langle \sigma_{1\alpha} \rangle (\langle \sigma_{2\beta} \sigma_{3\gamma} \rangle - \langle \sigma_{2\beta} \rangle \langle \sigma_{3\gamma} \rangle) - \langle \sigma_{2\beta} \rangle (\langle \sigma_{1\alpha} \sigma_{3\gamma} \rangle - \langle \sigma_{1\alpha} \rangle \langle \sigma_{3\gamma} \rangle) \\ &\quad - \langle \sigma_{3\gamma} \rangle (\langle \sigma_{1\alpha} \sigma_{2\beta} \rangle - \langle \sigma_{1\alpha} \rangle \langle \sigma_{2\beta} \rangle) - \langle \sigma_{1\alpha} \rangle \langle \sigma_{2\beta} \rangle \langle \sigma_{3\gamma} \rangle \\ &= \langle \sigma_{1\alpha} \sigma_{2\beta} \sigma_{3\gamma} \rangle - \langle \sigma_{1\alpha} \rangle \langle \sigma_{2\beta} \sigma_{3\gamma} \rangle - \langle \sigma_{2\beta} \rangle \langle \sigma_{1\alpha} \sigma_{3\gamma} \rangle - \langle \sigma_{3\gamma} \rangle \langle \sigma_{1\alpha} \sigma_{2\beta} \rangle \\ &\quad + 2 \langle \sigma_{1\alpha} \rangle \langle \sigma_{2\beta} \rangle \langle \sigma_{3\gamma} \rangle \end{aligned} \quad (76)$$

The non-classically correlated density operator $\tilde{\rho}$ for a three-qubit system can then be efficiently calculated using trilinear as well as bilinear non-classical connected correlation coefficients.

$$\begin{aligned} \tilde{\rho} &= \rho + \frac{1}{4} \sum_{\alpha, \beta, \gamma=x,y,z} \langle \sigma_{1\alpha} \rangle \langle \sigma_{2\beta} \rangle \langle \sigma_{3\gamma} \rangle \sigma_{1\alpha} \sigma_{2\beta} \sigma_{3\gamma} \\ &\quad - \frac{1}{8} \left[\sum_{\alpha, \beta=x,y,z} \langle \sigma_{1\alpha} \sigma_{2\beta} \rangle \sigma_{1\alpha} \sigma_{2\beta} \sum_{\gamma=x,y,z} \langle \sigma_{3\gamma} \rangle \sigma_{3\gamma} \right. \\ &\quad \quad + \sum_{\alpha, \gamma=x,y,z} \langle \sigma_{1\alpha} \sigma_{3\gamma} \rangle \sigma_{1\alpha} \sigma_{3\gamma} \sum_{\beta=x,y,z} \langle \sigma_{2\beta} \rangle \sigma_{2\beta} \\ &\quad \quad \left. + \sum_{\beta, \gamma=x,y,z} \langle \sigma_{2\beta} \sigma_{3\gamma} \rangle \sigma_{2\beta} \sigma_{3\gamma} \sum_{\alpha=x,y,z} \langle \sigma_{1\alpha} \rangle \sigma_{1\alpha} \right] \\ &\quad - \frac{1}{8} \left[\sum_{\alpha, \beta=x,y,z} \langle \sigma_{1\alpha} \rangle \langle \sigma_{2\beta} \rangle \sigma_{1\alpha} \sigma_{2\beta} \right. \\ &\quad \quad + \sum_{\alpha, \gamma=x,y,z} \langle \sigma_{1\alpha} \rangle \langle \sigma_{3\gamma} \rangle \sigma_{1\alpha} \sigma_{3\gamma} \\ &\quad \quad \left. + \sum_{\beta, \gamma=x,y,z} \langle \sigma_{2\beta} \rangle \langle \sigma_{3\gamma} \rangle \sigma_{2\beta} \sigma_{3\gamma} \right] \end{aligned} \quad (77)$$

It should be pointed out, that due the large number of involved matrix operations, the calculation of a non-classically correlated density operator $\tilde{\rho}$ by Ursell functions can become computationally expensive. The required computational cost increases exponentially with an increasing number of qubits in the observed system, yet it remains applicable for real-time simulations and visualizations in relatively small qubit systems.

To further clarify the introduced concepts, Fig. 22 provides a graphical illustration how genuine n -qubit entanglement-related correlations (i.e., connected correlations) can be determined experimentally. Two-qubit states are exemplarily visualized for which we simulated zz -measurement outcomes $m_A(k)$ and $m_B(k)$ based on which one can approximate the total and the compound (here: classical) correlation T_{12} and C_{12} . The genuine two-qubit entanglement-related connected correlation E_{12} (that is, the non-classical connected correlation coefficient $C_{z,z}^{12}$ in Eq. 73; note the change of notation from $C_{z,z}^{12}$ to E_{12} in order to prevent confusion with the compound correlation C_{12}) can then be calculated as the difference between the total and compound correlation according to Eq. 73. The examined states were chosen such that the corresponding connected correlation coefficients range between -1 and 1 .



$$|\psi_F\rangle : E_{12} = T_{12} - C_{12} \approx \overline{m_1(k) \cdot m_2(k)} - \overline{m_1(k)} \cdot \overline{m_2(k)}$$

$$\begin{aligned}
 &= \overline{\begin{matrix} \text{Heatmap 1} & \text{Heatmap 2} \\ \text{Heatmap 1} & \text{Heatmap 2} \end{matrix}} - \overline{\begin{matrix} \text{Heatmap 1} \\ \text{Heatmap 2} \end{matrix}} \cdot \overline{\begin{matrix} \text{Heatmap 1} \\ \text{Heatmap 2} \end{matrix}} \\
 &= \overline{\begin{matrix} \text{Green} \\ \text{Green} \end{matrix}} - \overline{\begin{matrix} \text{Red} \\ \text{Green} \end{matrix}} \\
 &= \begin{matrix} \text{Green} \\ -1.0 \end{matrix} - \begin{matrix} \text{Green} \\ -0.25 \end{matrix} = \begin{matrix} \text{Blue} \\ -0.75 \end{matrix}
 \end{aligned}$$

Fig. 22. Correlation isolation by Ursell functions in two-qubit states based on simulated measurement outcomes. Total and compound correlations (T_{12} and C_{12}) in a two-qubit system can be calculated based on measurement outcomes $m_1(k)$ and $m_2(k)$. For a finite number of measurements, the total zz-correlation $T_{12} \approx \overline{m_1(k) \cdot m_2(k)}$ can be approximated from the

individual computational basis measurement outcomes as introduced in Fig. 2 in the Results section. All values are given as expectation values (i.e., bright red corresponds to 1 and green to -1). The entanglement-related connected two-qubit zz-correlation E_{12} is then obtained by subtracting C_{12} from T_{12} . The visualized states are (from top to bottom): The Schmidt form states **(A)** $|\psi_A\rangle = 1/\sqrt{2}(|00\rangle + |11\rangle)$, **(B)** $|\psi_B\rangle = \cos \pi/6 |00\rangle + \sin \pi/6 |11\rangle$, **(C)** $|\psi_C\rangle = \cos \pi/12 |00\rangle + \sin \pi/12 |11\rangle$, and **(D)** $|\psi_D\rangle = |00\rangle$, the singlet state **(E)** $|\psi_E\rangle = 1/\sqrt{2}(|01\rangle - |10\rangle)$, **(F)** the generalized Schmidt form state $|\psi_F\rangle = \cos \pi/6 |01\rangle + \sin \pi/6 |10\rangle$, **(G)** $|\psi_G\rangle = 1/\sqrt{2}|00\rangle + 1/2(|01\rangle + |10\rangle)$, and **(H)** $|\psi_H\rangle = (-0.25090 - 0.099137i, 0.622241 + 0.377673i, -0.143036 - 0.404289i, -0.349897 + 0.301740i)^T$. An exemplary graphical calculation of the connected correlation E_{12} is shown for the state $|\psi_F\rangle$ at the bottom.

As the BEADS representation is based on LISA tensor operators $T_{j,m}^{(\ell')}$ with rank j and order m , we now show how non-classical correlation coefficients can be obtained in terms of these operators $T_{j,m}^{(\ell')}$.

In general, the non-classically correlated density operator can be written as

$$\tilde{\rho} = \rho - \sum_{j \in J(\ell')} \sum_{p=-j}^j \tilde{c}_{j,m}^{(\ell')} T_{j,m}^{(\ell')} \quad (78)$$

where $\tilde{c}_{j,m}^{(\ell')}$ is the sum of all correlation coefficients of compound correlations corresponding to the tensor operator $T_{j,m}^{(\ell')}$.

The purely classical bipartite correlation coefficients can be calculated as follows:

Rank $j = 0$:

$$\tilde{c}_{0,0}^{\{k,\lambda\}even} = \frac{1}{\sqrt{2^N}} \frac{1}{\sqrt{3}} (\langle \sigma_{kx} \rangle \langle \sigma_{\lambda x} \rangle + \langle \sigma_{ky} \rangle \langle \sigma_{\lambda y} \rangle + \langle \sigma_{kz} \rangle \langle \sigma_{\lambda z} \rangle) \quad (79)$$

Rank $j = 1$:

$$\tilde{c}_{1,-1}^{\{k,\lambda\}odd} = \frac{1}{\sqrt{2^N}} \frac{1}{\sqrt{2}} (\langle \sigma_{kz} \rangle \langle \sigma_{\lambda x} \rangle - \langle \sigma_{kx} \rangle \langle \sigma_{\lambda z} \rangle) \quad (80a)$$

$$\tilde{c}_{1,0}^{\{k,\lambda\}odd} = \frac{1}{\sqrt{2^N}} \frac{1}{\sqrt{2}} (\langle \sigma_{kx} \rangle \langle \sigma_{\lambda y} \rangle - \langle \sigma_{ky} \rangle \langle \sigma_{\lambda x} \rangle) \quad (80b)$$

$$\tilde{c}_{1,1}^{\{k,\lambda\}odd} = \frac{1}{\sqrt{2^N}} \frac{1}{\sqrt{2}} (\langle \sigma_{ky} \rangle \langle \sigma_{\lambda z} \rangle - \langle \sigma_{kz} \rangle \langle \sigma_{\lambda y} \rangle) \quad (80c)$$

Rank $j = 2$:

$$\tilde{c}_{2,-2}^{\{k,\lambda\}even} = \frac{1}{\sqrt{2^N}} \frac{1}{\sqrt{2}} (\langle \sigma_{ky} \rangle \langle \sigma_{\lambda x} \rangle + \langle \sigma_{kx} \rangle \langle \sigma_{\lambda y} \rangle) \quad (81a)$$

$$\tilde{c}_{2,-1}^{\{k,\lambda\}even} = \frac{1}{\sqrt{2^N}} \frac{1}{\sqrt{2}} (\langle \sigma_{kz} \rangle \langle \sigma_{\lambda y} \rangle + \langle \sigma_{ky} \rangle \langle \sigma_{\lambda z} \rangle) \quad (81b)$$

$$\tilde{c}_{2,0}^{\{k,\lambda\}even} = \frac{1}{\sqrt{2^N}} \frac{1}{\sqrt{6}} (-\langle \sigma_{kx} \rangle \langle \sigma_{\lambda x} \rangle - \langle \sigma_{ky} \rangle \langle \sigma_{\lambda y} \rangle + 2\langle \sigma_{kz} \rangle \langle \sigma_{\lambda z} \rangle) \quad (81c)$$

$$\tilde{c}_{2,1}^{\{k,\lambda\}even} = \frac{1}{\sqrt{2^N}} \frac{1}{\sqrt{2}} (\langle \sigma_{kx} \rangle \langle \sigma_{\lambda z} \rangle + \langle \sigma_{kz} \rangle \langle \sigma_{\lambda x} \rangle) \quad (81d)$$

$$\tilde{c}_{2,2}^{\{k,\lambda\}even} = \frac{1}{\sqrt{2^N}} \frac{1}{\sqrt{2}} (\langle \sigma_{kx} \rangle \langle \sigma_{\lambda x} \rangle - \langle \sigma_{ky} \rangle \langle \sigma_{\lambda y} \rangle) \quad (81e)$$

Here, $\{k, \lambda\}$ denotes an arbitrary bilinear subsystem of qubits and N is the total number of qubits in the system. Trilinear compound correlation coefficients expressed in terms of LISA tensor operator read as follows (Eq. 82–88). Note that as discussed previously, every trilinear tensor

$$\tilde{c}_{1,1,class.}^{\{\kappa,\lambda,\mu\tau_2\}odd} = \frac{1}{\sqrt{2^N}} \frac{1}{\sqrt{12}} \left(-2(\langle \sigma_{ky} \rangle \langle \sigma_{ly} \rangle \langle \sigma_{\mu x} \rangle + \langle \sigma_{kz} \rangle \langle \sigma_{lz} \rangle \langle \sigma_{\mu x} \rangle) + \langle \sigma_{kx} \rangle \langle \sigma_{ly} \rangle \langle \sigma_{\mu y} \rangle \right. \\ \left. + \langle \sigma_{kx} \rangle \langle \sigma_{lz} \rangle \langle \sigma_{\mu z} \rangle + \langle \sigma_{ky} \rangle \langle \sigma_{lx} \rangle \langle \sigma_{\mu y} \rangle + \langle \sigma_{kz} \rangle \langle \sigma_{lx} \rangle \langle \sigma_{\mu z} \rangle \right) \quad (85e)$$

$$\tilde{c}_{1,1,low-ord.}^{\{\kappa,\lambda,\mu\tau_2\}odd,(\kappa\lambda)\mu} = \frac{1}{\sqrt{2^N}} \frac{1}{\sqrt{12}} \left(-2(\langle \sigma_{ky} \sigma_{ly} \rangle \langle \sigma_{\mu x} \rangle + \langle \sigma_{kz} \sigma_{lz} \rangle \langle \sigma_{\mu x} \rangle) + \langle \sigma_{kx} \sigma_{ly} \rangle \langle \sigma_{\mu y} \rangle \right. \\ \left. + \langle \sigma_{kx} \sigma_{lz} \rangle \langle \sigma_{\mu z} \rangle + \langle \sigma_{ky} \sigma_{lx} \rangle \langle \sigma_{\mu y} \rangle + \langle \sigma_{kz} \sigma_{lx} \rangle \langle \sigma_{\mu z} \rangle \right) \quad (85f)$$

Bead $\ell' = \{\kappa, \lambda, m, \tau_3\}_{even}$, rank $j = 2$

$$\tilde{c}_{2,-2,class.}^{\{\kappa,\lambda,\mu\tau_3\}even} = \frac{1}{\sqrt{2^N}} \frac{1}{2} \left(\langle \sigma_{kx} \rangle \langle \sigma_{lz} \rangle \langle \sigma_{\mu x} \rangle - \langle \sigma_{ky} \rangle \langle \sigma_{lz} \rangle \langle \sigma_{\mu y} \rangle - \langle \sigma_{kz} \rangle \langle \sigma_{lx} \rangle \langle \sigma_{\mu x} \rangle \right. \\ \left. + \langle \sigma_{kz} \rangle \langle \sigma_{ly} \rangle \langle \sigma_{\mu y} \rangle \right) \quad (86a)$$

$$\tilde{c}_{2,-2,low-ord.}^{\{\kappa,\lambda,\mu\tau_3\}even,(\kappa\lambda)\mu} = \frac{1}{\sqrt{2^N}} \frac{1}{2} \left(\langle \sigma_{kx} \sigma_{lz} \rangle \langle \sigma_{\mu x} \rangle - \langle \sigma_{ky} \sigma_{lz} \rangle \langle \sigma_{\mu y} \rangle - \langle \sigma_{kz} \sigma_{lx} \rangle \langle \sigma_{\mu x} \rangle \right. \\ \left. + \langle \sigma_{kz} \sigma_{ly} \rangle \langle \sigma_{\mu y} \rangle \right) \quad (86b)$$

$$\tilde{c}_{2,-1,class.}^{\{\kappa,\lambda,\mu\tau_3\}even} = \frac{1}{\sqrt{2^N}} \frac{1}{2} \left(-\langle \sigma_{kx} \rangle \langle \sigma_{ly} \rangle \langle \sigma_{\mu y} \rangle + \langle \sigma_{kx} \rangle \langle \sigma_{lz} \rangle \langle \sigma_{\mu z} \rangle + \langle \sigma_{ky} \rangle \langle \sigma_{lx} \rangle \langle \sigma_{\mu y} \rangle \right. \\ \left. - \langle \sigma_{kz} \rangle \langle \sigma_{lx} \rangle \langle \sigma_{\mu z} \rangle \right) \quad (86c)$$

$$\tilde{c}_{2,-1,low-ord.}^{\{\kappa,\lambda,\mu\tau_3\}even,(\kappa\lambda)\mu} = \frac{1}{\sqrt{2^N}} \frac{1}{2} \left(\langle \sigma_{kx} \sigma_{ly} \rangle \langle \sigma_{\mu y} \rangle + \langle \sigma_{kx} \sigma_{lz} \rangle \langle \sigma_{\mu z} \rangle + \langle \sigma_{ky} \sigma_{lx} \rangle \langle \sigma_{\mu y} \rangle \right. \\ \left. - \langle \sigma_{kz} \sigma_{lx} \rangle \langle \sigma_{\mu z} \rangle \right) \quad (86d)$$

$$\tilde{c}_{2,0,class.}^{\{\kappa,\lambda,\mu\tau_3\}even} = \frac{1}{\sqrt{2^N}} \frac{1}{\sqrt{12}} \left(2(\langle \sigma_{ky} \rangle \langle \sigma_{lx} \rangle \langle \sigma_{\mu z} \rangle - \langle \sigma_{kx} \rangle \langle \sigma_{ly} \rangle \langle \sigma_{\mu z} \rangle) - \langle \sigma_{kx} \rangle \langle \sigma_{lz} \rangle \langle \sigma_{\mu y} \rangle \right. \\ \left. + \langle \sigma_{ky} \rangle \langle \sigma_{lz} \rangle \langle \sigma_{\mu x} \rangle + \langle \sigma_{kz} \rangle \langle \sigma_{lx} \rangle \langle \sigma_{\mu y} \rangle - \langle \sigma_{kz} \rangle \langle \sigma_{ly} \rangle \langle \sigma_{\mu x} \rangle \right) \quad (86e)$$

$$\tilde{c}_{2,0,low-ord.}^{\{\kappa,\lambda,\mu\tau_3\}even,(\kappa\lambda)\mu} = \frac{1}{\sqrt{2^N}} \frac{1}{\sqrt{12}} \left(2(\langle \sigma_{ky} \sigma_{lx} \rangle \langle \sigma_{\mu z} \rangle - \langle \sigma_{kx} \sigma_{ly} \rangle \langle \sigma_{\mu z} \rangle) - \langle \sigma_{kx} \sigma_{lz} \rangle \langle \sigma_{\mu y} \rangle \right. \\ \left. + \langle \sigma_{ky} \sigma_{lz} \rangle \langle \sigma_{\mu x} \rangle + \langle \sigma_{kz} \sigma_{lx} \rangle \langle \sigma_{\mu y} \rangle - \langle \sigma_{kz} \sigma_{ly} \rangle \langle \sigma_{\mu x} \rangle \right) \quad (86f)$$

$$\tilde{c}_{2,1,class.}^{\{\kappa,\lambda,\mu\tau_3\}even} = \frac{1}{\sqrt{2^N}} \frac{1}{2} \left(-\langle \sigma_{kx} \rangle \langle \sigma_{ly} \rangle \langle \sigma_{\mu x} \rangle + \langle \sigma_{ky} \rangle \langle \sigma_{lx} \rangle \langle \sigma_{\mu x} \rangle - \langle \sigma_{ky} \rangle \langle \sigma_{lz} \rangle \langle \sigma_{\mu z} \rangle \right. \\ \left. + \langle \sigma_{kz} \rangle \langle \sigma_{ly} \rangle \langle \sigma_{\mu z} \rangle \right) \quad (86g)$$

$$\tilde{c}_{2,1,low-ord.}^{\{\kappa,\lambda,\mu\tau_3\}even,(\kappa\lambda)\mu} = \frac{1}{\sqrt{2^N}} \frac{1}{2} \left(-\langle \sigma_{kx} \sigma_{ly} \rangle \langle \sigma_{\mu x} \rangle + \langle \sigma_{ky} \sigma_{lx} \rangle \langle \sigma_{\mu x} \rangle - \langle \sigma_{ky} \sigma_{lz} \rangle \langle \sigma_{\mu z} \rangle \right. \\ \left. + \langle \sigma_{kz} \sigma_{ly} \rangle \langle \sigma_{\mu z} \rangle \right) \quad (86h)$$

Here, $(\kappa\lambda)\mu$ denotes a bipartitioning of the three qubits denoted by indices κ , λ , and μ into a bilinear (indicated by parentheses) and a linear contribution which is reflected in the applied expectation values of Pauli product operators in the preceding equations. To eliminate all trilinear compound correlations, it is required to consider any possible partitioning of the involved qubits, i.e., $(\kappa\lambda)\mu$, $(\kappa\mu)\lambda$, and $(\lambda\mu)\kappa$.

The non-classically connected correlated density operator of a three-qubit system results in the following expression (Eq. 89). Here, the sets $\mathcal{B} = \{\{1,2\}_{even}, \{1,2\}_{odd}, \{1,3\}_{even}, \{1,3\}_{odd}, \{2,3\}_{even}, \{2,3\}_{odd}\}$ and $\mathcal{T} = \{\{1,2,3 \tau_1\}_{odd}, \{1,2,3 \tau_2\}_{even}, \{1,2,3 \tau_2\}_{odd}, \{1,2,3 \tau_3\}_{even}, \{1,2,3 \tau_3\}_{odd}, \{1,2,3 \tau_4\}_{even}\}$ correspond to the bilinear and trilinear LISA tensor operator subsets and the corresponding beads.

$$\begin{aligned} \rho_{ent} = & \rho - \sum_{\ell'_{bil} \in \mathcal{B}} \sum_{j \in J(\ell'_{bil})} \sum_{m=-j}^j \tilde{c}_{j,m}^{(\ell'_{bil})} T_{j,m}^{(\ell'_{bil})} \\ & - \sum_{\ell'_{tril} \in \mathcal{T}} \sum_{j \in J(\ell'_{tril})} \sum_{m=-j}^j \left(\tilde{c}_{j,m,low-ord.}^{(\ell'_{tril}), (12)3} + \tilde{c}_{j,m,low-ord.}^{(\ell'_{tril}), (13)2} + \tilde{c}_{j,m,low-ord.}^{(\ell'_{tril}), (23)1} - 2\tilde{c}_{j,m,class.}^{(\ell'_{tril})} \right) T_{j,m}^{(\ell'_{tril})} \quad (89) \end{aligned}$$

S8 Asymmetric correlations

In quantum computing, measurements are commonly performed along the z-axis. Other measurement directions, if required by the experiment or algorithm, with Bell tests (see section S22) being a prominent example, are not always directly achievable in some hardware architectures.

In general, the expectation value of a particular measurement is given by the expectation value of a measurement operator M

$$\langle M \rangle = \langle \psi | M | \psi \rangle = \text{Tr}(M\rho) \quad (90)$$

As is shown in section S22, it is always possible to transform the state of the qubits that are to be measured by local rotations such that the intended measurement can be implemented as a z- (or any other fully symmetric) measurement.

Nonetheless, as BEADS is a complete visualization, the question arises how, when being given arbitrary measurement directions for a set of qubits, to deduce $\langle M \rangle$, or the closely related bit parity probability, solely based on the BEADS representation of the qubit system state.

At this point we recall that in case of fully symmetric measurements, i.e., all qubits are measured along the same direction, it is sufficient to directly read off the correlation expectation value from the corresponding fully permutationally symmetric T-Bead (or E-Bead in case of maximally entangled states) along the measurement direction (see Results section). In the following, we show how the BEADS representation can be used to obtain correlation expectation values of asymmetric measurements. ***Note that we present this as a proof of principle rather than a recommended strategy to determine correlations of asymmetric measurements, as alternative approaches such as applying local transformations to perform symmetric measurements are directly and intuitively visualizable in the BEADS representation (see section S22).***

As was pointed out in the Results section, T-Beads which do not correspond to fully permutation symmetric components cannot be interpreted directly. For such beads, the spherical function value along an arbitrary direction generally represents a linear combination of correlation expectation values. For example, the value of the antisymmetric bead $T\{1,2\}_{odd}$ along the z-axis corresponds to $(\langle \sigma_{1x}\sigma_{2y} \rangle - \langle \sigma_{1y}\sigma_{2x} \rangle)/2$, and thus, includes the expectation values of two different combinations of measurement directions. This also implies that because of these multiple contributions, translating the expectation values obtained from such beads to bit parity probabilities (see Results section) is mathematically feasible, yet the resulting values do only have indirect physical implications for distinct projective measurements. Instead, such T-Bead values can be applied in the *calculation* of correlation expectation values of asymmetric measurements, i.e., measurements for which the individual measurement directions do not co-align, which we will show in the following.

For any symmetric or asymmetric combination of measurement directions, we can deduce the correlation expectation value by formulating the measurement operator. In case of a two-qubit measurement of an arbitrary bilinear subsystem $\{k,l\}$ with measurement directions $\vec{r}_k = (r_{kx}, r_{ky}, r_{kz})^T$ corresponding to spherical coordinates (θ_k, ϕ_k) and $\vec{r}_l = (r_{lx}, r_{ly}, r_{lz})^T$ corresponding to (θ_l, ϕ_l) , it is possible to express the corresponding measurement operator $M = \sigma_{kr_k} \sigma_{lr_l}$ in terms of Pauli operators

$$\begin{aligned} M &= (r_{kx}\sigma_{kx} + r_{ky}\sigma_{ky} + r_{kz}\sigma_{kz})(r_{lx}\sigma_{lx} + r_{ly}\sigma_{ly} + r_{lz}\sigma_{lz}) \\ &= r_{kz}r_{lz} \sigma_{kz}\sigma_{lz} + r_{kx}r_{lz} \sigma_{kx}\sigma_{lz} + r_{ky}r_{lz} \sigma_{ky}\sigma_{lz} + \\ &\quad r_{kz}r_{lx} \sigma_{kz}\sigma_{lx} + r_{kx}r_{lx} \sigma_{kx}\sigma_{lx} + r_{ky}r_{lx} \sigma_{ky}\sigma_{lx} + \\ &\quad r_{kz}r_{ly} \sigma_{kz}\sigma_{ly} + r_{kx}r_{ly} \sigma_{kx}\sigma_{ly} + r_{ky}r_{ly} \sigma_{ky}\sigma_{ly} \end{aligned} \quad (91)$$

which can be rewritten in terms of spherical coordinates and unscaled LISA tensor operators

$$\begin{aligned}
M = & \cos \theta_1 \cos \theta_2 \left(\frac{1}{\sqrt{3}} T_{0,0}^{\{k,l\}even} + \frac{2}{\sqrt{6}} T_{2,0}^{\{k,l\}even} \right) + \\
& \sin \theta_1 \cos \phi_1 \cos \theta_2 \left(\frac{1}{\sqrt{2}} T_{2,1}^{\{k,l\}even} - \frac{1}{\sqrt{2}} T_{1,-1}^{\{k,l\}odd} \right) + \\
& \sin \theta_1 \sin \phi_1 \cos \theta_2 \left(\frac{1}{\sqrt{2}} T_{2,-1}^{\{k,l\}even} + \frac{1}{\sqrt{2}} T_{1,1}^{\{k,l\}odd} \right) + \\
& \cos \theta_1 \sin \theta_2 \cos \phi_2 \left(\frac{1}{\sqrt{2}} T_{2,1}^{\{k,l\}even} + \frac{1}{\sqrt{2}} T_{1,-1}^{\{k,l\}odd} \right) + \\
& \sin \theta_1 \cos \phi_1 \sin \theta_2 \cos \phi_2 \left(\frac{1}{\sqrt{3}} T_{0,0}^{\{k,l\}even} - \frac{1}{\sqrt{6}} T_{2,0}^{\{k,l\}even} + \frac{1}{\sqrt{2}} T_{2,2}^{\{k,l\}even} \right) + \\
& \sin \theta_1 \sin \phi_1 \sin \theta_2 \cos \phi_2 \left(\frac{1}{\sqrt{2}} T_{2,-2}^{\{k,l\}even} - \frac{1}{\sqrt{2}} T_{1,0}^{\{k,l\}odd} \right) + \\
& \cos \theta_1 \sin \theta_2 \sin \phi_2 \left(\frac{1}{\sqrt{2}} T_{2,-1}^{\{k,l\}even} - \frac{1}{\sqrt{2}} T_{1,1}^{\{k,l\}odd} \right) + \\
& \sin \theta_1 \cos \phi_1 \sin \theta_2 \sin \phi_2 \left(\frac{1}{\sqrt{2}} T_{2,-2}^{\{1,2\}} + \frac{1}{\sqrt{2}} T_{1,0}^{\{k,l\}odd} \right) + \\
& \sin \theta_1 \sin \phi_1 \sin \theta_2 \sin \phi_2 \left(\frac{1}{\sqrt{3}} T_{0,0}^{\{k,l\}even} - \frac{1}{\sqrt{6}} T_{2,0}^{\{k,l\}even} - \frac{1}{\sqrt{2}} T_{2,2}^{\{k,l\}even} \right) \tag{92}
\end{aligned}$$

We further include the previously introduced BEADS scaling factors for each tensor operator (see section S5) and form the differences $\Delta_\theta = \theta_k - \theta_l$ and $\Delta_\phi = \phi_k - \phi_l$ as well as the sums $\Sigma_\theta = \theta_k + \theta_l$ and $\Sigma_\phi = \phi_k + \phi_l$ of polar and azimuthal angles, respectively. Hence, the measurement operator expectation value $\langle M \rangle$ reads

$$\begin{aligned}
\langle M \rangle = & \langle T_{0,0}^{\{k,l\}even'} \rangle \left[\cos \Delta_\theta \cos^2 \frac{\Delta_\phi}{2} + \cos \Sigma_\theta \sin^2 \frac{\Delta_\phi}{2} \right] + \\
& \langle T_{1,-1}^{\{k,l\}odd'} \rangle \left[\sin \Sigma_\theta \sin \frac{\Delta_\phi}{2} \sin \frac{\Sigma_\phi}{2} - \sin \Delta_\theta \cos \frac{\Delta_\phi}{2} \cos \frac{\Sigma_\phi}{2} \right] + \\
& \langle T_{1,0}^{\{k,l\}odd'} \rangle \left[\frac{\sin \Delta_\phi}{2} (\cos \Sigma_\theta - \cos \Delta_\theta) \right] + \\
& \langle T_{1,1}^{\{k,l\}odd'} \rangle \left[\sin \Delta_\theta \sin \frac{\Sigma_\phi}{2} \cos \frac{\Delta_\phi}{2} + \sin \Sigma_\theta \sin \frac{\Delta_\phi}{2} \cos \frac{\Sigma_\phi}{2} \right] + \\
& \langle T_{2,-2}^{\{k,l\}even'} \rangle \left[\frac{\sin \Sigma_\phi}{2} (\cos \Delta_\theta - \cos \Sigma_\theta) \right] + \\
& \langle T_{2,-1}^{\{k,l\}even'} \rangle \left[\sin \Delta_\theta \sin \frac{\Delta_\phi}{2} \cos \frac{\Sigma_\phi}{2} + \sin \Sigma_\theta \sin \frac{\Sigma_\phi}{2} \cos \frac{\Delta_\phi}{2} \right] + \\
& \langle T_{2,0}^{\{k,l\}even'} \rangle \left[\frac{\cos \Delta_\theta}{2} \left(1 - \frac{\cos \Delta_\phi}{2} \right) + \frac{\cos \Sigma_\theta}{2} \left(1 + \frac{\cos \Delta_\phi}{2} \right) \right] + \\
& \langle T_{2,1}^{\{k,l\}even'} \rangle \left[-\sin \Delta_\theta \sin \frac{\Delta_\phi}{2} \sin \frac{\Sigma_\phi}{2} + \sin \Sigma_\theta \cos \frac{\Delta_\phi}{2} \cos \frac{\Sigma_\phi}{2} \right] + \\
& \langle T_{2,2}^{\{k,l\}even'} \rangle \left[\frac{\cos \Sigma_\phi}{2} (\cos \Delta_\theta - \cos \Sigma_\theta) \right] \tag{93}
\end{aligned}$$

Here, $\langle T_{j,m}^{(\ell')} \rangle$ denotes scaled expectation values of the LISA tensor operator $T_{j,m}^{(\ell')}$ that can be obtained from the corresponding bead. Note that these expectation values are, in general, not to be confused with those of the rotated scaled axial tensor operators $R_{\alpha\beta} \tilde{T}_{j,0}^{(\ell')}$ introduced in section S6 which are applied to reconstruct the entire BEADS representation experimentally. Here, we aim to isolate the individual tensor operator components that, when deduced from the corresponding spherical function, may include further scaling factors specific to the tensor operator order, respectively.

Expectation values of rank $j = 1$ components can be directly obtained by reading off the spherical function values of the antisymmetric bead $T\{k,l\}_{odd}$ along the following Cartesian coordinate axes.

$\langle T_{1,-1}^{\{k,l\}_{odd'}} \rangle$ is given by the value of $T\{k,l\}_{odd}$ along the y-axis, $\langle T_{1,0}^{\{k,l\}_{odd'}} \rangle$ is given by value of $T\{1,2\}_{odd}$ along the z-axis, and $\langle T_{1,1}^{\{k,l\}_{odd'}} \rangle$ is given by the value of $T\{k,l\}_{odd}$ along the x-axis.

To determine the expectation values of all $j = \{0, 2\}$ components, we can take values of the symmetric bead $T\{k,l\}_{even}$ along six angular directions which involve the z-axis $R_z = (0^\circ, 0^\circ)$, the x-axis $R_x = (90^\circ, 0)$, the y-axis $R_y = (90^\circ, 90^\circ)$, the xy-bisecting axis $R_{xy} = (90^\circ, 45^\circ)$, the xz-bisecting axis $R_{xz} = (45^\circ, 0^\circ)$, and the yz-bisecting axis $R_{yz} = (45^\circ, 90^\circ)$.

The scaled tensor operator component expectation values can then be determined by solving the underlying system of equations which yields the solutions:

$$\langle T_{0,0}^{\{k,l\}_{even'}} \rangle = \frac{1}{3}(R_x + R_y + R_z) \quad (94a)$$

$$\langle T_{2,-2}^{\{k,l\}_{even'}} \rangle = R_{xy} - \frac{1}{2}(R_x + R_y) \quad (94b)$$

$$\langle T_{2,-1}^{\{k,l\}_{even'}} \rangle = R_{yz} - \frac{1}{2}(R_y + R_z) \quad (94c)$$

$$\langle T_{2,0}^{\{k,l\}_{even'}} \rangle = \frac{1}{3}(2R_z - R_x - R_y) \quad (94d)$$

$$\langle T_{2,1}^{\{k,l\}_{even'}} \rangle = R_{xz} - \frac{1}{2}(R_x + R_z) \quad (94e)$$

$$\langle T_{2,2}^{\{k,l\}_{even'}} \rangle = \frac{1}{2}(R_x - R_y) \quad (94f)$$

Based on Eq. 93 we can now find expressions of special cases for which the calculation simplifies greatly.

1. Measurements in the transverse (xy) plane

Measuring two qubits in the transverse plane implies that $\theta_1 = \theta_2 = 90^\circ$, $\Delta_\theta = 0^\circ$, and $\Sigma_\theta = 180^\circ$. Thus, Eq. 93 reduces to

$$\begin{aligned} \langle M \rangle = & \cos \Delta_\phi \left(\langle T_{0,0}^{\{k,l\}_{even'}} \rangle - \frac{1}{2} \langle T_{2,0}^{\{k,l\}_{even'}} \rangle \right) - \sin \Delta_\phi \langle T_{1,0}^{\{k,l\}_{odd'}} \rangle + \\ & \sin \Sigma_\phi \langle T_{2,-2}^{\{k,l\}_{even'}} \rangle + \cos \Sigma_\phi \langle T_{2,2}^{\{k,l\}_{even'}} \rangle \end{aligned} \quad (95)$$

2. Measurements in vertical half planes

In the case of two-qubit measurements with measurement directions that span a closed vertical half plane delimited by the z-axis $\phi = \phi_1 = \phi_2$, $\Delta_\phi = 0$, and $\Sigma_\phi = 2\phi$ for which Eq. 93 becomes

$$\begin{aligned} \langle M \rangle = & \cos \Delta_\theta \left(\langle T_{0,0}^{\{k,l\}even'} \rangle + \frac{1}{4} \langle T_{2,0}^{\{k,l\}even'} \rangle \right) + \frac{3 \cos \Sigma_\theta}{4} \langle T_{2,0}^{\{k,l\}even'} \rangle + \\ & \sin \Delta_\theta \left(\sin \phi \langle T_{1,1}^{\{k,l\}odd'} \rangle - \cos \phi \langle T_{1,-1}^{\{k,l\}odd'} \rangle \right) + \\ & \sin \Sigma_\theta \left(\sin \phi \langle T_{2,-1}^{\{k,l\}even'} \rangle + \cos \phi \langle T_{2,1}^{\{k,l\}even'} \rangle \right) + \\ & \frac{\cos \Delta_\theta - \cos \Sigma_\theta}{2} \left(\sin 2\phi \langle T_{2,-2}^{\{k,l\}even'} \rangle + \cos 2\phi \langle T_{2,2}^{\{k,l\}even'} \rangle \right) \end{aligned} \quad (96)$$

In Bell tests (section S22), measurements are commonly implemented such that one qubit is measured along the z-axis ($\theta_1 = 0^\circ$) or x-axis ($\theta_1 = 90^\circ$) while the second qubit is measured along a tilted axis ($\theta_2 = 45^\circ$ or $\theta_2 = 135^\circ$) and $\phi_1 = \phi_2 = 0$ which all corresponds to measurement directions in the xz-half plane. Hence, for measurements in the $(\pm x)z$ -half planes we can further simplify Eq. 96 which gives

$$\begin{aligned} \langle M \rangle = & \cos \Delta_\theta \left(\langle T_{0,0}^{\{k,l\}even'} \rangle + \frac{\langle T_{2,0}^{\{k,l\}even'} \rangle}{4} + \frac{\langle T_{2,2}^{\{k,l\}even'} \rangle}{2} \right) + \\ & \cos \Sigma_\theta \left(\frac{3 \langle T_{2,0}^{\{k,l\}even'} \rangle}{4} - \frac{\langle T_{2,2}^{\{k,l\}even'} \rangle}{2} \right) \pm \\ & \sin \Sigma_\theta \langle T_{2,1}^{\{k,l\}even'} \rangle \mp \sin \Delta_\theta \langle T_{1,-1}^{\{k,l\}odd'} \rangle \end{aligned} \quad (97)$$

Similarly, for measurements in the $(\pm y)z$ -half plane we can simplify Eq. 96

$$\begin{aligned} \langle M \rangle = & \cos \Delta_\theta \left(\langle T_{0,0}^{\{k,l\}even'} \rangle + \frac{\langle T_{2,0}^{\{k,l\}even'} \rangle}{4} - \frac{\langle T_{2,2}^{\{k,l\}even'} \rangle}{2} \right) + \\ & \cos \Sigma_\theta \left(\frac{3 \langle T_{2,0}^{\{k,l\}even'} \rangle}{4} + \frac{\langle T_{2,2}^{\{k,l\}even'} \rangle}{2} \right) \pm \\ & \sin \Sigma_\theta \langle T_{2,-1}^{\{k,l\}even'} \rangle \pm \sin \Delta_\theta \langle T_{1,1}^{\{k,l\}odd'} \rangle \end{aligned} \quad (98)$$

Trilinear correlations, i.e., correlations between three qubits can be determined in an analogue fashion. If one aims to measure three qubits $\{k,l,m\}$ in three independent arbitrary measurement directions $\vec{r}_k = (r_{kx}, r_{ky}, r_{kz})^T$, $\vec{r}_l = (r_{lx}, r_{ly}, r_{lz})^T$, and $\vec{r}_m = (r_{mx}, r_{my}, r_{mz})^T$, the corresponding correlation expectation value can then, based on the BEADS representation of the system state prior to the measurement, be determined by the following equation. Here, using angular directions in terms of spherical coordinates does not provide any benefit with respect to simplifications. Hence, all expressions are given in terms of Cartesian components.

$$\begin{aligned}
\langle M \rangle = & \langle T_{1,-1}^{\{k,l,m \tau_1\}odd'} \rangle \left[\frac{1}{3} (r_{ky}r_{lz}r_{3m} + r_{kz}r_{ly}r_{mz} + r_{kz}r_{lz}r_{my}) + \right. \\
& \left. (r_{ky}r_{lx}r_{mx} + r_{kx}r_{ly}r_{mx} + r_{kx}r_{lx}r_{my}) + r_{ky}r_{ly}r_{my} \right] + \\
& \langle T_{1,0}^{\{k,l,m \tau_1\}odd'} \rangle \left[\frac{1}{3} (r_{kz}r_{lx}r_{mx} + r_{kx}r_{lz}r_{mx} + r_{kx}r_{lx}r_{mz}) + \right. \\
& \left. (r_{kz}r_{ly}r_{my} + r_{ky}r_{lz}r_{my} + r_{ky}r_{ly}r_{mz}) + r_{kz}r_{lz}r_{mz} \right] + \\
& \langle T_{1,1}^{\{k,l,m \tau_1\}odd'} \rangle \left[\frac{1}{3} (r_{kx}r_{lz}r_{mz} + r_{kz}r_{lx}r_{mz} + r_{kz}r_{lz}r_{mx}) + \right. \\
& \left. (r_{kx}r_{ly}r_{my} + r_{ky}r_{ly}r_{mx} + r_{ky}r_{lx}r_{my}) + r_{kx}r_{lx}r_{mx} \right] + \\
& \langle T_{3,-3}^{\{k,l,m \tau_1\}odd'} \rangle \left[(r_{ky}r_{lx}r_{mx} + r_{kx}r_{ly}r_{mx} + r_{kx}r_{lx}r_{my}) - r_{ky}r_{ly}r_{my} \right] + \\
& \langle T_{3,-2}^{\{k,l,m \tau_1\}odd'} \rangle \frac{\sqrt{3}}{2} \left[r_{ky}r_{lx}r_{mz} + r_{kx}r_{ly}r_{mz} + r_{ky}r_{lz}r_{mx} + \right. \\
& \left. r_{kz}r_{ly}r_{mx} + r_{kz}r_{lx}r_{my} + r_{kx}r_{lz}r_{my} \right] + \\
& \langle T_{3,-1}^{\{k,l,m \tau_1\}odd'} \rangle \frac{1}{3} \left[-(r_{ky}r_{lx}r_{mx} + r_{kx}r_{ly}r_{mx} + r_{kx}r_{lx}r_{my}) - 3r_{ky}r_{ly}r_{my} + \right. \\
& \left. 4(r_{ky}r_{lz}r_{mz} + r_{kz}r_{ly}r_{mz} + r_{kz}r_{lz}r_{my}) \right] + \\
& \langle T_{3,0}^{\{k,l,m \tau_1\}odd'} \rangle \frac{1}{2} \left[-(r_{kz}r_{lx}r_{mx} + r_{kx}r_{lx}r_{mz} + r_{kx}r_{lz}r_{mx}) \right. \\
& \left. -(r_{kz}r_{ly}r_{my} + r_{ky}r_{lz}r_{my} + r_{ky}r_{ly}r_{mz}) + 2r_{kz}r_{lz}r_{mz} \right] \\
& \langle T_{3,1}^{\{k,l,m \tau_1\}odd'} \rangle \frac{1}{3} \left[-(r_{kx}r_{ly}r_{my} + r_{ky}r_{lx}r_{my} + r_{ky}r_{ly}r_{mx}) - 3r_{kx}r_{lx}r_{mx} + \right. \\
& \left. 4(r_{kx}r_{lz}r_{mz} + r_{kz}r_{lx}r_{mz} + r_{kz}r_{lz}r_{mx}) \right] + \\
& \langle T_{3,2}^{\{k,l,m \tau_1\}odd'} \rangle \frac{\sqrt{3}}{2} \left[(r_{kz}r_{lx}r_{mx} + r_{kx}r_{lz}r_{mx} + r_{kx}r_{lx}r_{mz}) + \right. \\
& \left. -(r_{ky}r_{ly}r_{mz} + r_{ky}r_{lz}r_{my} + r_{kz}r_{ly}r_{my}) \right] + \\
& \langle T_{3,3}^{\{k,l,m \tau_1\}odd'} \rangle \left[-r_{kx}r_{ly}r_{my} - r_{ky}r_{lx}r_{my} - r_{ky}r_{ly}r_{mx} + r_{kx}r_{lx}r_{mx} \right] + \\
& \langle T_{1,-1}^{\{k,l,m \tau_2\}odd'} \rangle \frac{1+\sqrt{3}}{6} \left[-2(r_{kz}r_{lz}r_{my} + r_{kx}r_{lx}r_{my}) + (r_{ky}r_{lz}r_{mz} + r_{kz}r_{ly}r_{mz}) + \right. \\
& \left. (r_{ky}r_{lx}r_{mx} + r_{kx}r_{ly}r_{mx}) \right] + \\
& \langle T_{1,0}^{\{k,l,m \tau_2\}odd'} \rangle \frac{1+\sqrt{3}}{6} \left[-2(r_{kx}r_{lx}r_{mz} + r_{ky}r_{ly}r_{mz}) + (r_{kz}r_{lx}r_{mx} + r_{kx}r_{lz}r_{mx}) + \right. \\
& \left. (r_{kz}r_{ly}r_{my} + r_{ky}r_{lz}r_{my}) \right] + \\
& \langle T_{1,1}^{\{k,l,m \tau_2\}odd'} \rangle \frac{1+\sqrt{3}}{6} \left[-2(r_{kz}r_{lz}r_{mx} + r_{ky}r_{ly}r_{mx}) + (r_{kx}r_{ly}r_{my} + r_{ky}r_{lx}r_{my}) + \right. \\
& \left. (r_{kx}r_{lz}r_{mz} + r_{kz}r_{lx}r_{mz}) \right] + \\
& \langle T_{2,-2}^{\{k,l,m \tau_2\}even'} \rangle \frac{\sqrt{2}}{3} \left[2(r_{kx}r_{lx}r_{mz} - r_{ky}r_{ly}r_{mz}) - (r_{kx}r_{lz}r_{mx} + r_{kz}r_{lx}r_{mx}) + \right. \\
& \left. (r_{ky}r_{lz}r_{my} + r_{kz}r_{ly}r_{my}) \right] + \\
& \langle T_{2,-1}^{\{k,l,m \tau_2\}even'} \rangle \frac{\sqrt{2}}{3} \left[2(r_{ky}r_{ly}r_{mx} - r_{kz}r_{lz}r_{mx}) - (r_{ky}r_{lx}r_{my} + r_{kx}r_{ly}r_{my}) + \right. \\
& \left. (r_{kz}r_{lx}r_{mz} + r_{kx}r_{lz}r_{mz}) \right] + \\
& \langle T_{2,0}^{\{k,l,m \tau_2\}even'} \rangle \frac{1}{\sqrt{2}} \left[r_{ky}r_{lz}r_{mx} + r_{kz}r_{ly}r_{mx} - (r_{kx}r_{lz}r_{my} + r_{kz}r_{lx}r_{my}) \right] + \\
& \langle T_{2,1}^{\{k,l,m \tau_2\}even'} \rangle \frac{\sqrt{2}}{3} \left[2(r_{kz}r_{lz}r_{my} - r_{kx}r_{lx}r_{my}) - (r_{kz}r_{ly}r_{mz} + r_{ky}r_{lz}r_{mz}) + \right. \\
& \left. (r_{kx}r_{ly}r_{mx} + r_{ky}r_{lx}r_{mx}) \right] + \\
& \langle T_{2,2}^{\{k,l,m \tau_2\}even'} \rangle \frac{\sqrt{2}}{3} \left[-2(r_{ky}r_{lx}r_{mz} + r_{kx}r_{ly}r_{mz}) + (r_{kz}r_{lx}r_{my} + r_{kx}r_{lz}r_{my}) + \right. \\
& \left. (r_{kz}r_{ly}r_{mx} + r_{ky}r_{lz}r_{mx}) \right] +
\end{aligned}$$

$$\begin{aligned}
& \langle T_{1,-1}^{\{k,l,m \tau_3\}odd'} \rangle \frac{1}{\sqrt{2}} [(r_{ky}r_{lz}r_{mz} - r_{kz}r_{ly}r_{mz}) + (r_{ky}r_{lx}r_{mx} - r_{kx}r_{ly}r_{mx})] + \\
& \langle T_{1,0}^{\{k,l,m \tau_3\}odd'} \rangle \frac{1}{\sqrt{2}} [(r_{kz}r_{lx}r_{mx} - r_{kx}r_{lz}r_{mx}) + (r_{kz}r_{ly}r_{my} - r_{ky}r_{lz}r_{my})] + \\
& \langle T_{1,1}^{\{k,l,m \tau_3\}odd'} \rangle \frac{1}{\sqrt{2}} [(r_{kx}r_{lz}r_{mz} - r_{kz}r_{lx}r_{mz}) + (r_{kx}r_{ly}r_{my} - r_{ky}r_{lx}r_{my})] + \\
& \langle T_{2,-2}^{\{k,l,m \tau_3\}even'} \rangle \sqrt{\frac{2}{3}} [(r_{kx}r_{lz}r_{mx} - r_{kz}r_{lx}r_{mx}) + (r_{kz}r_{ly}r_{my} - r_{ky}r_{lz}r_{my})] + \\
& \langle T_{2,-1}^{\{k,l,m \tau_3\}even'} \rangle \sqrt{\frac{2}{3}} [(r_{kx}r_{lz}r_{mz} - r_{kz}r_{lx}r_{mz}) + (r_{ky}r_{lx}r_{my} - r_{kx}r_{ly}r_{my})] + \\
& \langle T_{2,0}^{\{k,l,m \tau_3\}even'} \rangle \frac{1}{\sqrt{6}} [2(r_{ky}r_{lx}r_{mz} - r_{kx}r_{ly}r_{mz}) + (r_{ky}r_{lz}r_{mx} - r_{kz}r_{ly}r_{mx}) - \\
& \quad (r_{kx}r_{lz}r_{my} + r_{kz}r_{lx}r_{my})] + \\
& \langle T_{2,1}^{\{k,l,m \tau_3\}even'} \rangle \sqrt{\frac{2}{3}} [(r_{kz}r_{ly}r_{mz} - r_{ky}r_{lz}r_{mz}) + (r_{ky}r_{lx}r_{mx} - r_{kx}r_{ly}r_{mx})] + \\
& \langle T_{2,2}^{\{k,l,m \tau_3\}even'} \rangle \sqrt{\frac{2}{3}} [(r_{kz}r_{ly}r_{mx} - r_{ky}r_{lz}r_{mx}) + (r_{kz}r_{lx}r_{my} - r_{kx}r_{lz}r_{my})] + \\
& \langle T_{0,0}^{\{k,l,m \tau_4\}even'} \rangle \frac{1}{\sqrt{3}} [(r_{kx}r_{ly}r_{mz} - r_{ky}r_{lx}r_{mz}) + (r_{ky}r_{lz}r_{mx} - r_{kz}r_{ly}r_{mx}) + \\
& \quad (r_{kz}r_{lx}r_{my} - r_{kx}r_{lz}r_{my})] \tag{99}
\end{aligned}$$

Individual scaled expectation values $\langle T_{j,m}^{(\ell')} \rangle$ can again be deduced based on values of the involved beads along specific directions. The $T_{\{k,l,m \tau_1\}odd}$ T-bead is composed of ten different spherical tensor operator components. Hence, we require ten different spherical function values of $T_{\{k,l,m \tau_1\}odd}$ obtained at angular directions $R_z = (0^\circ, 0^\circ)$, $R_x = (90^\circ, 0^\circ)$, $R_{-y} = (90^\circ, 270^\circ)$, $R_{xy} = (90^\circ, 45^\circ)$, $R_{(-x)y} = (90^\circ, 135^\circ)$, $R_1 = \left(\cos^{-1} \sqrt{\frac{3}{5}}, 0^\circ\right)$, $R_2 = \left(\cos^{-1} \left(-\sqrt{\frac{3}{5}}\right), 0^\circ\right)$, $R_3 = \left(\cos^{-1} \sqrt{\frac{3}{5}}, 45^\circ\right)$, $R_4 = \left(\cos^{-1} \left(-\sqrt{\frac{3}{5}}\right), 45^\circ\right)$, and $R_5 = \left(\cos^{-1} \sqrt{\frac{3}{5}}, 135^\circ\right)$ where $\cos^{-1} \sqrt{\frac{3}{5}} \approx 39.23^\circ$ and $\cos^{-1} \left(-\sqrt{\frac{3}{5}}\right) \approx 140.77^\circ$. In principle, the choice of angular directions is arbitrary as long the underlying equations specifying the spherical function values along the chosen directions are linearly independent. We chose directions which correspond to roots of the involved spherical harmonics such that the obtained expressions become as simple as possible. The desired expectation values can then be calculated as:

$$\langle T_{1,-1}^{\{k,l,m \tau_1\}odd'} \rangle = \frac{2}{15} R_x - \frac{2}{5} R_y + \frac{\sqrt{2}}{15} R_{xy} + \frac{\sqrt{2}}{5} R_{(-x)y} + \frac{\sqrt{5}}{6} (R_3 + R_4) - \frac{\sqrt{10}}{12} (R_1 + R_2) \tag{100a}$$

$$\langle T_{1,0}^{\{k,l,m \tau_1\}odd'} \rangle = -\frac{2\sqrt{3}}{15} R_x + \frac{\sqrt{15}}{6} (R_5 - R_4) + \frac{\sqrt{30}}{12} (R_1 + R_2) + \frac{\sqrt{6}}{15} (R_{xy} - R_{(-x)y}) \tag{100b}$$

$$\langle T_{1,1}^{\{k,l,m \tau_1\}odd'} \rangle = \frac{4}{15} R_x + \frac{\sqrt{2}}{5} (R_{xy} - R_{(-x)y}) + \frac{\sqrt{10}}{12} (R_1 + R_2) \tag{100c}$$

$$\langle T_{3,-3}^{\{k,l,m \tau_1\}odd'} \rangle = \frac{1}{2} R_{-y} + \frac{\sqrt{2}}{4} (R_{xy} + R_{(-x)y}) \tag{100d}$$

$$\langle T_{3,-2}^{\{k,l,m \tau_1\}odd'} \rangle = \frac{2}{9} R_x + \frac{\sqrt{2}}{9} (-R_{xy} + R_{(-x)y}) + \frac{5\sqrt{5}}{18} (R_3 - R_5) - \frac{5\sqrt{10}}{36} (R_1 + R_2) \tag{100e}$$

$$\begin{aligned} \langle T_{3,-1}^{\{k,l,m \tau_1\}odd'} \rangle &= \frac{2}{15}R_x + \frac{1}{10}R_y - \frac{11\sqrt{2}}{60}R_{xy} - \frac{\sqrt{2}}{20}R_{(-x)y} + \frac{\sqrt{5}}{6}(R_3 + R_4) \\ &\quad - \frac{\sqrt{10}}{12}(R_1 + R_2) \end{aligned} \quad (100f)$$

$$\begin{aligned} \langle T_{3,0}^{\{k,l,m \tau_1\}odd'} \rangle &= R_z + \frac{2\sqrt{3}}{15}R_x + \frac{\sqrt{15}}{6}(R_4 - R_5) - \frac{\sqrt{30}}{12}(R_1 + R_2) + \\ &\quad \frac{\sqrt{6}}{15}(-R_{xy} + R_{(-x)y}) \end{aligned} \quad (100g)$$

$$\langle T_{3,1}^{\{k,l,m \tau_1\}odd'} \rangle = -\frac{7}{30}R_x + \frac{\sqrt{2}}{20}(-R_{xy} + R_{(-x)y}) + \frac{\sqrt{10}}{12}(R_1 + R_2) \quad (100h)$$

$$\begin{aligned} \langle T_{3,2}^{\{k,l,m \tau_1\}odd'} \rangle &= \frac{2}{9}R_x - \frac{5\sqrt{5}}{18}(R_2 - R_1 - R_4 + R_5) - \frac{5\sqrt{10}}{36}(R_1 + R_2) + \\ &\quad \frac{\sqrt{2}}{9}(-R_{xy} + R_{(-x)y}) \end{aligned} \quad (100i)$$

$$\langle T_{3,3}^{\{k,l,m \tau_1\}odd'} \rangle = \frac{1}{2}R_x + \frac{1}{2\sqrt{2}}(-R_{xy} + R_{(-x)y}) \quad (100j)$$

The expectation values of rank $j = 1$ components of $T\{k,l,m \tau_2\}odd$ or $T\{k,l,m \tau_3\}odd$ can be deduced by directly reading off values along the Cartesian coordinate axes as we previously showed in terms of antisymmetric bilinear correlations.

Rank $j = 2$ component expectation values of $T\{k,l,m \tau_2\}even$ or $T\{k,l,m \tau_3\}even$ can be calculated from the spherical function values at $R_z = (0^\circ, 0^\circ)$, $R_x = (90^\circ, 0^\circ)$, $R_y = (90^\circ, 90^\circ)$, $R_{xy} = (90^\circ, 45^\circ)$, and $R_{xz} = (45^\circ, 0^\circ)$ by the following relations:

$$\langle T_{2,-2}^{\{k,l,m \tau_k\}even'} \rangle = R_{xy} + \frac{1}{2}R_z \quad (101a)$$

$$\langle T_{2,-1}^{\{k,l,m \tau_k\}even'} \rangle = R_{yz} + \frac{1}{2}R_x \quad (101b)$$

$$\langle T_{2,0}^{\{k,l,m \tau_k\}even'} \rangle = R_z \quad (101c)$$

$$\langle T_{2,1}^{\{k,l,m \tau_k\}even'} \rangle = R_{xz} - \frac{1}{2}(R_x + R_z) \quad (101d)$$

$$\langle T_{2,2}^{\{k,l,m \tau_k\}even'} \rangle = R_x + \frac{1}{2}R_z \quad (101e)$$

where $k \in \{2,3\}$. $\langle T_{0,0}^{\{k,l,m \tau_4\}even'} \rangle$ can be directly determined by reading off the value of the corresponding bead along any arbitrary direction.

We stress that the relations discussed in this chapter have been presented as a proof of principle rather than a recommended strategy to determine correlations of asymmetric measurements, as alternative approaches such as applying local transformations to perform symmetric measurements are directly and intuitively visualizable in the BEADS representation (see section S22).

2 Technical details, concepts, and design

S9 BEADS color schemes

The BEADS representation uses two color schemes to represent the different types of information that are contained in a quantum state. In this article, we use a *red-green discontinuous* color scale which features shaded red and green colors to quantify expectation values (and bit parity probabilities in case of fully symmetric contributions) of local single-qubit components, classical correlation or lower-order connected correlations. On the other hand, connected correlations (E-Beads) are represented by a *yellow-blue discontinuous* color scheme. Both scales are shown in Fig. 1, 3 and 5 in the Results section. Note that here we use diverging color schemes which are black for the special case where the corresponding expectation value is $\langle M \rangle = 0$ (or where the related bit parity probability p is 0.5) and which diverge to a bright red or yellow color for the case $\langle M \rangle = 1$ ($p = 0$) and a bright green or blue color for the case $\langle M \rangle = -1$ ($p = 1$).

Indeed, it would be possible to utilize a single uniform color scheme for all correlation components. However, different colorings increase the distinguishability of the visualized information and, in particular, highlight the importance of non-classical connected correlations which occur in entangled states in quantum computing.

The introduced color scales can be chosen to be continuous or discontinuous. By default, we use color scales which are shaded discontinuously despite, at a first glance, using a continuous color scheme theoretically appears to be the best option to faithfully represent the information encoded in a quantum state as expectation values $\langle M \rangle$ can vary continuously between -1 and 1 . However, the human eye is poorly adapted to recognizing subtle differences in color. Hence, to improve the accessibility of the BEADS representation, we intentionally accept the loss of a negligible portion of information that comes with the proposed discontinuity to enable a direct and fast quantitative estimation of relevant numerical information by counting the bands, e.g., between the black band and a color of interest. This is a well-known approach which is commonly applied in the context of contour lines in surface plots or geographic maps.

Alternative color schemes can nonetheless be applied to the BEADS representation without limitations to represent different levels of information and to account for special requirements. We present some additional exemplary continuous and discontinuous color scale variants in Fig. 23. The DROPS color schemes which are adopted from the SpinDrops software (40) are constructed by a simple linear interpolation of red to black to green. Compared to the red-green and yellow-blue discontinuous color scales, color shadings are hard to distinguish for roughly similar expectation values. The same applies to the remaining continuous variants despite using optimized colors to enhance detail perceptibility.

The BEADS representation is not restricted to vivid colors, i.e., all information can also be visualized by using greyscale schemes. Yet, since different nuances of grey are in general harder to distinguish, we consider non-greyscale color schemes as being practically more suitable. However, a very simplistic greyscale color scheme which we denote *black-white high contrast* (and also the full color high contrast analogues *red-green*, *yellow-blue*, *red-blue* and *yellow-green high contrast*) can be used as a possible convenient entry point to the BEADS representation as it allows to visualize a reduced set of information qualitatively which is suited to explain basic concepts and properties with respect to projective measurements, correlations, and symmetries in a simplified manner (see Fig. 24 for an example application). High contrast BEADS representations can also be easily sketched by hand.

We are well-aware that combining red and green color in one color scale (and to a lesser degree yellow and blue) may pose a severe problem for people with color blindness. For such cases, one

can apply shuffled versions of the standard scales which combine red with blue as well as yellow with green, thus, avoiding conflicting colors.

To facilitate the spatial perception of beads as spherical objects, specular and ambient lighting can be optionally applied in the BEADS representation. These lighting methods are used in figures throughout this article.

Using two colormaps to distinguish between correlation types and a correlation separation approach as introduced in supplementary section S7 further allows us to add another layer of information with respect to representing total correlations: As we have shown, e.g., in Fig. 9 (see Results section), any T-Bead (total correlation bead) can be represented such that its color along an arbitrary direction corresponds to the absolute total correlation by its brightness and the ratio between connected to compound correlations by its hue.

In the following, we use the short notations c_E (non-classical connected correlations), c_C (compound correlations) and $c_T = c_E + c_C$ (total correlations) to denote *correlation expectation values* which are obtained by applying Ursell function as explained in section S7. To calculate the T-Bead color along an arbitrary direction, we first determine the correlation component colors Γ_E and Γ_C by reading off the colors from the corresponding color scales at the absolute total correlation expectation value multiplied with the signs of c_E or c_C , i.e., at $\text{sgn}(c_k) \cdot |c_T|$ where $c_k \in \{c_E, c_C\}$. We then blend these two colors, expressed as RGB vectors, based on a blending angle ϑ_{blend} which can be calculated as

$$\vartheta_{blend} = \text{atan} \frac{|c_E|}{|c_C|} \quad (102)$$

The T-Bead vertex color is then given by

$$\Gamma_T = \Gamma_C + \frac{2\vartheta_{blend}}{\pi} (\Gamma_E - \Gamma_C) = \begin{pmatrix} R_C \\ G_C \\ B_C \end{pmatrix} + \frac{2\vartheta_{blend}}{\pi} \left[\begin{pmatrix} R_E \\ G_E \\ B_E \end{pmatrix} - \begin{pmatrix} R_C \\ G_C \\ B_C \end{pmatrix} \right] \quad (103)$$

Following this approach and by applying the default discontinuous color schemes (see Fig. 23), we thus obtain the color wheel shown in Fig. 25 that specifies a unique color for any possible combination of correlation components and where the radius from the center corresponds to the absolute total correlation. Moreover, the horizontal and vertical diameters correspond to the original unblended color scales, respectively. Note that here, we use the correlation angle $\phi_{corr} = \text{atan} \frac{c_E}{c_C}$ to describe the ratio between the correlation components. Plotting ϕ_{corr} against the total correlation further illustrates that the total correlation sign changes at $\phi_{corr} = 3\pi/4 = 135^\circ$ and $\phi_{corr} = 7\pi/4 = 315^\circ$. For these values, $c_E = -c_C$, and thus, $c_T = 0$ which implies that such combinations of correlation components will always be represented by black color independent of the magnitudes of c_E and c_C . Based on these findings one may further infer that not all depicted colors and the underlying combinations of correlations are physically reachable. However, we show the full color wheel to clarify the construction.

Knowing the ratios between compound to connected correlations, we can also extract corresponding characteristic color scales as diameters of the color wheel (see Fig. 25) in the angular direction specified by ϕ_{corr} . Fig. 26 shows some color scales for different ratios of correlation components ($c_E : c_C$).

To further clarify the method, we provide an exemplary visualization of a Schmidt form state (corresponding to a Schmidt angle $\theta = \pi/4$) in Fig. 27 that illustrates the construction in detail. Here, $c_C = c_E = 0.5$, and thus, $c_T = 1.0$. First, we pick the compound correlation color Γ_C at $\text{sgn}(c_C) \cdot |c_T|$ from the red-green discontinuous and the non-classical connected correlation color Γ_E at $\text{sgn}(c_E) \cdot |c_T|$ from the yellow-blue discontinuous color scale. Both colors are then blended according to Eq. 103 by using the mixing angle $\vartheta_{blend} = \text{atan}(1) = \pi/4 = 45^\circ$ which gives the correlation color Γ_T .

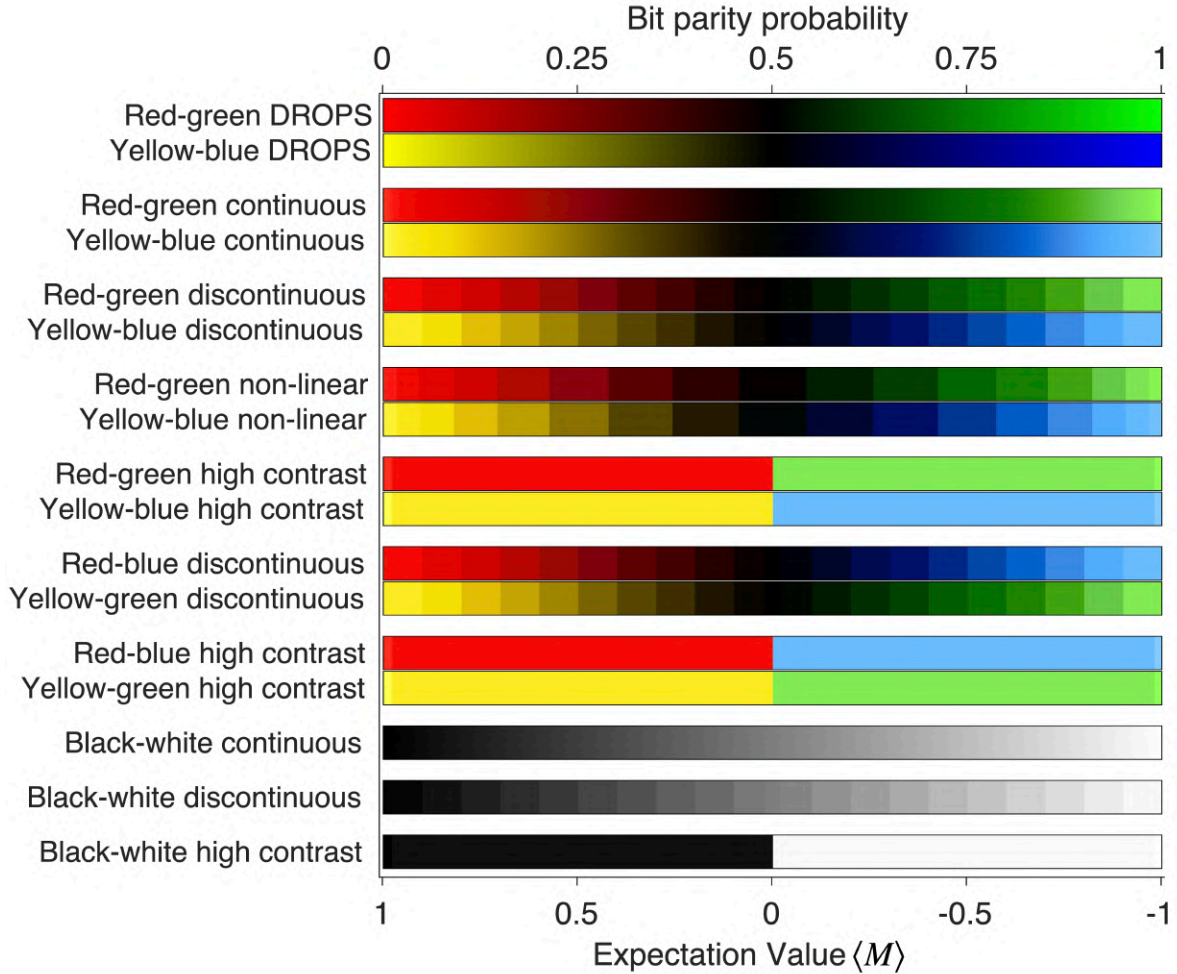


Fig. 23. BEADS color scheme variants. Color scales which are intended to be used jointly are shown in pairs. The DROPS scales refer to the color scheme used in SpinDrops (40). The scales are given in terms of bit parity probabilities and expectation values. For discontinuous color schemes, each color increment covers a range of 0.1. The non-linear color scheme, results in equiangular color increments in case of Q-Beads. For each pair of color scales, the upper scheme corresponds to single-qubit and compound correlations, whereas the lower color scheme encodes for entanglement-associated connected correlations. All color scales which are not continuous use special slightly brighter colors for expectation values $\langle M \rangle \approx \pm 1$. In addition, high contrast color scales are grey (black-white high contrast) or black (all remaining high contrast scales) for values $\langle M \rangle \approx 0$.

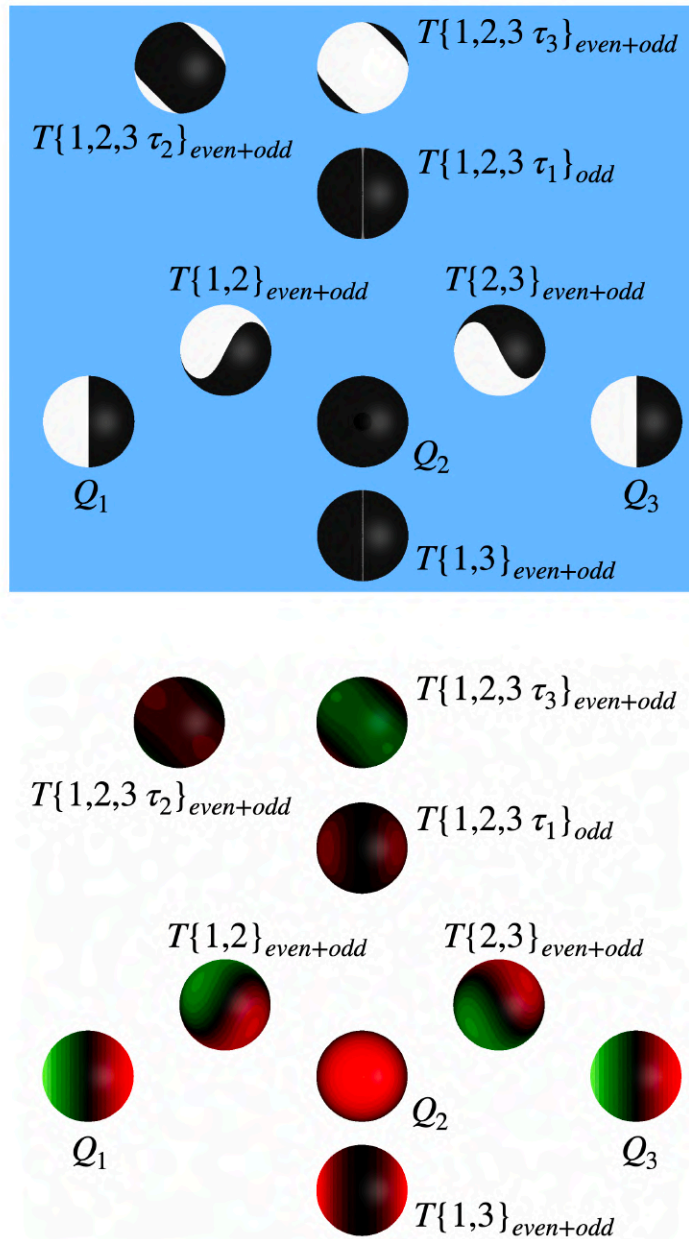


Fig. 24. High contrast color scheme representation of a three-qubit state. High contrast color schemes such as the black-white high contrast scheme used in the visualization of the fully separable state $|+ 0 +\rangle = 1/2(|000\rangle + |001\rangle + |100\rangle + |101\rangle)$ (top) are useful in providing a clear overview of patterns and orientations of the involved beads. It is also easy to sketch by hand. The visualizations are given in terms of total correlations which are purely classical due to the separability of the state. Unlike in the standard BEADS visualization, we combined beads of even and odd symmetries of the same subsets (which in this case is possible as the combined correlation expectation values still lie between -1 and 1 and thus, the color schemes remain applicable) to reveal more elaborate surface patterns which are highly recognizable in the high contrast picture. For comparison, the same state is visualized using the standard red-green discontinuous color scheme (bottom).

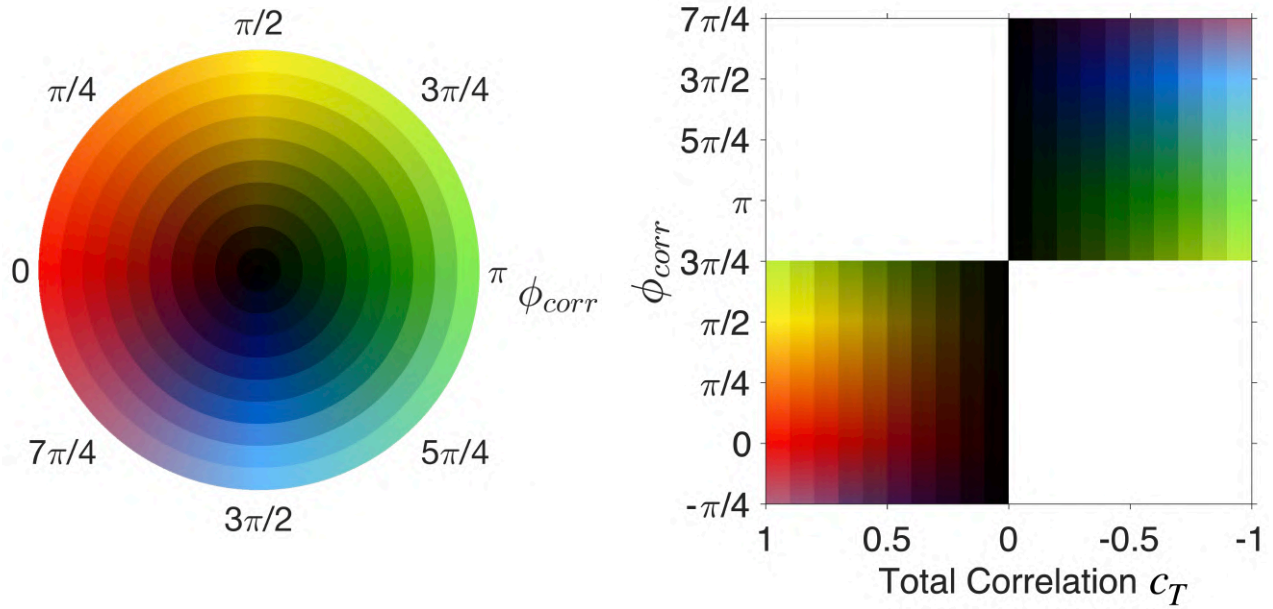


Fig. 25. Total correlation BEADS color wheel (left) and ϕ_{corr} vs. c_T 2D plot (right). In the color wheel, the magnitude of the total correlation corresponds to the radius from the center and the ratio of the individual correlation components determines the angular direction ϕ_{corr} in which to read off the color. The connected and compound correlation color scales are given by the vertical and horizontal diameters of the color wheel, respectively. Plotting ϕ_{corr} against c_T illustrates two special cases at $3\pi/4 = 135^\circ$ and $7\pi/4 = 315^\circ$ where the total correlation is always zero due to the components c_T and c_E having the same magnitudes but opposite signs.

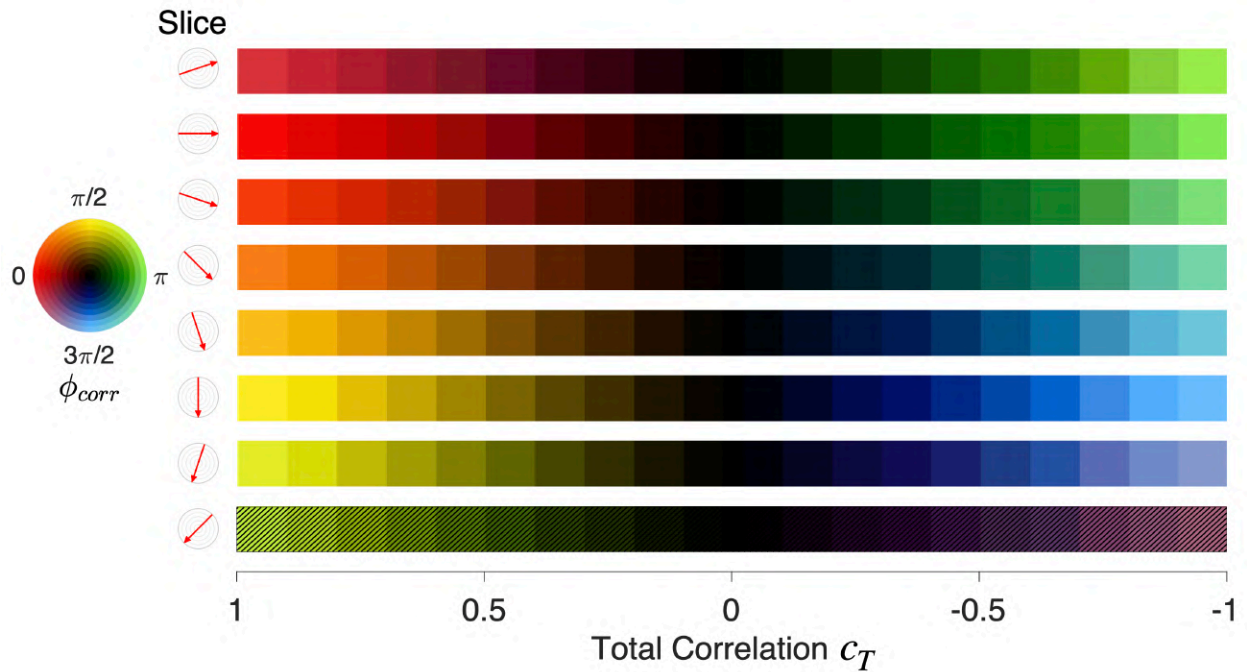


Fig. 26. Total correlation color scales for different ratios of correlation compounds. All color scales correspond to diametric slices of the color wheel (left) at specific angular directions indicated by arrows, respectively. The displayed cases, from top to bottom, comprise correlation component ratios $c_E : c_C$ of $(-1):3$, $0:1$, $1:3$, $1:1$, $3:1$, $1:0$, $3:(-1)$, and $1:(-1)$. Note that for the last scale, all colors except black are physically unreachable ($c_T = 0$) which is indicated by a hatching.

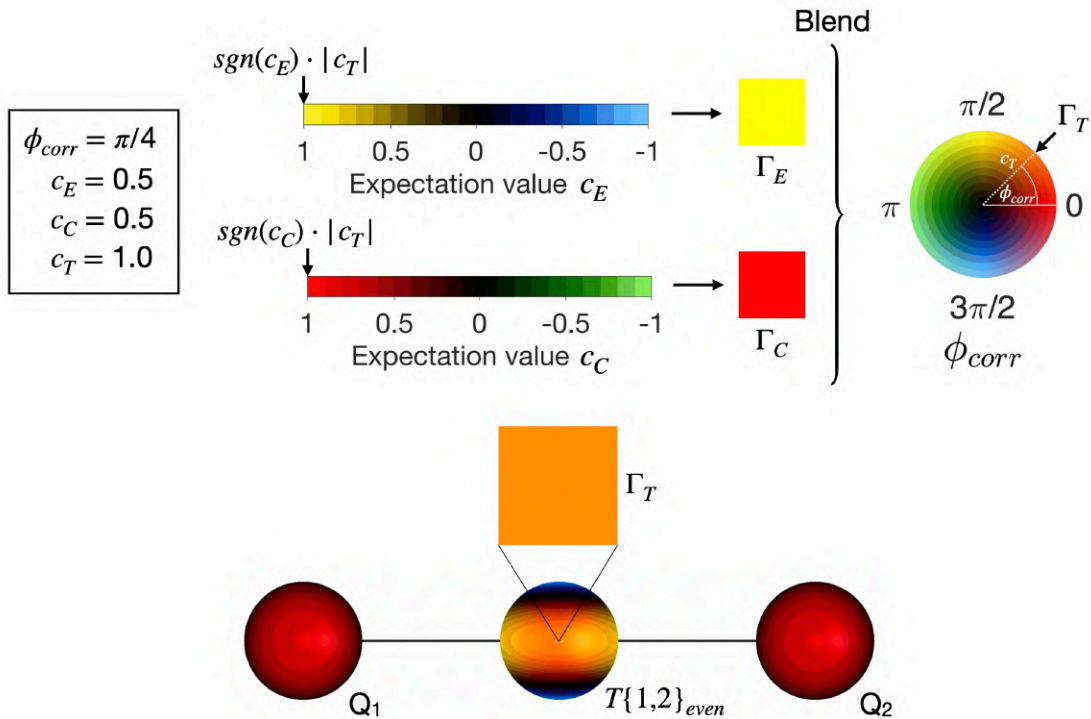


Fig. 27. Total correlation color generation in the BEADS representation. In the BEADS representation of the state $|\psi\rangle = \cos(\pi/8)|00\rangle + \sin(\pi/8)|11\rangle$, we determine the bilinear total correlation color Γ_T along the z -axis by picking colors Γ_E and Γ_C from the basic color scales at $sgn(c_k) \cdot |c_T|$, where sgn is the sign function and $c_k \in \{c_E, c_C\}$, which are then blended as described by Eq. 103.

S10 Further simplifications and plotting variants

In the Results section, we provided an overview of simplifications which can be made to reduce the amount of information while providing sufficient insights into aspects of interest. In Table 5, among the simplifications which have been introduced in Fig. 9 of the main text, we summarize the *display types* A to J, which are also shown in Fig. 28 for the case of a two-qubit system. The most important display types A, B, F, and H are indicated by bold face letters in Table 5.

Instead of using the introduced total correlation color wheel (see Fig. 25) to indicate the ratio of connected and compound correlations in every spatial direction (A), it is always possible to just use a single color scheme, e.g., the red-green scheme to represent Q-Beads and total correlations (B). Clearly, this still allows to predict measurement outcomes without limitations, however, there is no visual indication on entanglement-related correlations.

As is the standard approach used in the DROPS representation (37) beads of different point symmetries corresponding to the same subsystem (and permutation symmetry τ -sublabel) can always be combined to create a more compact display as is shown for the display types C, E, and G. This reduces the number of beads while the displayed information remains complete. However, in this case it is not sufficient to view the representation from a single perspective, as, for spherical functions of undefined point symmetry, it is not possible to make assertions about the function values on the hidden hemisphere. This display type (C, E, G) is also disadvantageous in that it does generally not allow a uniform interpretation of the introduced BEADS color schemes. This is because the individual beads are designed such that the spherical function values are bounded (in terms of expectation values) representation $-1 \leq b^{(\ell')}(\theta, \phi) \leq 1$ and by summing up multiple beads of different point symmetries, these bounds may well be exceeded, thus requiring extended color scales. In addition, components of different permutation symmetries are combined. For instance, the permutation-symmetric and antisymmetric bilinear components combine which does impede the direct outcome prediction of symmetric two-qubit measurements.

If correlations are not of particular interest, it is further possible to omit any correlation bead but to include the entanglement arc to indicate the magnitude (norm) of entanglement-related correlation components. It is clear, that this approach does by no means provide complete information, however, it is sufficient to indicate whether a pure state is entangled while providing a detailed representation of single-qubit components (I).

At this point, we shall also discuss alternative plotting variants of the BEADS representation which go beyond the introduced methods (plot on the surface of a sphere or plot with absolute function value as radius from origin). Indeed, as is shown in Fig. 29, it is also possible to plot the normalized spherical function on a sphere, that is, the original spherical function scaled such that the maximum absolute function (expectation) value becomes 1. The norm of the density operator component $\rho^{(\ell')} = \sum_{j \in J(\ell')} \sum_{m=-j}^j c_{j,m}^{(\ell')} T_{j,m}^{(\ell')}$ corresponding to a bead $b^{(\ell')}$ can then be represented by the radius r or the volume of the sphere on which the normalized function is plotted, i.e., the sphere radius is given by

$$r = \|\rho^{(\ell')}\| = \sqrt{\text{Tr}(\rho^{(\ell')}\rho^{(\ell')})} \quad (104)$$

or

$$r = \sqrt[3]{\frac{3}{4\pi} \|\rho^{(\ell')}\|} = \sqrt[3]{\frac{3}{4\pi} \sqrt{\text{Tr}(\rho^{(\ell')}\rho^{(\ell')})}} \quad (105)$$

This is advantageous in that it always ensures the appearing colors to have full brightness at the maximum absolute function value which would eventually result in darker colors in the standard BEADS plotting approach. However, this renormalization of spherical function values prevents a direct interpretation of the color, i.e., a color cannot be directly assigned to a specific expectation value or bit parity probability without further considering the sphere radius on which the function is plotted on.

Table 5: Overview and classification of BEADS display variants. The display types in bold face **A**, **B**, **D**, **F**, and **H** are most commonly used. All variants are classified with respect to the displayed types of beads, auxiliary elements (entanglement arcs), colors, symmetries, and the completeness of the representation.

Display type	Beads				Ent. arc	Colors	Point sym.	Perm. sym.	Completeness	Figure
	Q	T	E	C						
A	✓	✓	–	–	✓	⊗	$e \leftrightarrow o$	$s \leftrightarrow a, \tau$	✓	9A, 28A
B	✓	✓	–	–	✓	○	$e \leftrightarrow o$	$s \leftrightarrow a, \tau$	✓	28B
C	✓	✓	–	–	✓	⊗	$e + o$	$s + a, \tau$	✓	28C
D	✓	–	✓	✓	✓	⊙	$e \leftrightarrow o$	$s \leftrightarrow a, \tau$	✓	9B, 28D
E	✓	–	✓	✓	✓	⊙	$e + o$	$s + a, \tau$	✓	28E
F	✓	–	✓	–	✓	⊙	$e \leftrightarrow o$	$s \leftrightarrow a, \tau$	✓	9C, 28F
G	✓	–	✓	–	✓	⊙	$e + o$	$s + a, \tau$	✓	28G
H	✓	–	✓	–	✓	⊙	$e \parallel o$	S	–	9D, 28H
I	✓	–	–	–	✓	○	o	–	–	28I
J	✓	–	–	–	–	○	o	–	–	9E, 28J

Legend:

- ⊗ Full total correlation color scheme (see section S9)
 - ⊙ Separate color schemes for Q-Beads and compound correlations (red-green), and connected correlations (yellow-blue)
 - Simple red-green color scheme
- $e \leftrightarrow o$ Separate display of even and odd spherical function point reflection symmetry
 $e + o$ Combined display of even and odd spherical function point reflection symmetry
 $e \parallel o$ Either even or odd point reflection symmetry display in dependence of linearity
 o Odd point reflection symmetry only
- $s \leftrightarrow a$ Separate display of bilinear permutationally symmetric and antisymmetric components
 $s + a$ Combined display of bilinear permutationally symmetric and antisymmetric components
 τ Separate display of τ permutation symmetries
S Totally permutation symmetric components only (e.g., corresponding to bilinear beads of even or trilinear τ_1 -beads of odd point reflection symmetry)

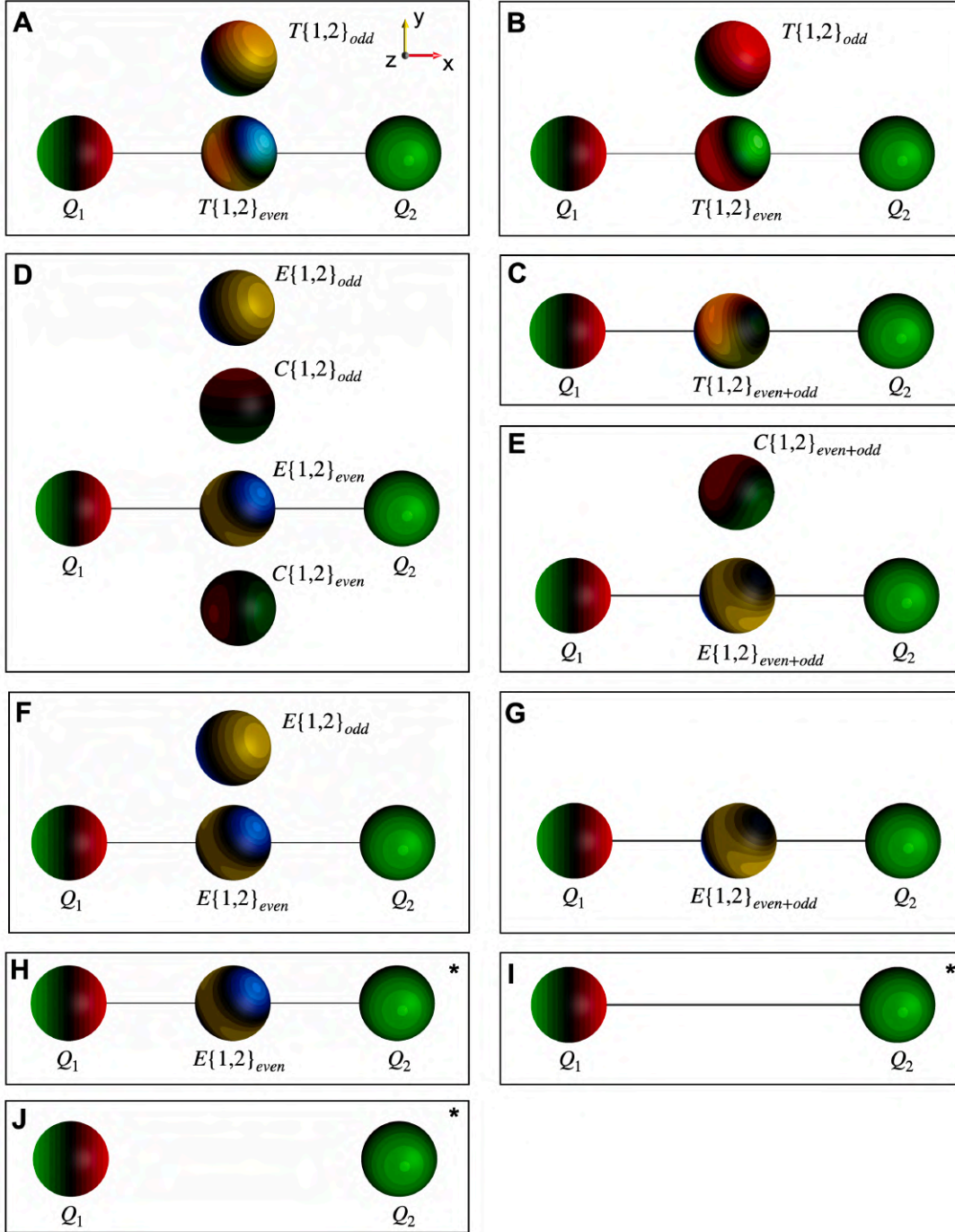


Fig. 28. Extended overview of BEADS variants. Possible variants of BEADS representations of quantum states (here, $|\psi\rangle = (-0.099893 + 0.207263i, 0.664132 - 0.077408i, -0.015899 - 0.323055i, 0.616169 - 0.125371i)^T$) include (A) total correlations with symmetry separation, (B) total correlations with symmetry separation using a single color scheme, (C) total correlations with combined symmetries, (D) separate correlations with full symmetry separation or (E) combined symmetries, (F) connected correlations with full symmetry separation or (G) combined beads, (H) fully permutation symmetric connected correlations, (I) no correlation beads with or (J) without entanglement arcs. Variants A-G all carry the full information required to reconstruct the density operator if the colors of *all* surface points can be accessed. If the beads are shown only

from one perspective, e.g., in the displayed top view, the variants with symmetry separation (A, B, D, and F) still make it possible to reconstruct the density operator because the information on the hidden hemisphere can be recovered due to the defined spherical function point symmetries of the beads (see section S2). The display variants H-J are marked with an asterisk to indicate that they only provide incomplete information about the density operator.

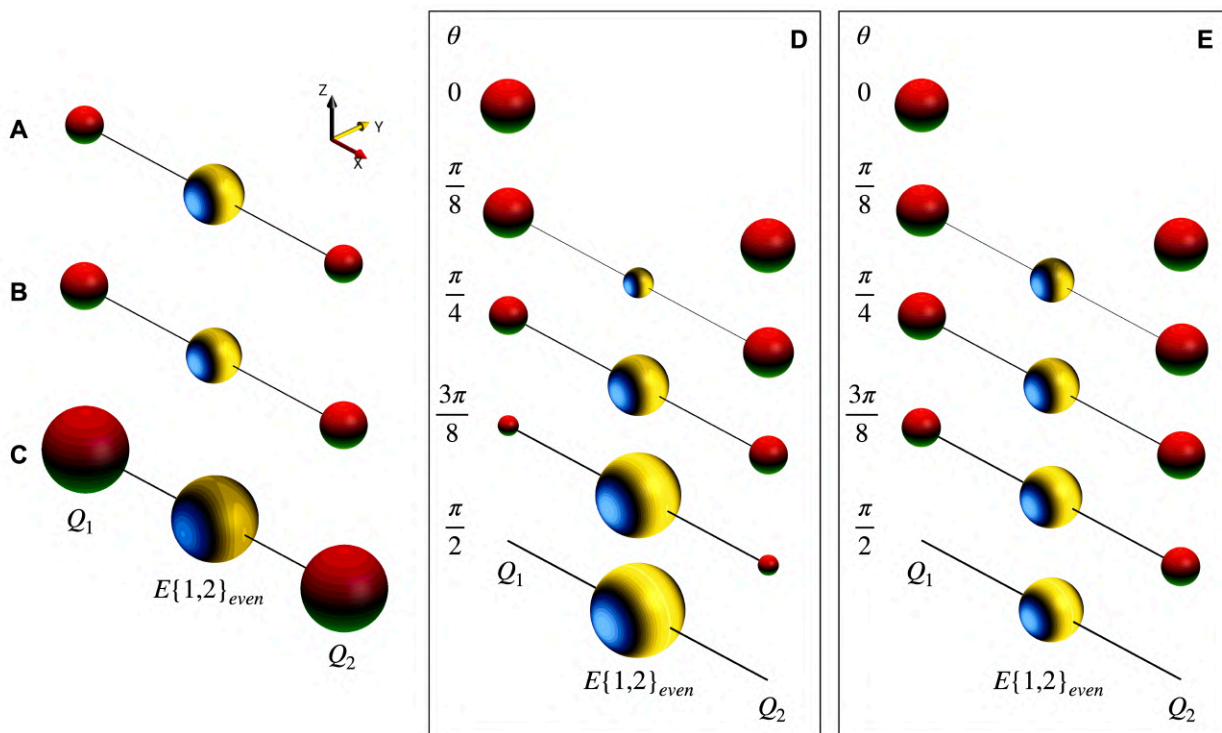


Fig. 29. BEADS representation plotting variants. Variants of the BEADS representation involve plotting of the spherical functions on spheres with radii corresponding to (A) the norm of the visualized density operator component or (B) chosen such that the sphere volume is equivalent to the density operator component norm. Unlike in the standard plotting method (C), both methods involve a normalization of spherical function values such that the maximum absolute value becomes 1, thus achieving full brightness of colors. For comparison with the previously introduced plotting methods (see Fig. 37 and Fig. 38 in section S14), Schmidt form states $|\psi_\theta\rangle = \cos \theta/2 |00\rangle + \sin \theta/2 |11\rangle$ are visualized by using (D) radii calculated according to Eq. 104 and (E) according to Eq. 105.

3 Comparison and classification

S11 Interpretation of the BEADS representation as a generalization of the Husimi function

As was briefly mentioned in the main text (see Results section), the BEADS representation can be viewed as a generalized Husimi function (20). A quantum state $|\psi\rangle$ (or its corresponding density operator ρ) can be represented by the Husimi function \mathcal{H} (avoiding the generally used symbol Q to prevent confusion with Q-Beads in the following) which is defined for arbitrary spatial directions (θ, ϕ) as (69, 70)

$$\mathcal{H}(\theta, \phi) = |\langle s(\theta, \phi) | \psi \rangle|^2 = \langle s(\theta, \phi) | \rho | s(\theta, \phi) \rangle \quad (106)$$

Note that for simplicity of calculation, this definition omits the originally introduced normalization by an additional factor $1/\pi$ (20) which is required to achieve normalization with respect to integration. Hence, for distinguishable particles such as qubits, \mathcal{H} is the expectation value with respect to separable coherent states $|s(\theta, \phi)\rangle$. In an N -qubit system, $|s(\theta, \phi)\rangle$ represent the subset of separable states for which all Bloch vectors co-align in spatial directions (θ, ϕ) , that is,

$$|s(\theta, \phi)\rangle = \left[\cos \frac{\theta}{2} |0\rangle + \sin \frac{\theta}{2} e^{i\phi} |1\rangle \right]^{\otimes N} \quad (107)$$

By definition, \mathcal{H} is non-negative and upper-bounded for quantum states, i.e., $0 \leq \mathcal{H}(\theta, \phi) \leq 1$. It is possible to show that the BEADS representation can be interpreted as a generalized Husimi function by a simple relation between \mathcal{H} and the beads spherical functions $b^{(\ell')}$.

The Husimi function \mathcal{H} is indeed obtained as the scaled sum of the identity operator bead $b^{\{\emptyset\}}$, all Q-Beads $b^{\{k\}}$ and all totally permutation symmetric total correlation beads $b_T^{(\ell'_{sym})}$, where ℓ'_{sym} denotes sets which correspond to full permutation symmetry. For instance, for systems consisting of $N=2$ and $N=3$ qubits, Husimi functions \mathcal{H}_N are given by

$$\mathcal{H}_2 = \frac{1}{4} (b^{\{\emptyset\}} + b^{\{1\}} + b^{\{2\}} + b^{\{1,2\}_{even}}) = \frac{1}{4} (\emptyset + Q_1 + Q_2 + T\{1,2\}_{even}) \quad (108)$$

$$\begin{aligned} \mathcal{H}_3 &= \frac{1}{8} (b^{\{\emptyset\}} + b^{\{1\}} + b^{\{2\}} + b^{\{3\}} + b_T^{\{1,2\}_{even}} + b_T^{\{1,3\}_{even}} + b_T^{\{2,3\}_{even}} + b_T^{\{1,2,3\}_{\tau_1}_{odd}}) \\ &= \frac{1}{8} (\emptyset + Q_1 + Q_2 + Q_3 + T\{1,2\}_{even} + T\{1,3\}_{even} + T\{2,3\}_{even} + T\{1,2,3\}_{\tau_1}_{odd}) \end{aligned} \quad (109)$$

In the above relations, spherical function values of beads are interpreted as expectation values ($-1 \leq b^{(\ell')}(\theta, \phi) \leq 1$).

It is immediately clear, that the Husimi \mathcal{H} representation of a quantum state hence only captures the identity operator, single-qubit, and the permutationally symmetric components of a density operator. In contrast, the BEADS representation provides a separation of these components and further includes components corresponding to other permutation symmetries thus generalizing the function \mathcal{H} .

In Fig. 30, we provide a comparison of various states visualized by the standard BEADS and the Husimi \mathcal{H} representations which illustrates the equivalence of \mathcal{H} and the linear combinations of beads introduced in Eq. 108 and 109. It is obvious, that asymmetric density operators result in Husimi representations with small numeric values as non-permutation-symmetric components are neglected.

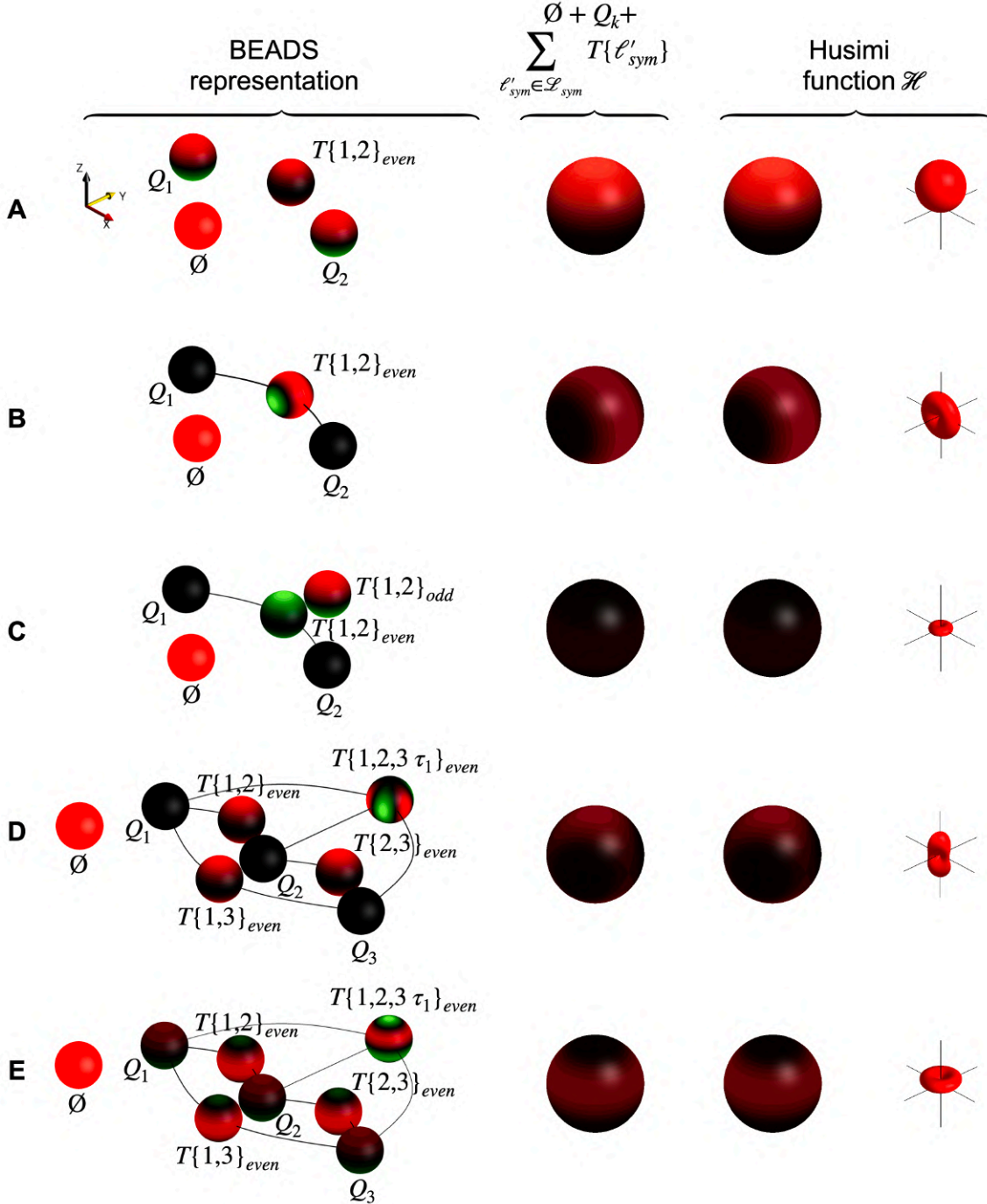


Fig. 30. The Husimi function corresponds to a linear combination of beads. Combining the identity bead, all Q-Beads, and all fully permutation symmetric T-Beads of a state gives the Husimi representation (by suitable rescaling, see Eq. 108 and 109). Using a single colorscheme (red-green discontinuous), the BEADS and Husimi representations (calculated based on Eq. 106, 108, and 109) of (A) $|00\rangle$, (B) $|\Phi^+\rangle = 1/\sqrt{2}(|00\rangle + |11\rangle)$, (C) $|\psi\rangle = 1/\sqrt{2}(|01\rangle - i|10\rangle)$, (D) $|GHZ\rangle = 1/\sqrt{2}(|000\rangle + |111\rangle)$, and (E) $|W\rangle = 1/\sqrt{3}(|001\rangle + |010\rangle + |100\rangle)$ are visualized for comparison. The absolute function value is plotted as distance from the origin in the rightmost column to improve the visibility of small function values such as in the highly antisymmetric case (C).

S12 Comparison with other representations

A detailed evaluation of various quantum mechanical representations with respect to different criteria which complements the Discussion section in the main text is given in Table 6. The assessed visualizations comprise the BEADS, DROPS (37), PROPS (71), Bloch vector (6,7), dimensional circle notation (52), and the Qiskit implementations of cityscape plots (51) as well as the Q-Sphere (51).

Fig. 31 is an extended version of Fig. 4 (see Results section) which includes additional visualizations such as standard state vectors and dimensional circle notations (52) as well as the imaginary part cityscape plots which were omitted in the main text.

In Fig. 32 we illustrate the equivalence of Q-Beads and Bloch vectors. Here, it is obvious that the Bloch vector strictly points to the red pole of the Q-Bead. However, Q-Beads prove to be easily interpretable in terms of expectation values and measurement probabilities independent of the viewing perspective. Indeed, this is not the case for Bloch vectors which are virtually indistinguishable when the view direction is parallel or anti-parallel to the Bloch vector. More importantly, in order to correctly determine the components of a Bloch vector in a straightforward fashion, which is required for determining single-qubit expectation values, the view direction must be orthogonal to the Bloch vector components of interest. In the BEADS representation, this is independent of the perspective.

As the BEADS representation is a derivative of the DROPS representation (37) and both visualizations may appear the same at first glance, we provide a detailed comparison in Fig. 33 which demonstrates important differences between the representations. DROPS, which are defined such that the integral over the spherical functions is normalized, can be described as a generalized Wigner function. While the DROPS representation can reveal symmetry properties of a visualized operator or reveal basic rotations, compared to BEADS, it does not provide direct quantitative information on entanglement-related correlations, or in general, correlations and hence it is significantly less useful for understanding gates or algorithms in quantum information.

Correlation matrix visuals (CMVs) as introduced by Mukherjee et al. (49) and applied in (50) yield visualizations of symmetric non-classical connected two-qubit (the concept can be extended to more qubits) correlations which, at first glance, look very similar to corresponding BEADS representations (plotted with absolute spherical function values as distance from the origin). However, the construction protocol of CMVs involves the generation of volumetric data from a connected correlation tensor (49)

$$Q(C_{ij}, r) = r^T C_{ij} r \quad (110)$$

and the corresponding quadratic form (49)

$$Q_f(C_{ij}, r) = \frac{Q(C_{ij}, r)}{(1 + r^2)^{3/2}} \quad (111)$$

based on which the visualization is obtained as an isosurface (level set) at arbitrarily chosen isovalues P , i.e., the surface at which $Q_f(C_{ij}, r) = P$ (in (49) the proposed values of are $P = \pm 0.01$). While this choice prohibits uniqueness of the representation in the first place, the distance of the CMV surface to the origin is only an approximation and is only proportional to permutation symmetric connected correlation components but does not provide a direct map of the numerical correlation coefficients which would allow to directly read off the correlation expectation values or related bit parity probabilities as is possible for fully symmetric components in the BEADS representation. In addition, CMVs commonly do not provide a faithful

representation of the visualized correlations in proximity to the origin, i.e., the CMV, depending on the choice of the level set and the overall size of the correlation, may not cover regions where the correlation adopts values close to zero, which leads to gaps between the CMV lobes, and thus, the correlation represented by the CMV is undefined in certain directions. We provide a visual comparison of BEADS and CMVs in Fig. 34.

	Quantum BEADS representation (QuBeads app)	DROPS representation (SpinDrops app)	PROPS representation	Bloch vector representation (e.g. in QuBeads app)	Cityscape plot of density operator (Qiskit)	Q-Sphere (Qiskit)	Dimensional circle notation
Visualization is <ul style="list-style-type: none"> - general - accurate - complete - adaptable with respect to balance of completeness vs. simplicity - interactive/responsive - easy to interpret 	●●●●●●	●●●●○●	●●●●○●	○●●●●●	●●●●○●	●●●●○●	●●●●○● (a)
Applicable to <ul style="list-style-type: none"> - single qubit system - two qubit system - three or more qubit systems - pure states - mixed states 	●●●●●●	●●●●●●	●●●●●●	●●●●●●	●●●●●●	●●●●○●	●●●●○●
Directly visualizes <ul style="list-style-type: none"> - spatial orientation of qubits - spatial orientation of entanglement-based correlations - rotations of qubits and entanglement-based correlations - direction-dependent expectation values - probabilities of measurement outcomes - reduced single qubit density operator - entanglement of (sub) set of qubits - compound correlations of (sub) set of qubits - total correlations of (sub) set of qubits - type and amount of entanglement/correlations - spatial symmetries of states - permutational symmetry of states - global phase 	●●●●●●●●●●	●●●●○●●●	○●●●○●●●	●●●●○●●●	○ (b)	○ (b)	○ (b)
Didactically valuable to clearly <ul style="list-style-type: none"> - visualize a seamless transition from bit to qubit - see single-qubit gates as rotations - see effect of non-selective single qubit gates on entanglement-based correlations as rotation - see the effect of projective measurements - visualize simultaneously the full range of possible measurement outcomes 	●●●●●●	○●●●○●	○●●●○●	○●●●○●	○●●●○●	○●●●○●	○●●●○●
Is useful for <ul style="list-style-type: none"> - understanding of quantum gates - design of quantum gates - analysis of quantum algorithms - design of quantum algorithms - prediction of measurement probabilities 	●●●●○●	○●●●○●	○●●●○●	○●●●○●	○●●●○●	○●●●○●	●●●●○●
Can be augmented by <ul style="list-style-type: none"> - also displaying numerical values - creation of tangible 3D models 	●●	○●	○●	●●	○●	●●	○●
Can be used for <ul style="list-style-type: none"> - outreach to general public - education of high-school students - education of bachelor and master students - research in quantum information processing 	●●●●●●	○●●●○●	○●●●○●	○●●●○●	○●●●○●	○●●●○●	○●●●○●

(a) The authors are not aware of a publicly available software tool that automates the visualization of the dimensional circle notation representation.
(b) Limited to the probability to obtain each computational basis state.
(c) The global phase of a state in the Q-Sphere representation is eliminated for simplicity in the current Qiskit version but could easily be shown by adapting the program accordingly.

Table 6. Evaluation of various representations designed for the visualization of quantum mechanics. Representations either fully meet a criterion (black dots), partially meet a criterion (black circles with white filling) or do not meet a criterion (light gray circle).

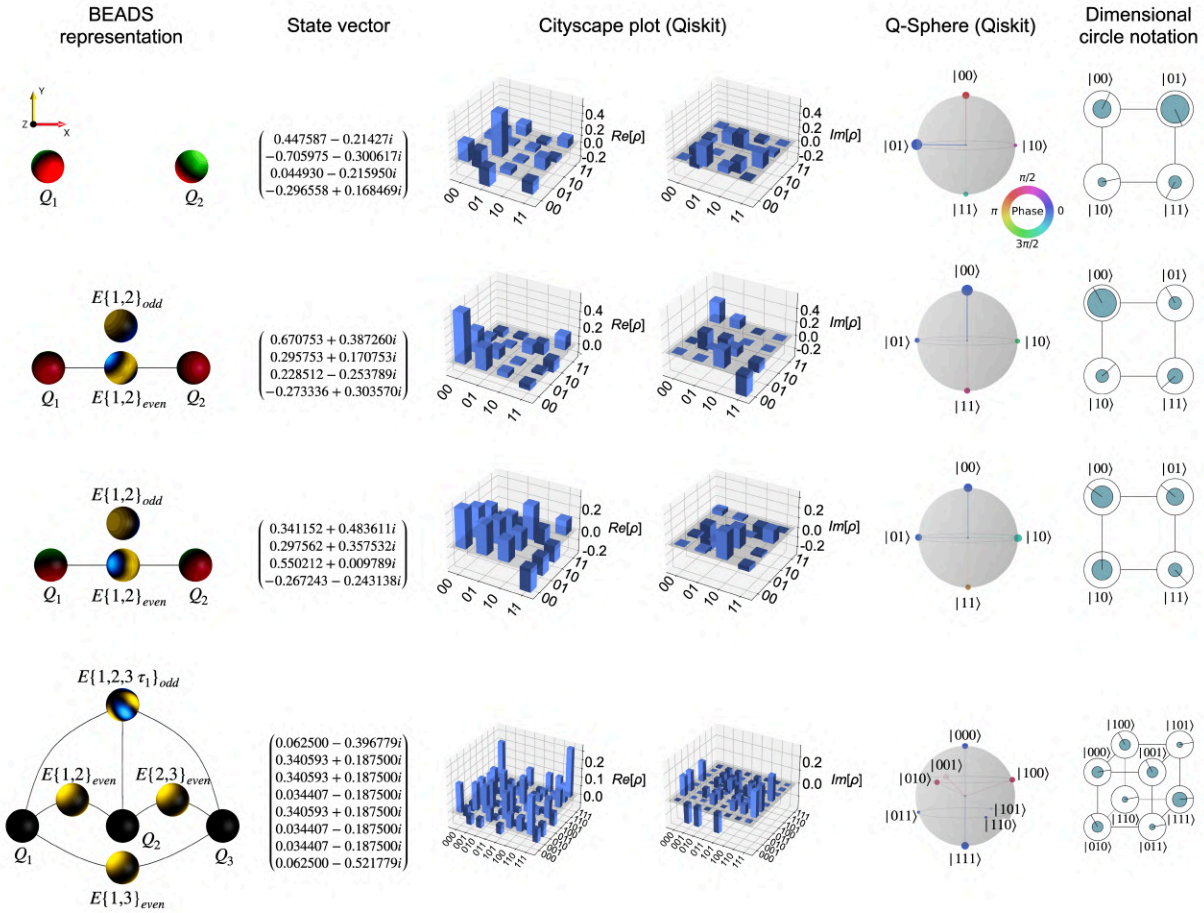


Fig. 31. BEADS, state vector, cityscape, Q-Sphere, and dimensional circle notation (DCN) representation of several quantum states. The global phase is not visualized by the cityscape and BEADS representations since these visualizations are density operator based. In the published Q-Sphere representation (51), the global phase is adjusted with respect to the maximum element of the state vector (prioritizing elements closer to the end of the vector due to the little-endian convention in Qiskit) such that this element becomes positive real. The dimensional circle notation (52) yields a faithful representation of the global phase. The visualized examples comprise a fully separable state (top), two partially entangled two-qubit states which only differ by a global 45° -rotation around the x-axis (center), and a maximally entangled three-qubit state which is the GHZ state rotated by a -60° -rotation around the xy-bisecting axis (bottom).

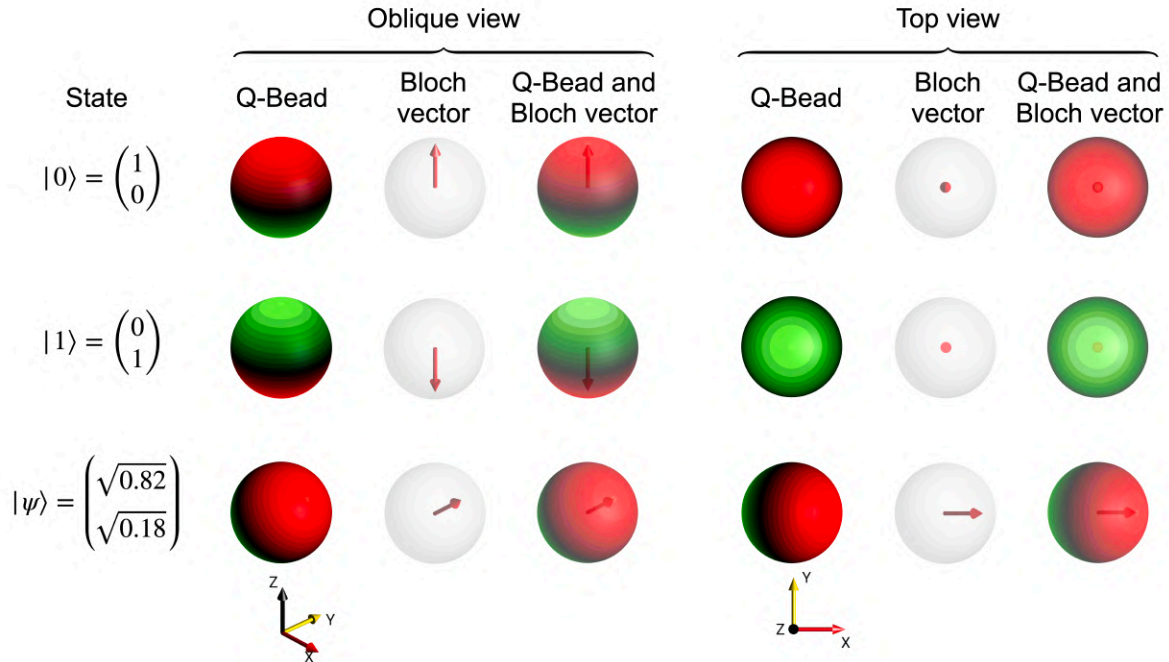


Fig. 32. Comparison between Q-Beads and the Bloch vector. Q-Beads and Bloch vectors (6, 7) are visualized for different single-qubit states in oblique and top views. The Bloch vector is equivalent to the Q-Bead and exactly points to the red pole of the corresponding Q-Bead which can be readily seen by overlapping both representations. Yet, the direction of a Bloch vector is not unambiguously identifiable when the viewing direction co-aligns with the Bloch vector. This is shown for the states $|0\rangle$ and $|1\rangle$ where the Bloch vectors are parallel or anti-parallel to the z -axis, respectively. In top view, i.e., when looking in the negative z -direction, the Bloch vectors corresponding to both states are virtually indistinguishable and in particular, in case of mixed states it is impossible to determine the z -component of the Bloch vector whereas the Q-Bead colors ensure an unambiguous assignment. Moreover, Bloch vector components can only be determined if the view direction is orthogonal to the components of interest. For instance, predicting the expectation values $\langle \sigma_z \rangle$ requires to correctly determine the z -component of the Bloch vector which is difficult, while in the BEADS representation $\langle \sigma_z \rangle$ is represented by the Q-Bead colors at the north pole which can be interpreted with relative ease.

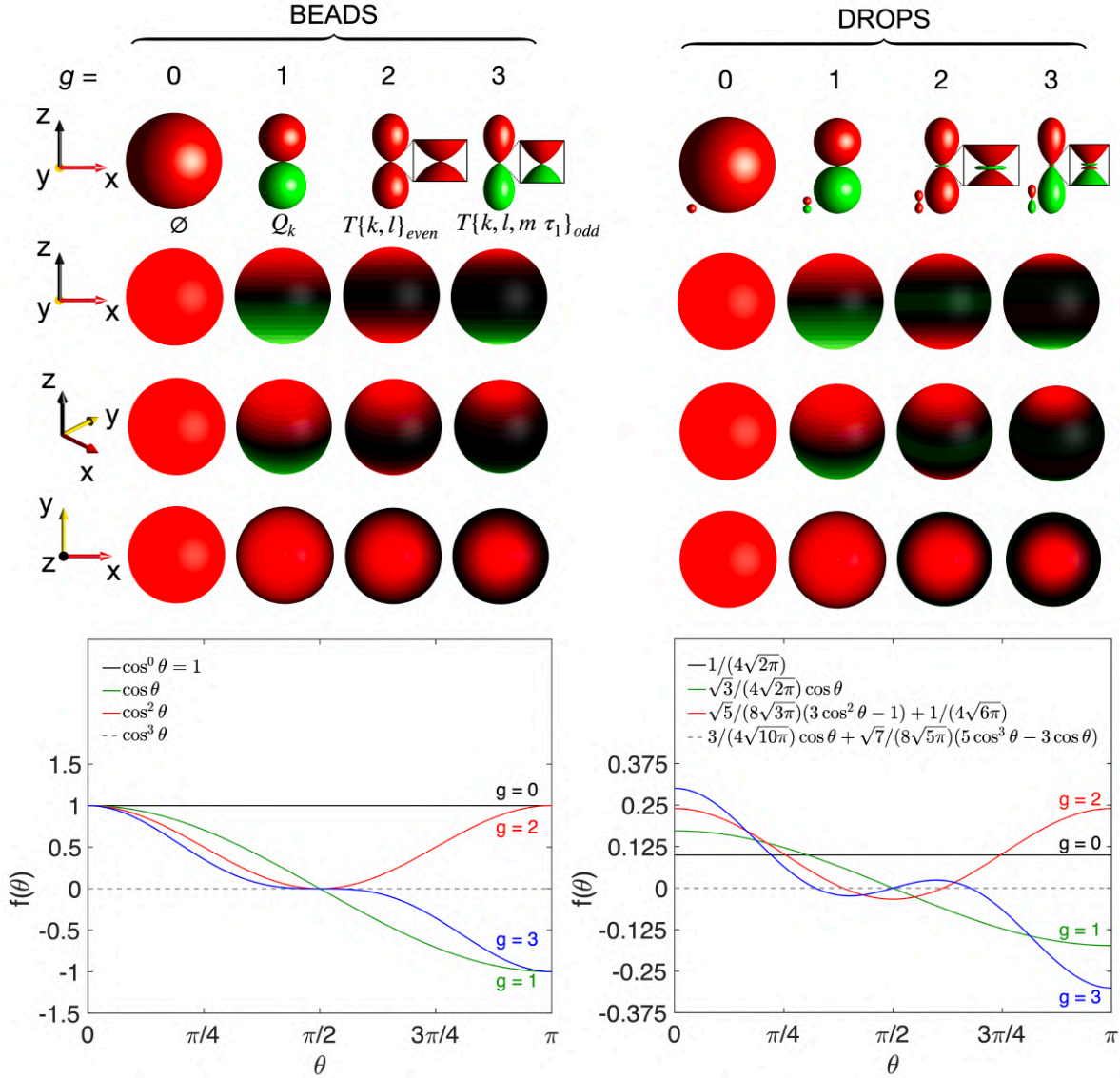


Fig. 33. Comparison between BEADS and DROPS. For a simple and direct visual comparison of shapes and surface patterns, we show the axially symmetric spherical BEADS and DROPS (37) representations of g -linear scaled Pauli-Z operators which reach a maximum function value of 1. The spherical functions are plotted with the absolute function value as distance from the origin (first row) and standard (spherical, second to fourth row) polar plots. Note the differences in bilinear and trilinear shapes highlighted by zoomed views. In case of BEADS, spherical function values along the z -axis directly correspond to expectation values $\langle \sigma_{kz} \rangle$, $\langle \sigma_{kz} \sigma_{lz} \rangle$ (where $k, l \in \{1, 2, 3\}$), and $\langle \sigma_{1z} \sigma_{2z} \sigma_{3z} \rangle$ obtained for the state $|000\rangle$. However, the DROPS representation of $|000\rangle$ corresponds to the extremely small droplets plotted in the first row and the remaining DROPS spherical functions are scaled for a direct comparison with the BEADS representation. The bottom plots display the underlying (unscaled) spherical functions of Pauli-Z operators which reduce to simple powers of cosine functions in the BEADS picture. The beads function values directly correspond to Pauli-Z expectation values which are all zero for $\theta = \pi/2$. In the DROPS picture the spherical functions of Pauli-Z operators are represented by more complicated linear combinations of cosine functions.

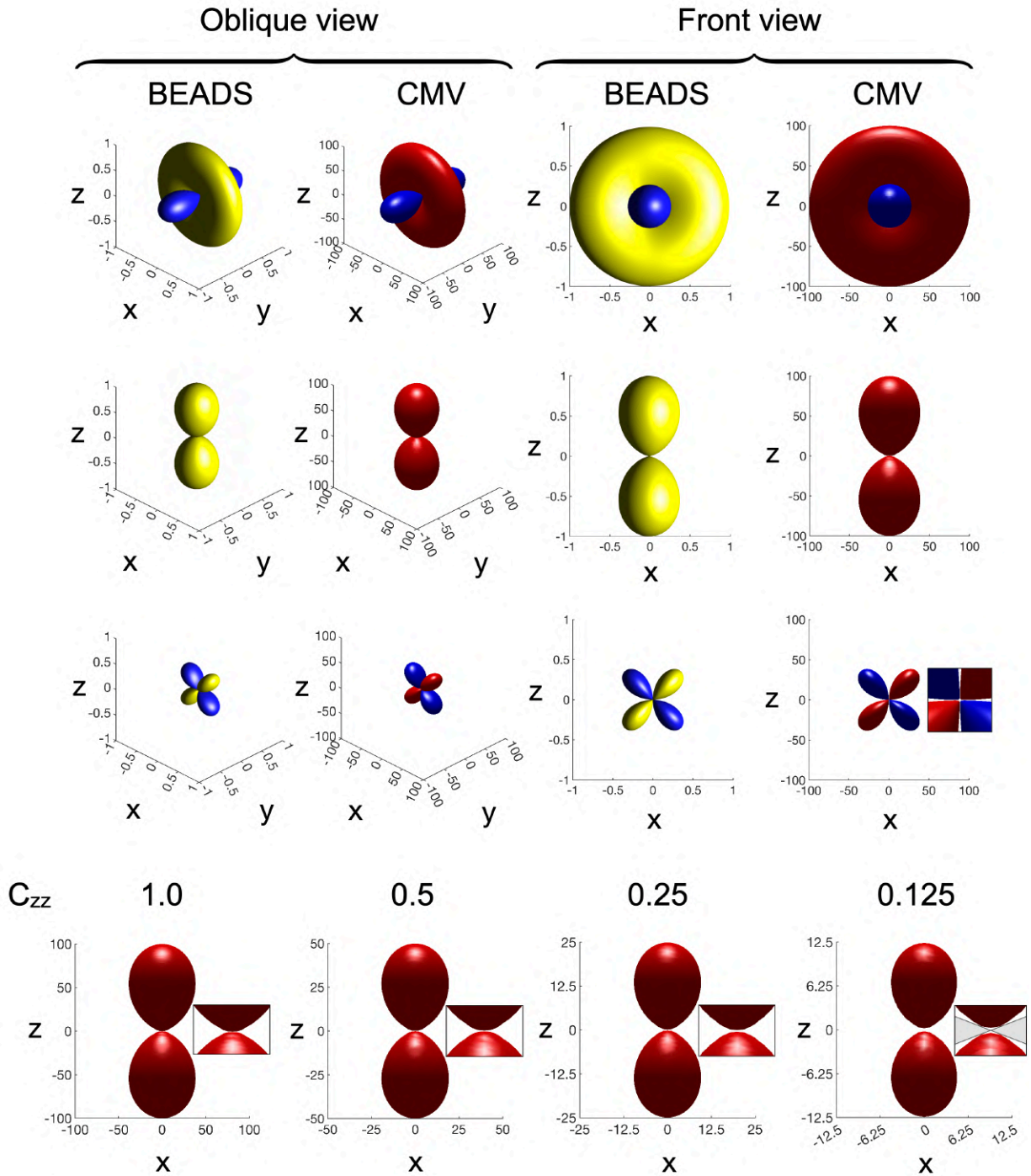


Fig. 34. Comparison between BEADS and correlation matrix visuals (CMVs, $P = \pm 0.01$). Color schemes were adopted from the original publications (49, 50) and are irrelevant for this comparison. The visualized examples (from top to bottom) comprise the bilinear connected correlation of the Bell state $|\Phi^+\rangle = 1/\sqrt{2} (|00\rangle + |11\rangle)$, for which the corresponding correlation tensor has nonzero elements $C_{xx} = 1$, $C_{yy} = -1$, $C_{zz} = 1$, the bilinear correlation in GHZ states (e.g., $|\text{GHZ}\rangle = 1/\sqrt{2} (|000\rangle + |111\rangle)$), where only $C_{zz} = 1$, and the symmetric bilinear cloverleaf-shaped correlation component between Q_1 and Q_2 or Q_1 and Q_3 in the state

$|\psi\rangle = 1/2 (|000\rangle - |011\rangle + |100\rangle + |111\rangle)$ with $C_{xz} = 1$. While the top three examples look almost identical to the corresponding BEADS representation (plotted with magnitude of the spherical function value as distance from the origin), the size of the surfaces (see axes) differs greatly and the underlying correlations in arbitrary directions are only faithfully represented in the BEADS representation whereas the CMV surface is merely proportional to and furthermore only an approximation of the represented correlations in arbitrary directions. The zoomed view shown in the third row reveals a gap between the cloverleaf lobes of the CMV at the origin which is not present in the BEADS representation and where the CMV surface and thus the correlation expectation values in a range of directions are undefined. In the bottom row, CMVs of zz -correlations with varying correlation values are shown which reveal a similar gap between CMV lobes of which the relative size increases with decreasing correlation expectation values. In the rightmost case, grey areas in the zoomed view indicate directions in which the correlation is undefined.

S13 Hierarchy of models, representations, and material tokens

In Fig. 35 and Fig. 36 we provide a hierarchical overview of models, representations and material tokens (72–74). The BEADS representation can be classified as a visual representation but is not a physical model which can perform quantum computation on its own.

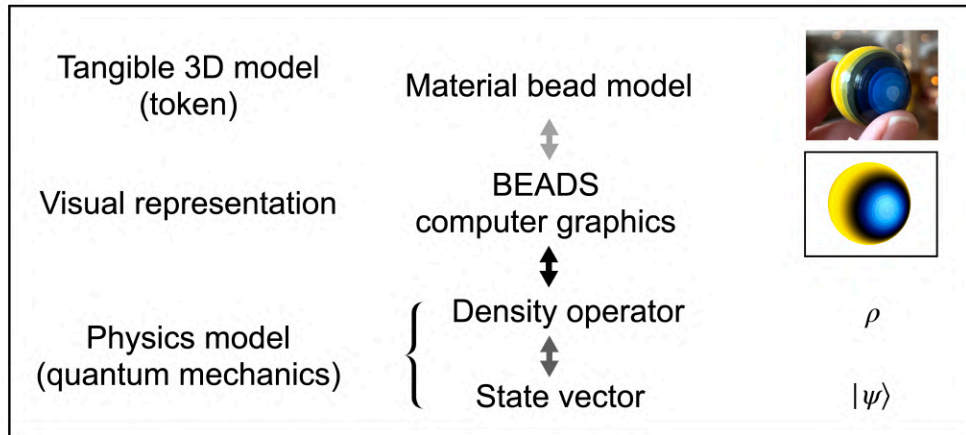


Fig. 35. Relation between an abstract quantum state vector, its density operator, its visual quantum beads representation, and a corresponding tangible three-dimensional model (token). The left column indicates the most important involved general classes of representations and models, the middle column provides concrete concepts for the BEADS representation of quantum states, and in the right column, typical symbols and exemplary illustrations are shown. The mapping between the density operator of a (pure or mixed) state of an individual quantum system (consisting of one or more qubits) and the BEADS representation is exact in both directions (indicated by a black double-headed arrow). To visualize the state of a pure quantum system, which can always be expressed as a ket vector, the state can also be uniquely mapped to the corresponding density operator (and hence visualized) but the - in general irrelevant - global phase of the state is lost. Therefore, the inverse mapping between the density operator of a pure state and a corresponding ket state is only unique up to the global phase. This loss of the global phase information is schematically indicated by a dark grey double-headed arrow. On the one hand, this property is beneficial because it slightly simplifies the BEADS representation. On the other hand, it is important to remember that the quantum bead representation cannot be used to illustrate the effect of an operation, which only changes the global phase of a given state of interest. Depending on the used method to create material beads, the mapping between the ideal BEADS representation and material beads can be more- or less exact (indicated by the light-grey double-headed arrow). However, even imperfect tangible 3D models, such as hand-colored wooden spheres or hand-made glass beads can be highly useful to understand simple quantum gates, such as the X-gate and the Hadamard gate and to roughly predict the probability of measurement outcomes. Both 2D computer graphic visualizations representations and material 3D models help to create a clear mental picture of quantum states and of their properties.

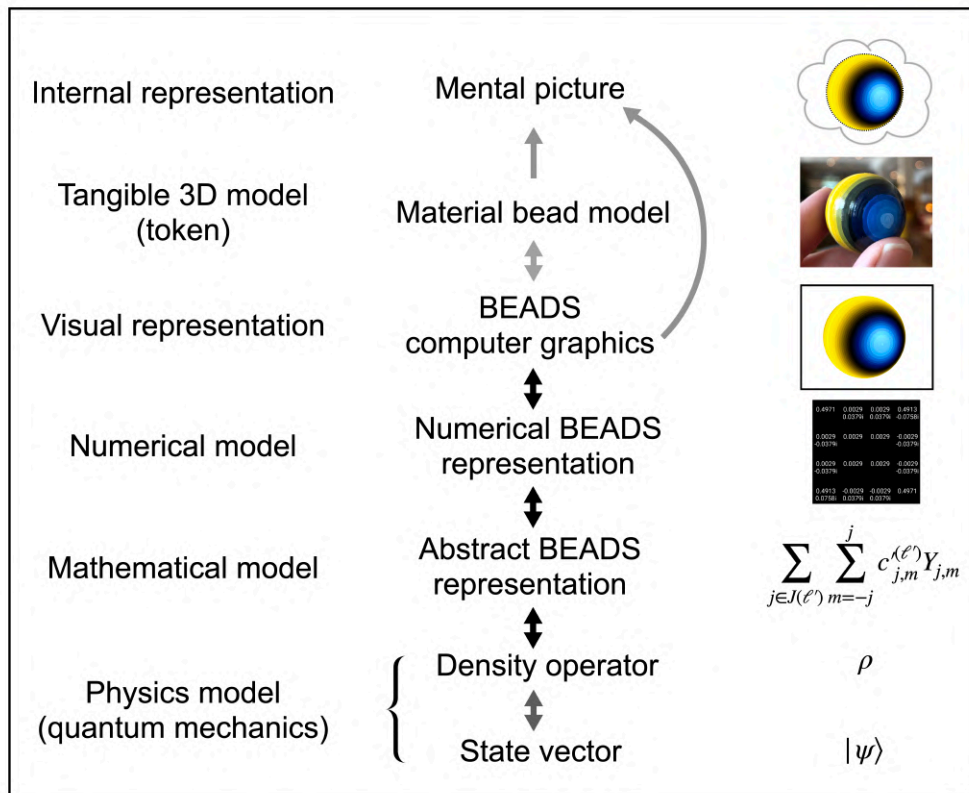


Fig. 36. Detailed relation between an abstract quantum state vector, its density operator, its visual quantum beads representation, and a corresponding tangible three-dimensional model (token). A more detailed classification of various intermediate model and representation layers between an abstract quantum state, its density operator, its visualization, and the creation of a clear mental picture of the state, such as was shown in Fig. 35, is shown.

4 Application examples

S14 Partially entangled states

BEADS representations shown in the Results section of the main text are mainly based on visualizing Q-Beads and n -qubit connected correlation in the form of E-Beads. Indeed, as we discussed in section S7, omitting compound correlations in the visualization of quantum states does not result in any loss of information and the n -qubit connected correlation (E-Beads) together with linear components (Q-Beads) are sufficient to characterize an entire quantum state (44).

As we saw in the Results section, measurement outcomes of maximally entangled states can be directly predicted from E-Beads and outcomes of fully separable states can be deduced from Q-Beads only. When it comes to partially entangled states though, it is required to consider total correlations to forecast the correct measurement outcomes of a state.

Before analyzing the BEADS representation of a partially entangled state, it is thus reasonable to choose the visualized information such that the desired aspect of interest is intuitively represented: if one is interested in learning about the degree and structure (e.g., possible symmetries, locality, etc.) of the entanglement and entanglement-related correlations, it is sufficient to examine E-Beads, whereas if measurement predictions are the main focus, one should view T-Beads instead.

For symmetric n -qubit measurements, outcomes can then be directly deduced from the spherical function value of the n -linear symmetric T-Bead along the chosen measurement direction. Detailed background information on the color schemes for total correlations is given in section S9.

As an example, the Schmidt form states (53) ($|\psi\rangle = \cos \theta/2 |00\rangle + \sin \theta/2 |11\rangle$) which were previously shown in terms of genuine two-qubit connected correlations in Fig. 5 in the Results section are visualized including total correlations in Fig. 37 and Fig. 38. Indeed, it is immediately clear from the BEADS representations that the states remain fully correlated along the z -axis (value 1.0) independent of the choice of the Schmidt angle θ which is not directly evident when looking at the corresponding E-Beads. Hence, one can thus predict that only measurement results of bit parity 0, i.e., either $|00\rangle$ or $|11\rangle$, are expected if we perform a two-qubit z -measurement on any of the states. However, as the entanglement depends on θ the probability to measure one of the possible outcomes varies and can be straightforwardly determined by analyzing one of the Q-Beads. For instance, for $\theta/2 = \pi/8$, we find an expectation value of $\langle \sigma_{1z} \rangle = \langle \sigma_{2z} \rangle = 1/\sqrt{2} \approx 0.71$ which corresponds to a probability of $p_{|1\rangle} = (1 - 1/\sqrt{2})/2 \approx 14.6\%$ to measure $|1\rangle$ for one of the qubits whereas for $\theta/2 = \pi/4$, $p_{|1\rangle} = 0.5 = 50\%$. Since for all values θ we know that the state is fully correlated when measuring both qubits, it follows that $p_{|1\rangle} = p_{|11\rangle}$ and $p_{|00\rangle} = 1 - p_{|11\rangle}$.

A prominent three-qubit example of a partially entangled state is the W-state (56) $|W\rangle = 1/\sqrt{3}(|100\rangle + |010\rangle + |001\rangle)$ which was also introduced in the Results section but visualized with respect to genuine n -qubit connected correlations. Fig. 39 provides BEADS representations of the W-state in terms of total, non-classical and compound correlation (see section S7 for a mathematical guide on how to separate different types of correlations by applying Ursell functions). For a three-qubit z -measurement, considering the $T_{\{1,2,3\} \text{ odd}}$ T-Bead, it can be seen that the W-state is fully anticorrelated and we would hence only expect outcomes of bit parity 1, i.e., $|111\rangle$, $|100\rangle$, $|010\rangle$, or $|001\rangle$ (any outcome of bit parity 0 has zero probability). Note that one also measures $|111\rangle$ with zero probability though, which arises from the correlations in the W state being more intricate than for GHZ states (see discussion in the Results section). To see why $|111\rangle$ cannot be observed as an outcome solely from the BEADS representation, we examine

contributions represented by Q-Beads and T-Beads in the BEADS picture. In Fig. 39, expectation values along the z-axis are provided for all beads and we can calculate the related bit parity probabilities according to Eq. 1 of the Results section. Thus, we can write a system of equations:

$T\{1,2,3 \tau_1\}_{odd}$:

$$(I) p(|111\rangle) + p(|100\rangle) + p(|010\rangle) + p(|001\rangle) = \frac{1 - (-1)}{2} = 1 \quad (112)$$

and

$$p(|000\rangle) = p(|011\rangle) = p(|101\rangle) = p(|110\rangle) = 0 \quad (113)$$

$T\{k,l\}_{even}$:

$$(IIa) p(|100\rangle) + p(|010\rangle) = \frac{1 - (-1/3)}{2} = \frac{2}{3} \quad (114a)$$

$$(IIb) p(|100\rangle) + p(|001\rangle) = \frac{2}{3} \quad (114b)$$

$$(IIc) p(|010\rangle) + p(|001\rangle) = \frac{2}{3} \quad (114c)$$

Q_k :

$$(IIIa) p(|100\rangle) + p(|111\rangle) = \frac{1 - (1/3)}{2} = \frac{1}{3} \quad (115a)$$

$$(IIIb) p(|010\rangle) + p(|111\rangle) = \frac{1}{3} \quad (115b)$$

$$(IIIc) p(|001\rangle) + p(|111\rangle) = \frac{1}{3} \quad (115c)$$

where $p(\cdot)$ is the probability to measure the state denoted in parenthesis. We can solve this system by the relation

$$(IV) = (IIa - IIIa) \quad p(|100\rangle) + p(|010\rangle) - p(|100\rangle) - p(|111\rangle) = \frac{2}{3} - \frac{1}{3} = \frac{1}{3} \quad (116)$$

$$(IIIb + IV) \quad 2p(|010\rangle) = \frac{2}{3} \rightarrow p(|010\rangle) = \frac{1}{3} \quad (117)$$

Repeating this procedure for the remaining equations gives $p(|100\rangle) = p(|010\rangle) = p(|001\rangle) = 1/3$ and $p(|111\rangle) = 0$.

Fig. 39 further provides a visualization of the W state only in terms of compound correlations, that is, connected correlations are omitted. Here, the trilinear compound correlation $C\{1,2,3 \tau_1\}_{odd}$ component is large in comparison to the purely classical bilinear correlations $C\{k,l\}_{even}$ due to significant contributions from lower-order connected correlations.

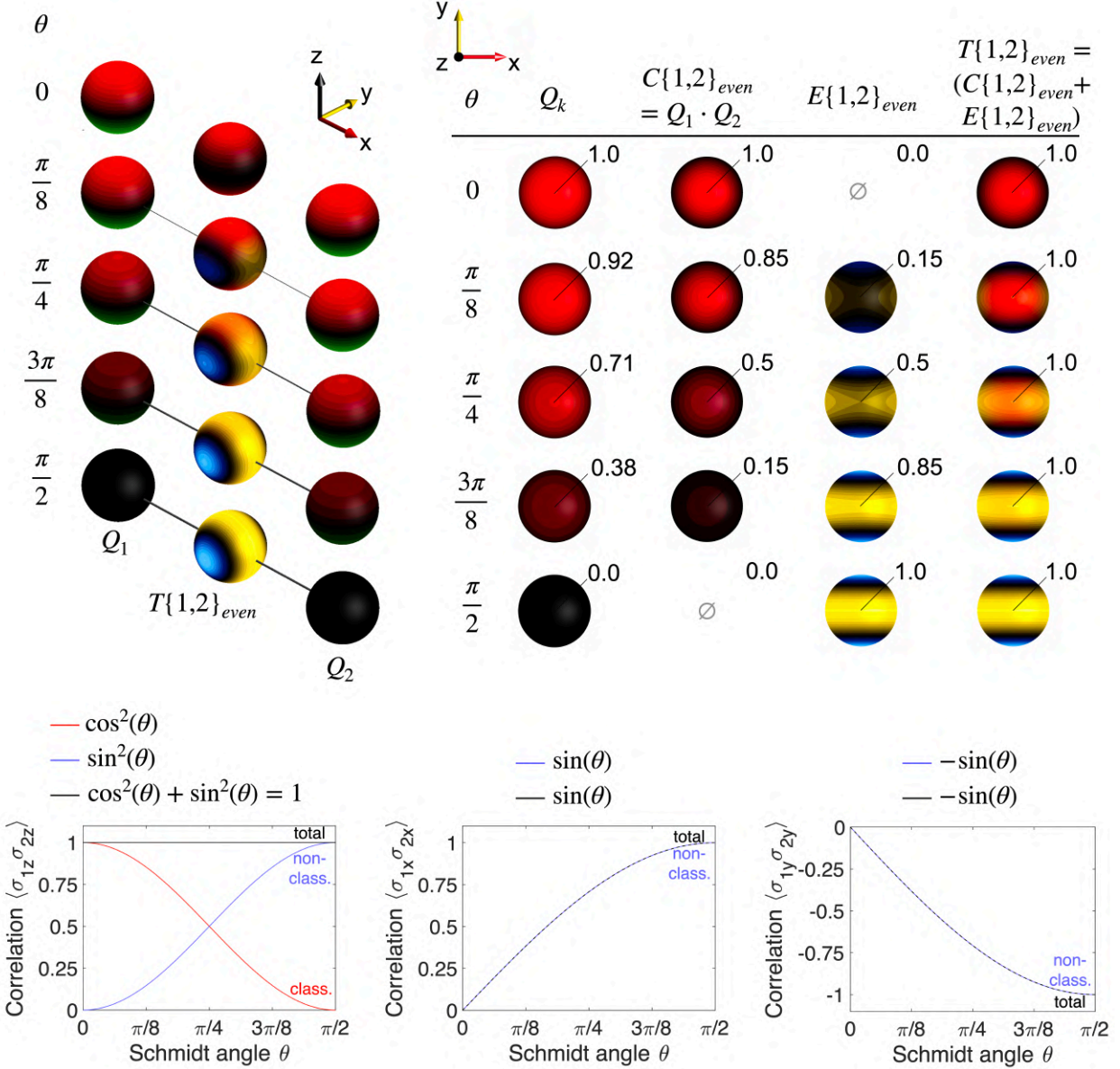


Fig. 37. Correlations in two-qubit Schmidt form states. The total correlation BEADS representations of states of the Schmidt form (53) $|\psi\rangle = \cos \theta/2 |00\rangle + \sin \theta/2 |11\rangle$ are shown for different Schmidt angles θ . Q-Beads Q_k , total correlations $T\{1,2\}_{even}$, entanglement-related connected correlations $E\{1,2\}_{even}$ and compound correlations $C\{1,2\}_{even}$ are shown tabularly on the right. Expectation values along the z-axis are displayed for all beads. Indeed, states of the presented form are always fully correlated for measurements along the z-axis which is reflected by the indicated total correlation values (1.0 for any angle θ). However, by separating correlations we see that θ leads to an increase in entanglement up to $\theta/2 = \pi/4$ where the corresponding state becomes maximally entangled ($C\{1,2\}_{even} = \emptyset$) while $\theta/2 = 0$ corresponds to the fully separable state $|00\rangle$. For any case $0 < \theta < \pi/2$, the corresponding states are partially entangled, and measurement outcomes must be predicted based on total correlations. The bilinear total zz-correlation remains constant, yet compound and non-classical zz-correlations are described by quadratic cosine and sine functions, respectively. In contrast, xx- and yy-correlations only exist non-classically. The corresponding correlation curves in dependence of θ are shown at the bottom.

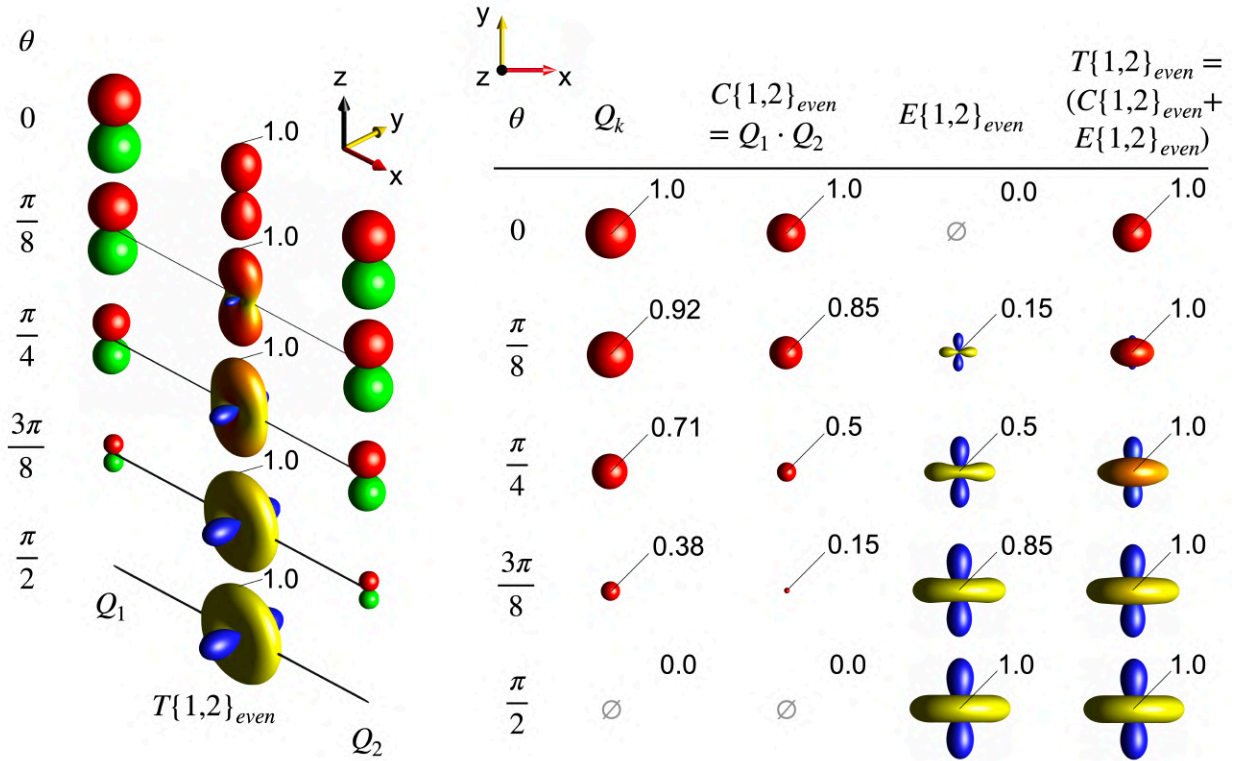


Fig. 38. BEADS representation of two-qubit Schmidt form states using radial plots. The visualized states are equivalent to those shown in Fig. 37, yet radial plots instead of the introduced polar plots are applied to visualize the beads, that is, the magnitude of the underlying expectation values in arbitrary directions correspond to the distance from the origin, respectively. Here, we use the *red-green* and *yellow-blue DROPS* color schemes and we apply the total correlation color blending approach introduced in supplementary section S9. The representation on the left clearly shows in a visual way that the *zz*-correlation has a constant value 1 for all values of θ .

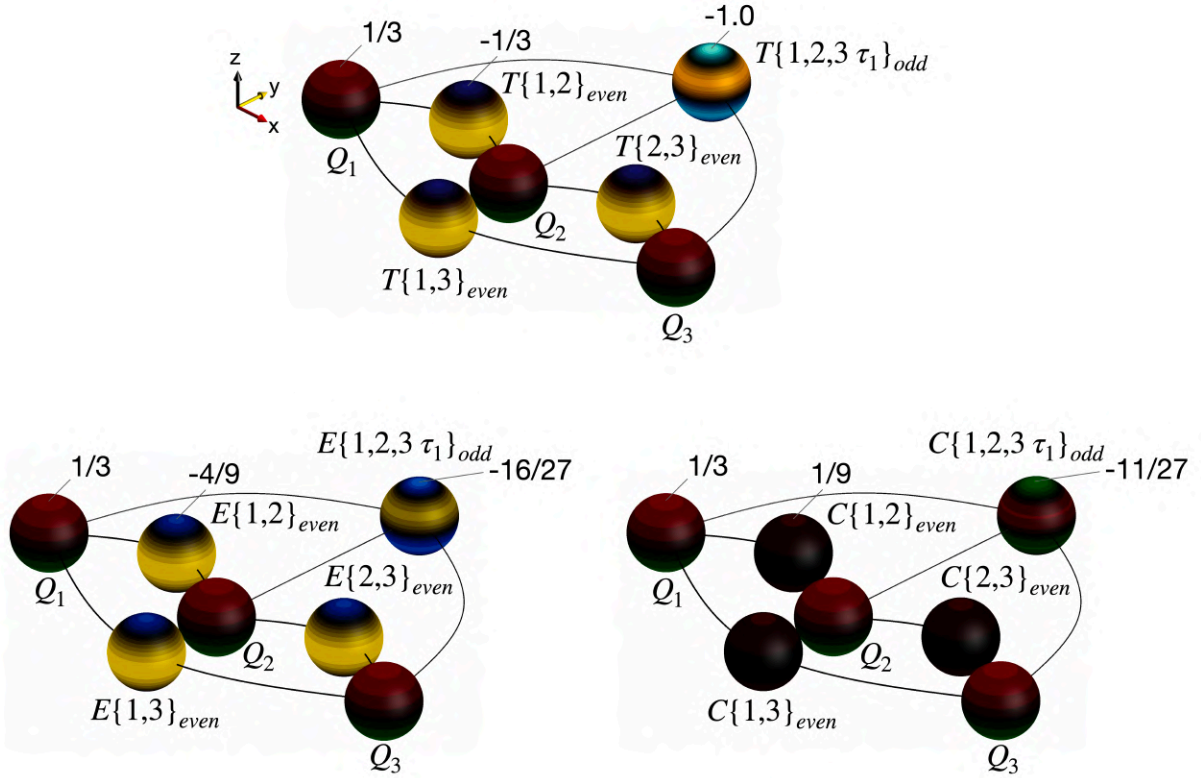


Fig. 39. Correlations in the three-qubit W-state. The total correlation BEADS representations of the W-state (56) $|W\rangle = 1/\sqrt{3}(|100\rangle + |010\rangle + |001\rangle)$ (top) reveals full three-qubit anticorrelation (indicated value at $T\{1,2,3\tau_1\}_{odd}$) along the z-axis. Separating connected (bottom left) from compound correlations (bottom right) reveals that all correlation components share the same axial symmetry for all beads. Specific correlation expectation values along the z-axis are indicated numerically in all representations.

S15 Quantum gates and system dynamics

Quantum gates are unitary transformations acting on qubits in quantum computing algorithms and communication protocols. Thus, it is essential to understand the working principles of the most important quantum gates. While the BEADS representation is not only able to visualize the *outcomes* of any gate operation for arbitrary inputs, it can also be used to monitor the *dynamics* that take place *during* the action of a gate.

Indeed, quantum gates have specific durations T depending on the particular physical implementation of the utilized qubits. In the simple case where a single quantum gate is implemented by a time-independent Hamiltonian \hat{H} , for any point in time $0 \leq t \leq T$ we thus obtain a propagator U describing the time evolution of the system (2):

$$U(t) = e^{-i\hat{H}t} \quad (118)$$

Hence, using the BEADS representation we can not only observe the result of a quantum gate ($t = T$) but understand the dynamics during the gate by visualizing the states $|\psi_t\rangle = U(t)|\psi\rangle$ at various points in time. As illustrated in Fig. 40, single-qubit gates implement simple rotations of the qubit state which are directly visualized by a corresponding rotation of the Q-Bead. By choosing suitable Hamiltonians \hat{H} , gates can be implemented such that the induced transformations are equivalent to simple rotations around desired axes for computational basis states. For instance, Pauli-X, -Y, and -Z gates (2) are implemented by 180° -rotations around the corresponding axis. Phase gates (indicated by φ in the circuit diagram), also implement z-rotations by an arbitrary phase angle φ , i.e., the Pauli-Z gate is a special case of a phase gate for which $\varphi = 180^\circ$.

The intermediate state at $t = T/2$, moreover, corresponds to the output state if one was to apply only half of the operation which is commonly denoted the square root of a quantum gate. In case of the Pauli-Y gate, the square root operation corresponds to a 90° -rotation about the y-axis. The \sqrt{Y} -gate transfers $|0\rangle$ to the superposition state $|+\rangle = 1/\sqrt{2}(|0\rangle + |1\rangle)$. This state is also obtained when performing a Hadamard H (2) or an axis cycling gate C (75–78) on the same input.

However, the Hadamard gate corresponds to a 180° -rotation around the xz-bisecting axis. In contrast, the axis cycling C-gate (75–78) implements a 120° -rotation around the axis $R = (\text{atan } \sqrt{2}, 45^\circ) \approx (54.74^\circ, 45^\circ)$, corresponding to the space diagonal of the cube spanned by the x, y, and z unit vectors. When looking at the dynamics *during* the gate, it is clear that the induced rotations differ greatly. Furthermore, performing multiples of the same gates in series yields differing (intermediate) outputs. Fig. 41 displays the discussed gates (H, C, \sqrt{Y}) applied four times in a row on an initial input state $|0\rangle$. One can directly see that the Hadamard gate gives the initial input state when applied two times in a row. Hence, it is said to be self-inverse. On the other hand, applying a \sqrt{Y} two times outputs $|1\rangle$ and one has to perform the operation for another two times to regain the initial input state. The axis cycling gate, as its name suggests, cycles the coordinate x-, y-, and z-axes, i.e., the computational basis (z-basis) input state is first rotated onto the x-axis, followed by a rotation onto the y-axis by the second execution of the gate, etc. Hence, this gate requires three executions until it reproduces the initial input state.

The underlying property which describes how often a gate has to be performed in order to give the original input state is called period of a quantum gate and as shown, can be determined visually by using the BEADS representation.

It should be further pointed out, that the inverse of a single-qubit gate simply corresponds to a rotation around the same axis but with reversed rotation direction. As an exception, gates

implemented by 180° -rotations, e.g., the Pauli-X, Y, and Z, or the Hadamard gate are self-inverse, i.e., both rotation directions ($\pm 180^\circ$) have the same effect for which the inverse operation is simply given by the standard gate rotation, respectively.

The effect of multiqubit quantum gates in the BEADS representation goes beyond simple rotations of individual beads. As briefly discussed in the Results section of the main text, multiqubit gates can induce rotations, scalings (change of brightness), and morphing. Recall that morphing describes changes in surface patterns which can only occur for correlation beads (E-Beads, C-Beads, and T-Beads). As can be seen in Fig. 42, the induced effects depend on the choice of input states. For instance, when performing controlled operations, e.g., a controlled X-gate (CNOT or CX) or a controlled phase gate, with the control qubit (Q_1 in the examples shown in Fig. 42) in computational basis state $|1\rangle$, the gates lead to simple rotations of the target qubit Q-Beads Q_2 .

On the other hand, performing a CNOT on a system with the control qubit being in an equal superposition state, e.g., $|+\rangle$ and the target being in a computational basis state creates entanglement, and thus, causes simultaneous rotations and scalings on both Q-Beads and scaling and morphing on the E-Beads.

By using the BEADS representation to visualize the dynamics of multiqubit gates, we can further observe if entanglement is created temporarily during the action of the quantum gate, even if the input and output states are not entangled. In fact, this is a common phenomenon that, for example, occurs for SWAP gates. As can be seen in Fig. 42, the SWAP gate (2) intermittently leads to a maximally entangled state at time step $T/2$ when swapping qubits in computational basis states (provided the qubits are in differing basis states).

Moreover, with the BEADS representation it is possible to explore possible applications of more complicated gates such as the Toffoli gate (double-controlled NOT gate) (2) shown in Fig. 43. Here, we can directly see that both control qubits in computational basis states implement a controlled rotation of the target qubit, whereas using an equal superposition on one control qubit while keeping the second control to a computational basis state effectively creates a Bell pair between the target qubit and the control qubit, which was input in a superposition state, in a controlled fashion, e.g., here, in dependence of the state of Q_1 .

Implementations of gates such as the SWAP gate, which can be realized as a cascade of three CNOT gates (see Fig. 44), can be reproduced in the BEADS picture. After performing such a series of CNOT gates, the Q-Beads orientations correspond to the swapped input orientations just as in case of SWAP gate (see Fig. 42).

Last, as an extension to our discussion on the effects on single-qubit states, the effects of single-qubit operations on multiqubit entangled states shall be discussed. For example, in Fig. 45 we visualize the transformation of the Bell pair $|\Phi^+\rangle = 1/\sqrt{2}(|00\rangle + |11\rangle)$ by applying a \sqrt{X} -gate globally, i.e., to all qubits involved in the entanglement (or more general the correlation), for which we find that the E-Bead is simply rotated according to the rotation induced by the quantum gate on the physical qubits. This serves as a general rule and is applicable to any n -qubit correlation bead (E-, T-, or C-Bead). If local rotations, e.g., a Y-gate, are applied on just a subset of the involved qubits (for instance, only on Q_1 in Fig. 45) various effects can occur. The E-Bead is morphed if the spatial correlation properties change. As an example, in the second circuit of Fig. 45, the $E\{1,2\}_{\text{even}}$ E-Bead morphs from its original appearance to a fully blue bead corresponding to the singlet state $|\Psi^-\rangle = 1/\sqrt{2}(|01\rangle - |10\rangle)$. This morphing by selective local gates is quite typical. However, there are important exceptions such as the last example presented in Fig. 45 where selective gates induce simple rotations of a correlation bead which can be readily identified in the BEADS picture. These arise due to special transformation rules which

prominently occur in the analysis of multiple-quantum coherence (8) yet go beyond the scope of this work. Furthermore, E-Beads are scaled when local rotations cause a transfer to E-Beads of different permutation symmetry, e.g., from $E\{1,2\}_{even}$ to $E\{1,2\}_{odd}$, where the former is dimmed and the brightness of the latter E-Bead increases.

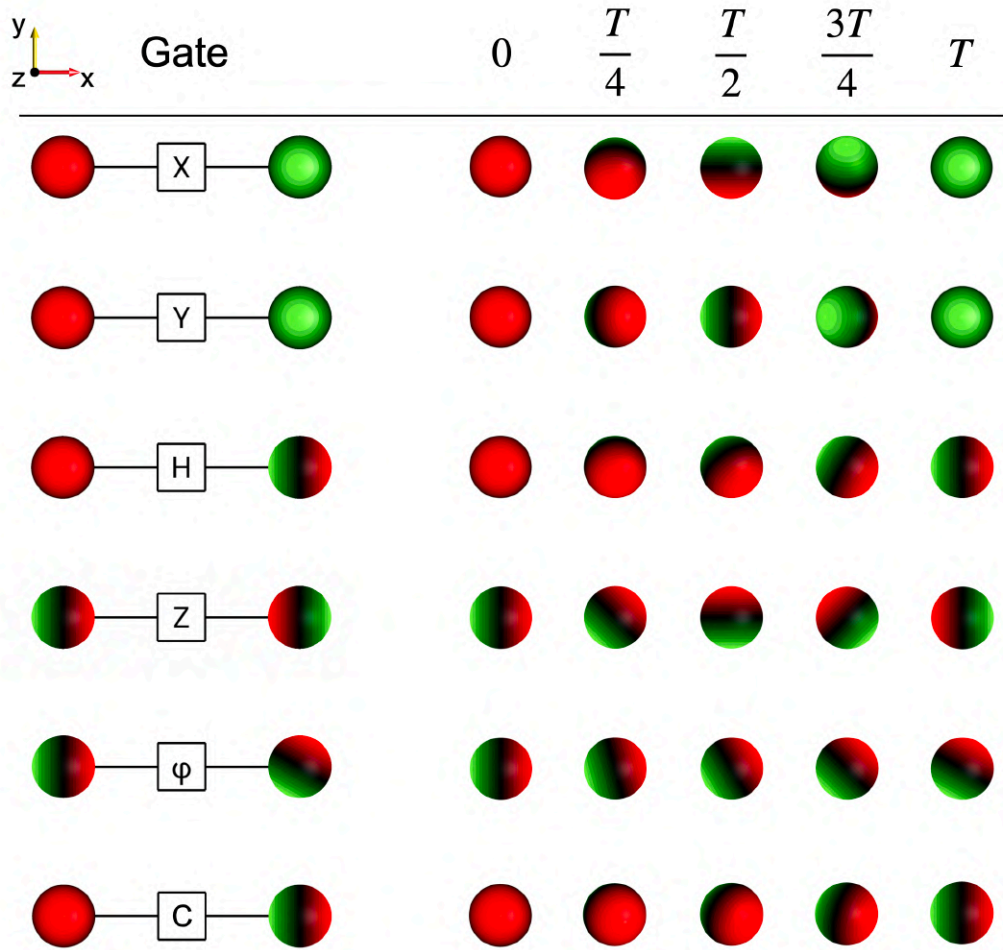


Fig. 40. Single-qubit gates visualized by the BEADS representation \otimes . Single-qubit quantum gates such as Pauli (X, Y, Z), Hadamard (H), phase (φ), or axis cycling gates (C) implement rotations which are visualized by the BEADS representation. The overall action of the gate is shown on the left whereas the dynamics which occur during the gate are outlined by BEADS representations (Q-Beads) of qubit states at different time steps during the operation (right). The Q-Beads at $T/2$ correspond to the output of the square root of each quantum gate. The symbol φ represents a phase gate (here the phase angle is chosen to be 60°).

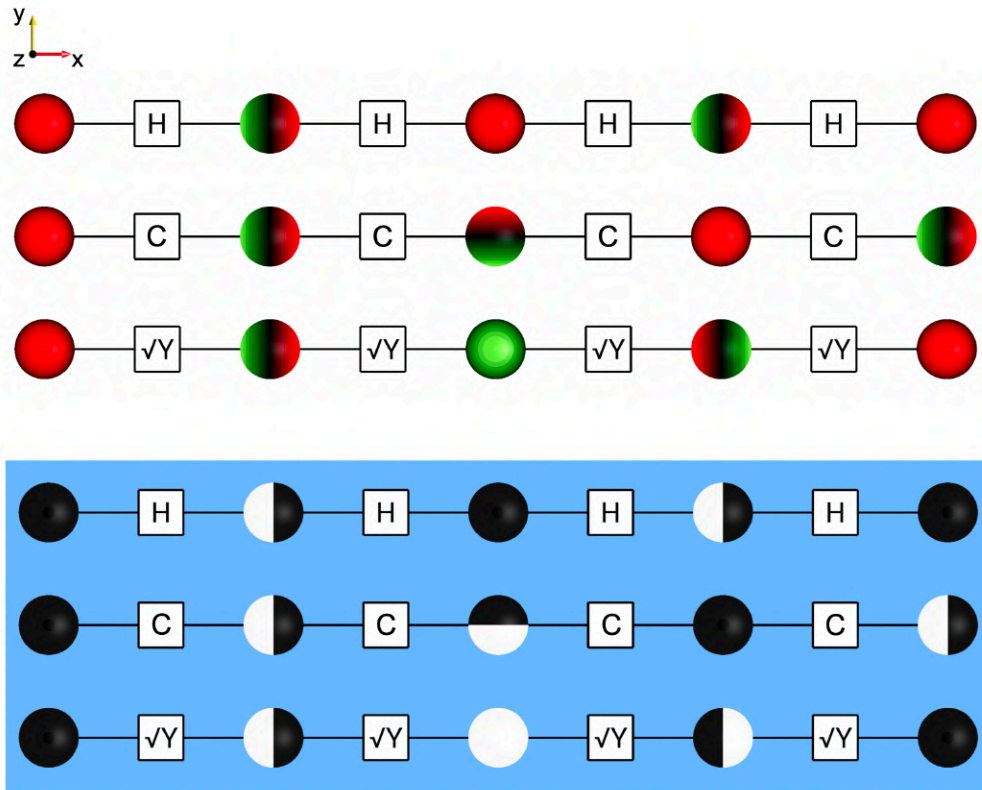


Fig. 41. Comparison of Hadamard, \sqrt{Y} and axis cycling gates \emptyset . H, C (75–78), and \sqrt{Y} gates can be applied to bring qubits in computational basis states (here $|0\rangle$) into superposition. As visualized by the BEADS representation, the gates differ in their period which results in different (intermediate) output states when performing multiples of each gate in a row. The period P of each gate can be directly read off in the BEADS picture ($P_H = 2$, $P_C = 3$, $P_{\sqrt{Y}} = 4$). The high-contrast variant of the picture (bottom) gives a clear overview which allows for a simplified comparison of the individual Q-Bead orientations.

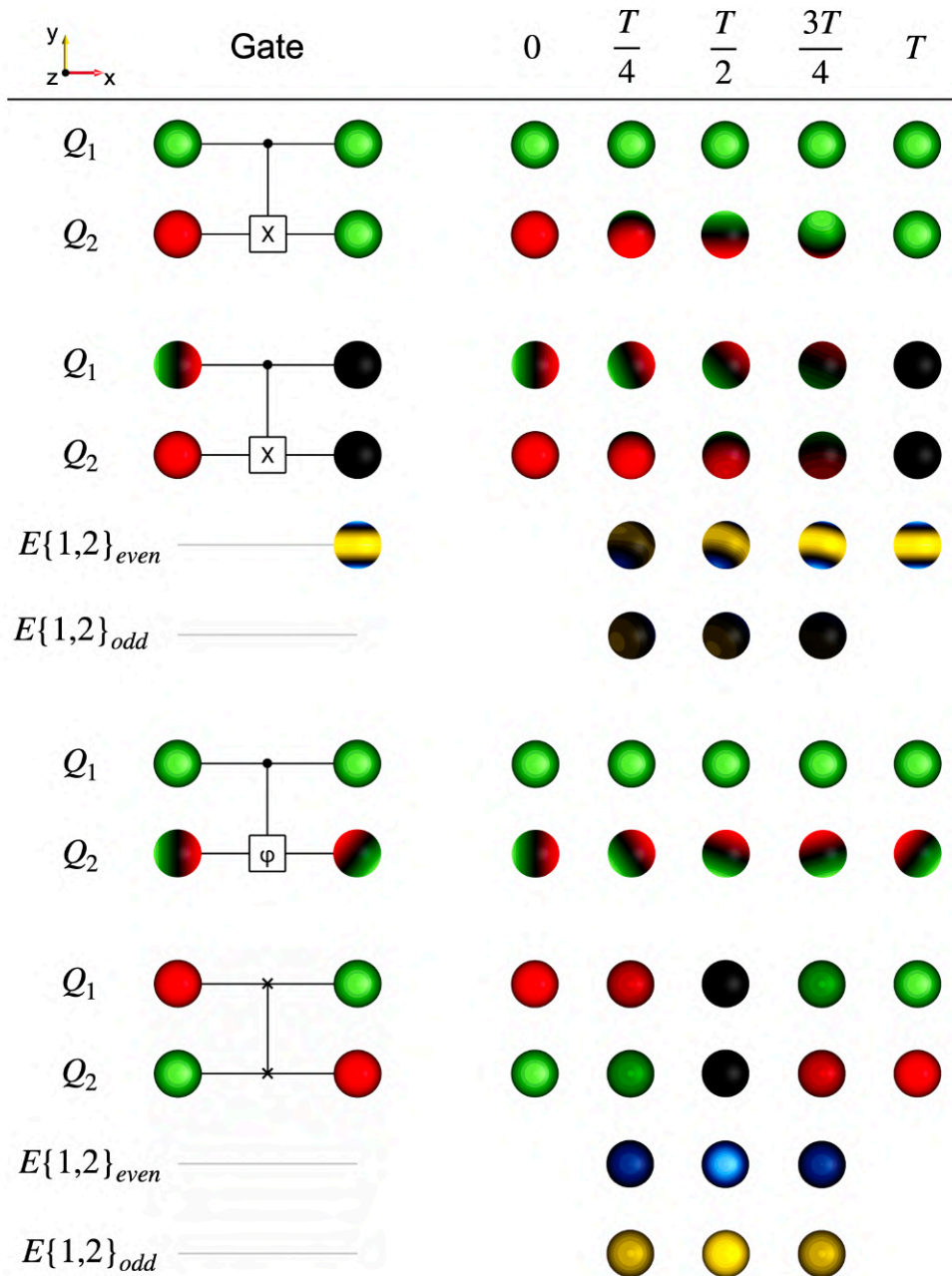


Fig. 42. Two-qubit gates visualized by the BEADS representation \otimes . The dynamics of two-qubit quantum gates such as CNOT, controlled phase, or SWAP gates are not limited to simple rotations in the BEADS representation. Depending on the choice of input states, in the case of controlled gates, we observe simple rotations of the target Q-Beads or more complicated transformations which involve rotations, scalings, and morphing when the system becomes entangled or disentangled. The SWAP gate intermittently creates entanglement which is not evident when examining only the input and output states of the operation but can be directly seen when visualizing the underlying dynamics using the BEADS representation. The overall action of the gate is shown on the left whereas the dynamics which occur during the gate are outlined on the right. The visualized states at time steps $T/2$ correspond to the output of the square root of each quantum gate.

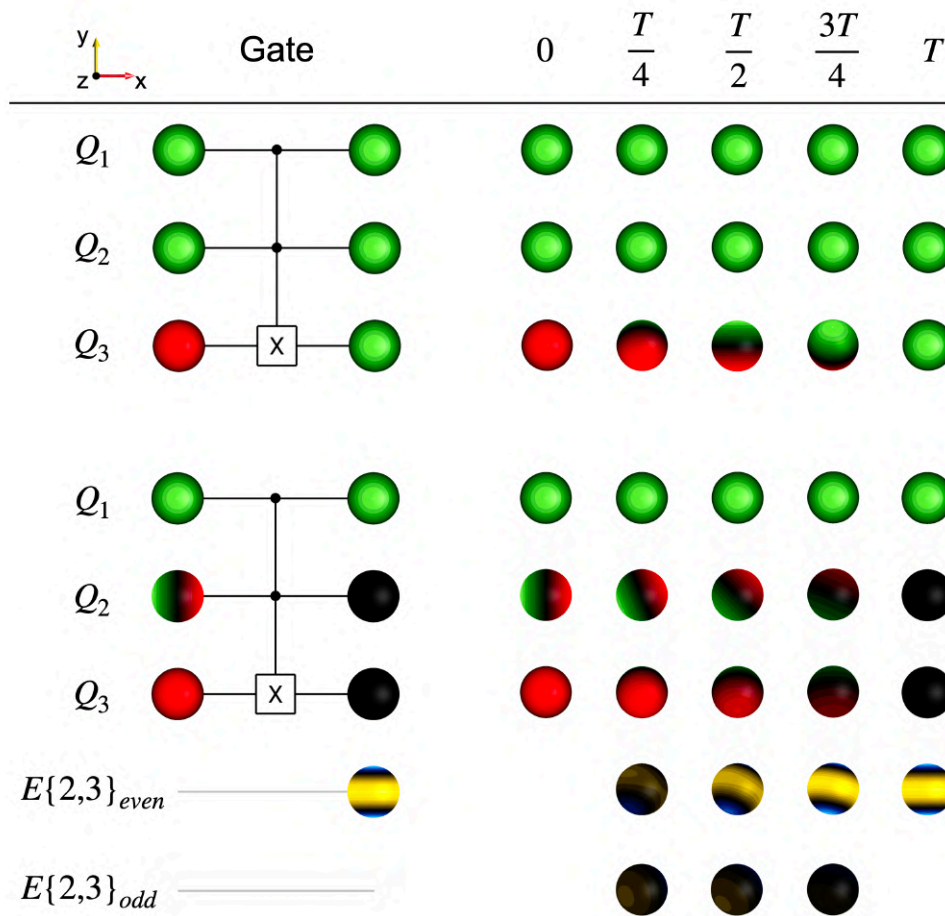


Fig. 43. Three-qubit Toffoli-gate visualized by the BEADS representation \otimes . Different applications of the Toffoli gate (double-controlled X-gate) become clear by using the BEADS representation to visualize different outcomes. Computational basis states $|1\rangle$ of both control qubits induce simple rotations of the target Q-Bead (top). By using a computational and an x-basis input on the controls, it is possible to generate Bell pairs in a controlled manner which is clear from the characteristic E-Bead surface pattern of $E\{2,3\}_{even}$ (bottom).

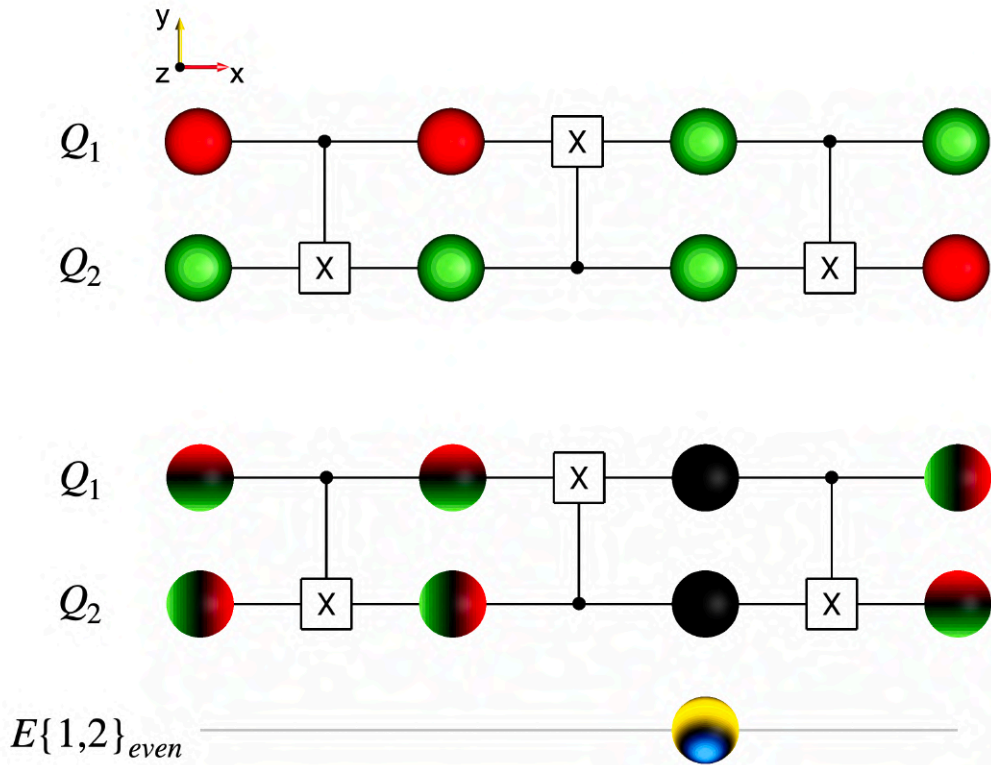


Fig. 44. Implementing a SWAP gate by a cascade of CNOT gates \otimes . Performing a series $CNOT_{12} - CNOT_{21} - CNOT_{12}$ (where the first number indicates the control and the second number denotes the target qubit), implements a SWAP gate. In the visualizations above, this can be understood by comparing the initial input with the final output orientations of both Q-Beads. The input state in the top example is $|01\rangle$ whereas in the bottom example, the input is $|R+\rangle = 1/2(|00\rangle + |01\rangle + i|10\rangle + i|11\rangle)$.

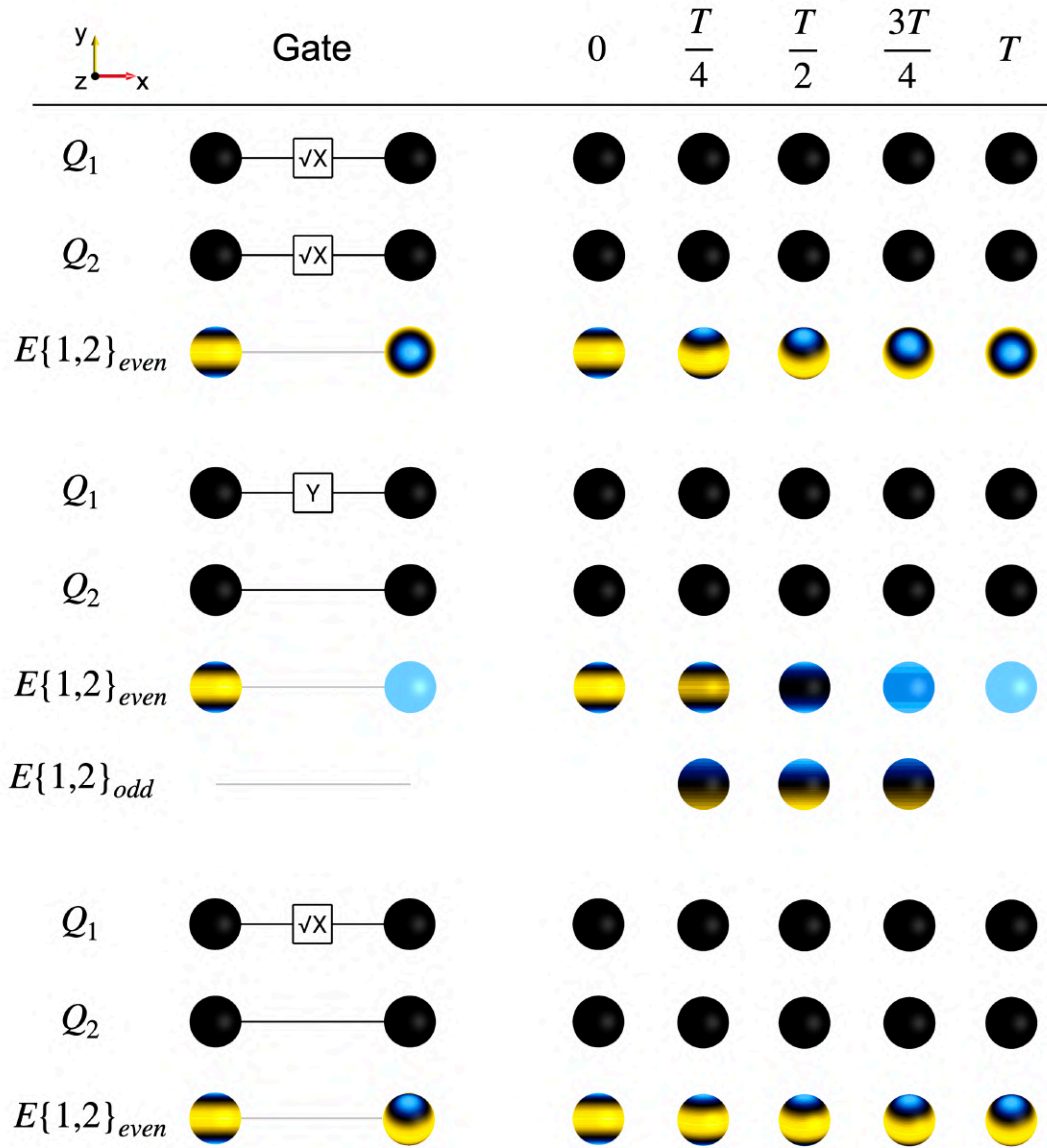


Fig. 45. Effects of single-qubit gates on two-qubit entangled states \otimes . Global rotations (top), i.e., rotations which are induced by the same single-qubit gate being applied to all qubit which are involved in a particular entanglement component simply rotate the corresponding E-Bead analogously. Applying single-qubit gates locally (on a subset of the involved qubits) in general causes morphing, i.e., a change in surface pattern (center example), yet the amount of entanglement remains unchanged. Exceptions exist for which a local rotation induces a simple rotation of the E-Bead. In the bottom example, the E-Bead representing the Bell state $|\Phi^+\rangle = 1/\sqrt{2}(|00\rangle + |11\rangle)$ is rotated by 45° (half of the gate rotation angle) around the x-axis by applying 90° -rotation around said axis (\sqrt{X} -gate) on qubit Q_1 . This arises due to more elaborate transformation rules which are commonly observed for multiple-quantum coherences. Such exceptions can be readily identified in the BEADS picture.

S16 NMR implementations of quantum gates

In this article, we mostly consider quantum gates from a theoretical perspective and do not focus on specific experimental implementations, which depend on the choice of hardware. However, we can also use the BEADS representation to explore whether and how particular quantum gates can be achieved on distinct hardware.

Liquid state nuclear magnetic resonance (NMR) was one of the first platforms which allowed to realize registers of few qubits and to perform basic quantum algorithms (2). Coupled systems of nuclear spins-1/2 which constitute qubits in NMR, can, e.g., be manipulated by applying radiofrequency pulses, i.e., local rotations on individual spins and by letting the system evolve under an Ising-type interaction of the spins.

As shown in Fig. 46, by using these building blocks, it is possible to implement a CNOT gate (up to a global phase) between two spins with zero offset frequency as a sequence of pulses and Ising interactions (79, 80). This can be shown mathematically by calculating the total propagator U of the displayed pulse sequence:

$$\begin{aligned}
 U &= e^{-i\left(\frac{\sigma_{1z}\pi}{2} - \frac{\sigma_{2z}\pi}{2}\right)} \cdot e^{-i\frac{\sigma_{2x}\pi}{2}} \cdot e^{-i\frac{\sigma_{1z}\sigma_{2z}\pi}{2}} \cdot e^{-i\frac{\sigma_{2y}\pi}{2}} \\
 &= e^{-i\frac{\pi}{4}} \begin{pmatrix} 1 & 0 & 0 & 0 \\ 0 & 1 & 0 & 0 \\ 0 & 0 & 0 & 1 \\ 0 & 0 & 1 & 0 \end{pmatrix} = e^{-i\frac{\pi}{4}} \text{CNOT}_{12}
 \end{aligned} \tag{119}$$

which is the CNOT gate up to an experimentally irrelevant global phase factor $e^{-i\frac{\pi}{4}}$.

Using the BEADS representation, we can directly verify that the action of the introduced pulse sequence implements the desired CNOT operation. In Fig. 46, we chose an input state $|-1\rangle$, where the first spin is in state $|-\rangle$ and the second spin is in state $|1\rangle$, which is well-known to give the singlet state $|\Psi^-\rangle = 1/\sqrt{2}(|01\rangle - |10\rangle)$ under transformation by a CNOT gate (see section S17). Indeed, the output state is $|\Psi^-\rangle$ which is represented by the characteristic uniformly colored blue E-Bead $E\{1,2\}_{\text{even}}$ indicating full anticorrelation in any direction.

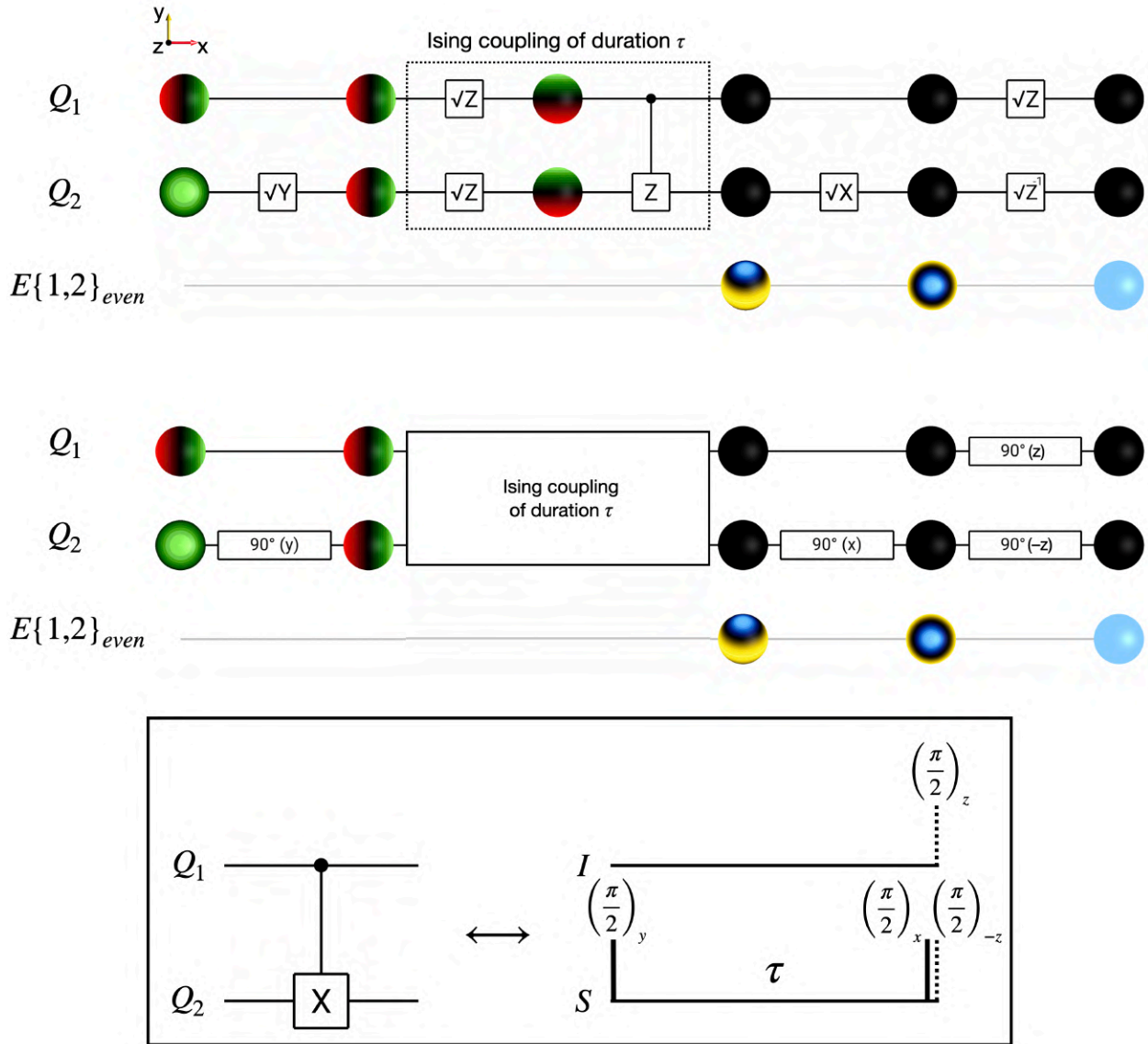


Fig. 46. Implementation of a CNOT gate in NMR-based quantum computing \emptyset . A CNOT gate between two qubits Q_1 and Q_2 can be implemented as a sequence of radiofrequency pulses and an Ising-interaction between two heteronuclear spins-1/2 which are denoted I and S (bottom). Here, the delay time $\tau = 1/(2J)$, where J is the coupling constant. The NMR sequence is visualized by equivalent BEADS-augmented circuits using standard gate notations (top) and NMR pulse labels (center). Applying the sequence to qubits in an initial state $|-1\rangle$ yields the maximally entangled singlet state $|\Psi^-\rangle = 1/\sqrt{2}(|01\rangle - |10\rangle)$ which matches the action of the CNOT operation.

S17 Bell states

BEADS representations of the four Bell states (81) $|\Phi^+\rangle = 1/\sqrt{2}(|00\rangle + |11\rangle)$, $|\Phi^-\rangle = 1/\sqrt{2}(|00\rangle - |11\rangle)$, $|\Psi^+\rangle = 1/\sqrt{2}(|01\rangle + |10\rangle)$, and $|\Psi^-\rangle = 1/\sqrt{2}(|01\rangle - |10\rangle)$ and the corresponding generating circuits are shown in Fig. 47. Note that the states $|\Phi^+\rangle$, $|\Phi^-\rangle$, and $|\Psi^+\rangle$ are equivalent up to global rotations. $|\Psi^-\rangle$, the singlet state, is fully anticorrelated in all spatial directions and thus has an entirely different correlation BEADS visualization.

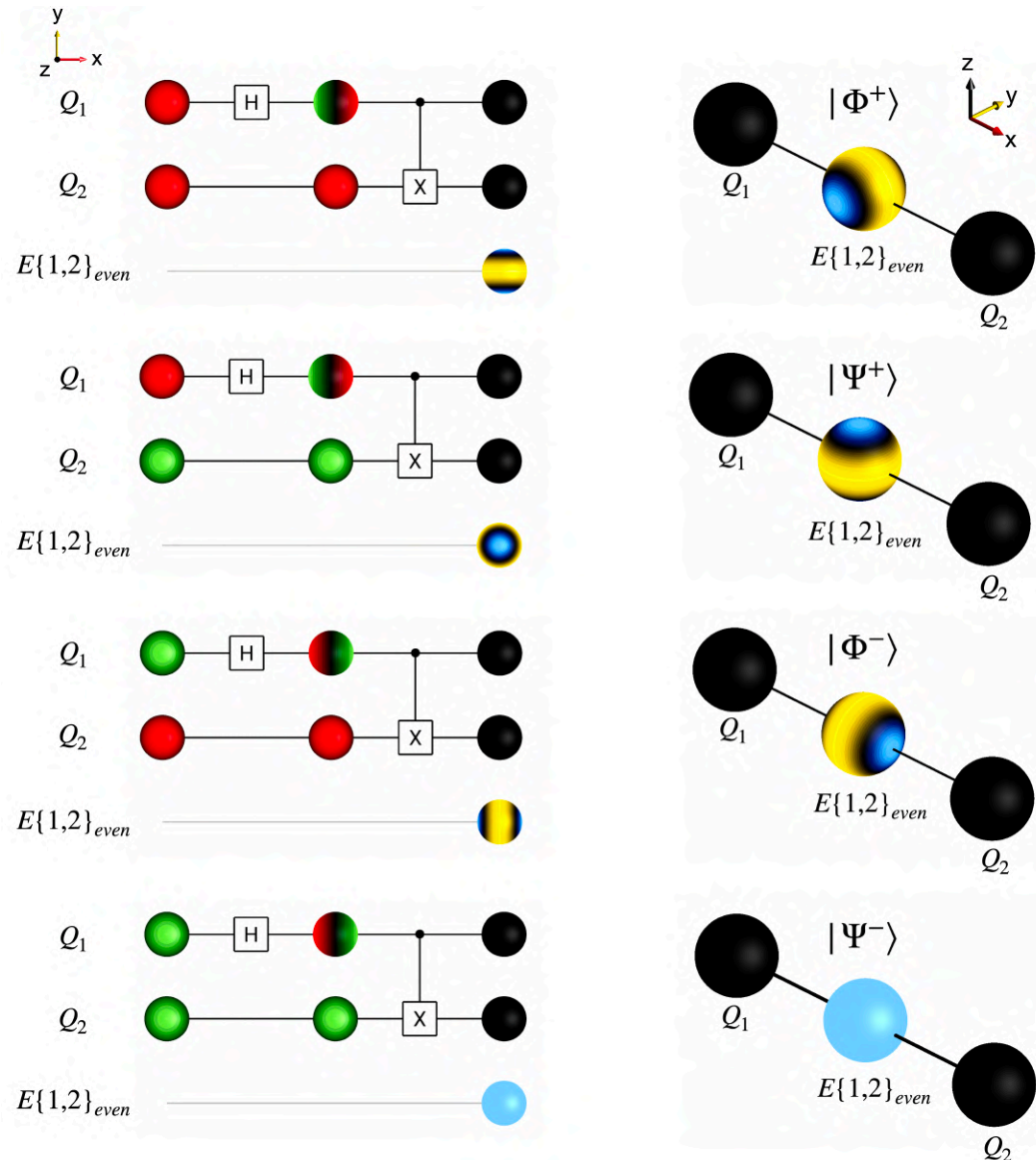


Fig. 47. BEADS representation of Bell states and generating circuits \otimes . Bell states are generated by choosing a two-qubit computational basis states and applying a circuit H_1 -CNOT $_{12}$ to the system. Depending on the choice of initial state, one obtains one of four Bell states $|\Phi^+\rangle = 1/\sqrt{2}(|00\rangle + |11\rangle)$, $|\Psi^+\rangle = 1/\sqrt{2}(|01\rangle + |10\rangle)$, $|\Phi^-\rangle = 1/\sqrt{2}(|00\rangle - |11\rangle)$, or $|\Psi^-\rangle = 1/\sqrt{2}(|01\rangle - |10\rangle)$ where all except the latter are equivalent up to global rotations.

S18 Graph states

Graph states are an important class of entangled multiqubit states which, as their name suggests, can be described by graphs and which have broad applications ranging from the study of entanglement to measurement-based quantum computing (57, 82).

Graph states can be created by applying controlled Z-gates (CZ) to an N -qubit system with all qubits in the equal superposition state $|+\rangle = 1/\sqrt{2}(|0\rangle + |1\rangle)$. In the graph which represents the state, the individual qubits correspond to vertices and each CZ_{kl} operation implements an edge between vertices k and l . In general, a graph state $|G\rangle$ is thus defined as (57)

$$|G\rangle = \prod_{k,l \in E} CZ_{kl} |+\rangle^{\otimes N} \quad (120)$$

where E denotes the set of all edges. Note that all CZ-gates mutually commute and hence they can be either applied simultaneously or sequentially in any desired order to reach the graph state $|G\rangle$. Fig. 48 shows a three-qubit quantum circuit using the BEADS representation during which several graph states are generated by consecutively adding edges to the previous graph, respectively. Indeed, in the BEADS visualization we can readily see that after the first CZ operation (CZ_{12}) only two qubits (Q_1 and Q_2) are entangled and the resulting E-Bead surface pattern of $E\{1,2\}_{even}$ is equivalent to that of the Bell states (aside from the singlet state, see section S17) up to a global rotation. Performing a second CZ operation between qubits Q_2 and Q_3 further entangles the system. As all Q-Beads are black at this point, the state is maximally entangled, i.e., entanglement exists between all qubits, even though in the corresponding graph not all vertices are connected by edges. This represents an important observation which can potentially lead to misconceptions when first studying graph states: The edges in a graph are indirectly connected to entanglement in the corresponding graph state, but missing edges do not strictly imply that the corresponding vertices, i.e., qubits, are not entangled. We can further see this when applying a third CZ-gate which gives a complete triangle graph. The state is still maximally entangled, i.e., the amount of entanglement has not changed, however, the intrinsic structure of the entanglement has altered to fully permutation symmetric components (see E-Beads) only. This graph state is the GHZ state up to a global rotation of 90° around the x-axis. The discussed states are shown in detail using an adapted layout, where the Q-Beads are arranged in the identical form as the vertices illustrating the graph states (in this case in a triangle) and where in addition the simplified display type H (cf. Table 5 and Fig. 28) is applied, and using the standard BEADS layout in Fig. 49.

Graph states further play an important role in modern quantum information science as they can be interconverted according to simple rules. As briefly discussed before, graph states are a popular choice in measurement-based quantum computing since the action of (Pauli) measurements on these states follows simple relations. For instance, a computational basis measurement performed on one qubit corresponds to removing the dedicated vertex and all its connected edges from the graph yielding a state which is again a graph state up to outcome-dependent local corrections (57, 82) This is exemplarily visualized by experiment A in Fig. 50 where qubit Q_2 is measured in the triangle graph state and we find a residual state which corresponds to the graph state with a single edge between Q_1 and Q_3 . Here, the BEADS representation allows to directly tell the correction rule which amounts to a Z-gate on all neighbors of the measured vertex which were previously connected to the latter by an edge when the measurement outcome is $m_z = -1$ (qubit measured in state $|1\rangle$). In addition, local (classically controlled) corrections, which also can be directly

inferred from the BEADS representation (e.g., \sqrt{Y} if $m_z = 1$ or $\sqrt{Y^{-1}}$ if $m_z = -1$), have to be applied to bring back the measured qubit to the superposition state $|+\rangle$. Another important transformation of graph states is given by so-called local complementation which can be achieved by applying a unitary $\sqrt{S_v}$ such that (57, 82)

$$\sqrt{S_v} = e^{-i\frac{\pi}{4}\sigma_{vx}} \prod_{k \in \mathcal{N}_v} e^{i\frac{\pi}{4}\sigma_{kz}} \quad (121)$$

where v denotes the target vertex and \mathcal{N}_v is the set of all neighboring vertices connected to v by an edge. Note that this corresponds to performing a \sqrt{X} -gate on the vertex v and a $\sqrt{Z^{-1}}$ -gate (inverse square root of Z-gate) on all neighboring vertices. Local complementation causes an inversion of all edges between vertices in \mathcal{N}_v , i.e., edges are created if they were not present before the operation and vice versa. Since local complementation only involves local gates, the total amount of entanglement is not changed, yet edges are created or eliminated. In the second experiment (**B**) illustrated in Fig. 50 we visualize how the triangle graph state can be created by local complementation of Q_2 . By comparing the complemented state with the BEADS representations of states in Fig. 49 and Fig. 50, we can indeed directly verify that the transformation yields the intended graph state up to obvious classically controlled corrections.

A different way of creating edges between non-connected vertices can be achieved by y-measurements. In contrast to z-measurements where a vertex and its connected edges are removed from a graph, y-measurements additionally lead to a complementation of the neighboring vertices similar to what was observed for local complementation (57, 82). Once again, the resulting state is a graph state up to local correction and we can directly tell the y-measurement correction rule by examining the BEADS representation of the y-measurement circuit in Fig. 50. Here, the following rule applies: A $\sqrt{Z^{-1}}$ -gate has to be performed on all vertices in the neighborhood \mathcal{N}_v of the measured qubit Q_v when the measurement outcome is $m_y = 1$ (corresponding to a state $|R\rangle = 1/\sqrt{2}(|0\rangle + i|1\rangle)$) and a \sqrt{Z} -gate in case of outcome $m_y = -1$ (state $|L\rangle = 1/\sqrt{2}(|0\rangle - i|1\rangle)$) (57, 82).

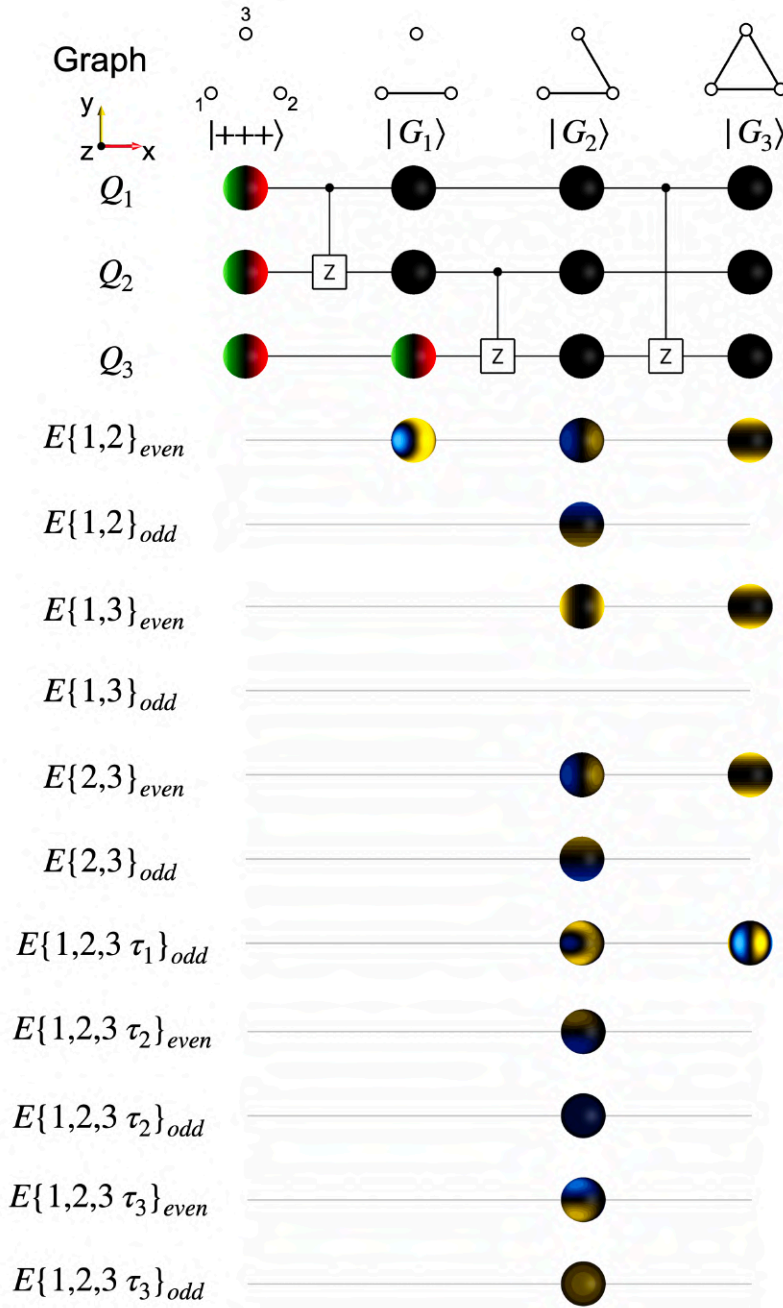


Fig. 48. Creation of three-qubit graph states by performing CZ-gates \emptyset . Starting with an initial state $|+++ \rangle = 1/\sqrt{8}(|000\rangle + |001\rangle + |010\rangle + |011\rangle + |100\rangle + |101\rangle + |110\rangle + |111\rangle)$, controlled Z-gates are performed between pairs of qubits consecutively which gives graph states $|G_k\rangle$ with the underlying graphs shown above the states. The graph states from left to right are: $|G_1\rangle = 1/\sqrt{8}(|000\rangle + |001\rangle + |010\rangle + |011\rangle + |100\rangle + |101\rangle - |110\rangle - |111\rangle)$, $|G_2\rangle = 1/\sqrt{8}(|000\rangle + |001\rangle + |010\rangle - |011\rangle + |100\rangle + |101\rangle - |110\rangle + |111\rangle)$, $|G_3\rangle = 1/\sqrt{8}(|000\rangle + |001\rangle + |010\rangle - |011\rangle + |100\rangle - |101\rangle - |110\rangle - |111\rangle)$. Note that $|G_2\rangle$ and $|G_3\rangle$ are both maximally entangled and equivalent up to local transformations (see experiment **B** in Fig. 50) despite having different numbers of edges.

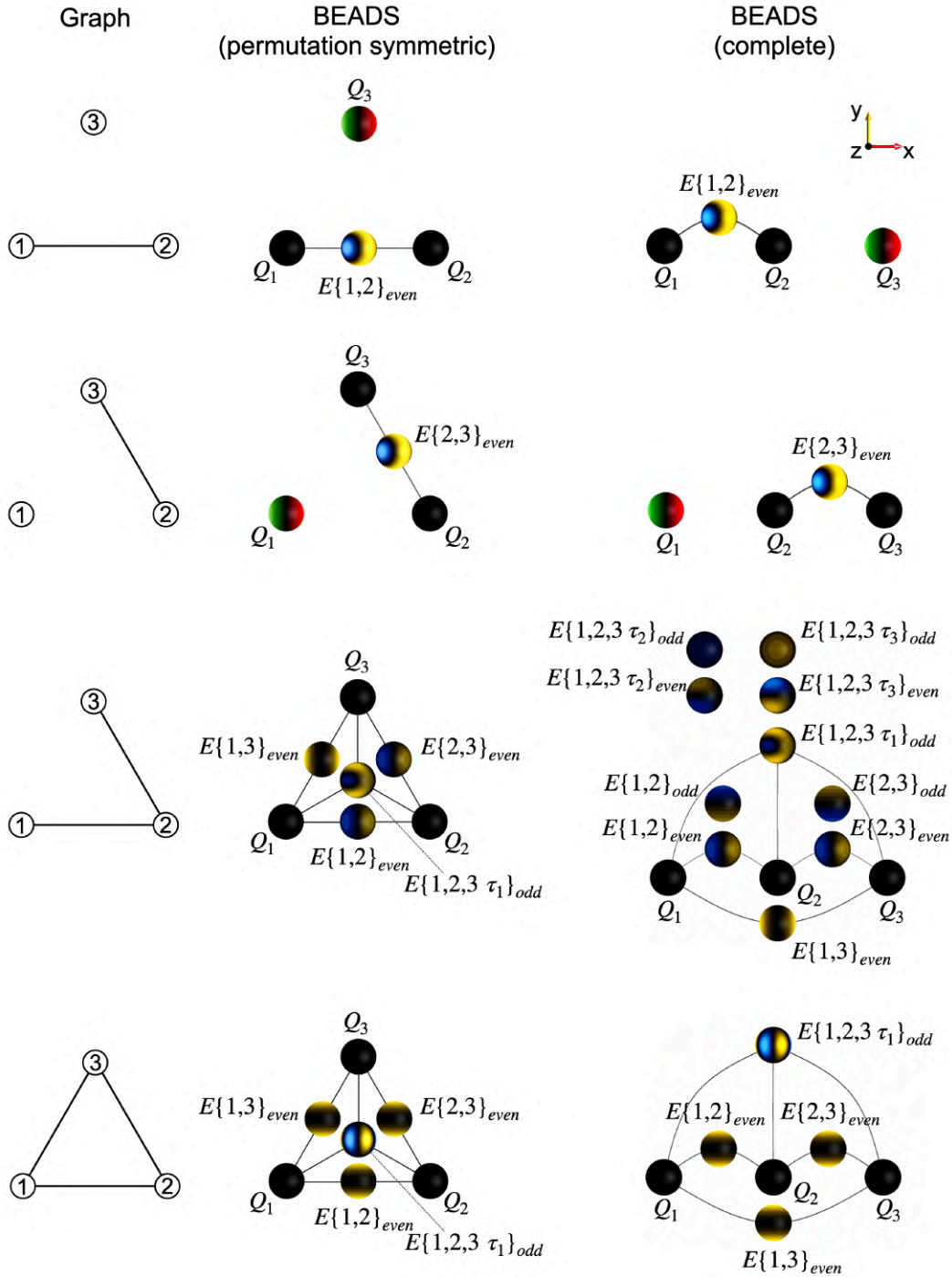
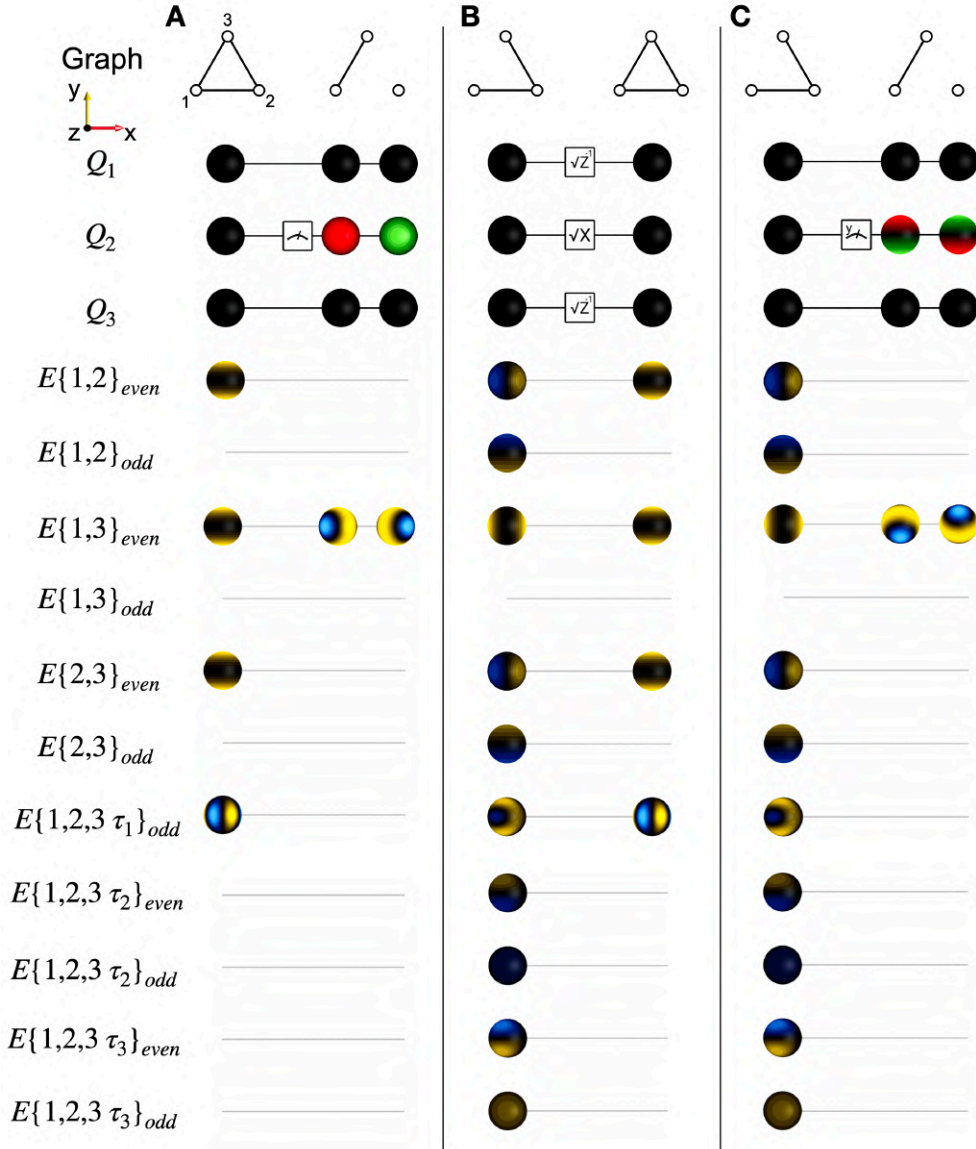


Fig. 49. BEADS visualizations of graph states. Arranged in a triangular layout of beads showing only fully permutation symmetric components (center), the BEADS representations resemble the corresponding graphs. Complete BEADS visualizations of the graph states in standard layout reveal further symmetry properties. Graph states with only one edge (top two examples) correspond to Bell pairs up to a global rotation of the entangled qubits. The chain and triangle graph states (bottom examples) are both maximally entangled, but the triangle graph state is fully symmetric (only fully symmetric E-Beads are nonzero) whereas the chain graph state (second to bottom) has considerable asymmetries.



S19 Extended analysis of Grover's algorithm

Using the BEADS representation, we can directly compare the effects of different implementations of the same circuit building block of Grover's algorithm (58) in the BEADS representation on a visual level. The remaining steps of the circuit are identical as in the initially discussed circuit (see Results section).

The top circuit in Fig. 51 displays an alternative approach to the two-qubit example shown in the Results section. Note that here we use two system qubits represented by Q-Beads Q_1 and Q_2 which are initialized in the $|0\rangle$ state and an ancilla qubit denoted Q_a which is initialized to $|1\rangle$. Applying a Hadamard to every qubit rotates the corresponding Q-Beads such that they become oriented parallel (state $|+\rangle$) or antiparallel (state $|-\rangle$) of the ancilla qubit to the x-axis. We exemplarily use the same solution 01, however, unlike in the Results section where the circuit features a phase oracle, this circuit features a Boolean oracle which is implemented by a generalized Toffoli gate on the ancilla qubit with both system qubits serving as controls or anticontrols (depending on the solution bit string being 1 or 0 at each bit position, respectively). Note that it is only the system qubits that are affected by this operation and the oracle maximally entangles the system qubits while the ancilla qubit is left unchanged in state $|-\rangle$.

Indeed, this example nicely visualizes the *phase kickback* phenomenon (2) where the kickback from the target ancilla qubit induces exactly the same transformation on the system qubits as we observed for the phase oracle U_ω in the previous circuit, yet at the cost of an additional required qubit. The following global Hadamard operation which serves as the initial basis transform of the operator U_s simply rotates the E-Beads. The gate $U_0 = 2|00\rangle\langle 00| - \mathbb{I}$, where \mathbb{I} is the identity matrix, fully disentangles the system. The terminal global Hadamard operation orients the Q-Beads along the z-axis.

The three-qubit Grover search at the bottom of Fig. 51 displays the same circuit as was introduced in the Results section. In the single solution case, using the BEADS representation one can visually estimate the probability p_{solution} to measure the correct solution. Indeed, this probability is given by (59)

$$p_{\text{solution}} = \left[\frac{1}{\sqrt{s}} \sin \left((2t + 1) \operatorname{asin} \sqrt{\frac{s}{D}} \right) \right]^2 \quad (122)$$

where s is the number of solutions, D is the size of the search space, and t is the number of Grover iterations. Indeed, after four iterations we find the Q-Beads almost in equal superpositions, i.e., a measurement at this point would yield nearly random outcomes ($p_{\text{solution}} = 1.22\%$). After six iterations though, we almost find perfect alignment ($p_{\text{solution}} = 99.98\%$) of the Q-Beads and all-zero E-Beads which corresponds to measuring the solution almost with certainty.

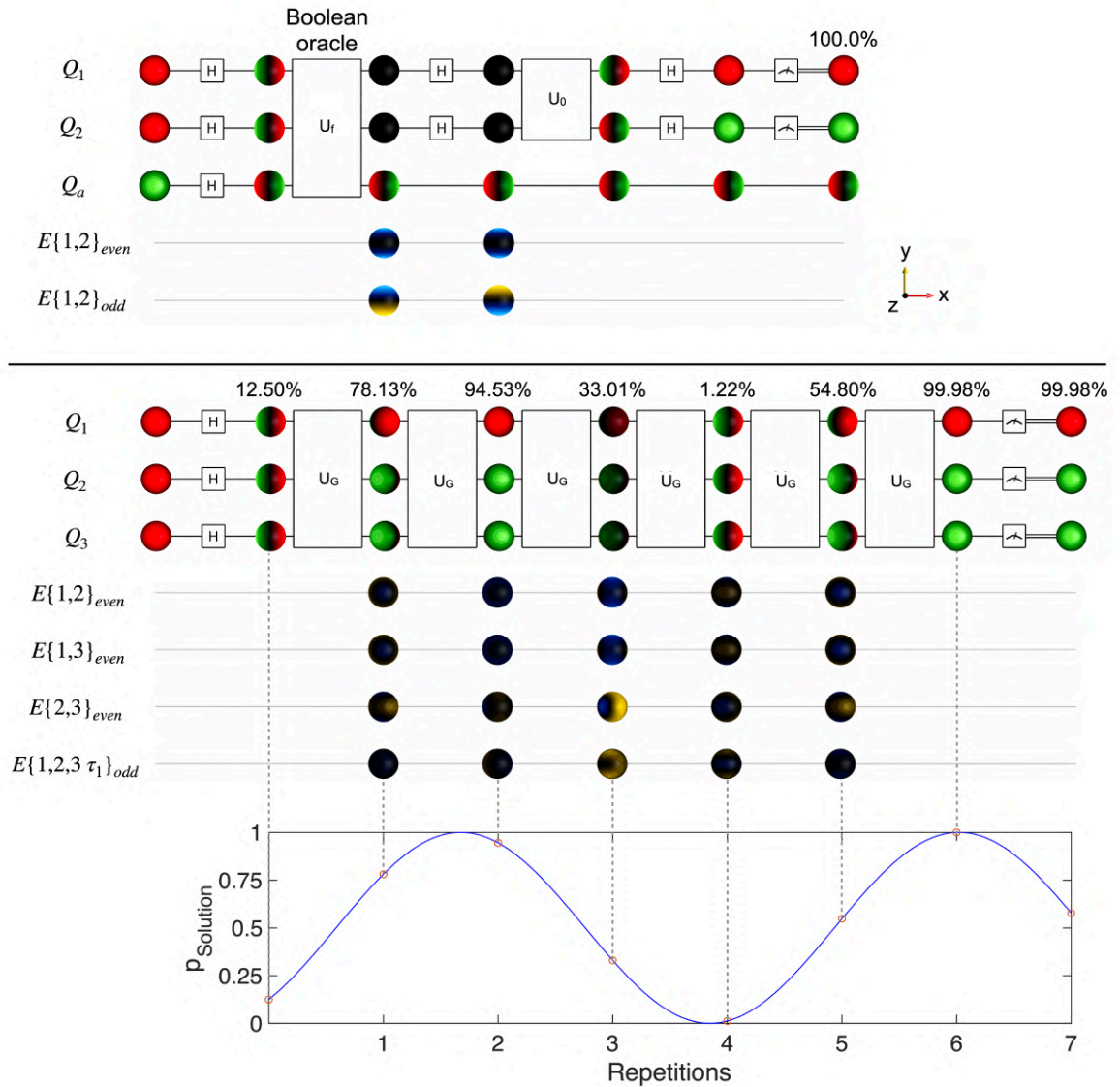


Fig. 51. BEADS-augmented circuit representation of Grover's algorithm \otimes . Grover's quantum search algorithm (58) is visualized for two system qubits using a Boolean oracle implemented by using an additional ancilla qubit (top) and three qubits (bottom). Using the BEADS representation, steps, where entanglement is maximum or minimum, can be readily identified and one can directly read off the solution. For three qubits, visualizing the outcomes of each Grover iteration U_G reveals where a solution can be measured with high probability which would otherwise have to be analyzed using analytical functions such as displayed by the plot at the bottom. In the three-qubit circuit, the probability of measuring the correct solution is indicated above the BEADS-augmented circuit after each Grover iteration.

S20 Quantum teleportation examples

Here, we provide further examples of the quantum teleportation protocol (60) for different initial states and BEADS representation variants.

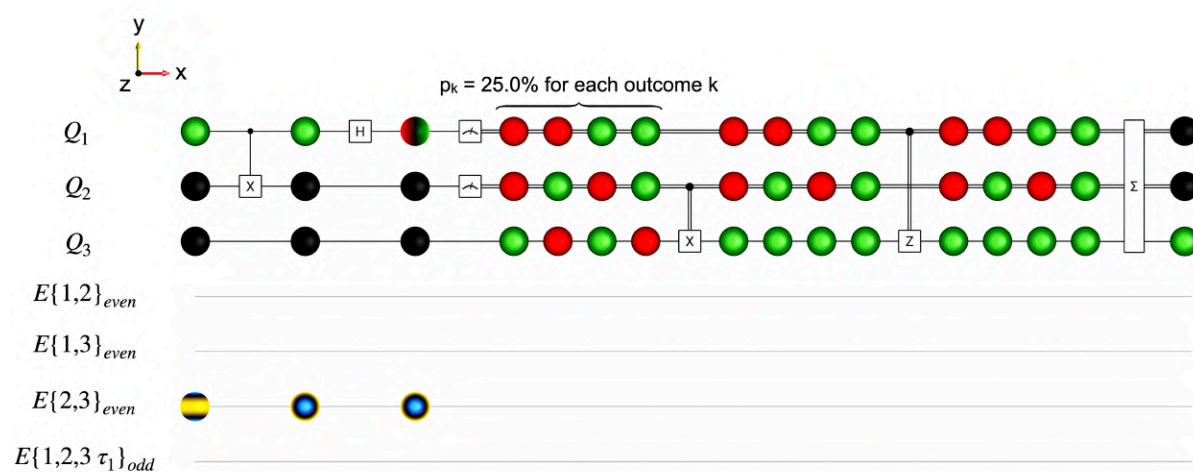


Fig. 52. Teleportation of the computational basis state $|1\rangle$. The computational basis state $|1\rangle$ is teleported from qubit Q_1 to Q_3 . Initially, qubits Q_2 and Q_3 form a Bell pair $|\Phi^+\rangle = 1/\sqrt{2}(|00\rangle + |11\rangle)$ which can be created according to the standard protocol as shown in the Results section and section S17 of the supplementary material. The initial CNOT_{12} -gate causes a simple rotation (special case, see transformations induced by multiqubit gates in section S15) of the Bell pair E-Bead which in the BEADS representation can be directly seen to be transformed into the Bell state $|\Psi^+\rangle = 1/\sqrt{2}(|01\rangle + |10\rangle)$ (cf. Fig. 47 in section S17). The subsequent Hadamard gate causes a rotation of Q_1 to give the single-qubit superposition state $|-\rangle = 1/\sqrt{2}(|0\rangle - |1\rangle)$. From the E-Bead we can further tell that Q_2 and Q_3 are now fully anticorrelated, i.e., the qubits adopt opposite basis states when one of the qubits is measured along the z-axis. Moreover, we find the Q-Bead Q_1 to be black along the z-axis which corresponds to a probability of 50% to measure the qubit in state $|1\rangle$. Hence, upon measurement of qubits Q_1 and Q_2 we observe four possible outcomes with strictly opposite outcomes of Q_2 and Q_3 due to the discussed anticorrelation and uncorrelated results for Q_1 . In this case, the following correction by a (classically) controlled X-gate on Q_3 based on the outcome of Q_2 already corrects all Q-Beads such that the teleportation is complete after this step (Q_3 is in state $|1\rangle$ in all outcome scenarios). Indeed, as can be expected, we observe no effect of the (classically) controlled Z-gate due to the axial symmetry with respect to the z-axis of Q-Beads representing computational basis states. The final step in the circuit is the weighted sum (mixed state) of all outcome scenarios which nicely depicts that we achieved to teleport the desired state $|1\rangle$ with certainty (see Q_3) independent of the measurement outcomes.

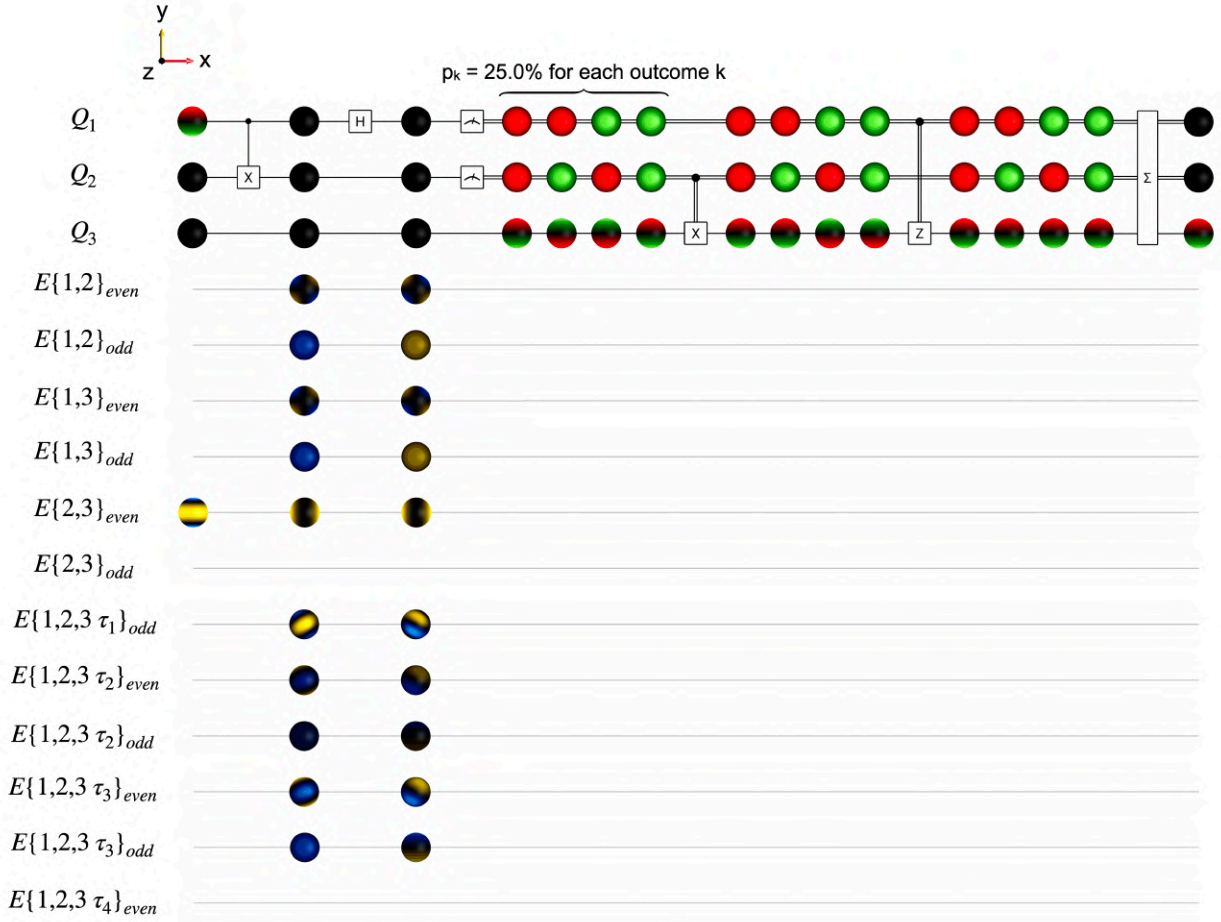


Fig. 53. Teleportation of the y-basis state $|R\rangle$. The y-basis state $|R\rangle = 1/\sqrt{2}(|0\rangle + i|1\rangle)$ is teleported from qubit Q_1 to Q_3 . Initially, qubits Q_2 and Q_3 form a Bell pair $|\Phi^+\rangle = 1/\sqrt{2}(|00\rangle + |11\rangle)$. The initial CNOT₁₂-gate entangles the first qubit with the Bell pair which can be seen by the trilinear E-Beads which arise due to genuine three-qubit entanglement. After applying the Hadamard gate to Q_1 we can see that the permutation symmetric E-Bead $E\{1,2\}_{even}$ is black along the z-axis and hence, there is no bilinear zz-correlation between Q_1 and Q_2 , i.e., equal outcomes for both qubits are to be expected with a probability of 50%. From the E-Bead $E\{2,3\}_{even}$ it becomes clear that there is only bilinear xx-correlation between the corresponding qubits and all nonzero odd bilinear E-Beads correspond to yx-correlations. A deeper analysis of the trilinear E-Beads (see section S7) reveals that the qubits are fully zzy-correlated (which can also be deduced by comparing the individual outcomes) for which Q_3 results in the state $|R\rangle$ if the product of measurement outcomes $m_1 \cdot m_2 = 1$ and in $|L\rangle = 1/\sqrt{2}(|0\rangle - i|1\rangle)$ otherwise. The following correction by the (classically) controlled X-gate on Q_3 based on the outcome of Q_2 corrects the state of Q_3 in the second scenario but transforms Q_3 in the fourth scenario such that the state of Q_3 , undesirably, is now $|L\rangle$. Yet, the (classically) controlled Z-gate undoes this action as well as it corrects Q_3 in the third outcome case such that Q_3 finally aligns according to the desired state in all scenarios. The final step in the circuit is the weighted sum (mixed state) of all outcome scenarios which nicely depicts that teleportation of the desired state $|R\rangle$ was achieved with certainty (see Q_3) independent of the measurement outcomes.

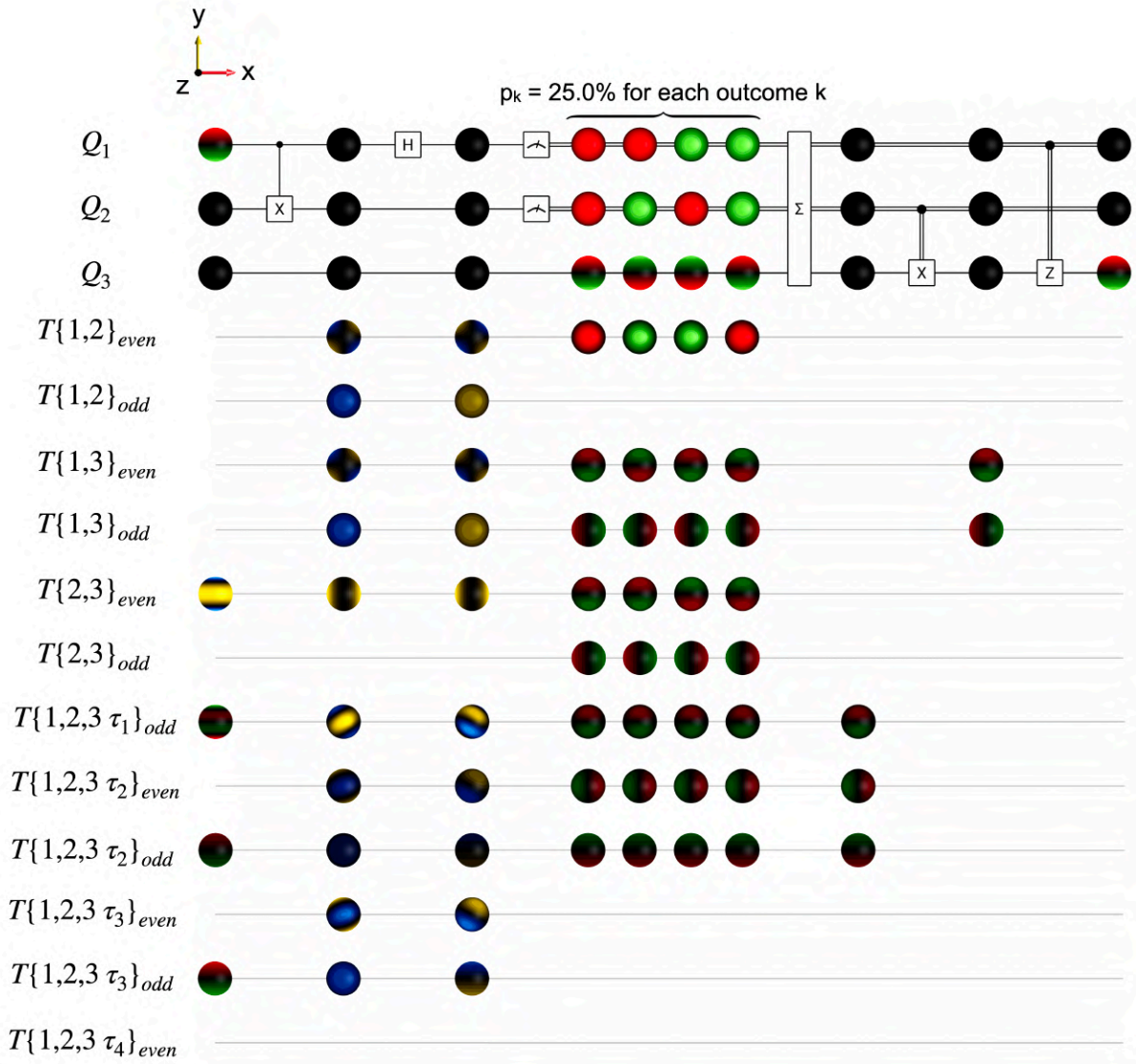


Fig. 54. Teleportation of the y-basis state $|R\rangle$ using a mixed state BEADS representation \otimes . The y-basis state $|R\rangle = 1/\sqrt{2}(|0\rangle + i|1\rangle)$ is teleported from qubit Q_1 to Q_3 (for a variant see Fig. 8 in the Results section or Fig. 53 in this chapter). A detailed description of the circuit is also given in Fig. 53. Here, the different states after the measurement are combined to form a mixed state which does only comprise correlations (all Q-Beads are black). It becomes clear though, that despite the intriguingly different BEADS representation in comparison to the pure state equivalent (Fig. 53) performing the correction steps on this mixed state still gives the desired result where Q_3 is in the state $|R\rangle$.

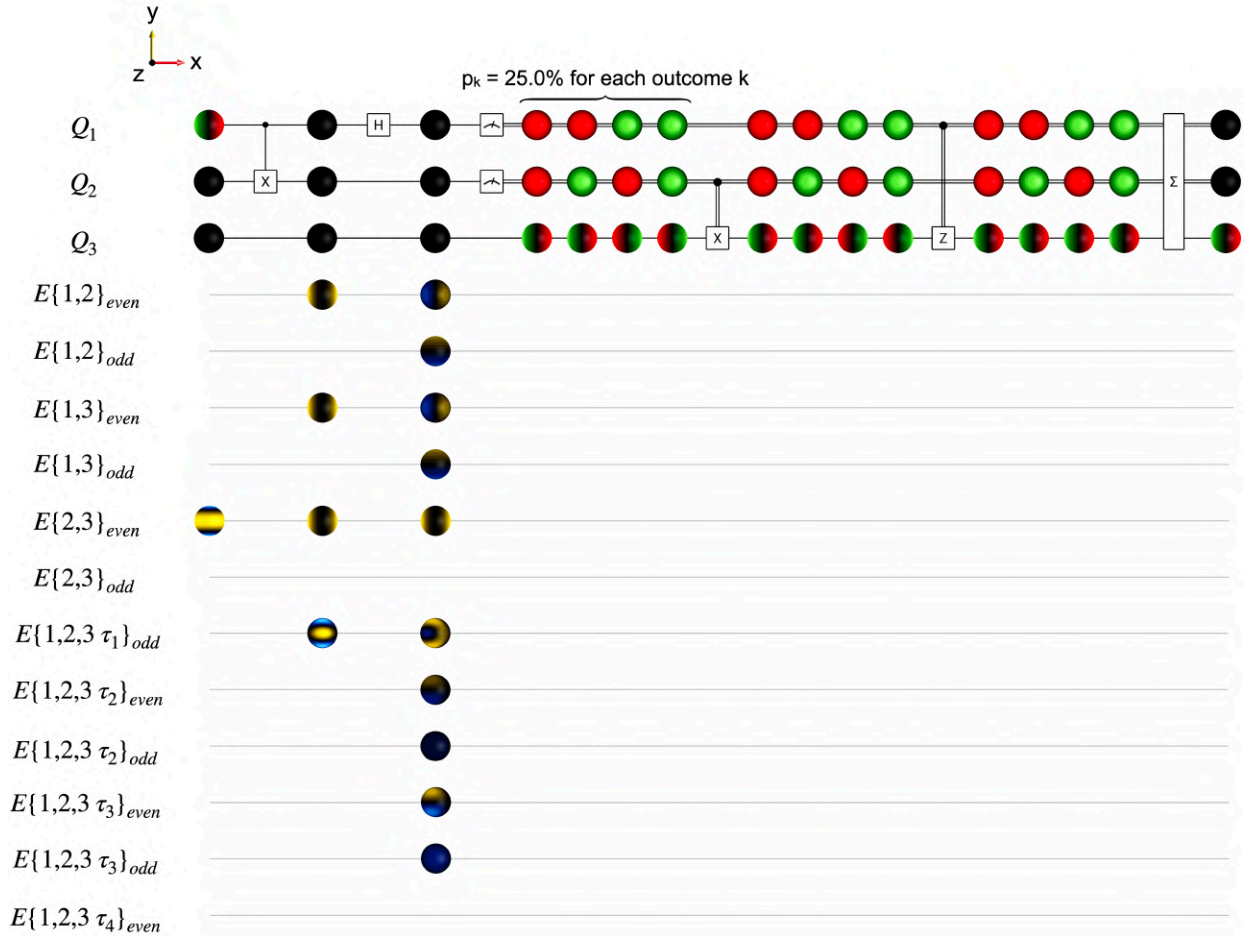


Fig. 55. Teleportation of the x-basis state $|+\rangle$. The x-basis state $|+\rangle = 1/\sqrt{2}(|0\rangle + |1\rangle)$ is teleported from qubit Q_1 to Q_3 . Initially, qubits Q_2 and Q_3 form a Bell pair $|\Phi^+\rangle = 1/\sqrt{2}(|00\rangle + |11\rangle)$. The initial $CNOT_{12}$ -gate entangles the first qubit with the Bell pair which can be seen by the trilinear E-Beads which emerge due to genuine three-qubit entanglement. After applying the Hadamard gate to Q_1 we find that all permutation symmetric E-Beads ($E\{1,2\}_{even}$, $E\{1,3\}_{even}$, $E\{2,3\}_{even}$, $E\{1,2,3\tau_1\}_{odd}$) are black along the z-axis and hence, there is no bilinear zz-correlation between the qubits i.e., equal outcomes for Q_1 and Q_2 are to be expected with a probability of 50%. Further analysis reveals full zx-correlation between qubits Q_1 and Q_3 (for mathematical details see section S7) which can also be deduced from the individual measurement outcomes of both qubits. Moreover, unlike in the teleportation of a y-basis state (Fig. 53), the measurement outcomes are trilinearly uncorrelated for the shown measurement. Hence, the discussed zx-correlation leads to Q_3 resulting in state $|+\rangle$ if the outcome of the first qubit is $m_1 = 1$ (corresponding to Q_1 in state $|0\rangle$) and in state $|-\rangle = 1/\sqrt{2}(|0\rangle - |1\rangle)$ otherwise. It then can be seen that the following correction by the (classically) controlled X-gate on Q_3 does not have any impact as the possible states of Q_3 are invariant under rotations around the x-axis. All required corrections are thus implemented by the (classically) controlled Z-gate and we find that Q_3 aligns according to the desired state in all scenarios. The final step in the circuit is to take the weighted sum (mixed state) of all outcome scenarios which also nicely depicts that teleportation of the desired state $|+\rangle$ was achieved with certainty (see Q_3) independent of the measurement outcomes.

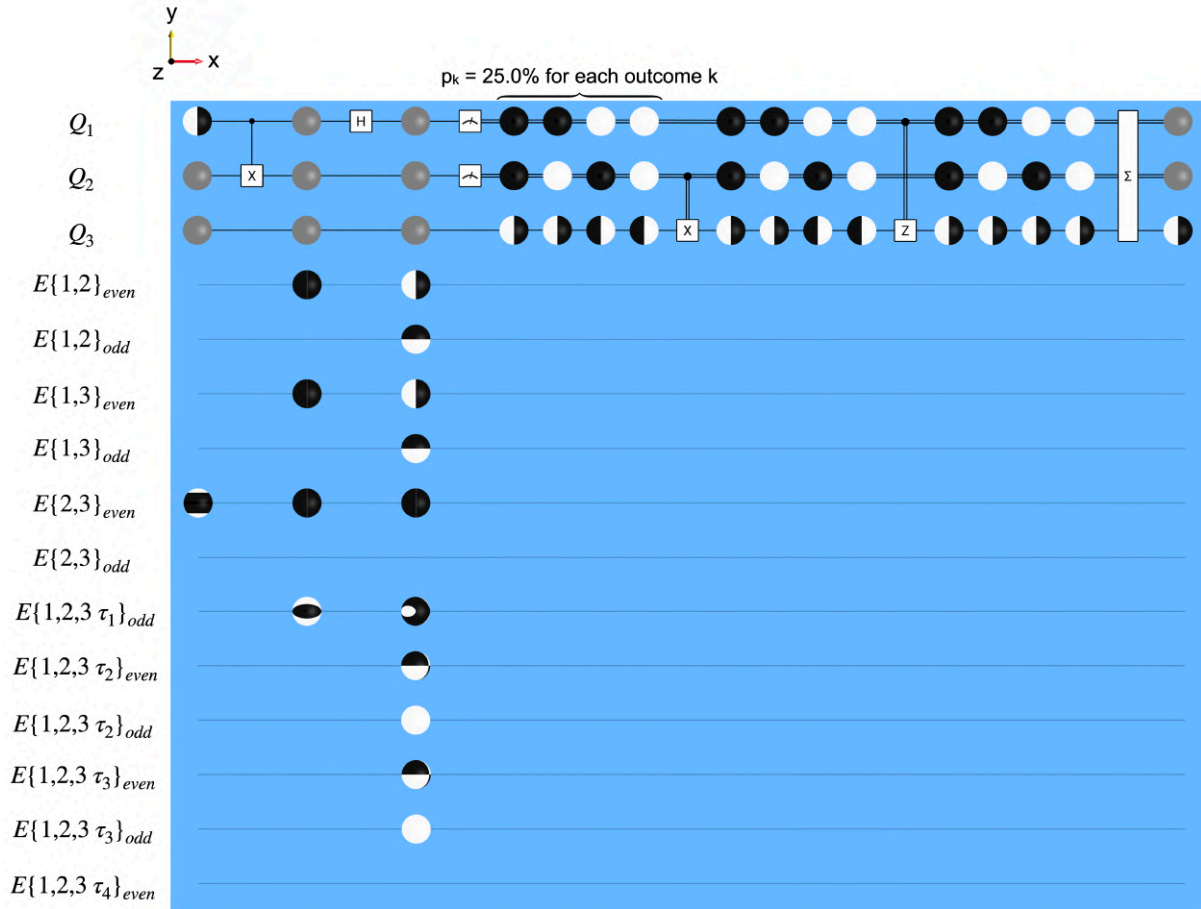


Fig. 56. Teleportation of the x-basis state using the high contrast black and white BEADS color scheme \ominus . The x-basis state $|+\rangle = 1/\sqrt{2}(|0\rangle + |1\rangle)$ is teleported from qubit Q_1 to Q_3 . For a detailed analysis see Fig. 55. The high contrast scheme (cf. section S9) allows for a clear overview on beads orientations and surface patterns which may serve as a starting point for deeper analysis as was performed in Fig. 55.

S21 Entanglement swapping

Entanglement swapping (60) represents a fundamental protocol in quantum communication which is required to implement communication modules such as the quantum repeater introduced by Briegel et. al. (61). It allows to entangle particles which are separated by large distances based on the manipulation of two Bell pairs. The basic building block hence requires four qubits and can be visualized using BEADS as is shown in Fig. 57.

The swapping protocol is exemplarily visualized for a set of initial Bell pairs between qubits Q_1 and Q_2 , as well as Q_3 and Q_4 constituting the state $|\psi\rangle = |\Phi^+\rangle \otimes |\Phi^+\rangle = 1/2(|0000\rangle + |0011\rangle + |1100\rangle + |1111\rangle)$ where once again $|\Phi^+\rangle = 1/\sqrt{2}(|00\rangle + |11\rangle)$. These Bell pairs can be created by the standard procedure discussed in the main text and in section S17 which is also visualized in the circuit in Fig. 57. A Bell measurement is then performed on Q_2 and Q_3 which, after classically controlled corrections, yields a new Bell entangled pair between Q_1 and Q_4 while the entanglement between the qubits of the initial Bell pairs is destroyed. Thus, the entanglement is said to be swapped.

It should be pointed out though, that the actual measurement operation, which are z-measurements on Q_2 and Q_3 , after a basis transformation as shown at the bottom of Fig. 57, as holds for any projective *single-qubit* measurement, cannot create entanglement. However, the measurements can be used to *localize* existing entanglement in a specific bipartite subsystem (60–62). Indeed, the preceding basis transformation, more specifically the CNOT₂₃ gate, further entangles the system yielding the state $|\psi'\rangle = 1/(2\sqrt{2})(|0000\rangle + |0100\rangle + |0011\rangle + |0111\rangle - |1101\rangle + |1001\rangle - |1110\rangle + |1010\rangle)$ which is maximally entangled and has genuine four-qubit entanglement (i.e., the entanglement is shared between all four qubits). By measuring Q_2 and Q_3 , the entanglement gets localized between Q_1 and Q_4 in form of one of the four maximally two-qubit entangled Bell states (see section S17) in dependence of the measurement outcomes. The entangled state $|\psi'\rangle$ is not shown in Fig. 57 for reasons of compactness and clarity. In the BEADS picture, we can further see that the correction operations which take the measurement outcomes of Q_2 and Q_3 as classical controls yield the same Bell pair $|\Phi^+\rangle$ between Q_1 and Q_4 for any combination of measurement outcomes.

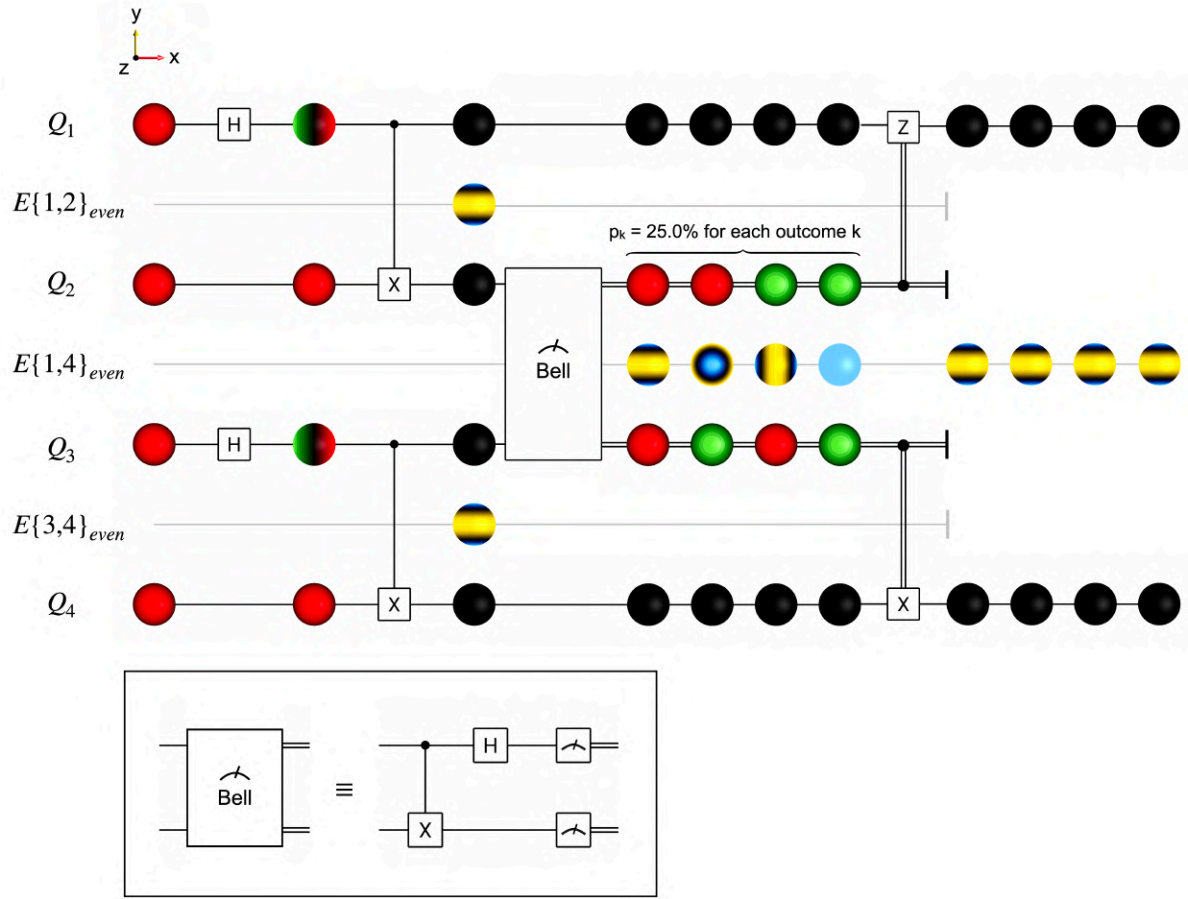


Fig. 57. BEADS representation of the entanglement swapping protocol. Bell pairs $|\Phi^+\rangle$ are created between qubits Q_1 and Q_2 as well as Q_3 and Q_4 . Performing a Bell measurement (the corresponding sequence of actual gates and measurements is shown at the bottom) on Q_2 and Q_3 and subsequent correction gates depending on the measurement outcomes swaps the entanglement to a new Bell pair $|\Phi^+\rangle$ between Q_1 and Q_4 (61).

S22 Bell's theorem

Bell's theorem (81) states that entanglement has implications for correlations of measurement outcomes in quantum mechanical experiments that cannot be explained by local hidden-variables. Here, we examine two possible approaches to demonstrate Bell's theorem in experimental implementations and highlight how these can be easily understood using the BEADS representation on a conceptual level especially in view of deriving correlation expectation values of asymmetric measurements.

1. The CHSH inequality

The CHSH inequality which can be written as (83)

$$|S| \leq 2 \quad (123)$$

and where

$$S = C(r_1, r_2) + C(\tilde{r}_1, r_2) + C(\tilde{r}_1, \tilde{r}_2) - C(r_1, \tilde{r}_2) \quad (124)$$

is one of the most prominent tools to reveal contradictions with local hidden-variable theories in quantum mechanics. It can be shown to always be fulfilled for local hidden-variable theories (83). Here, $C(a, b)$ denotes the correlation between measurement outcomes obtained when measuring one qubit in a pair of qubits along direction a and the other one in direction b . The measurement directions expressed in spherical coordinates (θ, ϕ) are chosen to be $r_1 = (0^\circ, 0^\circ)$, $\tilde{r}_1 = (90^\circ, 0^\circ)$ for the first qubit and $r_2 = (45^\circ, 0^\circ)$, $\tilde{r}_2 = (135^\circ, 0^\circ)$ for the second qubit (83). Any state for which $|S| > 2$ violates the inequality and thus contradicts the concept of local hidden-variables (83).

As an example, we examine the Bell state $|\Phi^+\rangle = 1/\sqrt{2}(|00\rangle + |11\rangle)$. As briefly stated in section S8, we can determine the correlations C *numerically* as the expectation values of the corresponding measurement operators

$$C(r_1, r_2) = \langle \Phi^+ | \sigma_{1z} \left(\frac{\sigma_{2x} + \sigma_{2z}}{\sqrt{2}} \right) | \Phi^+ \rangle = \frac{1}{\sqrt{2}} \quad (125a)$$

$$C(\tilde{r}_1, r_2) = \langle \Phi^+ | \sigma_{1x} \left(\frac{\sigma_{2x} + \sigma_{2z}}{\sqrt{2}} \right) | \Phi^+ \rangle = \frac{1}{\sqrt{2}} \quad (125b)$$

$$C(\tilde{r}_1, \tilde{r}_2) = \langle \Phi^+ | \sigma_{1x} \left(\frac{\sigma_{2x} - \sigma_{2z}}{\sqrt{2}} \right) | \Phi^+ \rangle = \frac{1}{\sqrt{2}} \quad (125c)$$

$$C(r_1, \tilde{r}_2) = \langle \Phi^+ | \sigma_{1z} \left(\frac{\sigma_{2x} - \sigma_{2z}}{\sqrt{2}} \right) | \Phi^+ \rangle = -\frac{1}{\sqrt{2}} \quad (125d)$$

which gives $S = 2\sqrt{2}$ and thus violates the inequality shown in Eq. 123.

Using the BEADS representation, we can choose between three different strategies to derive these correlations *graphically*. Note that Bell test experiments such as those based on finding violations of the CHSH inequality yield statistical results, i.e., must be repeated many times to show a contradiction with local-hidden variable theory.

As a first and preferred option, which is denoted method **A** in Fig. 58, we can transform the Bell state by applying local rotations around the $-y$ -axis by the polar angles defining the measurement direction for each of the qubits which effectively rotate the original measurement direction vectors onto the z -axis. For example, for measurement directions (\tilde{r}_1, r_2) we apply a 90° -rotation on Q_1

and a 45° -rotation on Q_2 , around the $-y$ -axis, respectively. This enables us to treat the originally asymmetric measurement as a symmetric measurement in the computational basis and we can directly read off the corresponding correlations as the value of the symmetric E-Bead $E\{1,2\}_{even}$ along the z -axis. Note that since $|\Phi^+\rangle$ is maximally entangled, $E\{1,2\}_{even}$ is equivalent to the total correlation bead $T\{1,2\}_{even}$. Moreover, since we perform a symmetric measurement, $E\{1,2\}_{odd}$ is irrelevant for the interpretation. As can be seen in Fig. 58, for any combination of measurement directions except (r_1, \tilde{r}_2) we obtain the same positive correlation expectation value of $C = 1/\sqrt{2}$ along the z -axis. For (r_1, \tilde{r}_2) , which corresponds to the subtracted term in Eq. 124, we get an anticorrelated state with $C = -1/\sqrt{2}$, and thus, reach a value $S = 4/\sqrt{2} = 2\sqrt{2} > 2$ in total, clearly violating inequality 123.

As a second approach **B**, we can perform a projective measurement on one of the qubits, e.g., on the first qubit Q_1 along direction r_1 (z -axis) or \tilde{r}_1 (x -axis), exclusively. Note that the order of measurements is irrelevant, i.e., it is also possible to measure Q_2 first. However, in the following, we assume the case where Q_1 is measured. We can predict the state of the second qubit Q_2 based on the BEADS representation of the initial Bell state which is yellow and hence fully correlated ($E\{1,2\}_{even} = 1$) in both measurement directions (see Fig. 59 and the color scale in Fig. 5 of the Results section). Hence, upon measuring Q_1 , Q_2 will align identically as Q_1 . The outcomes of Q_1 are assigned values of ± 1 corresponding to the eigenvalues of the measurement operator, e.g., in case of a z -measurement we assign 1 if we measured Q_1 in state $|0\rangle$ and -1 if we measured $|1\rangle$. It is now possible to directly read off the single qubit expectation values of Q_2 along r_2 and \tilde{r}_2 . All possible scenarios are shown in Fig. 59 and the single-qubit expectation values are illustrated by corresponding color patches and numerical values. Finally, the wanted correlation values can be calculated as the product of single-qubit expectation values determined for both qubits and we get:

$$C(r_1, r_2) = C(\tilde{r}_1, r_2) = C(\tilde{r}_1, \tilde{r}_2) = 1 \cdot \frac{1}{\sqrt{2}} = (-1) \cdot \left(-\frac{1}{\sqrt{2}}\right) = \frac{1}{\sqrt{2}} \quad (126)$$

and

$$C(r_1, \tilde{r}_2) = (-1) \cdot \frac{1}{\sqrt{2}} = 1 \cdot \left(-\frac{1}{\sqrt{2}}\right) = -\frac{1}{\sqrt{2}} \quad (127)$$

Last, we put into perspective how one can apply the relations presented in section S8 to derive the correlations numerically solely based on the BEADS representation of $|\Phi^+\rangle$ (method **C**). Since all measurements are performed within the xz -half plane, we can apply Eq. 97. Moreover, as the examined Bell state does not have an antisymmetric component we can further simplify to

$$\begin{aligned} \langle M \rangle = C(a, b) = & \cos \Delta_\theta \left(\langle T_{0,0}^{\{k,l\}_{even'}} \rangle + \frac{\langle T_{2,0}^{\{k,l\}_{even'}} \rangle}{4} + \frac{\langle T_{2,2}^{\{k,l\}_{even'}} \rangle}{2} \right) + \\ & \cos \Sigma_\theta \left(\frac{3 \langle T_{2,0}^{\{k,l\}_{even'}} \rangle}{4} - \frac{\langle T_{2,2}^{\{k,l\}_{even'}} \rangle}{2} \right) + \\ & \sin \Sigma_\theta \langle T_{2,1}^{\{k,l\}_{even'}} \rangle \end{aligned} \quad (128)$$

The required scaled tensor operator expectation values (cf. section S8) can then be obtained by reading off the E-Bead values at characteristic positions as indicated in Fig. 60 and inserting them in Eq. 94 which gives

$$\langle T_{0,0}^{\{k,l\}even'} \rangle = \frac{1}{3}(R_x + R_y + R_z) = \frac{1}{3}(1 - 1 + 1) = \frac{1}{3} \quad (129a)$$

$$\langle T_{2,0}^{\{k,l\}even'} \rangle = \frac{1}{3}(2R_z - R_x - R_y) = \frac{1}{3}(2 - 1 + 1) = \frac{2}{3} \quad (129b)$$

$$\langle T_{2,1}^{\{k,l\}even'} \rangle = R_{xz} - \frac{1}{2}(R_x + R_z) = 1 - \frac{1}{2}(1 + 1) = 0 \quad (129c)$$

$$\langle T_{2,2}^{\{k,l\}even'} \rangle = \frac{1}{2}(R_x - R_y) = 1 \quad (129d)$$

and by inserting these values in Eq. 128, as in the previously discussed approaches, we again obtain $C(r_1, r_2) = C(\tilde{r}_1, r_2) = C(\tilde{r}_1, \tilde{r}_2) = 1/\sqrt{2}$ and $C(r_1, \tilde{r}_2) = -1/\sqrt{2}$.

2. The GHZ experiment

Another illustrative way to prove Bell's theorem is given by the GHZ experiment (84). Here, we leave a numerical analysis such as was described in Eqs. 125 to the reader and focus on the BEADS representation.

We start with the well-known GHZ state $|\text{GHZ}\rangle = 1/\sqrt{2}(|000\rangle + |111\rangle)$ which is visualized in Fig. 61. Unlike in the previously introduced Bell test experiments, absolute contradictions between quantum mechanics and local hidden-variable theory can be revealed by using only four different measurement settings in the GHZ experiment. These settings include a symmetric measurement of all qubits along the x-axis and three asymmetric three-qubit measurements where two qubits are measured along the y-axis and one qubit is measured along the x-axis (i.e., a $y_1y_2x_3$, a $y_1x_2y_3$, and a $x_1y_2y_3$ -measurement). It is then possible to compare the product of measured correlations

$$\Pi_C = \langle \sigma_{1x}\sigma_{2x}\sigma_{3x} \rangle \cdot \langle \sigma_{1x}\sigma_{2y}\sigma_{3y} \rangle \cdot \langle \sigma_{1y}\sigma_{2x}\sigma_{3y} \rangle \cdot \langle \sigma_{1y}\sigma_{2y}\sigma_{3x} \rangle \quad (130)$$

with the corresponding prediction of local hidden variable theory Π_{LHV} , where the measurement outcome of every single qubit k along direction d is predetermined by a hidden-variable v_{kd} for which

$$\Pi_{LHV} = v_{1x}v_{2x}v_{3x} \cdot v_{1x}v_{2y}v_{3y} \cdot v_{1y}v_{2x}v_{3y} \cdot v_{1y}v_{2y}v_{3x} = v_{1x}^2v_{1y}^2v_{2x}^2v_{2y}^2v_{3x}^2v_{3y}^2 \quad (131)$$

It is clear, that due to all hidden-variables being real numbers, Π_{LHV} must be positive. An illustrative explanation of the GHZ-experiment is given in (85).

To predict possible outcomes of the fully symmetric x-measurement, we analyze the $E\{1,2,3 \tau_1\}_{odd}$ bead ($= T\{1,2,3 \tau_1\}_{odd}$ due to the state being maximally entangled) which reveals a maximum positive three-qubit correlation expectation value of 1 along the x-axis. At this point, it should be recalled that a positive n -qubit correlation implies an even number of qubits in the "down" state (eigenvalue -1) with respect to the corresponding measurement direction after the measurement. Hence, we expect outcomes $|+++ \rangle$, $|+-- \rangle$, $|-+- \rangle$, and $|--+\rangle$ with equal probability

(25%). For the different asymmetric three-qubit measurements, the corresponding correlations can once more be determined using different approaches in the BEADS representation.

As discussed for CHSH inequalities, we can first transform the GHZ state such that the measurement direction vectors are effectively coaligned (variant **A** in Fig. 61). This can be efficiently achieved by applying inverse square roots of Pauli-Z gates on the two qubits which are to be measured along the y-axis. This rotates all measurement directions to the x-axis, and thus, allows us to view the intended measurement as a fully symmetric x-measurement and to directly read off the measurement expectation value along the x-axis. Note that all bilinear E-Beads in the BEADS representation of the GHZ state are axially symmetric and $E\{1,2,3 \tau_1\}_{odd}$ has a threefold rotational symmetry with respect to the z-axis, the transformation results in only $E\{1,2,3 \tau_1\}_{odd}$ being rotated by $(\varphi_1 + \varphi_2 + \varphi_3)/3$ around the negative z-axis. Here, two of the rotation angles φ_k , where the index denotes the k -th qubit, are 90° (square root of Z), whereas the third angle is 0, respectively, and thus, the trilinear E-Bead is rotated by 60° around the negative z-axis. It is now possible to directly read off the correlation expectation value along the x-axis which results in being -1 , i.e., full anticorrelation, for any of the asymmetric measurements. We expect measurement outcomes $|---\rangle$, $|-++\rangle$, $|+-+\rangle$, and $|++-\rangle$ with equal probability (25%).

We obtain the same correlation values if we perform single-qubit measurements on two of three qubits (variant **B** in Fig. 61). For instance, we measure the first qubit Q_1 along the x-axis. This results in Q_2 and Q_3 being entangled in one of two Bell states ($|\Phi^+\rangle$ or $|\Phi^-\rangle$) depending on the outcome of Q_1 . If we then proceed to measure Q_2 along the y-axis, Q_2 and Q_3 , since being maximally anticorrelated ($|\Phi^+\rangle$, blue color along y-axis) or correlated ($|\Phi^-\rangle$, yellow color along y-axis), adopt opposite or equal y-basis states, respectively. In Fig. 61, it is clear, that possible measurement outcomes for the $x_1 y_2 y_3$ -measurement are $|+RL\rangle$, $|+LR\rangle$, $| -RR\rangle$, and $| -LL\rangle$. As was discussed previously, we can now form products of single-qubits outcomes which here strictly results in overall correlation values of -1 .

Alternatively (method **C** in Fig. 61), we can apply the relations introduced in section S8. To determine the expectation values for a particular combination of measurement directions, e.g., $x_1 y_2 y_3$, numerically based on the BEADS representation of $|\text{GHZ}\rangle$, we first identify any tensor operator component that is dependent on the desired measurement directions in Eq. 99 (see section S8). For instance, for an $x_1 y_2 y_3$ -measurement, only the $E\{1,2,3 \tau_1\}_{odd}$ E-Bead has non-zero expectation values for the GHZ-state. Thus, we only find the components $T_{1,1}^{\{1,2,3 \tau_1\}_{odd}}$ and $T_{3,3}^{\{1,2,3 \tau_1\}_{odd}}$ to be relevant and Eq. 99 simplifies to

$$\langle \sigma_{1x} \sigma_{2y} \sigma_{3y} \rangle = \frac{1}{3} \langle T_{1,1}^{\{1,2,3 \tau_1\}_{odd'}} \rangle - \langle T_{3,3}^{\{1,2,3 \tau_1\}_{odd'}} \rangle \quad (132)$$

Note that this equation only includes τ_1 operator components as the examined GHZ state does not show any further trilinear symmetry components.

We can calculate the expectation values $\langle T_{1,1}^{\{1,2,3 \tau_1\}_{odd'}} \rangle$ and $\langle T_{3,3}^{\{1,2,3 \tau_1\}_{odd'}} \rangle$ by reading off spherical function values and applying them according to equations Eq. 100 (see section S8). We obtain

$$\begin{aligned}
\langle T_{1,1}^{\{1,2,3 \tau_1\}odd'} \rangle &= \frac{4}{15} R_x + \frac{\sqrt{2}}{5} (R_{xy} - R_{(-x)y}) + \frac{\sqrt{10}}{12} (R_1 + R_2) \\
&= \frac{4}{15} + \frac{\sqrt{2}}{5} \left(-\frac{1}{\sqrt{2}} - \frac{1}{\sqrt{2}} \right) + \frac{\sqrt{10}}{12} \left(\frac{2}{5} \sqrt{\frac{2}{5}} + \frac{2}{5} \sqrt{\frac{2}{5}} \right) = 0
\end{aligned} \tag{133a}$$

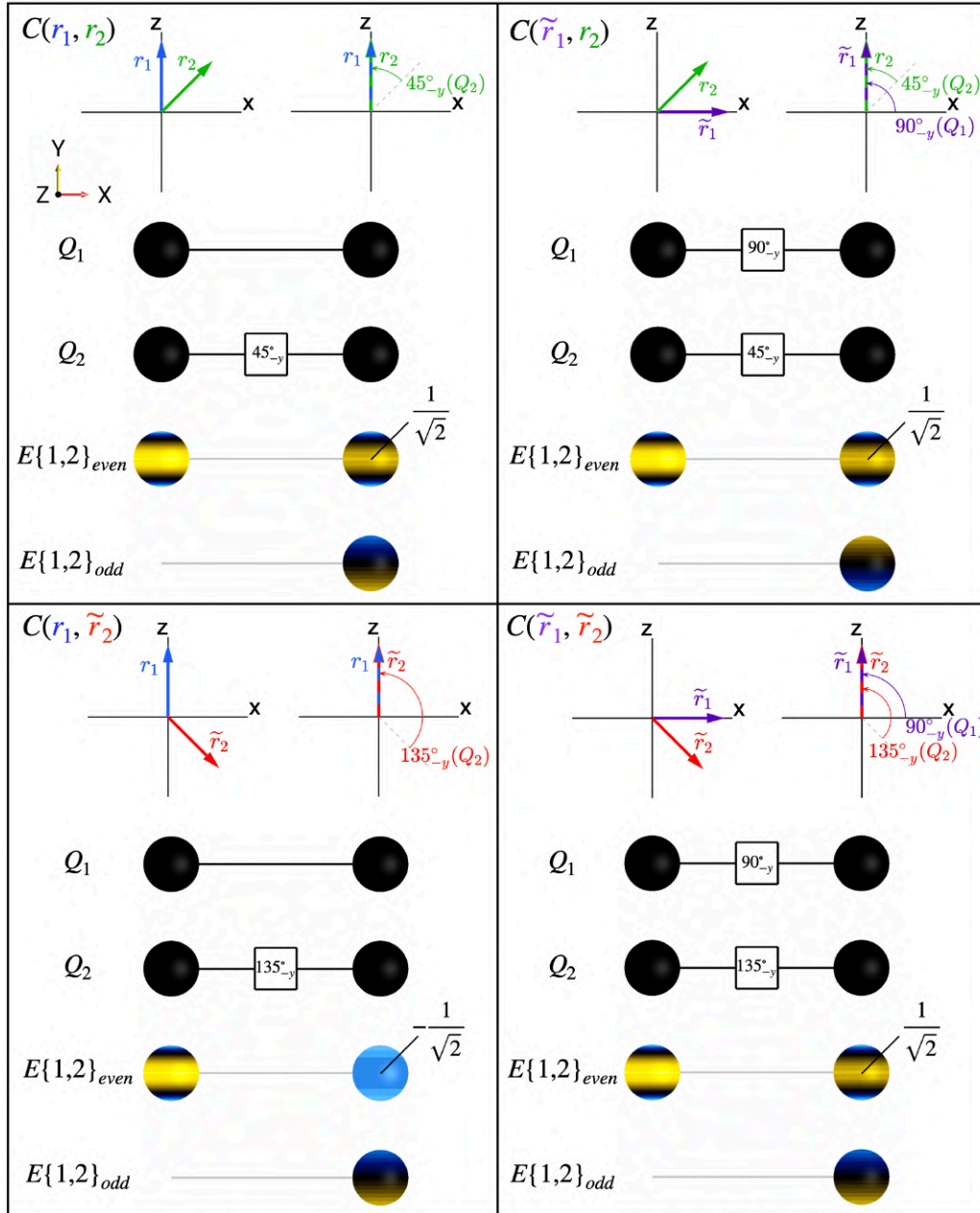
$$\langle T_{3,3}^{\{1,2,3 \tau_1\}odd'} \rangle = \frac{1}{2} R_x + \frac{1}{2\sqrt{2}} (R_{(-x)y} - R_{xy}) = \frac{1}{2} + \frac{1}{2\sqrt{2}} \left(\frac{1}{\sqrt{2}} + \frac{1}{\sqrt{2}} \right) = 1 \tag{133b}$$

Fig. 61 explicitly shows the spherical function values at vertices R_x , $R_{(-x)y}$ and R_{xy} , R_1 , and R_2 . Repeating this procedure for all remaining measurement directions yields

$$\langle \sigma_{1x} \sigma_{1y} \sigma_{1y} \rangle = \langle \sigma_{1y} \sigma_{1x} \sigma_{1y} \rangle = \langle \sigma_{1y} \sigma_{1y} \sigma_{1x} \rangle = \frac{1}{3} \langle T_{1,1}^{\{1,2,3 \tau_1\}odd'} \rangle - \langle T_{3,3}^{\{1,2,3 \tau_1\}odd'} \rangle = -1 \tag{134}$$

which matches the results obtained with methods **A** and **B**.

Based on our findings for the GHZ state, i.e., full correlation when measuring all qubits along the x-axis but full anticorrelation when measuring one qubit along the x-axis and the remaining qubits along the y-axis, we can now examine whether these findings are compatible with the principle of locality. From the obtained correlations, it is clear that $\Pi_C = 1 \cdot (-1) \cdot (-1) \cdot (-1) = -1$. Indeed, if quantum mechanics would be a local theory, the outcomes observed for each individual qubit would instead multiply to 1 according to Eq. 131.



$$\begin{aligned}
 [45^\circ_y] &= [90^\circ_x] [45^\circ_z] [90^\circ_{-x}] = [\sqrt{X}] [T^{-1}] [\sqrt{X}^{-1}] \\
 [90^\circ_{-y}] &= [90^\circ_x] [90^\circ_{-z}] [90^\circ_{-x}] = [\sqrt{X}] [S^{-1}] [\sqrt{X}^{-1}] \\
 [135^\circ_{-y}] &= [90^\circ_x] [135^\circ_z] [90^\circ_{-x}] = [\sqrt{X}] [S^{-1}] [T^{-1}] [\sqrt{X}^{-1}]
 \end{aligned}$$

Fig. 58. CHSH inequality in case of the Bell state $|\Phi^+\rangle = 1/\sqrt{2}(|00\rangle + |11\rangle)$ – method A. The required correlations (denoted in the top left corners) between measurement outcomes which are applied in the CHSH inequality can be determined from the BEADS representation by applying local rotations to the qubits such that the measurement directions are effectively transformed to the z -axis which allows to directly read off the correlation value from $E\{1,2\}_{even}$ along the z -axis.

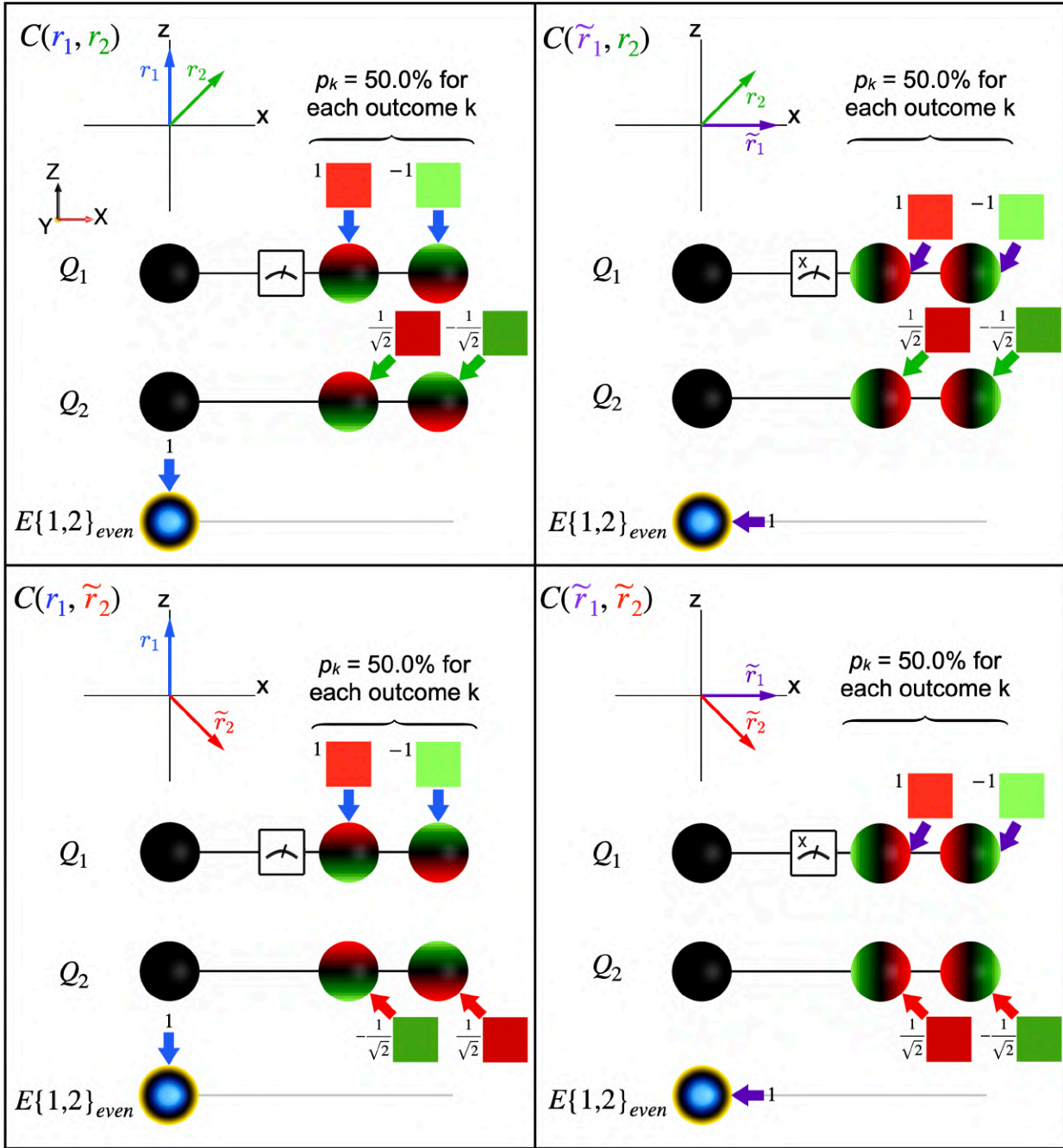


Fig. 59. CHSH inequality in case of the Bell state $|\Phi^+\rangle = 1/\sqrt{2}(|00\rangle + |11\rangle)$ – method B. By performing single-qubit measurements on one qubit, the correlations (denoted in the top left corner of every box) which have to be applied in the CHSH inequality can be calculated as products of the single-qubit expectation values obtained from the corresponding Q-Beads.

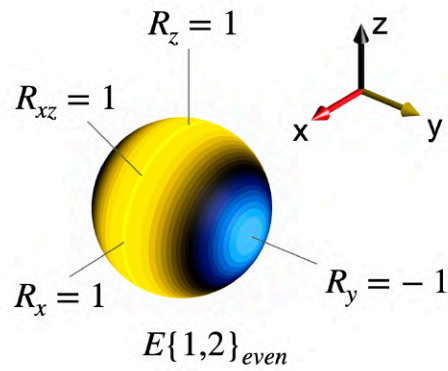


Fig. 60. CHSH inequality in case of the Bell state $|\Phi^+\rangle = \frac{1}{\sqrt{2}}(|00\rangle + |11\rangle)$ – method C. By reading off the spherical function values of $E\{1,2\}_{even}$ along the indicated directions, the correlations of interest can be determined numerically.

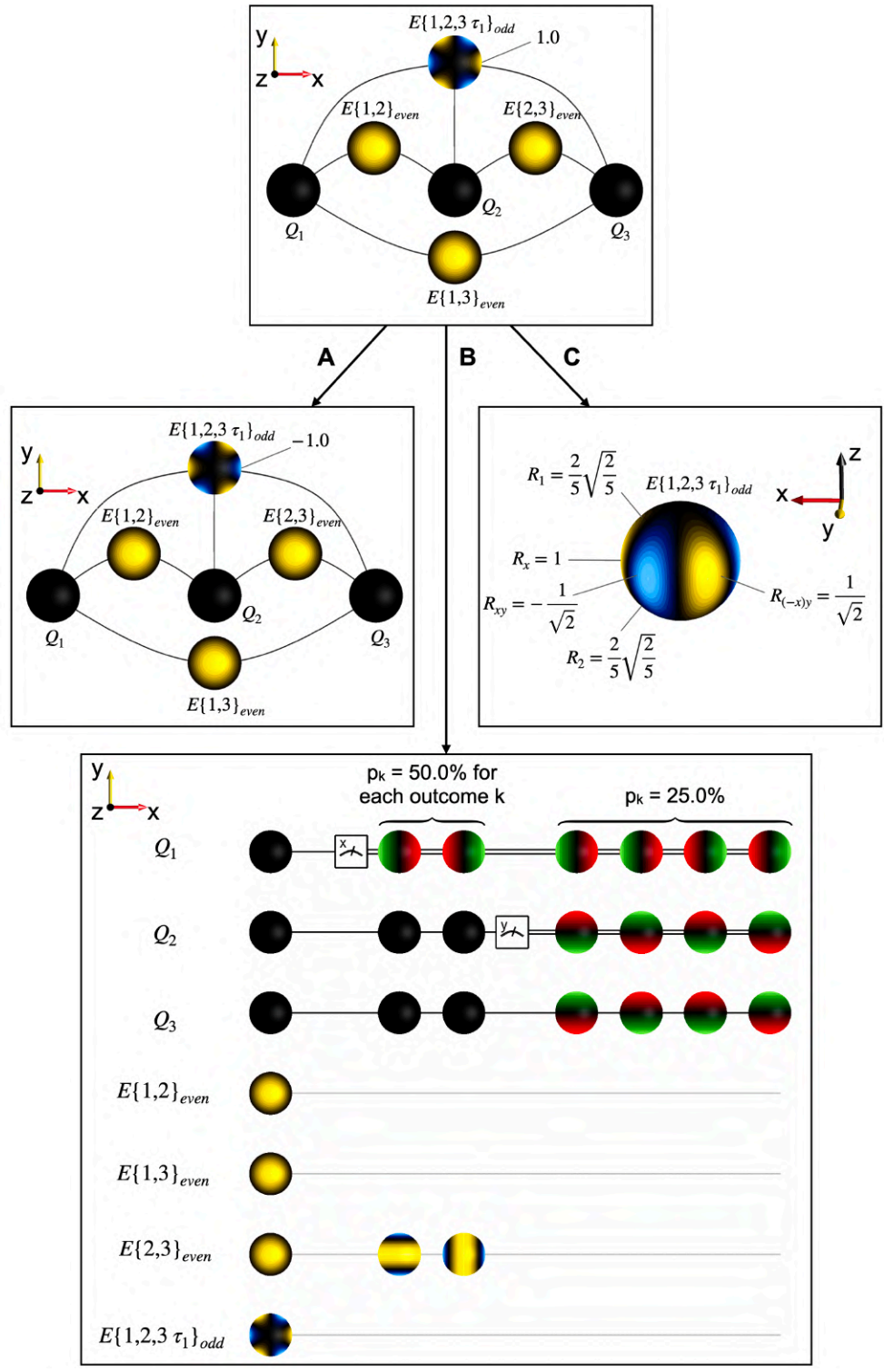


Fig. 61. The GHZ experiment. Measurement outcomes are fully correlated when the GHZ-state is measured along the x-axis, yet the outcomes are fully anti-correlated when measuring two qubits along the y- and the remaining qubit along x-axis which contradicts a local hidden-variable theory. Using BEADS, the corresponding correlations can be once more determined by local transformations (A), single-qubit measurements (B) or numerically (C).

S23 QuBeads – a dynamical simulation software using the BEADS representation

We have developed a powerful interactive software named *QuBeads application*, *QuBeads app*, or simply *QuBeads* which uses the BEADS representation to simulate and visualize the dynamics of qubit systems in quantum circuits. QuBeads is a modified descendant of the SpinDrops app (40) which was developed to offer DROPS visualizations in the context of nuclear magnetic resonance. Currently, the QuBeads software is able to support visualizations of system of up to three qubits and will be extended to feature larger qubit systems in the near future. The software is highly responsive, offers all variants of the BEADS representation discussed in this article, and features a palette of the most common quantum gates and supports the setup of custom quantum circuits following a user-friendly intuitive modular approach that does not require any coding. Indeed, all BEADS visualizations in this article were generated by using the QuBeads software.

QuBeads can be downloaded and installed on all common operating systems. The software (beta version) and detailed installation guides are available via the following link:

<https://github.com/denhub97/QuBeads>

In QuBeads, we offer two main visualization modes: the standard BEADS mode (Fig. 62) which provides a visualization of the current system state at any point during the simulation and the so-called BEADS-augmented circuit mode (Fig. 63) which provides a visualization of the chosen quantum circuit and provides the BEADS representations of the system states after each operation (i.e., gates or measurements).

Note that for dynamical simulations in QuBeads, the action of a gate is distributed over the *entire* timestep in the corresponding circuit visualization to optimally visualize the dynamics. Timesteps are separated by vertical lines in standard BEADS mode circuits (see, e.g., bottom of Fig. 62) and by beads in the BEADS-augmented circuit mode (cf. Fig. 63).

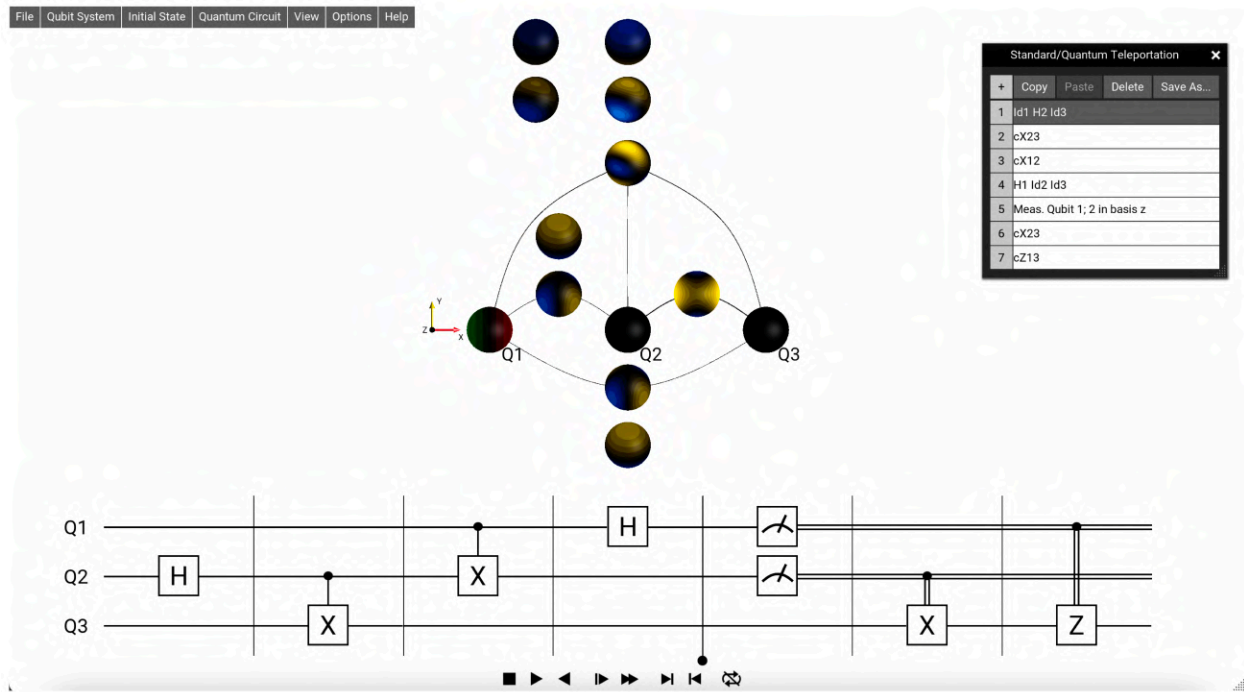


Fig. 62. Standard BEADS mode in the QuBeads app. A custom quantum circuit can be simulated dynamically. The system state is monitored by a corresponding BEADS representation at runtime. In QuBeads, quantum circuits can be configured by an intuitive modular setup which uses a graphical interface (see smaller window) and does not require any coding.

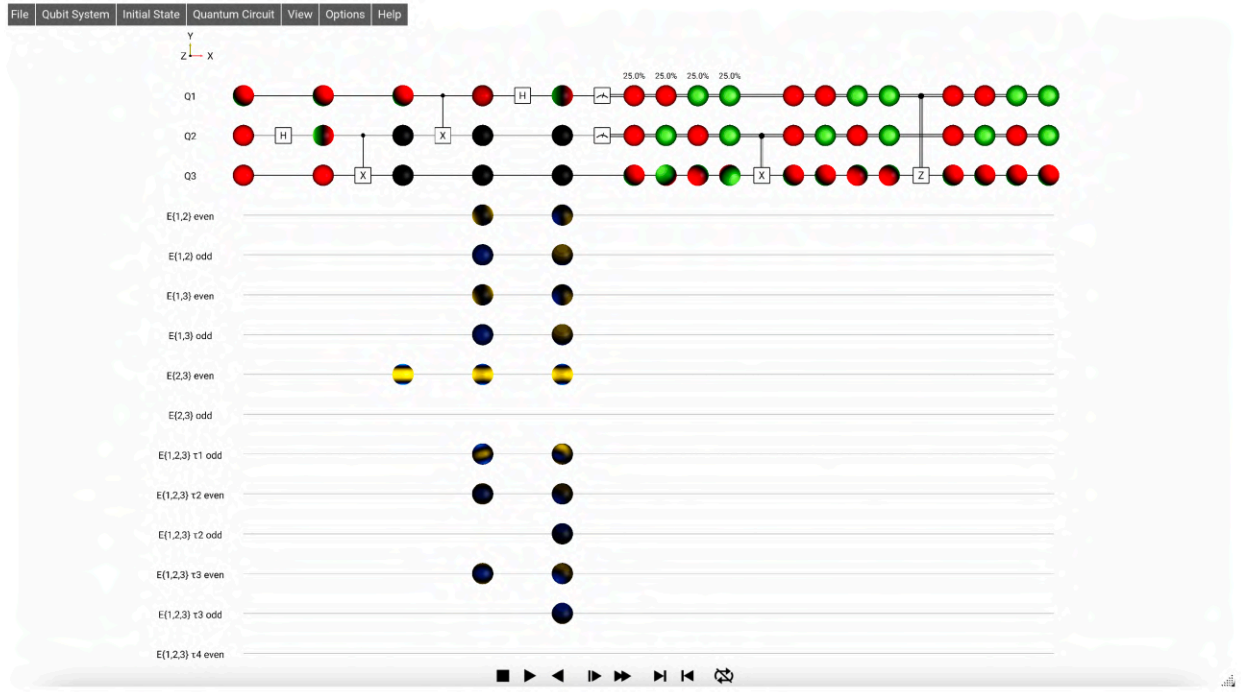
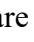


Fig. 63. BEADS-augmented circuit mode in the QuBeads app. A custom quantum circuit and beads corresponding to the system states after each individual operation are visualized. Possible measurement outcomes are simulated and optionally shown simultaneously.

Supplementary video

We provide a video which includes numerous dynamical simulations using the BEADS representation. Throughout this article, examples are marked by a screen symbol  if they are shown in the video.

The video is subdivided into chapters which can be used for fast navigation in most media player devices (e.g., by clicking the “»” menu or using *Command + Shift + arrow keys* in the QuickTime player on MacOS, or by using the Playback → Chapters menu in VLC). The video playback can be precisely controlled by using two-finger trackpad gestures in many media players.

Recall that for dynamical simulations in the QuBeads application, which was used to create the video, the action of a gate is distributed over the *entire* timestep in the corresponding circuit visualization. Timesteps are separated by vertical lines in standard BEADS mode circuits (see, e.g., bottom of Fig. 62 of section S23) and by beads in the BEADS-augmented circuit mode (cf. Fig. 63).

The little quantum pocket guide

The little quantum pocket guide is the result of a collaboration between the authors and the Munich Center of Quantum Science and Technology (MCQST). This guide explains the basics of quantum information on an intuitive and easily accessible level by using the BEADS representation. It is specifically targeted at lays.